University of Southampton

Faculty of Physical Sciences and Engineering

School of Physics and Astronomy

Pulsed laser deposition for the fabrication of all-crystalline resonant reflectors

by

Goby Adithya Govindassamy

ORCID ID: 0000-0002-3205-595X

Thesis for the degree of Doctor of Philosophy

April 2025

University of Southampton

Abstract

Faculty of Physical Sciences and Engineering
School of Physics and Astronomy
Doctor of Philosophy
Pulsed laser deposition for the fabrication of all-crystalline resonant reflectors
by
Goby Adithya Govindassamy

The focus of this project was the development of all-crystalline dielectric resonant reflectors. The final goal to demonstrate the fabricability of single crystal high-reflectivity mirrors, which would potentially remove the limitations of the current state-of-the-art in terms of laser-induced damage threshold (LIDT). Two types of reflectors have been investigated: grating waveguide structures (GWS) and quarter-wave Bragg stacks. The novelty of the work presented in this thesis is the use of epitaxially grown crystalline films to improve the mechanical and thermal properties of the reflectors.

The deposition method of choice for this work was Pulsed Laser Deposition (PLD), owing to its versality and proven efficiency for the epitaxial growth of crystalline films. The project focussed on the optimisation of the growth of sesquioxides on sapphire (0001), in particular Sc_2O_3, Lu_2O_3 and Y_2O_3., and their characterisation in terms of crystallinity, scattering, LIDT and dispersion. Ion probe measurements demonstrated how the chamber background pressure and the target ablation fluence affected the energy of the plasma constituents, and hence the layer growth mechanism. Studying the effect of the pulse repetition rate revealed that with a decreasing repetition rate, the lattice constant of the Sc_2O_3 film decreased and the film became more textured.

The fabrication of the GWSs involved the epitaxial growth of Sc_2O_3 waveguides on etched sapphire substrates. Atomic force microscopy (AFM) measurements showed that the top surface of the waveguide followed the shape of structured substrate, due the high directivity of the PLD plasma. The final GWSs exhibited more than 85% reflectivity at 1030 nm and 70% reflectivity at 1970 nm, for both TE and TM polarisations. The main conclusion was that the uniformity of the waveguide thickness was critical to ensure a high-quality resonance. Bragg mirrors were also grown via PLD, with alternating quarter-wave layers of Sc_2O_3 and Y_2O_3. The reflectivity of the 101-layer sample reached more than 77% at the resonant wavelength, which was tuneable by scanning the surface of the sample. These results validate the possibility of epitaxially growing all-crystalline sesquioxide reflectors for photonics applications.

Table of Contents

Table of Tables

Table of Figures

Research Thesis: Declaration of Authorship

Print name: Goby Adithya Govindassamy

Title of thesis: Pulsed laser deposition for the fabrication of all-crystalline resonant reflectors

I declare that this thesis and the work presented in it are my own and has been generated by me as the result of my own original research.

I confirm that:

1. This work was done wholly or mainly while in candidature for a research degree at this University;
2. Where any part of this thesis has previously been submitted for a degree or any other qualification at this University or any other institution, this has been clearly stated;
3. Where I have consulted the published work of others, this is always clearly attributed;
4. Where I have quoted from the work of others, the source is always given. With the exception of such quotations, this thesis is entirely my own work;
5. I have acknowledged all main sources of help;
6. Where the thesis is based on work done by myself jointly with others, I have made clear exactly what was done by others and what I have contributed myself;
7. Parts of this work have been published as:
    - Govindassamy, G.A., Prentice, J.J., Lunney, J.G., Eason, R.W. and Mackenzie, J.I., 2022. Effect of laser repetition rate on the growth of Sc_2O_3 via pulsed laser deposition. Appl. Phys. A, 128.
    - Stehlik, M., Govindassamy, G.A., Zideluns, J., Lemarchand, F., Wagner, F., Lumeau, J., Mackenzie, J.I. and Gallais, L., 2022. Sub-picosecond 1030 nm laser-induced damage threshold evaluation of pulsed-laser deposited sesquioxide thin films. Optical Engineering, 61(7).
    - Mourkioti, G., Bashir, D., Govindassamy, G.A., Li, F., Eason, R.W., Graf, T., Abdou Ahmed, M., and Mackenzie, J.I., 2023. Sc_2O_3 on sapphire all-crystalline grating–waveguide resonant reflectors. Appl. Phys. B, 129.

Signature: .... Date: 19/04/2025..........................

Acknowledgements

This project was primarily funded by the European Union's Horizon 2020 research and innovation program under the Marie Sklodowska-Curie grant agreement No. 813159.

First and foremost, I would like to thank the person without whom none of this would have been possible: my primary supervisor Jacob. You were always there when I needed your help and rarely put pressure on me despite my relatively slow progress. I was glad that you gave me the autonomy that I needed to grow as researcher, while keeping an eye on me to make sure that I was not heading in the wrong direction. Going through PhD during the COVID period was not easy, but I managed to do it under your guidance.

I am also grateful to the rest of the PWSL research group for their huge support. In particular, Jake is the one who taught me the ABC of the PLD lab and helped me navigate through the various infrastructures around the university. I also received awesome advice from my second supervisor Rob Eason, who spent a significant part of his life working on PLD and finally passed the torch to the next generation.

I obviously cannot write this acknowledgement page without mentioning my fellow PhD student Georgia. We started this journey on the same day and supported each other for three years. You never failed to remind me of upcoming deadlines (hence your nickname Secretary Georgia), and in return, I became your tour guide when we travelled together for consortium meetings, conferences, and secondments. My only regret was never telling you that the last grating that you gave me exploded during PLD... Anyway, I am sincerely grateful that you chose me as your best man for your wedding. Do not hesitate to visit me in France, and as we say in your country: καλωσήρθατε!

I would like to also thank the members of the GREAT consortium. Marek perfectly planned my two-week visit at Institut Fresnel to make sure that I understood everything about LIDT measurements. I appreciate your sincere hard work on our publication. I am thankful to Adrian, who not only let me work in his lab in full autonomy, but also organised "extracurricular" activities in Bordeaux during the weekends. Danish is the one that I owe the most: I still cannot forget the taste of his biryani that I had the chance to enjoy at three different occasions. Finally, I appreciate how Anton introduced me to holographic recording and scanning-beam interference lithography, which have become my daily routine in Horiba Jobin-Yvon.

Lastly, I would like to thank my family and all my friends for their unwavering support. I was lucky to meet Joy during the Advanced Laser classes; she introduced me to Dreamcatcher and remains to this day my favourite Insomnia friend. I also thoroughly enjoyed the interactions with my fellow colleagues from the OpSoc committee, as well as the amazing social events organised by the Indian and K-pop societies.

Thank you all and best wishes!

Definitions and Abbreviations

AFM	Atomic Force Microscopy
FS	Fused Silica
FWHM	Full Width at Half Maximum
GGG	$Gd_3Ga_5O_{12}$
GREAT	Grating Reflector Enabled laser Applications and Training
GWS	Grating Waveguide Structure
LIDT	Laser-Induced Damage Threshold
MS	Magnetron Sputtering
PLD	Pulsed Laser Deposition
RHEED	Reflection High-Energy Electron Diffraction
TE	Transverse Electric
TM	Transverse Magnetic
XRD	X-Ray Diffraction
YAG	$Y_3Al_5O_{12}$
YGG	$Y_3Ga_5O_{12}$

Chapter 1 Introduction

1.1 Motivation

The field of photonics largely contributed to the advancements of modern technologies, especially with the fast development of laser-driven applications. Lasers have gradually become paramount in a wide range of fields: industrial manufacturing with laser drilling and wielding, medical procedures such as laser surgery and high-resolution microscopy, air and water pollution control, fibre telecommunication, etc (Kannatey-Asibu, 2009, Dinara et al., 2020, Hillard, 2020, Zelinger et al., 2004, Zyskind et al., 1992). In order to pursue this technological revolution, a better control over the spatial, spectral, and temporal properties of the light beam is crucial. This statement is particularly true for applications requiring ultrashort pulse durations or an extremely precise evaluation of distances: nuclear physics, attosecond sciences and the study of gravitational waves are typical examples (Antoine et al., 1996, Bunkowski et al., 2006, Gales et al., 2016).

Due to their dispersive nature, diffraction gratings are widely used in applications involving spectral splitting or recombination, such as spectroscopy, wavelength multiplexing, chirped-pulse amplification or pulse compression (Perry et al., 1999, Boyd et al., 1995, He et al., 1999). Chirped-pulse amplification is one of the most prominent innovations in the ultrashort pulse field, as it enables the amplification of the pulse energy by several orders of magnitude. Diffraction gratings play a pivotal role, since they are the key components for the stretching and compression of the laser pulse. Traditionally, pulse compression gratings are gold coated and reach around 80-95% diffraction efficiency. In the state-of-the-art high-power laser systems, the grating coating is regularly considered as a limitation because of its low damage threshold.

The combination of a waveguide with a sub-wavelength grating structure was shown to improve the overall efficiency of energy transfer into a desired diffraction order (Rosenblatt et al., 1997). Such a combination is known as a Grating Waveguide Structure (GWS) and has gained interest in the past few decades (Rosenblatt et al., 1997, Levy-Yurista and Friesem, 2000, Kappel et al., 2004). The main advantage of the GWS is that, with a proper design of the grating and the waveguide, it is theoretically possible to achieve >99.9% diffraction efficiency at the wavelength and angle of design. Exhibiting two separate resonances for TE and TM polarisation, this new type of reflectors meets the frequent requirement of high polarisation rate. Furthermore, tuneability of the wavelength of resonance is possible by varying the angle of incidence of the beam. Consequently, GWS is a suitable concept for spectral stabilisation, wavelength multiplexing and pulse compression, and several studies have successfully demonstrated their implementation in high-power lasers (Ahmed et al., 2011, Dietrich et al., 2017, Rumpel et al., 2014).

However, the current limitations of GWSs are their ability to disperse heat and their limited damage threshold, preventing them from being used in the state-of-the-art high-power laser systems. The goal of this project is to develop GWSs that demonstrate a performance beyond the current state-of-the-art in terms Laser-Induced Damage Threshold (LIDT) and high average power handling, while maintaining an excellent diffraction efficiency. So far, GWSs have only been investigated with amorphous waveguides, with fused silica often used as the substrate. The novelty of my work resides in the use of hard crystals like oxides, who exhibit better thermal and mechanical properties, to increase the LIDT of the final GWS. This type of crystal has never been used in GWSs, because of the complexity of growing crystalline waveguides with traditional deposition methods. As a matter of fact, most deposition methods with these high-melting-point oxides will produce either amorphous films, or at the very best, nanocrystals embedded in an amorphous film.

Multilayer dielectric coatings are another type of reflector that can produce high-reflectivity resonances without relying on metallic coatings. The multilayer coating technology is well-established and already widely used in the industry. Nevertheless, a similar issue as the GWSs arises when the laser power is scaled up: despite several methods developed with the aim of increasing their LIDT, multilayer coatings are often the element where the damage is initiated. In this report, we demonstrate the fabricability of all-crystalline quarter-wave Bragg stacks with a reflectance above 77%. These preliminary results suggest that a much higher reflectance can be reached with proper optimisation.

The work presented in this report focusses on the deposition of crystalline films using Pulsed Laser Deposition (PLD). This deposition method was proven to be very efficient for the epitaxial growth of materials with high melting points, like sapphire, sesquioxides, or garnets. PLD allows a precise control of the thickness of the film, which is critical for a device designed for a specific wavelength / angle of incidence and relying on resonances. The objective was to develop a reliable and reproducible protocol for the deposition of high-quality crystalline films for GWSs or multilayer coatings. Two wavelengths of interest were investigated: 1030 nm for the spectral stability of Yb-doped lasers, and 1970 nm for Tm-lasers.

1.2 Grating Waveguide Structures

1.2.1 Diffraction grating

A diffraction grating is an optical component with a groove pattern that diffracts light into several orders traveling in different directions (Figure 1.1 (a)). The spacing between these lines is typically on the order of the wavelength of interest, enabling the grating to split and diffract light through interference. The grating equation relates the grating period and the angle of the incident beam with the angles of the diffracted orders:

$$m\lambda = d(sin\theta_i + sin\theta_m)$$

Where m is the diffraction order (an integer), λ is the wavelength of the incident light, d is the spacing between the grating lines, θ_i is the angle of the incident light, and θ_m is the angle of the m-th diffracted order.

We define the absolute efficiency of a grating as the ratio between the power diffracted in the order of interest and the incident power. The Fresnel reflection on a mirror defines the theoretical limit of the efficiency for a grating made of the same material. As a result, the choice of the coating material is critical to increase the diffraction efficiency of the grating. While gold is commonly used for near-infrared applications due to its high reflectance above 700 nm (> 97%), aluminium is generally preferred for the lower end of the visible spectrum (Rakić et al., 1998, Shanks et al., 2016). On the other hand, some VUV and XUV applications (e.g. gratings for synchrotrons) might require uncommon metals that exhibit a better reflectance at those wavelengths, such as rhodium, ruthenium, or palladium. Furthermore, some laser applications only require a very high reflectance at the laser wavelength, enabling the use of multilayer dielectric mirrors, which tend to have a short bandwidth and are therefore unsuitable for wide-bandwidth applications. An example of such application is the Laser Mégajoule in Bordeaux, which uses this type of gratings to focus laser beams onto a nuclear target for the study of inertial confinement fusion (Néauport et al., 2005).

Although the coating of the grating defines its potential maximum efficiency, another critical parameter is the groove profile. It is important to distinguish the absolute efficiency of a grating, which was defined in the previous paragraph, and its relative efficiency. The relative efficiency is the ratio between the power diffracted into the order of interest and the power that would be reflected by a mirror of the same coating as the grating, with the same deviation. This quantity can therefore assess the ability of a grating to direct the energy into a particular order without accounting for the coating. The relative efficiency is therefore directly determined by the groove profile.

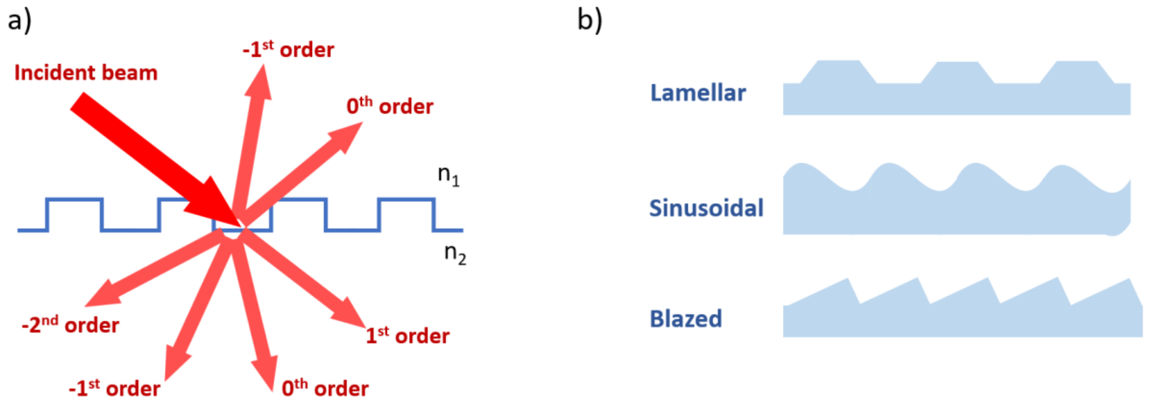

Figure 1.1: a) Working principle of a diffraction grating. b) Types of groove profiles.

A symmetrical groove profile (sinusoidal or lamellar profile) may limit the maximum relative efficiency. In the case where λ is negligible compared to the grating period d, the grating behaviour is qualified as "scalar" and the theoretical relative efficiency of a given order cannot exceed ~40% (Loewen et al., 1997). Nevertheless, when λ is in the same order as d, the grating can exhibit electromagnetic resonances that can theoretically bring the relative efficiencies close to 100%. This resonance is however only possible for either Transverse Electric (TE) or Transverse Magnetic (TM) polarisation, limiting the use of this type of gratings to high-polarisation-rate applications.

A blazed grating (triangular groove profile) redirects the energy preferably into a direction defined by the blaze angle. This allows the grating to overcome the 40%-relative-efficiency-limit of a symmetrical groove profile and potentially reach relative efficiencies above 90%, for both polarisations. However, the fabrication of blazed gratings is more complex than sinusoidal or lamellar gratings, and the control of the blaze angle can be challenging. A minor change in the blaze angle might cause a significant shift of the wavelength of maximum efficiency.

One of the main applications of diffraction gratings is spectroscopy. Due to their ability to disperse wavelengths, gratings are widely used to identify chemical elements present in various type of samples, whether they are in solid, gaseous or liquid form, or even plasma in particle accelerators.

The simplest form of a spectrometer / monochromator is the Czerny-Turner configuration (Figure 1.2 (a)), where the light coming from entrance slit is collimated by a spherical mirror, dispersed by the grating, and focused back on the exit slit by another spherical mirror (Loewen et al., 1997). The angle of incidence on the grating enables the selection of the wavelength to observe. Alternatively, the exit slit may be replaced by a CCD array to record the entire spectrum at once. In this example, the grating is simply made of straight parallel grooves with equal spacing, similar to the grating that were fabricated for our project.

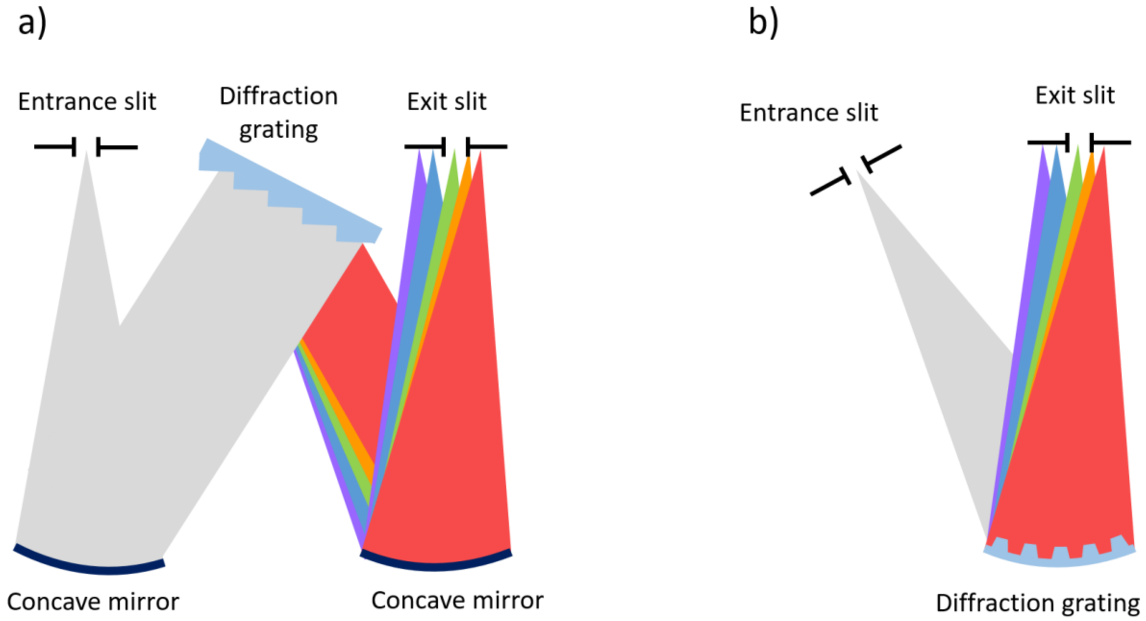

Figure 1.2: Layout of a) a Czerny-Turner monochromator and b) a monochromator with a holographic imaging grating.

Another attractive solution is the use of an imaging holographic grating (Figure 1.2 (b)). In this configuration, the grating handles the imaging by itself, eliminating the need for additional imaging optics, and therefore reducing the size, weight, and cost of the device. This type of grating is holographically recorded by two point sources, creating a more complex groove pattern. The position of these two points is carefully computed during the design process, to ensure that the optical aberrations are minimised in the spectrometer configuration, and as a result, achieve the highest resolution possible (Loewen et al., 1997).

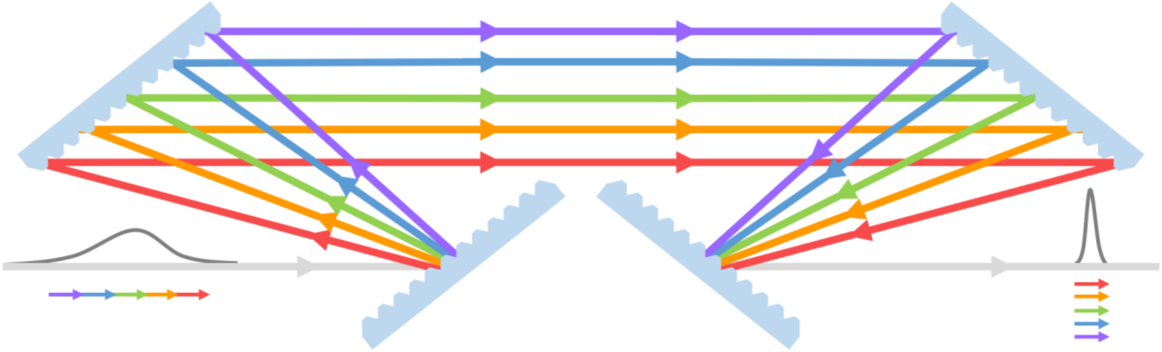

Figure 1.3: Working principle of laser pulse compression with a pair of grating. In the initial pulse, the longer wavelengths are ahead of the shorter ones. The propagation distance of the longer wavelengths is increased to have all the wavelengths in phase.

The second main application of diffraction gratings is pulse compression and stretching. This innovative use of gratings for the creation of “Chirped Pulse Amplification” was rewarded with the Physics Nobel Prize in 2018 (Strickland et al., 1985). At a time when the laser peak powers were not increasing anymore, this novel technique enabled the further amplification of pulses by temporally stretching them. The principle is illustrated in (Figure 1.3), where we can see that the travelling distance is not the same for all wavelengths. The same idea can be applied for the reverse process, i.e. compression of pulses.

1.2.2 Planar waveguides

In a planar waveguide, the waveguide layer has a higher refractive index than the substrate and the cover (Figure 1.4). The waveguide can support two types of mode: “true” guided modes or leaky modes (Snyder et al., 1983). In the case of a true guided mode, the effective index of the mode is lower than that of the waveguiding layer and higher than the media surrounding it (n_{cover}, $n_{subs} < n_{eff} < n_{waveguide}$). In terms of geometric optics, the mode propagating inside the waveguide experiences total internal reflection at the boundaries of the waveguide. On the other hand, a leaky mode will lose energy at each reflection at the interface of the waveguide. In this situation, the effective refractive index of the mode is higher than the cover but lower than the substrate ($n_{cover} < n_{eff} < n_{subs}$, $n_{waveguide}$).

The number of modes supported by the waveguide and their refractive indices are governed by the dispersion equations. They are obtained by solving the Maxwell equations and taking into account the boundary conditions at both interfaces. This produces different sets of solutions for TE and TM modes, which is critical for the design of GWSs.

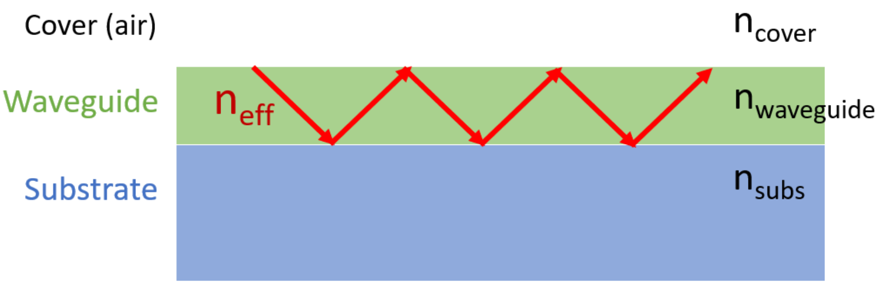

Figure 1.4: Beam propagating in a planar waveguide. The red arrows represent the total internal reflection

1.2.3 GWS and applications

A GWS is a combination of a sub-wavelength grating and a planar waveguide. The theory behind this type of structures has been thoroughly investigated in the past three decades, with (Rosenblatt et al., 1997) establishing the relationship between the GWS parameters (grating period, depth, waveguide thickness, refractive indices) and the resonance conditions. Rigorous coupled-wave analysis is generally employed to simulate the behaviour of a GWS.

The working principle of a GWS is illustrated in Figure 1.5. Under resonance condition (correct wavelength, angle of incidence and polarisation), a leaky propagation mode will be excited. The reflected and transmitted beam will be the result of interferences. With proper design of the grating and waveguide, it is possible to obtain destructive interferences for the transmitted beam and constructive interferences for the reflected beam. The opposite is also achievable, i.e. a 100% transmission and 0% reflection. The main reason for using a sub-wavelength grating is to limit the number of diffracted order and in the ideal case have the first order diffracted in the plane of the waveguide.

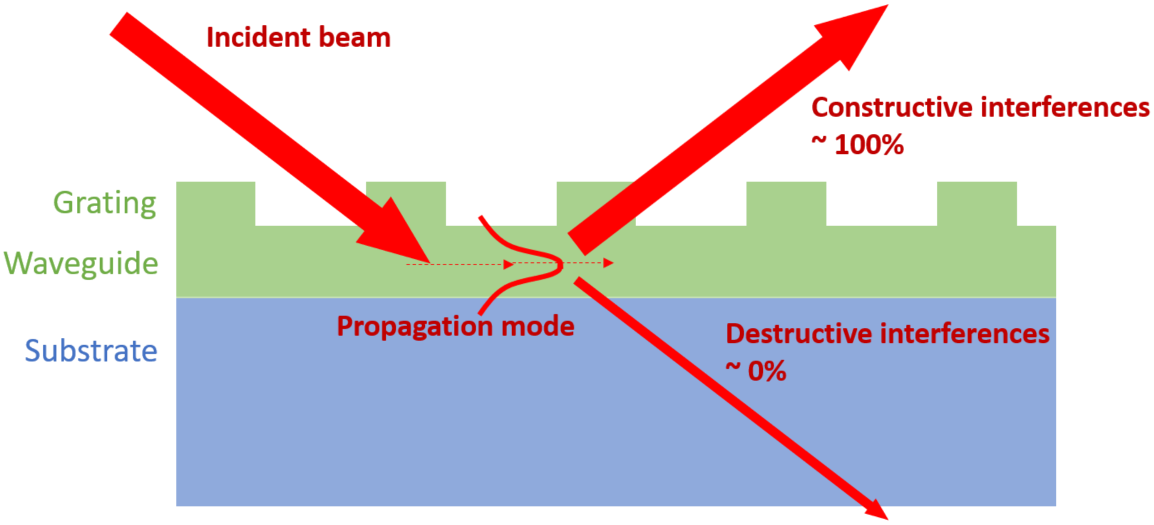

Figure 1.5: Working principle of a Grating Waveguide Structure. This GWS was designed to obtain ~0% transmission.

The grating coupling equations are different for TE and TM polarisation, which enables polarisation-selective applications. A direct consequence is the possibility of using a GWS as an end-cavity polarising mirror in a laser. In most laser systems, the discrimination of the polarisation is typically done by combining a high reflectivity mirror with either a Brewster plate or a thin film polariser. A GWS can offer the same performance with one component instead of two. This is the main application targeted by the GWS that I fabricated during this project. In my case, the GWS was made of a single-layer, and thus only works as a reflector (order 0 of the grating). As illustrated in Figure 1.5, it must therefore be used in the middle of the cavity, while a more complex multilayer GWS could potentially be used as an end-cavity mirror in Littrow configuration (order -1 of the grating overlapping with the incident beam).

A proper design also generates a high reflectivity over a narrow bandwidth, offering a good discrimination of the wavelength. This is paramount for lasing, where an appropriate gain-loss balance is required between the different longitudinal modes of the cavity. As an alternative, it is possible to simply use the dispersive power of the grating and only feedback a narrow bandwidth in the cavity. This wavelength selection is commonly done with the help of a Fabry-Perot etalon. However, a GWS can perform the same task, along with the polarisation selection mentioned earlier, effectively reducing the number of components inside the cavity. Within the emission bandwidth of the laser active medium, the laser wavelength can be tuned by changing the angle of incidence on the grating.

GWSs have the additional advantage to be high-power suitable. When they are used in reflective mode, they exhibit low loss and low thermal lensing because of the short distance of propagation inside the material.

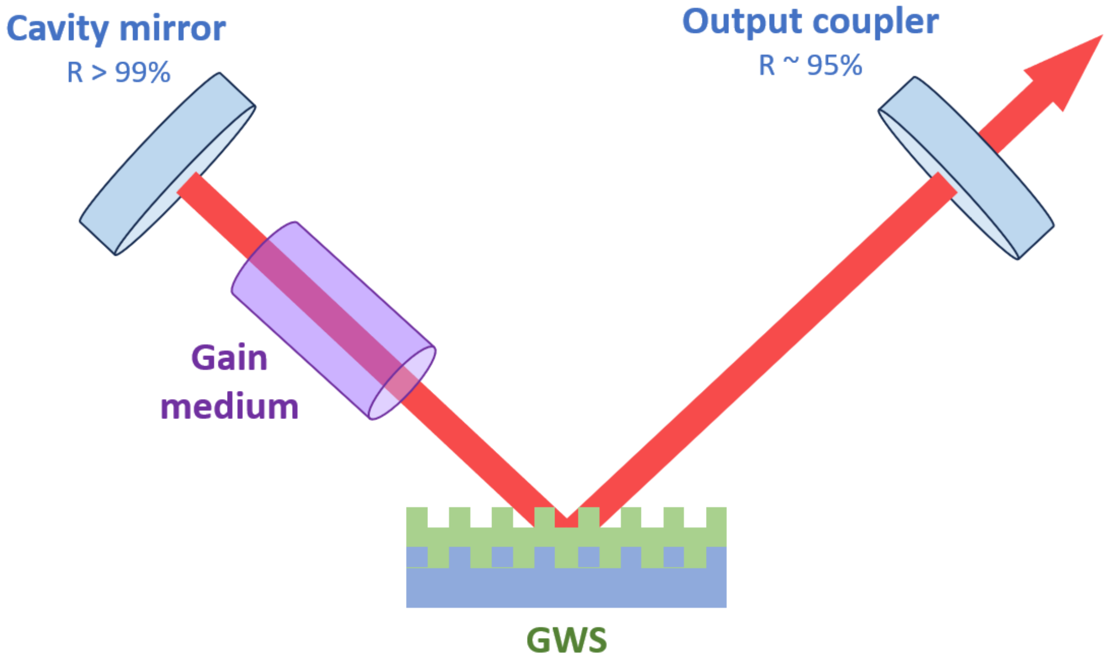

Figure 1.6: Example of laser cavity with a GWS used as a wavelength stabiliser. The polarisation is also imposed by the GWS, because the TE and TM resonances occur at two distinct angles of incidence.

1.2.4 State-of-the-art

High reflection coatings based on multilayers are now routinely fabricated. Coating design is a very well-established field, and it is common to see coatings with a reflectivity above 99% over a large bandwidth. However, these coatings are usually based on entirely or partially amorphous materials and little has been reported about mirrors based on hard crystals. One of the few examples is reported in (Sloyan et al., 2012), introducing a crystalline dielectric mirror with a quarter-wave stack structure deposited via PLD. This mirror, based on alternating layers of YAG and GGG, achieved more than 99 % reflectivity at the wavelength of design. LIDT values up to 33 J/cm^2 were measured in nanosecond regime with a repetition rate of 70 kHz.

The current state-of-the-art has been evaluated for the different applications targeted by GWSs, i.e. pulse compression, spectral and polarisation stabilisation. In most laser systems, the in-cavity discrimination of a polarisation is obtained with the help of a Brewster plate or a thin film polariser. The selection of the wavelength is sometimes done with an additional component such as a Fabry-Perot etalon. The advantage of a GWS is that both polarisation and wavelength selection can be done with one component which also serves as an end-cavity mirror.

A highly efficient GWS suitable for pulse compression has been fabricated with a design optimised to increase the LIDT (Gallais et al., 2020). The GWS consisted in a grating on top of a multilayer coating of amorphous Ta_2O_5 and SiO_2, and a diffraction efficiency up to ~ 99.5 % per single pass was achieved for the 1000-1050 nm wavelength range. The LIDT, measured at 1030 nm with a pulse duration of 500 fs, was close to 0.8 J/cm^2 for the best samples.

The spectral stabilisation of an Yb:LuAG thin-disk laser has been achieved by using an intracavity GWS (Dietrich et al., 2017). The frequency-doubled beam operated at 515 nm and the authors managed to obtain a record value of 51.6 % optical efficiency with an output power up to 1 kW. In this context, the optical efficiency is defined as the ratio of the power diffracted in the order of interest over the incident power. Concerning high-power diode lasers, Volume Bragg Gratings are commonly used for wavelength stabilisation and will act as a reference to evaluate the performances of our GWS.

The above studies involved GWS based on amorphous materials. To the best of my knowledge, no result has been reported in the literature about dielectric crystalline GWS. However, these achievements with amorphous materials demonstrate that the modelling and design theories based on rigorous coupled-wave analysis are well-established and can certainly be adapted to other types of materials, such as garnets or sesquioxides.

1.3 GREAT consortium and methodology

The "Grating Reflectors Enabled laser Applications and Training" (GREAT) Innovative Training Network is a European Union-funded research initiative under the Horizon 2020 Marie Skłodowska-Curie Actions program. The project brought together a consortium of renowned scientific institutions, academic partners, and private sector entities across Europe, including countries like Finland, France, Germany, and the United Kingdom. The primary objective of GREAT was to train 15 early-stage researchers (ESRs) in the development and application of GWSs. The project aimed to provide innovative approaches for the design, fabrication, and implementation of GWS in several laser systems.

The GREAT project addressed a significant shortage of qualified specialized personnel in the field of photonics, as identified by the European Technology Platform Photonics21. By training a new generation of scientists and engineers, the project aimed to strengthen Europe's competitive position in the photonics industry. The ESRs were embedded within various project partners and trained to work collaboratively to deliver groundbreaking research solutions and novel systems, addressing real-world problems. The training encompassed specific expertise related to their PhD projects, additional scientific training covering the entire fabrication chain from design to implementation of GWS devices, and complementary skills, including communications and entrepreneurial training.

The role of each ESR is briefly summarised below:

ESR 1 - Danish Bashir (Institut für Strahlwerkzeuge (IFSW)): Design and optical characterization of grating waveguide structures GWS.

ESR 2 - Ratish Rao (Laboratoire Hubert Curien): Fabrication of GWS for spectral (and linear polarization) stabilization and wavelength multiplexing for 9xx nm, 1030 nm and 2000 nm wavelength range.

ESR 3 - Giovanna Capraro (AMO GmbH): Development and optimization of a Nanoimprint Lithography process for the fabrication of highly efficient GWS.

ESR 4 - Marina Fetisova (University of Eastern Finland (UEF)): Fabrication and characterization grating waveguide structures for spectral shaping (stabilization and pulse compression) and wavelength multiplexing of high-power laser systems GWS.

ESR 5 - Fangfang Li (UEF): Fabrication of GWS for radial and azimuthal polarization shaping in high-power lasers

ESR 6 - Janis Zideluns (Institut Fresnel (IF)): Optical coatings for grating-waveguide structures with the use of Magnetron Sputtering.

ESR 7 - Goby Govindassamy (Optoelectronics Research Centre (ORC)): Crystalline Grating Waveguide Mirrors.

ESR 8 - Anton Savchenko (Institut für Technische Optik): Interference lithography (SBIL resp. SMILE) for the fabrication of circular and segmented GWS for the generation of beams with radial and azimuthal polarization.

ESR 9 - Georgia Mourkioti (ORC): Developing processes for sub-wavelength structuring of crystals.

ESR 10 - Marek Stehlík (IF): Laser damage resistance of materials and structures for grating-waveguide.

ESR 11 - Adrián Grande (Centre Technologique Alphanov): Highly efficient compressor for high average power and highenergy mid-IR femtosecond lasers.

ESR 12 - Ayoub Boubekraoui (IFSW): Spectral stabilization, pulse compression and Wavelength multiplexing of high-power solid-state lasers emitting at 1030nm and 2000 nm.

ESR 13 - Denys Didychenko (IFSW): Efficient intra-cavity and extra-cavity generation of beams radial and azimuthal polarization in high-power thin-disk lasers

ESR 14 - Muhammad Ghawas (University of Bordeaux): Picosecond and femtosecond high power Ytterbium fibre laser designed for optical parametric devices pumping.

ESR 15 - Sayed Muhammad Baker (DILAS GmbH): Investigation of the fundamentals of both wavelength stabilization and dense wavelength multiplexing concepts for diode laser bars using GWS.

The designs of the GWSs were directly provided by ESR1 and were therefore not investigated by me. In a similar way, the integration of my GWSs in real-life laser systems was beyond the scope of my work and was carried out by partners. I focussed mainly on the fabrication and characterisation process. A particular emphasis must be put on ESR9, who closely worked with myself for the fabrication of the crystalline GWS, and ESR6, who was in charge of the optical coatings with Magnetron Sputtering and thus provided a good comparison for the PLD-grown samples.

Since a GWS is the combination of a diffraction grating and a planar waveguide, the fabrication process involves the epitaxial growth of one or several layers of material, as well as the nano-structuring of the surface of the component. Figure 1.7 (a) illustrates the structure of samples which were produced in the context of this project. The etching of the bare substrate was performed by my colleague ESR9, whose objective was to develop a recipe to meet our grating's design parameters. The second half of the fabrication process, i.e. the growth of the crystalline waveguide on the substrate, was my main focus during this project and represents a significant portion of the work presented in this thesis. In particular, we explore the challenges related to the epitaxial growth of a film on a nano-structured substrate, which adds complexity compared to the growth on a simple flat surface. The design represented in Figure 1.7 (b) (not fabricated in this project) includes a high-reflection coating below the waveguide to increase the base reflectivity of the optical device. However, the initial deposition chamber could only hold one target and was therefore not suitable for the deposition of multilayer coatings. As a result, another part of my work involved the full design, fabrication, and integration of a new multi-target system to enable the epitaxial growth of multilayer coatings.

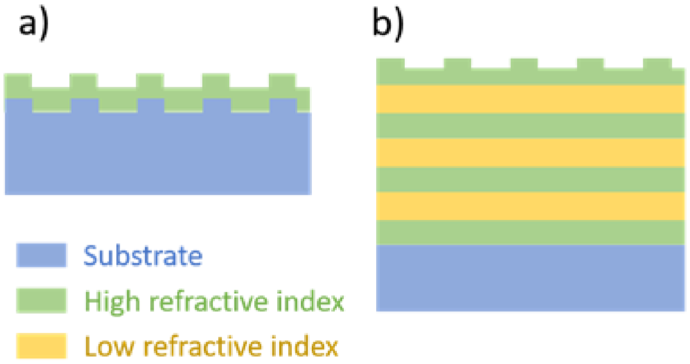

Figure 1.7: Example of Grating Waveguide Structures designed for this project (design b not fabricated).

1.4 List of publications

<u>Journal articles:</u>

- **Govindassamy, G.A.**, Prentice, J.J., Lunney, J.G., Eason, R.W. and Mackenzie, J.I., 2022. Effect of laser repetition rate on the growth of Sc_2O_3 via pulsed laser deposition. Appl. Phys. A, 128.
- Stehlik, M., **Govindassamy, G.A.**, Zideluns, J., Lemarchand, F., Wagner, F., Lumeau, J., Mackenzie, J.I. and Gallais, L., 2022. Sub-picosecond 1030 nm laser-induced damage threshold evaluation of pulsed-laser deposited sesquioxide thin films. Optical Engineering, 61(7).
- Mourkioti, G., Bashir, D., **Govindassamy, G.A.**, Li, F., Eason, R.W., Graf, T., Abdou Ahmed, M., and Mackenzie, J.I., 2023. Sc_2O_3 on sapphire all-crystalline grating–waveguide resonant reflectors. Appl. Phys. B, 129.

Planned submission for journal article:

- **Govindassamy, G.A.**, Mackenzie, J.I., 2024. Epitaxial growth of Y_2O_3/Sc_2O_3 Bragg mirrors with 100+ layers via pulsed laser deposition. Optics Express.

Conference submissions:

- Stehlik, M., **Govindassamy, G.A.**, Zideluns, J., Lemarchand, F., Wagner, F., Lumeau, J., Mackenzie, J.I. and Gallais, L., 2022. Sub-ps 1030 nm laser-induced damage threshold evaluation of pulsed-laser deposited sesquioxides and magnetron-sputtered metal oxide optical coatings. Laser-induced Damage in Optical Materials (SPIE Laser Damage, 2022), Rochester, NY, USA.
- Mourkioti, G., **Govindassamy, G.A.**, Li, F., Eason, R.W., Abdou Ahmed, M., Mackenzie, J.I., 2022. Crystalline Grating-Waveguide Resonant reflectors. 10th EPS-QEOD Europhoton Conference on Solid-State, Fibre, and Waveguide Coherent Light Sources (EUROPHOTON 2022), Hannover, Germany.

1.5 Report structure

The report will first introduce the relevant background to comprehend the context in which this project was conducted. The design requirements and the methodology will be presented to justify our step-by-step approach. The following chapter will present our experimental PLD setup, as well as the theory behind our characterisation methods for a better comprehension of the subsequent chapters. It also includes a review of the materials of interest and all the films deposited in the entirety of the project. Another chapter focusses on the deposition of sesquioxides, starting with an example of parametric growth optimisation, then highlighting key results on the repeatability of the PLD growth process and variations of the film properties (in particular the refractive index and thickness, which are critical for the fabrication of GWs). Another significant proportion of the research investigated the different growth modes of sesquioxides films and aimed at identifying the key parameters driving layer-to-layer growth or 3D-island growth. LIDT campaigns were conducted by a partner institute to determine the crystalline materials exhibiting the most attractive LIDT, as well as comparing them to traditionally used amorphous coatings. The last experimental chapter focusses on the main objective of this project, namely the fabrication and characterisation of the final crystalline reflectors. The first part of this chapter presents the work on the GWS samples for 1030-nm and 1970-nm application. The second part demonstrates how the new multi-target PLD setup was used for the epitaxial growth of Y_2O_3/Sc_2O_3 coatings with 100+ layers and a reflectance above 77% at the wavelength of design.

Chapter 2 Background

2.1 Crystalline growth

2.1.1 Crystal considerations

The key difference between an amorphous material and a crystalline material is that the latter has a periodicity at the atomic level (Figure 2.1). The lattice constant is a fundamental parameter that defines this periodicity of the atomic arrangement in the crystal. Before planning the growth of a crystalline film on a substrate, it is critical to verify whether the lattice constants of both materials match correctly, otherwise the excessive strain in the film may lead to dislocation (Figure 2.2 (a)), or the film may simply not grow at all.

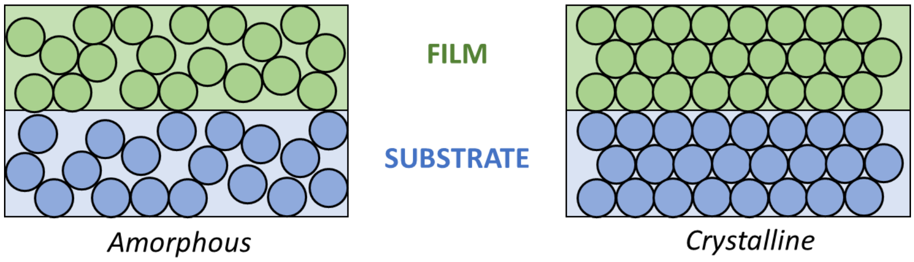

Figure 2.1: Diagram of the structure of the atoms in the case of amorphous deposition and crystalline deposition.

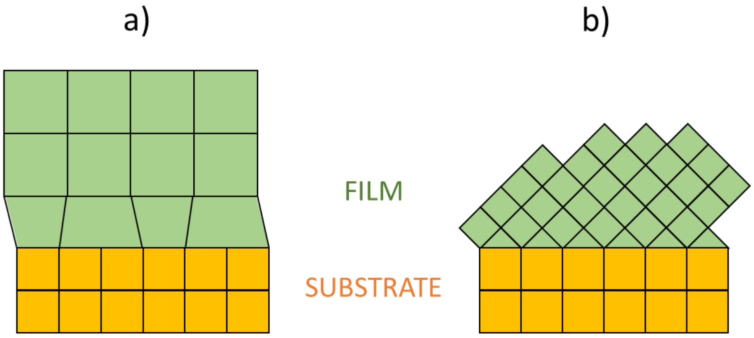

Figure 2.2: a) Dislocations resulting from a large lattice mismatch between the film and the substrate. b) A good match is obtained despite very different lattice constants.

Each crystal orientation is defined by a unique set of Miller indices (hkl), which describe the atomic planes within the crystal lattice. Different crystal orientations, such as (100), (110), (111), etc., correspond to different arrangements of atoms and spacing between atomic planes. As a result, the film and substrate do not necessarily need to have the same crystal orientation: in some cases, a different orientation of the film may have a good lattice match with the substrate. This principle is illustrated in Figure 2.2 (b), and will be further discussed in this chapter with specific examples relevant to the project.

The expression “epitaxial growth” refers to the growth of a perfect crystal without any defect in the lattice. For our application, such high level of crystallinity is not required. As highlighted in the introduction, the PLD-grown samples will be directly compared to the ones deposited via magnetron sputtering. In the best conditions, magnetron sputtering only manages to produce nanocrystals embedded in an amorphous film. Despite the defects that PLD-grown films might exhibit, they are much closer to a single crystal than the equivalent magnetron-sputtered films, and we can assume that the mechanical and thermal properties are significantly better. On the other hand, it is unlikely that the minor defects in these PLD films induce a much lower performance than the perfect crystal. For this reason, we will still inaccurately use the expression “epitaxial growth” to designate the PLD growth process, even though this terminology originally implies that the crystal is perfect.

2.1.2 X-ray diffraction

For epitaxial films grown via PLD, determining the orientation is critical to assess whether the film follows the substrate's orientation or exhibits defects like misalignment, mosaicity, twinning, etc. X-ray diffraction is a powerful technique for determining the orientation and structure of crystalline materials (Cullity, 1956, Lecomte, 2013, Birkholz et al., 2005, Pietsch et al., 2004). XRD relies on the observation of X-rays scattered by the periodic atomic planes within a crystal. The condition for constructive interference is given by Bragg’s law:

$$n\lambda = 2d\sin(\theta)$$

Where:

- n is an integer (order of diffraction),
- λ is the wavelength of the X-ray source,
- d is the interplanar spacing of the crystal lattice,
- θ is the angle of incidence (and diffraction).

When an X-ray beam is incident on a crystal, the orientation and spacing of the atomic planes determine the angles at which diffraction peaks occur. By identifying these diffraction angles, one can extract information about the crystal, which is why the diffraction pattern is often considered as a “fingerprint” of the crystal structure and orientation. Online databases like ICSD provide information on the expected position of the diffraction peaks for a specific material, along with the crystal orientation corresponding to each peak. Inversely, from a given diffraction angle, the distance between the crystal planes (and hence the lattice constant) can be calculated with Bragg’s law.

To characterise our crystalline films grown by PLD, we mostly relied on the two following XRD techniques:

- θ-2θ scans are used to determine the out-of-plane orientation by measuring diffraction peaks corresponding to planes parallel to the substrate (Figure 2.3). In that configuration, the incident angle and the detection angle are symmetrical with respect to the surface normal. The out-of-plane lattice constant can be directly computed from the position of the diffraction peaks.
- Rocking curves measure the width of a diffraction peak by tilting the sample slightly around a specific 2θ position. Narrow rocking curves indicate high-quality films with low mosaicity (crystal misorientation).

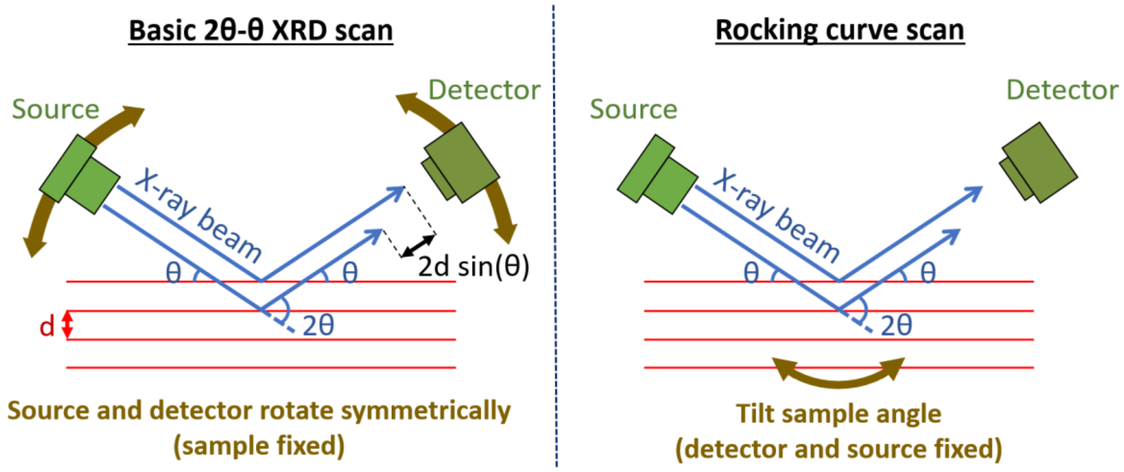

Figure 2.3: Working principle of a 2θ XRD scan and a rocking curve scan.

Some pole figures were recorded for different studies, but the results were not significant enough to be presented in this thesis. Other advanced XRD techniques, such as reciprocal space mapping, could have provided more detailed information about the orientation, strain, and lattice mismatch of films, but were not used in this project. Indeed, by mapping the diffracted intensity in reciprocal space, one can determine the epitaxial relationships between the film and the substrate, identify tilted or strained domains, and detect dislocations.

2.1.3 Lattice match

A significant part of this thesis focusses on the deposition of sesquioxide films on sapphire substrates. While sesquioxides have a cubic structure, the lattice of sapphire presents a hexagonal arrangement along the (0001) plane. However, the <111> orientation of sesquioxides such as Y_2O_3, Lu_2O_3 and Sc_2O_3 can potentially fit the <0001> orientation of sapphire, due to their 3-folded rotational symmetry. In that configuration, a perfect match between the substrate and the film would happen if the following condition is met: $\sqrt{2}\, a_{film} = 3\, a_{sapph}$, where a_{film} is the lattice constant of the film and a_{sapph} is the lattice constant of sapphire along the (1000) plane (Figure 2.4). For our materials of interest, this condition is almost met, with only a 2.5% lattice mismatch between Sc_2O_3 and sapphire. The risk of thermal stress during the cooling of the sample after deposition is also limited due to the very close thermal expansion coefficients of this group of sesquioxides with sapphire (Bar et al., 2003).

Interestingly, a perfect lattice match can be achieved in theory with a film of mixed-sesquioxides. With the correct stoichiometry of two or three of the above materials, the mismatch between the film and the substrate can be brought to zero. While the lattice mismatch still exists at the microscopic level in this type of “hybrid” films, the overall strain is indeed relieved with this method.

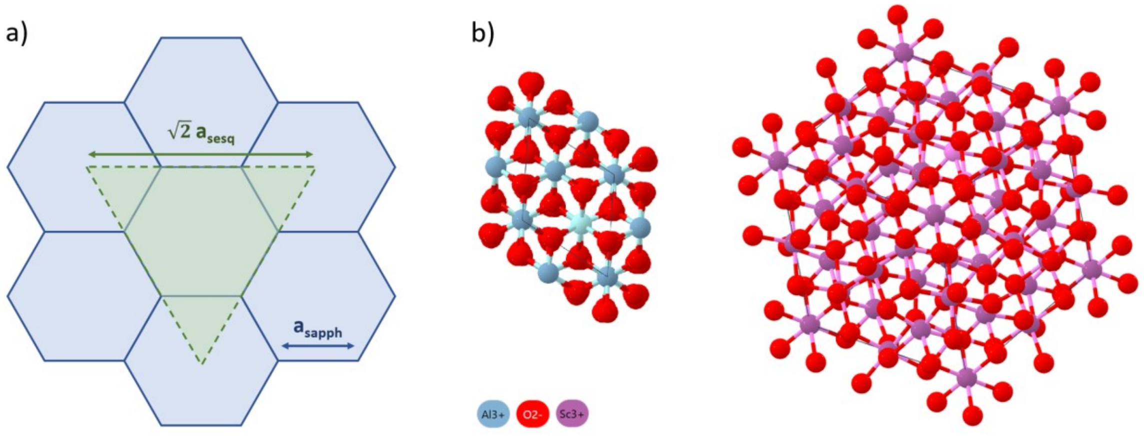

Figure 2.4: a) Illustration of the possible lattice match between the (0001) planes of the sapphire lattice and the <111> orientation of Y_2O_3, Lu_2O_3 and Sc_2O_3. b) Illustration of the atomic structure of the sapphire lattice in the <0001> orientation (left) and Sc_2O_3 in the <111> orientation (right).

2.2 Pulsed Laser Deposition

2.2.1 Introduction to PLD

PLD is a well-established film deposition method for the growth of crystalline films. Only a few years following the invention of the laser, (Smith, 1965) presented a basic setup that could be called the ancestor of PLD, with relatively low efficiency. It is only after the generalisation of Q-switching in the next decade that PLD started to gain interest and experience fast development, owing to the use of nanosecond ablation pulses, which is still the norm today. The late 1980s and the 1990s demonstrated the utility of PLD in many fields, such as the growth of lasers, or high-temperature superconducting films (Chiba et al., 1991, Gill et al., 1996). The progressive implementation of PLD machines in the industry contributed to the funding of further research projects to improve the quality of growth and explore new potential applications.

In a typical PLD setup, a high energy pulsed UV laser is commonly used to ablate the target and create a plasma plume that will deposit on the substrate (Figure 2.5). The target is usually made from powders of the material to be deposited, which means that the elements are present in the target in stoichiometric proportions. An advantage of PLD is the near conservation of the stoichiometry from target to film. A small difference might be observed if one of the elements is significantly more volatile than the others.

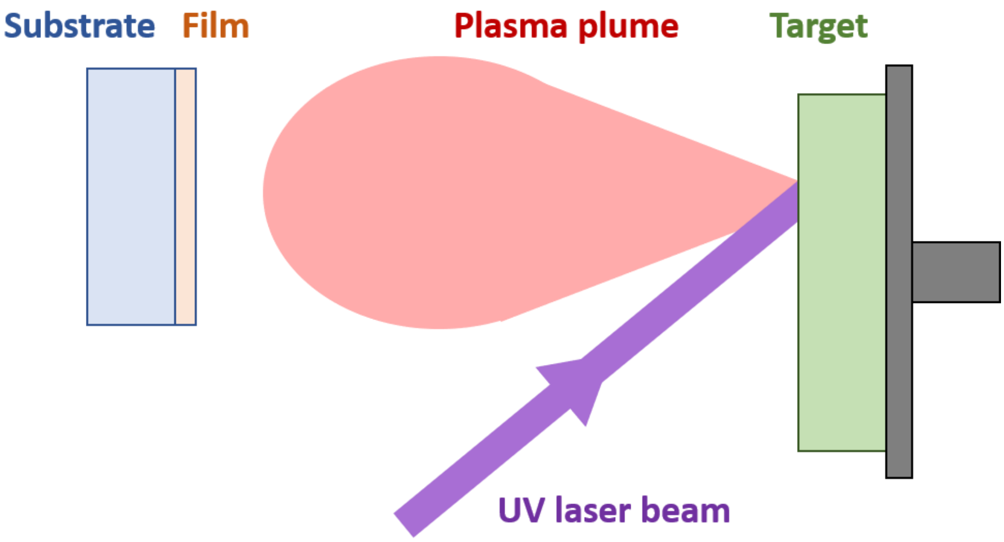

Figure 2.5: Schematic of a typical PLD setup.

Various theories have been developed to explain the complex mechanisms driving the ablation process. In the case of a ~20 ns pulse duration, the ablation can be described as a 4-step process (Ojeda-G-P et al., 2015). Firstly, the laser pulse is absorbed by the target, heating the surface locally. As the temperature increases, the material melts and then vaporises, forming a plume that initially stays close to the surface. At this stage, the laser pulse is still occurring and is now directly absorbed by the plume, ionising it partially and causing it to expand away from the target. The melting process alters the surface of the target which now exhibits some irregularities at the microscopic level. These irregularities remain after the surface cools down, become more defined over time, and are responsible for the ejection of clusters of material from the target.

A particularity of PLD is that the temperature of the substrate is higher than most deposition methods, typically above 500°C. The high substrate temperature is generally obtained with one of the two following methods:

- An electric heater can be placed in direct contact with the back surface of the sample.
- A laser beam can heat the rear surface of the sample if the substrate is strongly absorbing at the wavelength of operation.

Laser-beam heating gives access to higher deposition temperatures, which is more favourable for the growth of high-melting-point materials.

2.2.2 Plume expansion

Understanding the dynamics of the plume can be very useful to estimate the kinetic energy of the species arriving at the sample. While several complex models have been reported in the literature, they generally tend to be hard to adapt to different materials. Here we will focus on a simpler model that was proven to be accurate by (Sambri et al., 2008, Amoruso et al., 2008).

The plume, of total mass M_{plume}, is distributed over a thin hemispherical layer of radius *R*, centred on the target. In order to expand from a radius *R* to a radius *R+dR*, the plume must ‘push’ the gas present in that layer volume. As a consequence, the plume will lose some momentum that will depend on the density of the gas to be pushed ρ_{gas} (and thus on the pressure of the gas P_{gas} and its temperature) and the distance *R* from the target. Starting from this simple model, the equations can be derived to obtain the dependence of the plume front velocity *u* with the distance from the target (Sambri et al., 2008, Amoruso, 2018):

$$u(R) = c_0 \sqrt{\frac{b^2}{(a^3 + R^3)^2} - 1}$$

where $$c_0 = \sqrt{\frac{P_{gas}}{\rho_{gas}}}, \qquad a = \sqrt[3]{\frac{3\, M_{plume}}{2\pi\, \rho_{gas}}}, \qquad b = a^3 \sqrt{1 + (\frac{u_0}{c_0})^2}$$

The only unknown parameters during a deposition are the plume initial velocity u_0 at the target and the total mass of the plume M_{plume}. However, the latter can be easily estimated by weighing the target before and after deposition. For our nominal deposition parameters, we generally have a plume mass in the 0.1-1 µg range.

By integrating the equation giving the relationship between plume velocity and distance from target, it is possible to calculate the position of the plume front as a function of time. However, we need to know at least one point of this curve in order to perform a fit and deduce the rest of the curve. Ion probe measurements are a suitable solution to obtain the points needed for this fit (section 4.6.1.1).

In practice, with our materials of interest and the range of deposition parameters that we are using, the plasma plume is highly directional. This low angular dispersion, associated with the relatively high growth rate (later estimated to 20 atomic monolayers per second for Sc_2O_3 on sapphire), ensures that the deposition is conformal. This is an important advantage of PLD, since maintaining the original substrate profile has proven to be challenging for other sputtering methods. Typically, a trapezoidal grating profile would gradually become rounded, and the space between the grooves would reduce due the significant deposition on the sidewalls. The deposition of a multilayer coating on top of a grating cannot even be contemplated, since the initial grating profile would quickly disappear. The worst results are observed with slow and low-energy techniques, such as Chemical Vapour Deposition. This is where PLD can outperform other deposition methods, owing to its conformal nature.

2.2.3 Formation of islands in the film

Different growth modes are possible during deposition (Aziz, 2008): layer-by-layer growths (Frank-van der Merwe), island growth (Volmer-Weber), or layer-plus-island growth, where the film grows as 2D layers up until a critical thickness, beyond which 3D-clusters start forming (Stranski-Krastinov). We typically want to avoid 3D-island growth, which increases the film’s roughness and the number of dislocations. In contrast, layer-by-layer growth ensures that the film grows uniformly without discontinuities.

In most deposition methods, the energy of the adatoms is mainly determined by the temperature of the surface; the nucleation of the atoms is thus a purely thermal process, and their average diffusion length / mobility can be calculated from the temperature of deposition. For such a deposition method, an increase of the mobility of the adatoms may promote layer-by-layer growth: if the adatom lands on an island which is part of an unfinished layer, the adatom might diffuse to the edge of the island, fall to the lower terrace, and nucleate in the unfinished layer. If this adatom had a low mobility, it would stay on top of that island, which would progressively become a 3D island. An interesting observation is that the mobility of the adatoms is not only determined by the temperature, but also the background pressure.

In the case of PLD, we also need to consider the effect of the plume. Indeed, the particles of the plasma plume arrive on the surface with energy levels ranging from 10s of eV to 100s of eV, which is much higher than the energy levels involved in the thermal process (typically a few 0.1 eV). Ions and atoms incident on the surface have enough kinetic energy to shatter small islands and at least reduce the size of large islands (Ulbrandt et al., 2020a). Although this smoothing effect of the plume happens periodically, between pulses the thermal diffusion is predominant. The final morphology of the film is therefore a result of the balance between these two processes. Monte-Carlo simulations have been developed to understand the diffusion mechanisms and predict the formation of islands during PLD (Ulbrandt et al., 2020a, Willmott et al., 2006b, Jacobsen et al., 1998, Gabriel et al., 2020b).

Blank et al. developed a novel approach to promote layer-by-layer growth during PLD (Blank et al., 2000a). By using reflection high-energy electron diffraction (RHEED) oscillations during the deposition of $SrTiO_3$, they were able to determine the characteristic relaxation time of the adatoms on the surface, i.e. the time during which the adatoms diffuse on the surface before locking their position. This was measured to be typically in the 0.25-0.5 s range. On the other hand, a long inter-pulse time can favour the aggregation of larger islands, in particular if the surface is only partially covered with adatoms. This phenomenon is minimised if the surface coverage fraction is 100%, which mean that the top layer is complete and atomically flat. The new approach, called pulsed laser interval deposition, consisted in depositing as fast as possible the exact amount of material required to complete a unit-cell layer, and waiting for a duration longer than the relaxation time before the next set of pulses. The fast deposition phase ensures that the time during which the surface is partially covered is minimised, effectively reducing the chances of island ripening.

2.3 Materials of interest

2.3.1 Optical constants

The refractive index is a fundamental optical property of materials that describes how light propagates through a medium. It is a complex quantity, typically expressed as $\tilde{n} = n + i\kappa$, where n is the real part and κ is the imaginary part. The real part n, dictates the phase velocity of light in the material, while the imaginary part κ, is associated with the attenuation of the electromagnetic wave due to absorption.

The absorption process is governed by the interaction of the electromagnetic field with the material's electrons. When light propagates through a material, its oscillating electric field can induce electronic transitions between energy levels. It corresponds to the excitation of free electrons in metals, and transitions across the bandgap or between electronic states in semiconductors and insulators. Consequently, the absorption profile is wavelength-dependent and provides information about the electronic structure of the material.

The imaginary part of the refractive index κ is directly related to the material's absorption coefficient α, which quantifies how quickly the intensity of light decreases as it travels through the material. This relationship is given by $\alpha = 4\pi\kappa/\lambda$, where λ is the wavelength of light in vacuum. Therefore, a higher value of κ indicates a stronger absorption. For instance, metals exhibit high values of κ in the visible and infrared regions due to free-electron absorption, whereas semiconductors and dielectrics generally have strong absorption near their bandgap energies.

The real part of the refractive index is critical in the design of a GWS, as it is involved in the Fresnel reflection at each interface, in the grating dispersion equation in transmission mode, and also in the waveguiding conditions. However, the imaginary part also plays a major role, since the absorption at the wavelength of design might potentially decrease the efficiency of the reflector. Indeed, despite the short thickness of the waveguides in this project (1 µm or less), significant absorption might occur in the few 100s of µm travelled by the beam inside of the waveguide before most of the energy is radiated. For this reason, the complex refractive index must be determined for our materials of interest before designing the GWSs.

2.3.2 Ellipsometry

Ellipsometry is an optical technique that measures the change in polarisation state of the light reflected by a material. The method is based on the fact that polarised light interacts differently with a material depending on its optical properties, including the complex refractive index and the thickness (if the material is a thin film). With favourable measurement conditions and a rigorous model, ellipsometry can provide highly accurate, wavelength-dependent information about both the real and imaginary parts of the refractive index, as well as film thicknesses down to the nanometre scale.

A beam of polarised light is directed at the sample at a given incident angle. The interaction of this light with the material causes a change in the amplitude and phase of the light's TE and TM components. The resulting polarisation state of the reflected light is measured as two parameters: the ratio of the amplitudes Ψ and the phase difference Δ between them. These parameters are related to the material's complex Fresnel reflection coefficients, which depend on the refractive index, absorption, and thickness of the material. Ψ and Δ are fitted to theoretical models to extract material parameters. These models rely on the Fresnel equations, which describe how light reflects and refracts at interfaces between materials. For thin films, interference effects arising from multiple reflections within the layers are also taken into account. By varying the wavelength of the incident light, ellipsometry can provide spectral information about the refractive index n and extinction coefficient κ over a wide range of energies.

One of the key advantages of ellipsometry is its non-destructive nature, making it a favourable candidate for in situ and ex situ analysis of materials and thin films. Furthermore, its sensitivity to both the real and imaginary parts of the refractive index allow it to detect subtle changes in optical properties caused by variations in the manufacturing method. This has made ellipsometry a paramount characterisation method in fields such as photovoltaics, photonics, microelectronics, and surface science.

Some Y_2O_3, Lu_2O_3 and Sc_2O_3 films were grown on sapphire with minimal optimisation of the process. The dispersion curves of these samples were measured by ellipsometry by our partners in Laboratoire Hubert Curien, France. I compared the results to the corresponding curves found in the literature (Medenbach et al., 2001). As indicated by Figure 2.6, for our main material of interest Sc_2O_3, the refractive index of the deposited film is slightly higher than the bulk material. At 1030 nm, the difference in refractive index between film and bulk material is 0.0054 for Sc_2O_3 and only 0.0011 for Lu_2O_3. This difference may either be caused by additional stress in the film, or by an imperfect stoichiometry.

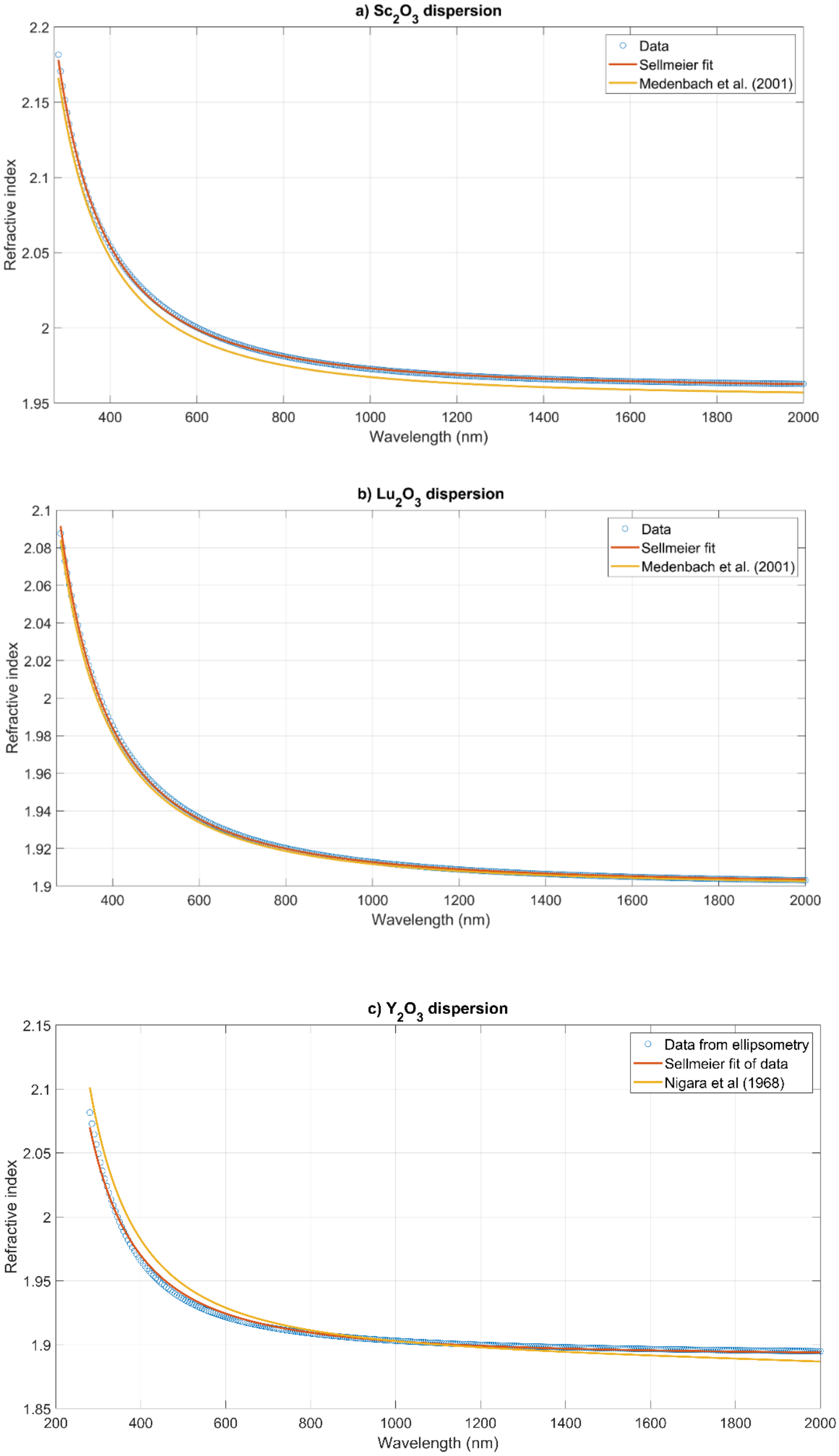

Figure 2.6: Dispersion curves of a) Sc_2O_3 , b) Lu_2O_3 and c) Y_2O_3 films deposited on sapphire. The data and the fitted curve are compared to results found in the literature (Medenbach et al., 2001).

Table 2.1: Comparison of the Sellmeier coefficients for as-grown films and bulk materials.

Material	Type	B coefficient	C coefficient
Sc_2O_3	bulk	2.817	0.0186
Sc_2O_3	film	2.838	0.0190
Lu_2O_3	bulk	2.609	0.0172
Lu_2O_3	film	2.612	0.0177
Y_2O_3	bulk	2.578	0.0192
Y_2O_3	film	2.5762	0.0169

All dispersion curves were fitted with the following Sellmeier equation:

$$n(\lambda)^2 = 1 + \frac{B\,\lambda^2}{\lambda^2 - C}$$

The coefficients for deposited films and bulk material are listed in Table 2.1.

Concerning the imaginary part, Lu_2O_3 was the only film to exhibit significant absorption, with κ reaching 0.0234 at 1030 nm and 0.0122 at 1970 nm. On the other hand, κ was lower than 10^{-4} in Y_2O_3 and Sc_2O_3, resulting in negligible absorption from these two materials. They are therefore good candidates for our crystalline reflectors.

2.3.3 Candidates for GWS

Several materials were investigated as potential candidates for our GWSs. Apart from the high diffraction efficiency, the devices must also satisfy the objectives in terms of LIDT and thermal conductivity.

Among the widely available substrates, YAG and sapphire present the advantage to be less expensive and of higher quality. The growth of garnets (such as YGG, GGG) in their <001> orientation was attempted on YAG (001) substrates. On the other hand, the growth of sesquioxides in their <111> orientation was performed on sapphire (0001) substrates. Table 2.2 summarises all combinations of substrate-film materials that have been deposited during the entire project. Note that the Y_2O_3 substrates were of poor quality; despite the manufacturer claiming it to be a single crystal, XRD scans did not reveal a strong crystallinity, nor a clear predominant orientation. This observation further justifies the use of YAG and sapphire substrate, whose XRD scan exhibit a single, strong thin peak at the expected 2θ angle.

Table 2.2: Combinations of materials that have been studied. One bi-layer structure has also been investigated (not listed on this table): Y_2O_3 (111) on Sc_2O_3 (111) on sapphire (0001).

Substrate	**Plane of deposition**	**Film**	**Dominant orientation**
YAG	(001)	YGG	<001>
YAG	(001)	GGG	<001>
YAG	(001)	YAG	<001>
YAG	(001)	Y_2O_3	<111>
YAG	(001)	Lu_2O_3	<111>
sapphire	(0001)	Y_2O_3	<111>
sapphire	(0001)	Lu_2O_3	<111>
sapphire	(0001)	Sc_2O_3	<111>
Y_2O_3	(111)	sapphire	<0001>

Table 2.3: Properties of the materials of interest. Refractive indices were measured via ellipsometry on our samples by our partners. Thermal conductivity and bandgap from the literature (Griebner et al., 2004, Giesting and Hofmeister, 2002, Slack and Oliver, 1971)

Formula	**Refractive index @ 1030 nm**	**Thermal conductivity (W/m/K) @ 300 K**	**Structure**
Y_2O_3	1.903	13.6	cubic
Lu_2O_3	1.912	12.5	cubic
Sc_2O_3	1.970	16.5	cubic
sapphire	1.776	38	hexagonal
YGG	1.941	9	cubic
GGG	1.971	10.3	cubic
YAG	1.832	11	cubic

The key properties of the materials of interest are listed in Table 2.3. Ellipsometry measurements were performed by our partners in Laboratoire Hubert Curien (France) to obtain the dispersion curve of all the materials deposited. While the thermal conductivity of YAG lies around 11 $W.m^{-1}.K^{-1}$ (Griebner et al., 2004), sapphire's thermal conductivity is close to 38 $W.m^{-1}.K^{-1}$ at room temperature

(White, 1995). Furthermore, the refractive index of sapphire is lower than YAG, allowing a larger refractive index contrast between the substrate and the film. Consequently, it seems more advantageous to select sapphire as the substrate for our grating waveguides.

In the past, quarter-wave stacks based on garnets have been successfully grown to obtain HR mirrors (Sloyan et al., 2012). However, despite the fact that they are harder to grow than garnets, the following aspects make sesquioxides more attractive for our GWSs:

- Sesquioxides have a higher thermal conductivity than garnets.
- The refractive index contrast between the film and the substrate is larger than garnets, favouring waveguiding and minimising the number of layers needed for a multilayer mirror.
- Among the materials investigated, the sesquioxides have a higher bandgap than the garnets, which can correlate to a higher one-shot LIDT.

As a result, most of the work reported in this document focusses on the deposition of sesquioxides on sapphire, with Sc_2O_3 being the best candidate, owing to its large refractive index contrast with sapphire compared to other sesquioxides.

2.4 Quarter-wave Bragg stack

The deposition of multilayers for crystalline mirrors requires an understanding of the Bragg reflector theory. The ultimate objective is to obtain high reflectivity at a particular wavelength and for a specific angle of incidence. In our case, the most interesting configuration is the simple quarter-wave stack, whose structure is illustrated in Figure 2.7. For simplification, the following discussion refers to a mirror designed for operation at normal incidence.

A multilayer is composed of layers of alternating materials. In this case, we present the behaviour of a multilayer composed of two materials only, one with a high refractive index n_H and the other one with a low refractive index n_L. When the incident beam arrives on a multilayer, it will be partially reflected at each interface because of the Fresnel reflection. A quarter-wave Bragg stack is designed in such a way that the waves reflected at each interface will all be in phase and hence add coherently. To obtain this phenomenon, the optical thickness of each layer is set to $\lambda/4$, λ being the wavelength where we want maximum reflection. As a result, each layer will add an optical path of $\lambda/2$ for a double pass. Moreover, when a light wave is reflected at an interface from a low refractive index medium to a high refractive index medium, it receives an additional π phase shift. Therefore, the wave reflected at the first interface will effectively be in phase with all the reflections at the following interfaces.

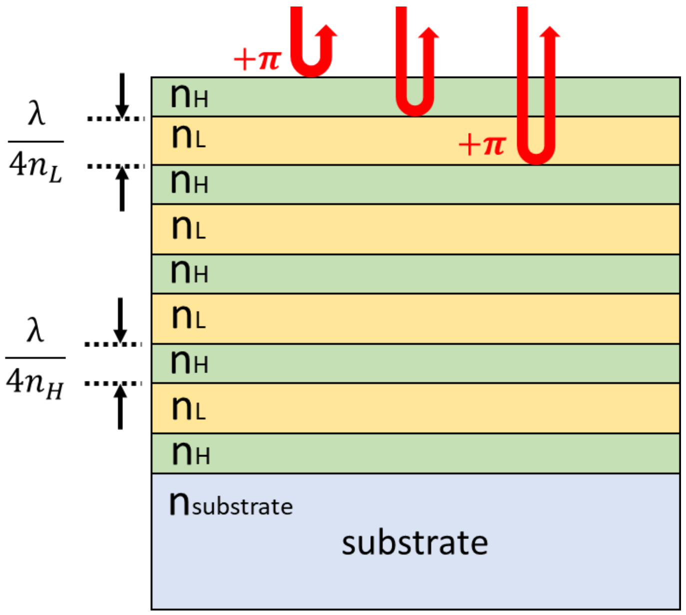

Figure 2.7: Diagram illustrating the working principle of a quarter-wave Bragg stack. n_H : high refractive index. n_L : low refractive index.

For operation at an angle different from 0^o, the same reasoning can be applied. The optical path δ added by each layer is related to the angle of incidence θ, the thickness of the layer *d* and the refractive index n by the following equation:

$$\delta = 2nd\ cos(\theta)$$

δ must be a multiple of the wavelength of interest to obtain high reflectivity.

In magnetron sputtering, SiO_2 is generally selected as the low-refractive-index material, not only because its deposition has been widely investigated, but also because of its high bandgap energy, which is favourable in terms of LIDT in the femtosecond regime. On the other hand, three high-refractive-index materials were studied by ESR6 Janis Zideluns : Nb_2O_5, Ta_2O_5 and HfO_2. The coating process of these three materials was optimised and the samples went through a similar characterisation step than our PLD-grown films to assess their quality and suitability for GWS. In particular, both deposition methods will be confronted in Chapter 4 with the LIDT study.

Chapter 3 Theory and experimental methods

In this chapter, we first introduce the PLD experimental setup used for our epitaxial film growths. Two different configurations of the PLD chamber are presented: the initial setup, which could only hold one target at a time and therefore only allowed the growth of single layers; and the multi-target system that I developed, which enabled the growth of multilayers. The following sections focus on standard methods that are recurrently used throughout the different chapters to quantify the amount of scattering light from a film and to process XRD data. Finally, the last section demonstrates how the thickness of a film is determined by measuring its transmission spectrum.

3.1 Pulsed Laser Deposition

3.1.1 Deposition chamber

Our deposition chamber is illustrated in Figure 3.1. A KrF excimer laser operating at 248 nm is focussed on the target to ablate its surface. The excimer controls allow the user to precisely select the energy of the pulse, the repetition rate and the total number of pulses launched for a deposition. A focussing lens is used to finely tune the spot size on the target surface (typically a 2 x 3.5 mm rectangular spot), hence the desired ablation fluence can be obtained by adjusting both pulse energy and spot size.

In order to obtain epitaxial growth, the atoms require higher energy levels than during amorphous deposition. This additional energy is provided by heating the substrate to temperatures often exceeding 500^{o}C. In our setup, the substrate is heated by a CO_2 laser operating at 10.6 µm. The standard substrate size used is 10 x 10 x 1 mm. A uniform heating of the substrate can be achieved using a ZnSe tetraprism that will transform the gaussian beam profile produced by CO_2 the laser into a square top-hat profile that matches the substrate. A beam splitter at the output of the laser reflects part of the beam to a powermeter, allowing the user to monitor the variations of heating power during the growth.

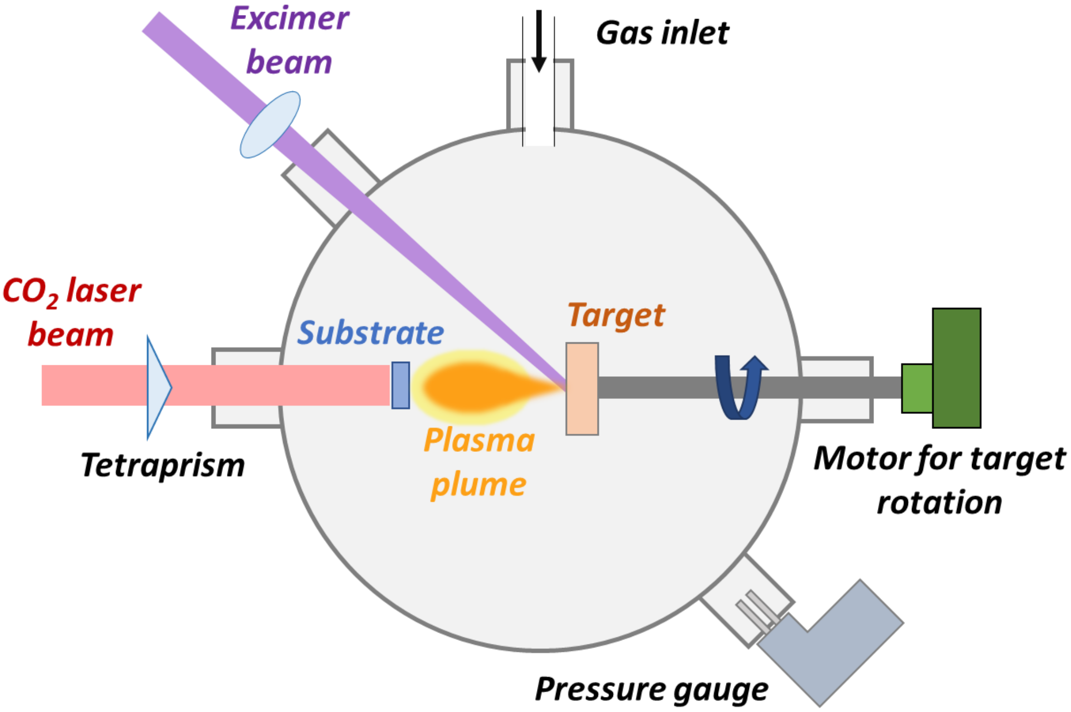

Figure 3.1: Illustration of the PLD setup. The mechanical systems driving the target rotation are different in the single-target and multi-target configurations and are detailed later in this chapter.

3.1.2 Standard deposition procedure

The following procedure summarises the key steps followed for our depositions. The values of power ramping speed, the repetition rate of the excimer and the number of pre-ablation pulses are nominal and were the same for all depositions unless stated otherwise.

- Vacuum pumps are activated to evacuate the air from the chamber (dry pump and turbomolecular pump).
- When the pressure reaches ~1 µbar, the O_2 gas inlet is opened and the gas flow is adjusted via a needle valve to obtain the desired pressure in the chamber.
- The power of the CO_2 laser is ramped up from 0 W to its final value. The speed of the ramp up is 2 W/min.
- Pre-ablation: before the actual deposition, a pre-ablation of 36000 pulses is performed at 100 Hz to remove any contaminant from the target's surface. The substrate is shielded during this step. In general, the pre-ablation is done only for the first deposition of a given day.
- Deposition: the desired number of ablation pulses are launched at 100 Hz after removing the shield protecting the substrate.
- At the end of the deposition, the CO_2 laser power is ramped down to zero at a speed of 0.5 W/min. This speed is slower than the ramp up speed to prevent any dislocation and damage

caused by the thermal stress, especially if the film and the substrate have significantly different thermal expansions.

- Vacuum pumps are deactivated and air is reintroduced in the chamber.

3.1.3 Error on deposition parameters

In this section, we evaluate how precisely the user can control the various deposition parameters. The error levels determined in this section are valid for all depositions presented in this thesis, unless stated otherwise. We will focus on the parameters over which the PLD operator has a *direct control*, i.e. parameters that can be *measured* and *adjusted* with the various controls of the setup. These parameters include:

- The UV pulse energy: measured with an energymeter and adjusted either via the excimer control pad or via MATLAB.
- The UV spot size: measured by burning fax paper and can be adjusted with the position of the focussing lens.
- The sample heating power: measured with a powermeter and can be adjusted with MATLAB by controlling the pulsed electrical command of the CO_2 laser.
- The chamber pressure: measured by a pressure gauge and adjusted with the needle valves of the gas inlet.
- The distance between the sample and the target: measured with a ruler adjusted by moving the sample holder.
- The various durations of each step: CO_2 laser power ramping up time, CO_2 laser power ramping down time, post-annealing time, pre-annealing time.

These parameters do not include:

- The sample temperature: although it can be adjusted with the heating power, there is no way to measure the temperature *in-situ*. Only a theoretical estimation is possible, and it does not take into account any variation that may occur if the sample is not placed exactly in the same way in the holder (causing heatsink issues). Therefore, the repeatability of the sample temperature cannot be established.
- Other parameters that cannot be measured or adjusted by the PLD operator with a straightforward method, because they depend on multiple parameters from the first list: growth rate, kinetic energy of the plasma plume, divergence of the plasma, etc.

Here we will focus on the first list and examine the precision of each adjustment. The importance and influence of the parameters of the second list will be evaluated in the next section.

UV pulse energy:

A Gentec-EO QE50LP-S-MB-D0 energymeter is placed on the path of the UV beam inside the chamber, allowing us to ignore any potential loss at the chamber window or before: therefore, the pulse energy measured corresponds exactly to the pulse energy incident on the target. The wavelength of measurement (248 nm) must be selected properly on the energymeter software. In most cases, the excimer was used in “constant voltage mode”; the operator gives the excimer a value of voltage between 19 kV and 26 kV for the electrical stimulation and the excimer does not use any feedback sensor to maintain a constant output energy. The pulse energy can potentially fluctuate during operation.

The excimer allows us to select the number of pulses that we want to fire and the energymeter software provides statistics about the mean pulse energy, the RMS deviation, etc. In the early stage of the project, I was advised to launch a series of 200 pulses and record the mean value. After getting more familiar with the setup, I realised that the excimer tends to fire a slightly higher energy for the first 50-100 pulses, before reaching a stable value. Consequently, I decided to change the protocol and fire 400 pulses, out of which only the last 200 pulses would be considered for the statistics. Interestingly, this choice was justified by the RMS deviation of the pulse energy, which was generally around 2.5% for the first 200 pulses and only 0.6% for the following 200 pulses. I also started to systematically record the value of RMS deviation as an additional criterion to detect any abnormal behaviour of the excimer laser. In the span of three years, a jump of the RMS deviation of the pulse energy only occurred a couple of times and generally indicated that the KrF gas inside the laser needed replacement.

Furthermore, I noticed that for a given stimulation voltage, the output pulse energy would slowly increase over the course of a day. Typical increase would range from 2% to 4%. For this reason, a second pulse energymeter measurement was systematically recorded after finishing all the depositions at the end of the day, to obtain a better estimate of the actual pulse energy for each deposition. A weighed average of the morning and evening measurements was calculated to reflect the fact that the pulse energy for the first deposition must have been closer to the morning measurement, while the pulse energy for the last deposition must have been closer to the evening measurement.

Overall, assuming that the energymeter is properly calibrated, we can assert that the UV pulse energy can be controlled pretty accurately. By anticipating the slow increase over the course of a day, the pulse energy can be set with a precision close to +/- 1%.

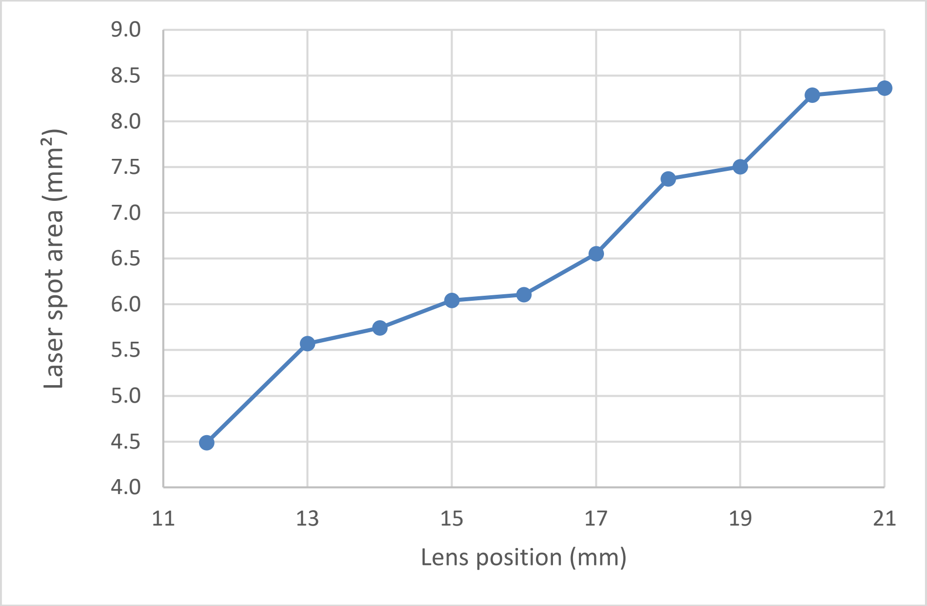

Figure 3.2: Area of the ablation spot depending on the position of the lens. Position 0 on this graph corresponds to the ablation spot being in the focal plane of the lens.

<u>UV spot size:</u>

The UV spot size is measured in the following way:

- The face of the target to be ablated is wrapped with some fax paper, taking extra care to minimise air bubbles between the paper and the target. The target is then placed on the target holder, at the same position as during deposition.
- We fire a single UV pulse, which is enough to burn the fax paper. The burn spot has very sharp edges, it is well delimited.
- After removing the target and fax paper from the holder, a vernier calliper with a reading precision of 0.01mm is used to measure the spot size.

The spot size can be varied by adjusting the position of the focusing lens, as illustrated by the measurement from Figure 3.2. Most of the depositions in this project were carried out with a spot area between 6 mm² and 8 mm², due to empirical observations. A few depositions explored the possibility of using a smaller spot size (down to 5 mm²) or a larger one (up to 10.8 mm²) with mitigated results.

The critical point for the spot size adjustment is not positioning the lens, which can be done with a reasonable precision, but rather measuring the spot dimensions. Although the vernier calliper used for the measurement has a 0.01 mm reading precision, if the fax paper is not laying perfectly flat on the target surface, the burnt spot might not be rigorously the same as the ablation spot (Figure 3.2). To improve the precision of the measurement, several spots are burnt across the target surface (up to 10 spots), and each of them are measured to calculate a mean value. This method averages out the variations of flatness of the fax paper on the target surface.

Heading power:

The sample is heated by a CO_2 laser which cannot directly receive an output power "set point". The laser is piloted by an electrical pulsed signal with variable duty-cycle, where an increasing duty-cycle corresponds to an increasing output power. In the preparation stage, the power of the CO_2 laser is measured *in-situ* with a thermal powermeter. The duty-cycle of the pilot signal is varied until the desired output power is reached. During the deposition, an *ex-situ* detector (Gentec-EO UP55N-300F-H12-D0) monitors the fluctuations of power near the output of the source. A calibration is regularly conducted, which consists in determining the exact ratio between the power incident on the ex-situ detector and power incident on the sample. This way, it is possible to know the power incident on the sample at any time during the deposition process thanks to the ex-situ detector.

The software receiving data from the ex-situ powermeter also provides statistics on the fluctuations of the CO_2 laser power. Naturally, the amplitude of the fluctuations depends on the duration of interest. The deposition of our typical waveguide only last for a few minutes, during which the RMS variation of the CO_2 laser power was generally between 0.5% and 1.5%. The fluctuations can be a little broader if we consider longer time frames, like that of the 2 Hz deposition for the repetition rate study (Chapter 5) which lasted 2h30min (2.6% RMS), or even the 151-layer Bragg mirror growth which lasted 1h30min (2.4% RMS).

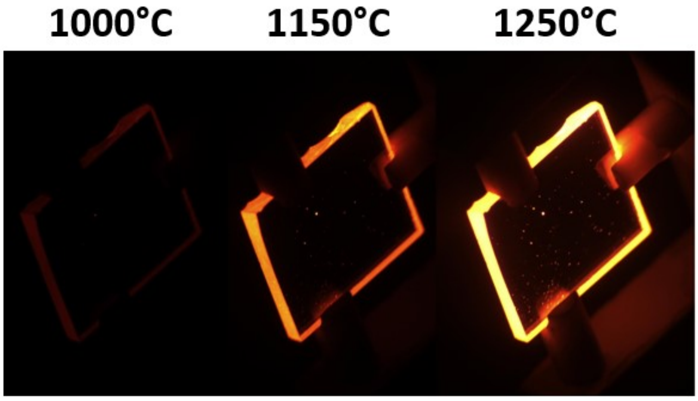

Figure 3.3: Photos of a sapphire substrate heated at different temperatures.

With the hypothesis of the sample thermal loss being mainly radiative, we can apply the Stefan-Boltzmann law and thus consider that the temperature of the sample T_{sample} is proportional to $P_{laser}^{0.25}$, where P_{laser} is the power of the CO_2 laser beam incident on the sample. Therefore, the relative fluctuations of T_{sample} are 4 times smaller than those of P_{laser} (note that in this case, T_{sample} is expressed in kelvins).

Chamber pressure:

The chamber gas inlet consists in three pipelines with individual needle valves to precisely adjust the flow of O_2, N_2 and Ar. Despite the pressure gauge providing us with a two-digit value, the manufacturer only claims a +/- 5% accuracy around our typical deposition pressure. For a growth optimisation study, the limiting factor would not be the accuracy of the measurement, but rather the reading precision: although the value displayed by the gauge might not be accurate, the chamber pressure is adjusted for all growths to obtain the same two-digit value. As a result, we can say that the 20 µbar O_2 pressure during our typical growth is set with a repeatability of +/- 0.5 µbar (display precision being 1 µbar).

Distance between the sample and the target:

The distance between the sample and the target can be measured with a simple scale and adjusted with a precision of +/- 1 mm. The position of the target and substrate holders were left untouched for the majority of the project to improve growth repeatability. The nominal distance of 55 mm was obtained empirically by previous studies, but the ion probe study presented in the next chapter aimed at justifying it, by evaluating the changes of the plume kinetics caused by a variation of distance.

3.1.4 Bi-directional ablation

A major issue inherent to PLD is the integration of clusters of material inside the thin film, inevitably leading to scattering loss and limiting the performance of the waveguide. It has been recently demonstrated that the number of particulates inside the film can be significantly reduced by implementing bi-directional target irradiation, which consists in ablating the target from two opposite angles of incidence (Prentice et al., 2019). This method slows down the build-up of irregularities on the surface of the target, which in turn reduces the ejection of particulates.

Bi-directional target ablation is implemented in both single-target and multi-target setups and is now routinely used. In our single-target setup, an offset cam drives the rotation of the target while translating it left and right. Figure 3.4: Drawing illustrating how bi-directional ablation works: the same spot can be ablated with two different positions of the target. illustrates how the same spot on a target can be ablated in two different positions of the target. From the perspective of the ablated spot, it seems like the laser beam comes from two different directions, separated by nearly 180°. To obtain an exact 180° between the two directions, you would need the centre of the target to pass through the laser beam, which is not recommended because of the risk of overablating the centre.

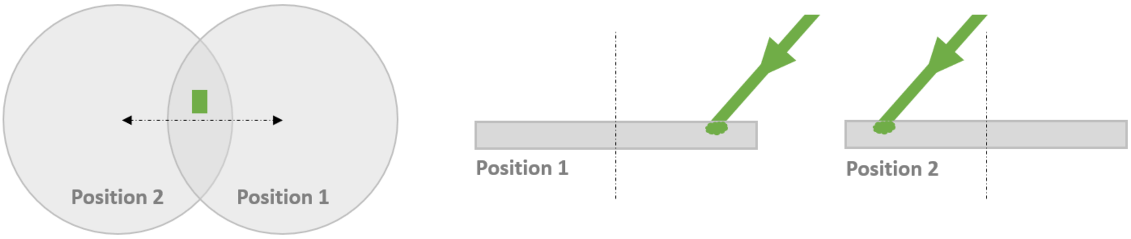

Figure 3.4: Drawing illustrating how bi-directional ablation works: the same spot can be ablated with two different positions of the target.

3.1.5 Multi-target system

3.1.5.1 Design

Many concepts were explored to enable the ablation of multiple targets while maintaining bi-directional ablation. One of many constraints was the limited number of ports available in the chamber to upgrade the system. Appendix A presents the various designs that were considered before converging towards the final solution.

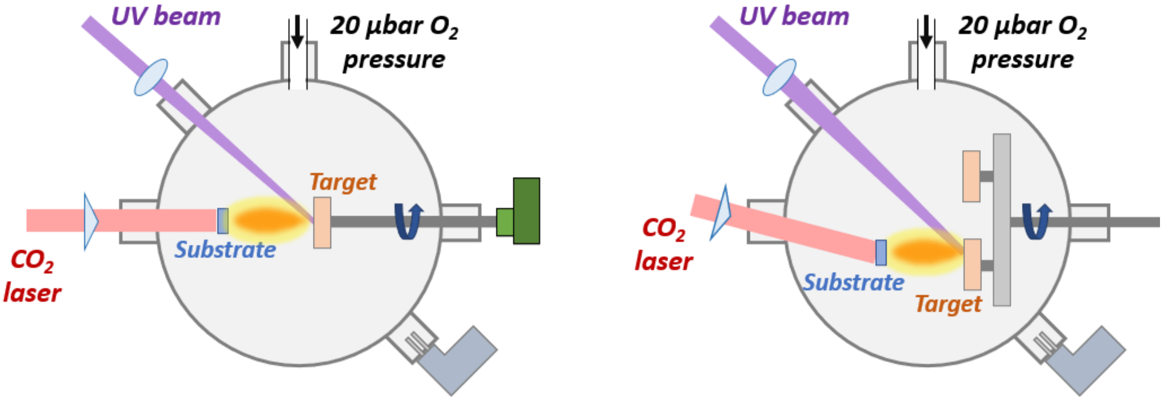

Figure 3.5: Single-target (left) and multi-target (right) PLD setup. In the multi-target system, the three targets are spined by a DC motor and the carousel is rotated by a stepper motor. Both motor axes are co-axial.

The final solution that was selected was a carousel capable of holding three targets (Figure 3.5 and Figure 3.6**Erreur ! Source du renvoi introuvable.**). Two co-axial rotational feedthroughs were attached to a chamber in cascade. A DC motor was connected to one of the feedthroughs and was used to spin the three targets at a constant speed of 120 rot/min. A stepper motor was driving the rotation of the entire carousel and fulfilled two roles: scanning the UV beam with the target to ablate the entire surface, and switching between targets to start a new layer. The principle of this mechanical designed was proposed by me and I made the initial drawings on CAD. I am thankful to

Mark Long from the mechanical workshop, who improved my basic design and fabricated the carousel. The basic electronic required to pilot the stepper motor was set up by me as well. Another important aspect is that the excimer must stop firing when we switch from one target to another. For that reason, I wrote a MATLAB code to control and synchronise both carousel and excimer laser. The code was also made user-friendly, so that the operator only needs to measure the ablation spot size and input the structure of the multilayer to grow. The system performs the adequate motions to produce the desired coating, while ablating the entire surface of the targets and ensuring bi-directional ablation.

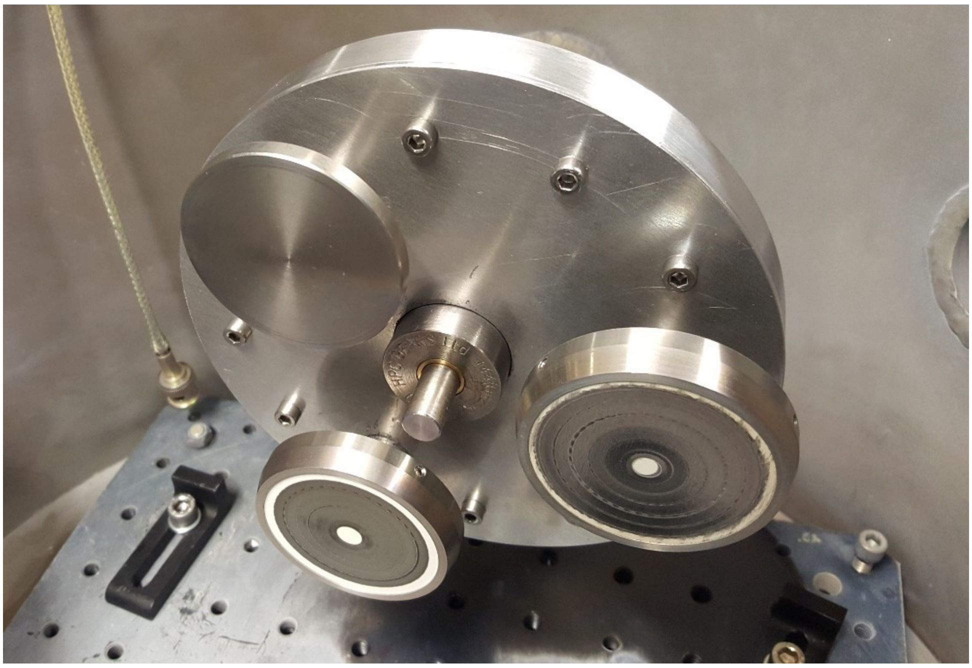

Figure 3.6: Photo of the carousel holding two targets

The mechanical principle of the system is illustrated in Figure 3.7. The DC motor spinning the targets is connected to a “shaft” rotation feedthrough, i.e. a feedthrough with a shaft on the air side and another one on the vacuum side. While the air side is connected to the motor, the shaft on the vacuum side is directly connected to a central gear inside the carousel, which drives the motion of three satellite gears (one on the axis of each target). The second rotation feedthrough is a “tube” feedthrough: it transfers the rotation of a tube on the air side to a tube on the vacuum side. The insides of both tubes are connected and filled with vacuum during operation, which explains how the long shaft between the first feedthrough and the carousel can exist despite the presence of the second feedthrough. The tube on the air side is rotated by the stepper motor, and the motion is transferred to the tube in the vacuum side, which is connected to the carousel frame. Because of this mechanical setup, the rotations of the carousel and the targets are entirely independent.

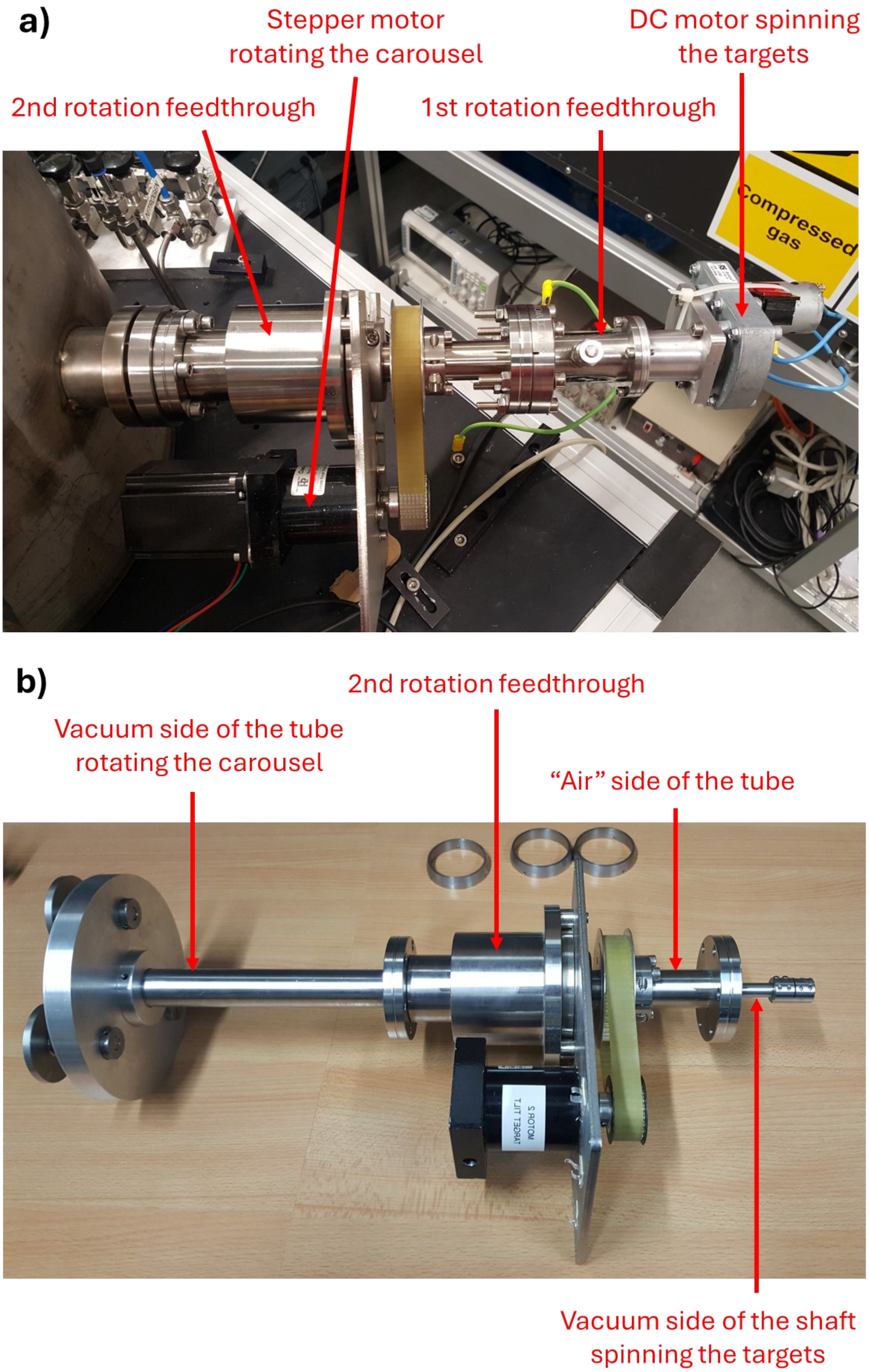

Figure 3.7: Two different views of the mechanical system driving the multi-target carousel.

3.1.5.2 Ablation pattern

Investigating the ablation pattern is absolutely critical, since the progressive degradation of the target surface has a significant impact on the film scattering. To extend the lifetime of a target as much as possible, it is necessary to:

- maximise the surface ablated on the target
- have a uniform ablation over the entire surface
- use bi-directional ablation

The criterion of a uniform ablation is also paramount to avoid creating curvature on the target surface. For instance, if the system ablates the centre of the target much more frequently than the edges, the surface might become slightly concave and cause an angular jitter on the plasma plume, which propagates in the direction perpendicular to the ablated surface.

The ablation pattern can be easily computed with basic trigonometry. The user only needs to measure the spot size and the distance between the spot and the centre of the target (Figure 3.8). These parameters are sufficient to place the ablation spot in our simulations. We consider three frames of reference:

- (X_{car}, Y_{car}) is centred on the axis of the carousel and does not rotate
- (X_{tar}, Y_{tar}) is centred on the axis of the target and does not rotate
- (X'_{tar}, Y'_{tar}) is centred on the axis of the target and rotates

The coordinates of the ablation spot are known and fixed in the (X_{car}, Y_{car}) frame of reference. We can successively compute the corresponding coordinates in the (X_{tar}, Y_{tar}) and (X'_{tar}, Y'_{tar}) as a function of $\theta_{carousel}$ and θ_{target}.

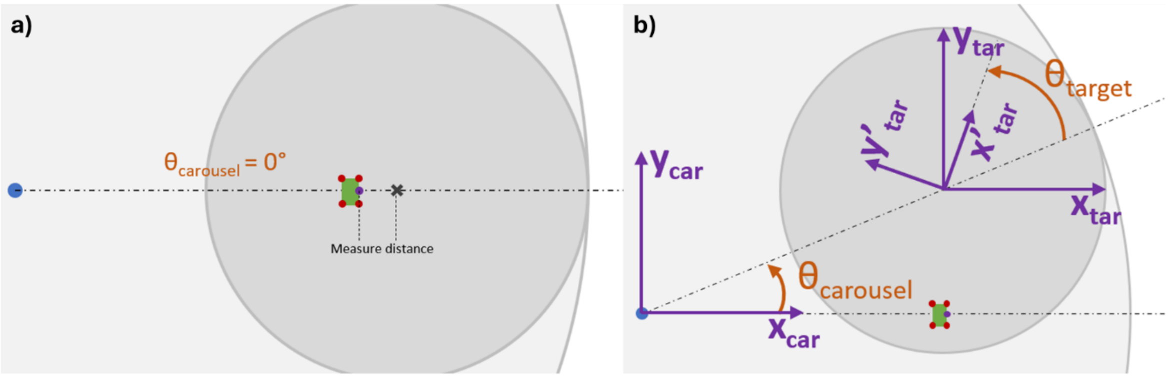

Figure 3.8: a) Illustration of the initial position of the target and the distance to measure. b) Frames of reference used for the simulation of the ablation pattern.

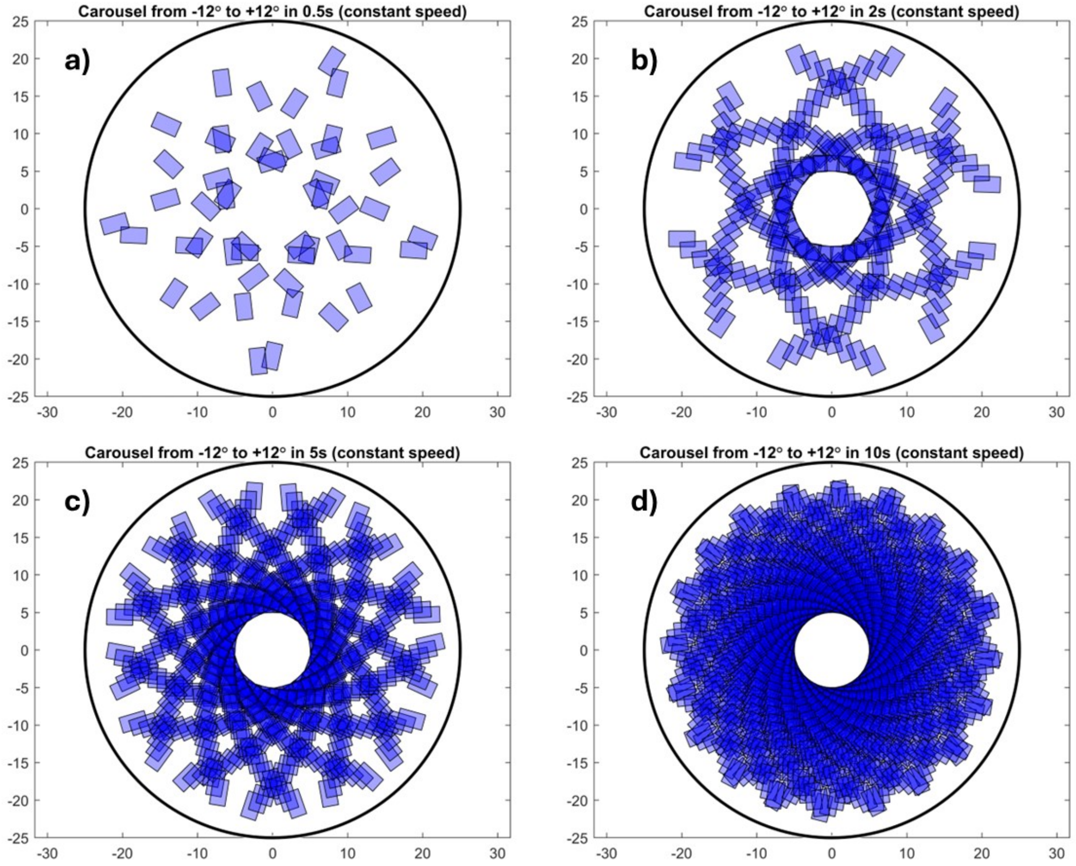

Figure 3.9: Example of how the target gets ablated over a) 0.5 second, b) 2 seconds, c) 5 seconds, and d) 10 seconds.

Two time parameters must be considered to determine the correct ablation pattern: the excimer ablation rate (generally 100 Hz) and the rotation speed of the target. Figure 3.9 illustrates how a wrong timing can affect the ablation pattern. In this example, the carousel is rotating back and forth at a constant speed, covering the 24° needed to scan most of the target's surface. Although it initially seems like some parts of the target are not covered, we observe that after 10 seconds, most of the surface has been ablated. However, the ablation over the surface is not uniform. For a given value of $\theta_{carousel}$, the ablation spot is located within two circles (see Figure 3.9). At a constant scanning speed of the carousel, the number of pulses ablating a ring close to the centre and a ring close to the edges is the same. However, the outer ring has a surface area much larger than the inner ring. For this reason, a constant scanning speed is not adapted to our needs.

The alternative solution that I selected was to successively ablate rings of different sizes to cover the entire target (Figure 3.10). The surface of the ablation spot is already known, and for a given value of $\theta_{carousel}$, the surface of the corresponding ring can be deduced from R_{min} and R_{max}. Therefore, we can determine the number of pulses required to, for instance, ablate a ring 10 times before moving to the next one. This number of pulses can be translated into a duration of ablation using the repetition rate of the excimer.

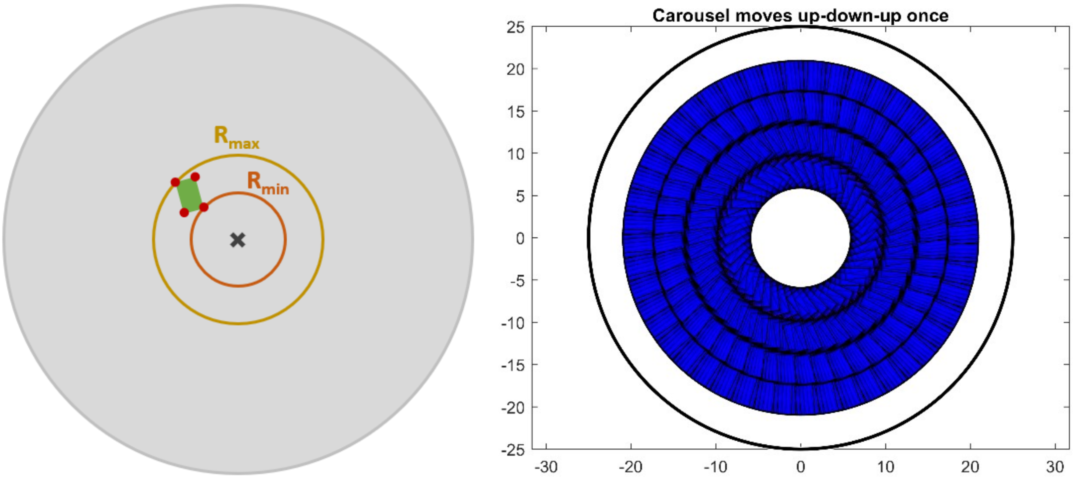

Figure 3.10: Ring ablated for a specific carousel angle $\theta_{carousel}$ (left) and ablation pattern generated by the MATLAB code (right).

Based on the spot size and its distance from the centre of the target, the MATLAB program directly determines the optimal number of rings to have the maximum ablation coverage on the target. It provides a table with the values of $\theta_{carousel}$ for each ring and the waiting time before moving to the next ring. This ablation pattern guarantees <u>uniform</u> and <u>bi-directional</u> ablation.

3.1.5.3 Bi-directional ablation

Bi-directional ablation is easily achievable by ablating each ring with both carousel positions of $\theta_{carousel}$ and $-\theta_{carousel}$ (Figure 3.11). The position of the ablation spot at 0° (in Figure 3.10) has also been chosen with bi-directional ablation in mind. Indeed, the laser spot could be aligned either on the left side or the right side of the target's centre. Nevertheless, placing it on the left side resulted in an angle closer to 180° between the two directions of ablation.

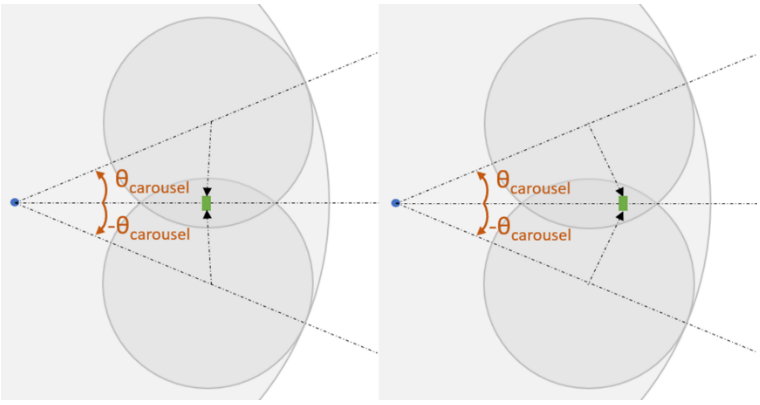

Figure 3.11: The same spot can be ablated by two different carousel angles. From the perspective of the spot, the angle between the two directions of the laser is closer to 180° when the spot is at the left of the target centre (left).

3.2 Characterisation of films

3.2.1 Scattering

For waveguiding applications, it is crucial to minimise the scattering losses from the film. Dark-field microscopy can be used to estimate the quantity of scattering points in the film (density and average size).

After each deposition, 15 dark-field images were recorded across the sample with a 10x magnification to have a good representation of the entire surface. In total, the combined 15 images covered around 10% of the 10x10 mm^2 sample area. A simple counting method based on each pixel's value was used to quantify objectively the amount of scattering. A pixel threshold value is chosen, for instance 10% of the maximum pixel value. Every pixel with a value higher than the threshold is counted as a scattering point, while the others are considered as non-scattering points. In this way, it is possible to calculate the percentage of scattering points in a dark-field image. Choosing a fixed threshold and the same microscope parameters (exposure, gain and source brightness) enabled us to objectively compare two different films.

While this method can be applied when the film is transparent and clear, a cloudy sample would exhibit a very bright background on the dark-field microscope, rendering the threshold method meaningless. In that situation, it is more adapted to plot a histogram of the pixel brightness to better understand the nature of the scattering.

3.2.2 XRD corrections

All XRD measurements in this thesis were conducted with a Rigaku Smartlab diffractometer.

Although the precision of the measurement is mainly intrinsic to the instrument, its accuracy can be impacted by several factors: miscut of the substrate, parallelism between the two faces of the substrate, particle between the sample and the XRD platform, etc. All of them will only cause a shift of the angle on the diffractogram, without distorting the curve itself. In our case, we want to compare films that were grown with different conditions and will therefore have XRD peaks at slightly different angles. By assuming that all substrates are identical, we can shift the XRD curves horizontally to superpose their substrate peak. According to the literature, the XRD peak for a (0001)-orientated sapphire substrate is around 41.7°. As a result, for each XRD measurement performed, we determine the position of the sapphire substrate peak and shift it to 41.70° (arbitrary value). An example is illustrated in Figure 3.12. The substrate peak is only defined by a few points because it has a high dynamic and is very narrow. In order to obtain a good precision on the exact position of the peak, we compute the centre of gravity of the peak.

The peak position of rocking curves was not specifically studied in this project. Since we only compared the width and height of the curves, we decided to shift all of them horizontally to match their peak maximum. This style of presentation of the graphs facilitates the comparison of the curves for the reader.

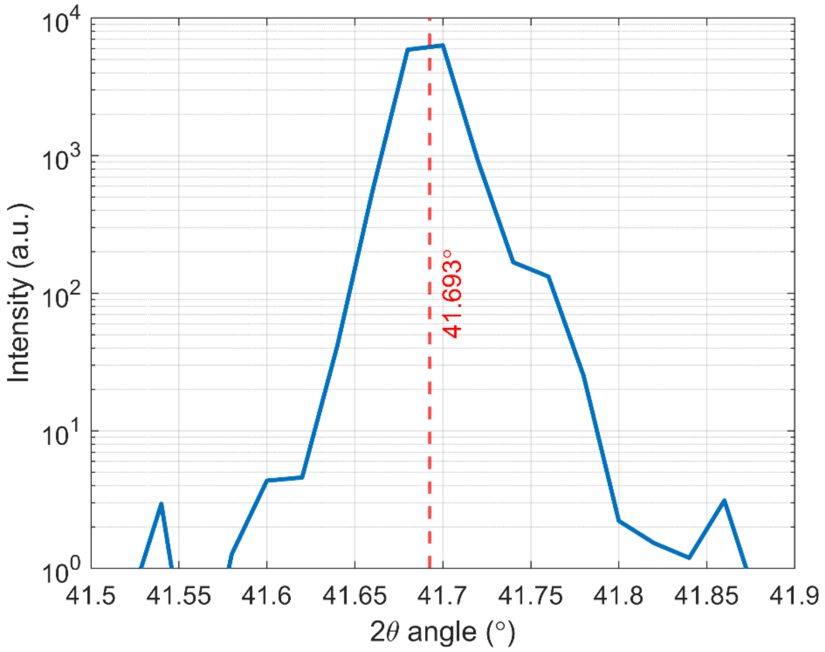

Figure 3.12: (0001) peak of a sapphire substrate from a XRD scan with step size of 0.02°. The centre of gravity of the peak was computed and plotted in red. The XRD scan will then be translated to have the centre of gravity of this peak at 41.70°.

3.2.3 Thickness

In the context of this project, we need a thickness measurement method that can be routinely performed. Ellipsometry not only requires an alteration of the sample's back surface to avoid the specular reflection, but it also involves a modelling process to extract the information that we want. Prism coupling measurement is another method which was explored (see section 4.5.2), but it is challenging to obtain a good contact between the film and the prism, and therefore the process can be time-consuming.

As an alternative, a simple setup illustrated in Figure 3.13 is used to obtain the transmission spectrum of the sample from 370 nm to 1000 nm. The sample is illuminated by a collimated broadband white light source at normal incidence, and the transmission spectrum is recorded by a spectrometer. For the typical range of thicknesses that we commonly use, several oscillations are visible in the transmission spectrum. The sample can be modelled as three interfaces between media of known dispersion curves. Therefore, for a given film thickness, it is possible to compute the theoretical transmission spectrum of the sample. Here, we assume that the dispersion curve does not significantly vary from one sample to another, which will be justified experimentally in section 4.5.2. Figure 3.14 shows an example of a transmission measurement being fitted to determine the thickness. In general, it is challenging to fit the entire spectra with only one thickness; we rather fit separately the low- and high- wavelength sections, which provides us with lower and upper bounds for the thickness. The mean of these two values is considered to be the actual thickness of the film.

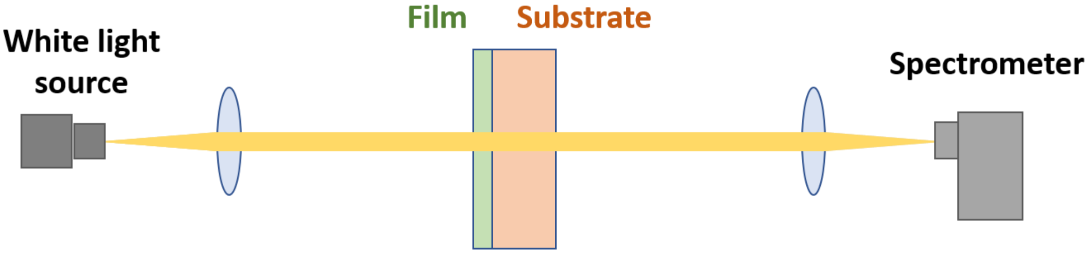

Figure 3.13: Experimental setup to measure the transmission spectrum of the sample.

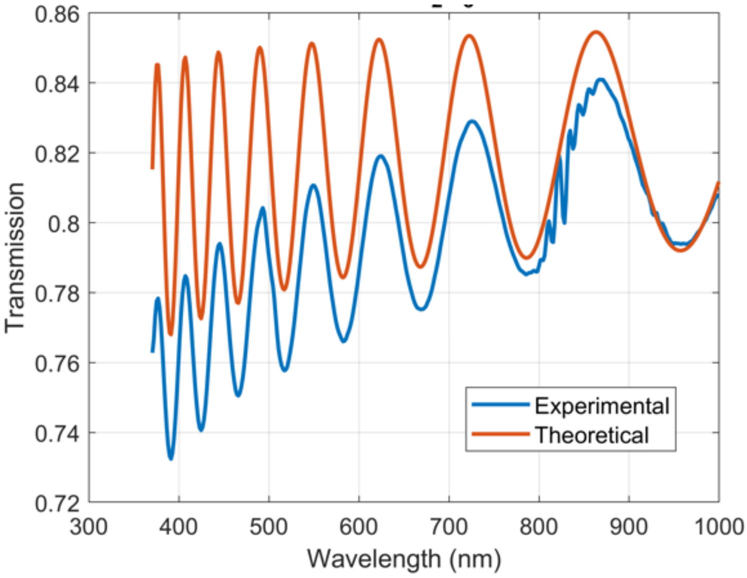

Figure 3.14: Illustration of the transmission spectrum of a Sc_2O_3 film grown on sapphire (blue) being fitted with a theoretical spectrum computed for a film thickness of 1091 nm (orange).

Another more sophisticated method was later developed. The Fourier transform of the measured spectrum is calculated first; a low-pass filter is applied to reduce the noise, while a high-pass filter aims at removing the contribution of the back surface (slow variation). When the inverse Fourier transform is applied, the oscillations are centred around a constant value, and the maxima and minima are easier to identify. Once again, we use a three-interface model to compute the theoretical transmission spectrum for a given film thickness, but we then apply the same filters as the measured data. Fitting the maxima and minima of the oscillations is supposedly easier without the slow variation over the spectrum. However, in practice, we find the same thickness and error range with both methods.

3.2.4 Bandgap

The bandgap measurements were performed by first recording the transmission of the sample in the UV range. The Tauc plot method is a standard method consisting in plotting $(\alpha E)^{1/n}$ as a function of E, where E is the photon energy and α the intrinsic absorption coefficient, and fitting the linear part of the curve to obtain the bandgap Figure 3.15 (a). n is equal to 2 if the transition corresponds to an indirect bandgap and ½ for a direct bandgap. All the Tauc plots in this thesis correspond to indirect bandgaps, we will therefore examine the quantity $\sqrt{\alpha E}$.

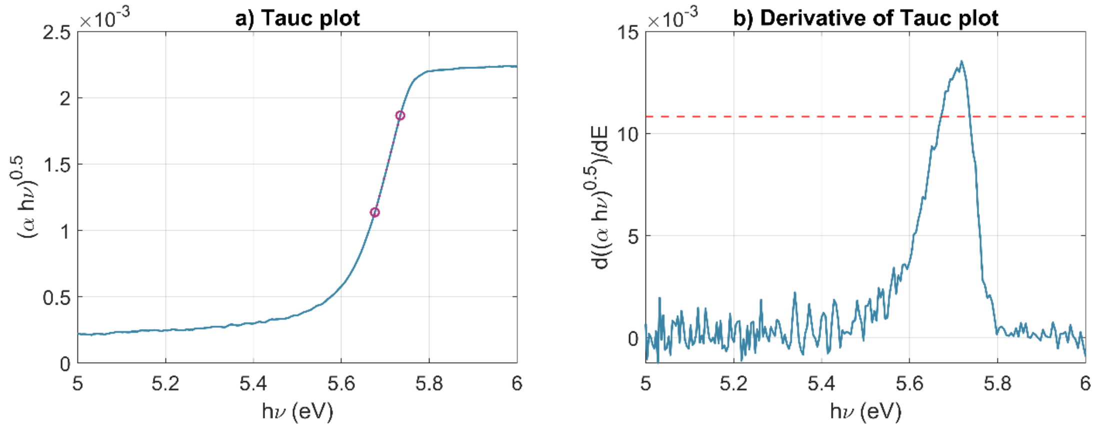

Figure 3.15: a) Tauc plot of a Lu_2O_3 film grown on sapphire. The purple circles represent the region selected for the linear plot, based on the criterion on the derivative. b) Derivative of the Tauc plot. The red dotted line represents the threshold of 80% of the highest slope.

The main incertitude with this method is that the linear part of the curve might not always be well-defined, and as a result, the computed value of the bandgap might differ depending on the selected region. To avoid any subjective input, I defined a procedure that was rigorously applied to all samples to allow for a fair comparison. The derivative of the Tauc plot was computed to find the highest slope of the graph. The linear part was defined as the region where the slope did not decrease by more than 20% from the highest slope Figure 3.15 (b). The linear fit was performed in that region for all samples discussed in this thesis.

Chapter 4 Sesquioxide growth optimisation

4.1 Introduction

The growth of sesquioxides via PLD has been widely investigated due to the rising interest of these crystals in the field of lasers and semiconductors (Parsonage et al., 2015, Gila et al., 2001, Beecher et al., 2014, Paulraj et al., 2016, Liu et al., 2007). While sesquioxides have already established themselves as attractive as laser hosts for rare-earth ions, their fabrication as single-crystal bulk remains complex, mainly because of their high melting point (~2780K for Lu_2O_3). PLD enables the growth of sesquioxides at around half of their melting point, which motivated numerous research studies on the epitaxial growth of sesquioxides via PLD for the fabrication of slab lasers and thin-disk lasers (Kuzminykh et al., 2007, Prentice et al., 2018, Bar et al., 2003, Kuzminykh et al., 2006, Parsonage et al., 2015, Beecher et al., 2014). In particular, the successful growth of sesquioxides on sapphire substrates in previous studies served as a basis for our own growth optimisation.

One key requirement for our sesquioxide waveguides is a low amount of scattering, which must be obtained by minimising particulates, crystal defects (dislocation, crystallites) and film roughness. Once again, studies have already put emphasis on the minimisation of these three elements in PLD-grown films, since slab lasers require sufficiently low propagation loss to enable lasing. One major step in this direction is the introduction of bi-directional target ablation, which was proven to effectively reduce the number and average size of particulates in the films (Prentice et al., 2019) and was used systematically for all growths in this project.

As disclosed in previous chapters, a particular emphasis was given to Sc_2O_3 which has the highest refractive index contrast with sapphire and whose growth did not present any additional challenges compared to Lu_2O_3 and Y_2O_3. While a certain number of optimisation studies can be found in the literature, it is worth noticing that a significant number of them were conducted with electric substrate heaters, which often limit the growth temperature to around 1000K (Kuzminykh et al., 2006, Liu et al., 2007). Although this temperature range is suitable for garnets, it might be too low for the epitaxial growth of high-quality Sc_2O_3 films. On the other hand, our PLD facility offers the possibility to easily reach a substrate temperature greater than 1500 K owing to laser heating.

In this chapter, we present the methodology for the growth optimisation of Sc_2O_3 films on sapphire, which was also applied to other materials. An additional study explored the limits of our PLD setup in terms of repeatability, which must be properly assessed to justify the lack of in-situ monitoring in the chamber, in particular the absence of substrate temperature monitoring. Finally, the last part of the chapter aims at validating our thickness measurement method by proving that the dispersion curve of the as-grown films does not change significantly.

4.2 Optimisation of Sc_2O_3 growth

The growth of Sc_2O_3 films on sapphire substrates had already been investigated in the past with our setup, which provided me with a starting set of deposition parameters.

From empirical results, it has been observed that PLD target ablation is the most efficient within a specific window of fluences outside which the number of scattering points embedded in the film rises significantly. On the other hand, the substrate temperature does not seem to have an impact on the film scattering when we limit ourselves to a range of temperature that guarantees a good crystallinity. This observation justified considering the effects of ablation fluence and substrate temperature to be independent as a first approximation, hypothesis which would later need to be validated with the actual results. As a consequence, the requirement of minimising waveguide propagation loss drove the choice of fluence ablation choice, while the optimisation of crystallinity via XRD was the main objective of substrate temperature optimisation.

Although the O_2 background pressure and the distance between substrate and target are also critical parameters, we chose to keep the nominal values of 0.020 mbar and 55 mm which were determined empirically through years of optimisation. In the next chapter, this choice will be justified by measuring the kinetics of the plumes with ion probing.

4.2.1 Target ablation fluence

The aim of the study presented in this section is to identify a range of ablation fluences which will minimise the number of scattering points in the film. The calculation of the percentage of scattering points is done from dark-field microscopy images of the films using the method described in section 3.1.1.

Eight Sc_2O_3 films were grown on 10 x 10 x 1 mm^3 sapphire substrates with different ablation fluences ranging from 1.00 J/cm^2 to 1.37 J/cm^2 (± 0.02 J/cm^2). The spot size was kept identical with an area of 7.2 mm^2, while the pulse energy was varied from 72 mJ to 99 mJ. The CO_2 laser heating power was 23W for all growths and the chamber was filled with O_2 at a background pressure of 0.02 mbar.

Dark-field microscopy images of the eight Sc_2O_3 films were captured to evaluate the amount of scattering. Figure 4.1 compares the dark-field images of four of the films grown with ablation fluences of 1.00, 1.10, 1.20 and 1.37 J/cm^2. The quantity and size of particulates is greatly decreased from 1.00 to 1.10 J/cm^2, and between 1.10 and 1.20 J/cm^2 the improvement is slower. This observation may indicate that 1.00 J/cm^2 is slightly above the ablation threshold: below that threshold, the UV pulse cannot vaporise and ionise the material properly, but can only melt it and eject large clusters of material. A progressive increase of scattering could also be observed from 1.20 to 1.37 J/cm^2, suggesting that the pulse fluence was becoming too high to optimally produce a particulate-free plasma. Numeric evaluation of the percentage of scattering points also confirmed this trend: 3.71%, 0.43%, 0.20% and 0.69%, respectively for 1.00, 1.10, 1.20 and 1.37 J/cm^2. As a result, we identified 1.10-1.30 J/cm^2 to be the optimal range for subsequent Sc_2O_3 film growth.

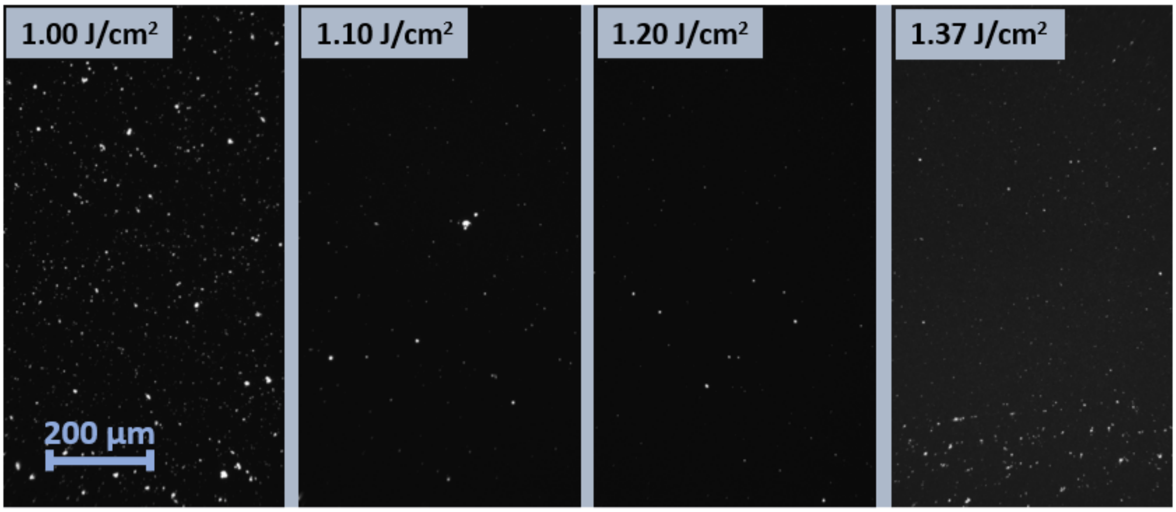

Figure 4.1: Dark-field images of Sc_2O_3 films deposited with different ablation fluences. The percentage of scattering points from left to right is 3.71%, 0.43%, 0.20% and 0.69%.

It must also be stated that for this entire range of fluences, the films exhibited good crystallinity, with XRD scans revealing a prominent (222) peak. This observation confirms that a small change in fluence (in this case 0.3 J/cm) do not significantly impact the crystallinity of the film.

4.2.2 Substrate temperature

The growth temperature, driven by the CO_2 laser, is generally the parameter causing the most drastic change on the film. In this section, we demonstrate how the optimal heating power of the laser for the growth of Sc_2O_3 was identified.

The following study consisted in growing eight films of Sc_2O_3 on (0001) sapphire substrates, with different CO_2 laser powers ranging from 16 W to 32 W. Assuming that the majority of heat losses are radiative (i.e. negligible heatsink from the substrate holder), we can apply the result from section 3.1.2 to calculate the theoretical growth temperature of the samples. Heating powers of 16 W and 32 W correspond approximately to 1250 K and 1490 K (980°C and 1220°C), respectively. The order of the growths was randomised to eliminate any systematic error caused by a drift in the PLD system, or by the degrading target. The growths were performed over three days and at the beginning of each day, the target surface was cleaned with an 18000-pulse pre-ablation (with the same pulse parameters as the depositions). The O_2 background pressure of the chamber was fixed at 0.020 mbar. The power of the CO_2 laser was ramped up at a speed of 2 W/min before deposition and decreased at 0.5 W/min after deposition. The spot size was 5.6 mm^2 and the pulse energy 67 mJ (fluence of 1.20 J/cm^2). A total of 36000 ablation pulses were used for each deposition.

A fast 2θ XRD scan was recorded for each sample between 20° and 80° with a scanning step of 0.02° and a speed of 20°/min, with the aim of comparing the full diffraction pattern. It was apparent that all samples exhibited a very high peak at 31.5°, which corresponds to the <111> orientation, i.e. the orientation of Sc_2O_3 having the best lattice match with (0001) α-Al_2O_3. No significant conclusion could be drawn from these fast scans alone, apart from the fact that the range of CO_2 laser powers resulting in a strongly <111>-orientated Sc_2O_3 film is about ~10W, which is larger than what you would typically observe for garnets. Indeed, the optimal growth temperature for garnet is closer to 1000-1100 K.

A high-resolution 2θ XRD scan was recorded for each sample with a scanning step of 0.002° and a speed of 1°/min. The scan was centered around the position of the (222) peak of Sc_2O_2 (around 31.5°), since it is the highest peak of the diffractograms. Figure 4.2 a displays the evolution of the height and position of the (222) peak for different heating powers, while the normalised plot in Figure 4.2 (b) highlights the change in shape and FWHM. The exact values of height, position and FWHM of these peaks are compiled in Table 4.1, as well as the corresponding lattice constants. Concerning the height of the peak, the film grown at 27W is the tallest, closely followed by the 25W-film. The 32W-film, although not far behind, has the disadvantage of exhibiting a disymmetric peak, which might be caused by annealing effects (studied more extensively in the next chapter). In terms of peak width, it is once again the 27W- and 25W-films that show the best values.

a)

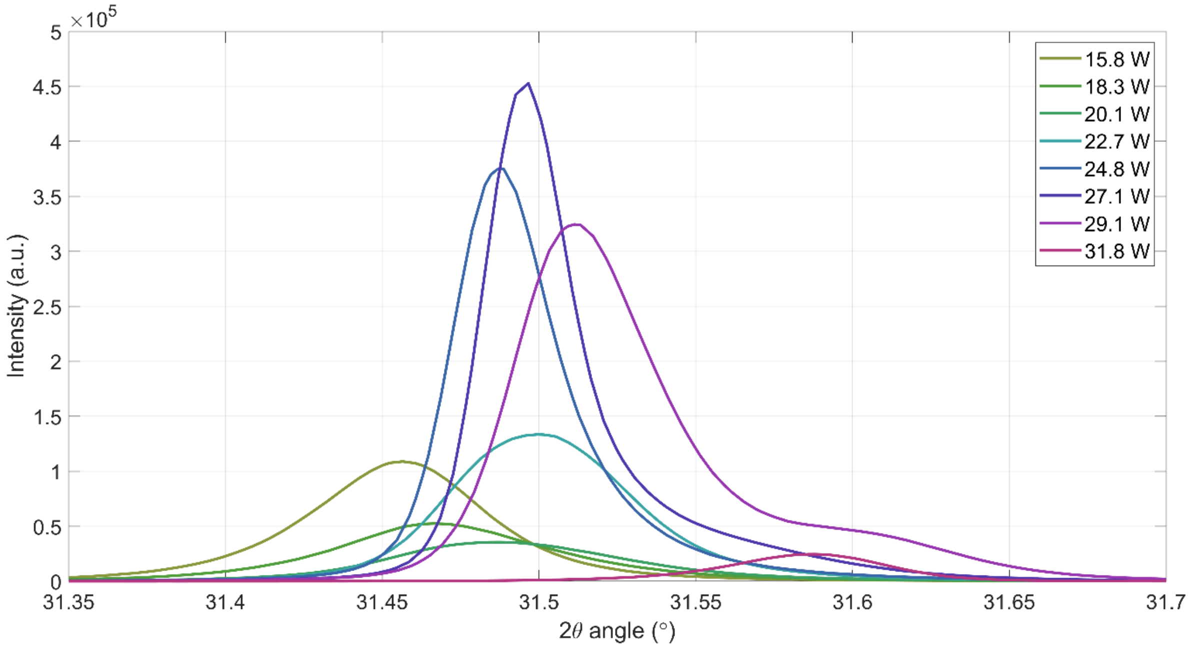

b)

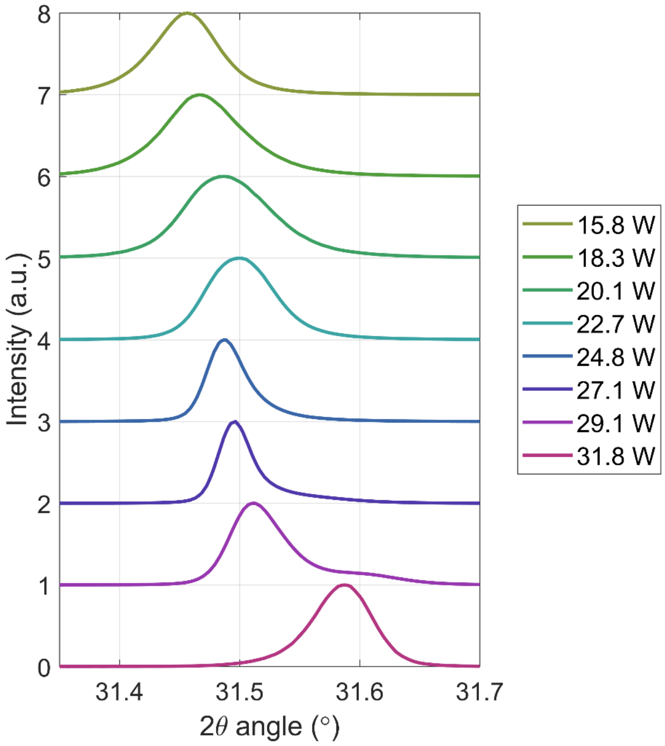

Figure 4.2: 2θ XRD scans of the (222) peak of Sc_2O_3 films grown with laser heating powers ranging from 15.8W to 31.8W. a) not normalised and b) normalised with an offset of 1 between each XRD curve.

Table 4.1: Characteristics of the (222) 2θ-peaks of Sc_2O_3 films grown with laser heating powers ranging from 15.8W to 31.8W. The lattice constant was calculated from the peak position.

CO_2 laser power (W)	Peak height (a.u.)	Peak position (°)	FWHM (°)	Lattice constant (Å)
15.8	1.09E+05	31.457	0.065	9.844
18.3	5.25E+04	31.467	0.077	9.841
20.1	3.56E+04	31.488	0.084	9.834
22.7	1.33E+05	31.500	0.066	9.831
24.8	3.75E+05	31.489	0.038	9.834
27.1	4.53E+05	31.497	0.033	9.832
29.1	3.25E+05	31.511	0.054	9.827
31.8	2.46E+04	31.588	0.057	9.804

To further assess the crystallinity of the samples, rocking curve scans were also recorded for each sample (Figure 4.4). 29W and 27W not only present the highest rocking curve peaks, but also the sharpest ones (FWHM of 0.19° and 0.25°, respectively). Nevertheless,the FWHM of the 25W and 23W films (0.37° and 0.43°) remain low compared to values that are referenced in the literature (Kortan et al., 2006, Kuzminykh et al., 2006, Kuzminykh et al., 2007).

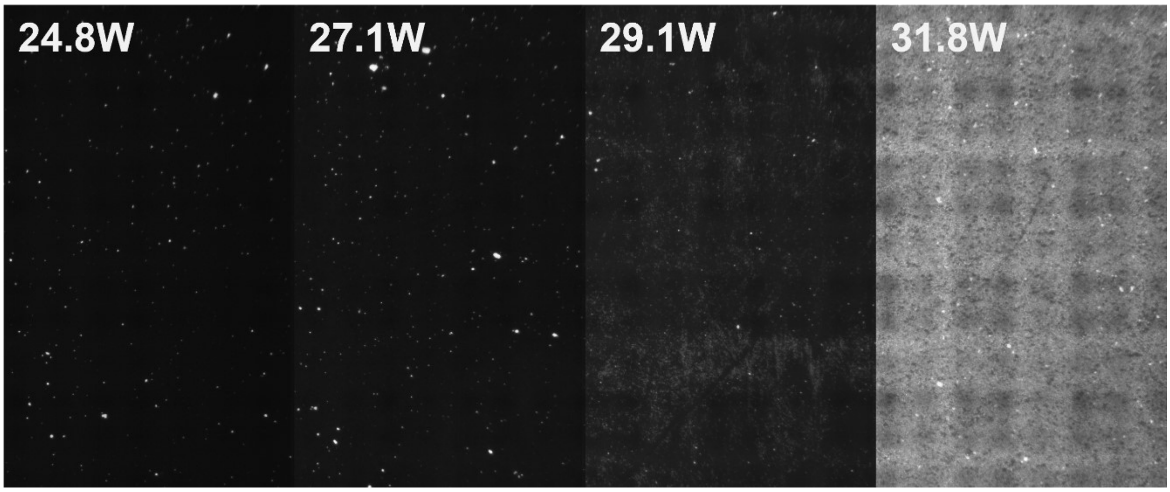

Figure 4.3: Dark-field microscopy images of Sc_2O_3 films grown with different CO_2 laser powers. Films grown with a power below 24.8 W look similar to the 24.8 W sample.

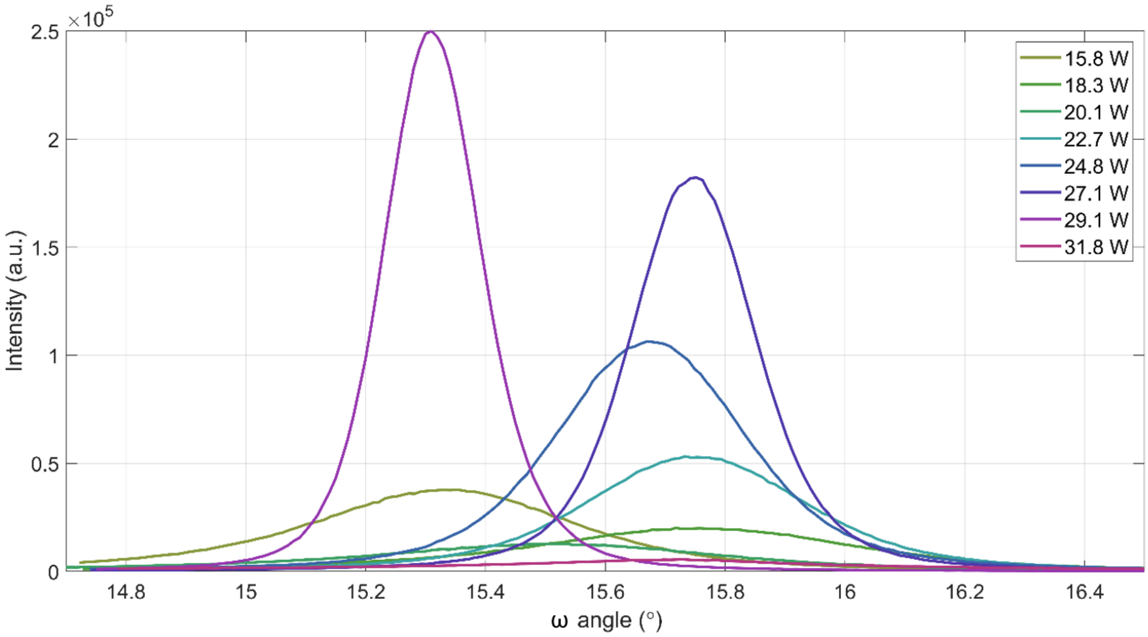

Figure 4.4: XRD rocking curves of the (222) peak of Sc_2O_3 films grown with laser heating powers ranging from 15.8 W to 31.8 W.

Beyond crystallinity, one critical aspect for our application is the amount of scattering from the films. A first visual inspection by eye was conducted immediately after removing the samples from the deposition chamber. The film grown at 32 W was almost opaque, while the film grown at 29 W was showing a slight cloudiness, barely perceptible by eye. Other films semed crystal clear. To assess the cloudiness of the samples with a little more objectivity, dark-field images of the films were recorded using the exact same parameters of exposure and gain. With the dark-field microscope, it was possible to detect some background scattering in the 27W-film that was not noticeable by eye (Figure 4.3). On the other hand, the samples grown at 25W and below only exhibited particulate scattering with no sign of background scattering. It is worth noting that the amount of particulates is roughly the same in all samples, regardless of the CO_2 laser power, strengthening the hypothesis that this variable depends mainly on the ablation fluence and background pressure.

Our main criteria to select the best CO_2 laser power is the amount of scattering: since our films are intended to be used as waveguides and high-reflectivity mirrors, it is indispensable to minimise scattering losses. Although epitaxial growth is also a critical aspect of our crystalline GWSs, I decided that there was overall more tolerance in terms of crystallinity compared to scattering. As a result, Sc_2O_3 thin films were mainly grown around 23W-25W for the rest of the project, because we demonstrated that the amount of scattering remains low without excessively compromising crystallinity.

4.3 Repeatability of the growth method

The degree of repeatability of our deposition setup was critical and had to be evaluated for several reasons. Firstly, a growth optimisation study is only relevant if the process is repeatable: the aim of such studies is to determine a set of growth parameters which produces the optimal output and will be used systematically for future growths. An unexpected drift in our system might prevent a given set of parameters to produce sufficiently similar samples on different runs. A slow drift over time would only present an issue on long-term, with the optimal set of parameters needing to be revised regularly (e.g. every few months or years). However, the optimisation study itself might be meaningless if the drift is too fast, since the different samples grown for the study over several days/weeks might not be comparable. The growth optimisation study in the previous section produced a trend in the position of the 2θ XRD peak, which is the proof that the PLD system has at least a certain degree of repeatability. But this new section goes one step further and aims at properly quantifying this degree of repeatability. A second important aspect to verify was the repeatability of the deposited thickness. The PLD setup did not have any in-situ thickness monitoring system; the thickness had to be measured after the end of the deposition process, on the setup presented in Figure 3.13. Therefore, for the deposition of the waveguides of our GWSs, the deposition rate had to be determined beforehand on a test sample. This method only makes sense if the thickness of the deposited layer is consistent from one growth to another, i.e. if the deposition rate does not vary significantly when we repeat the same deposition with the exact same parameters. The primary goal here was to quantify any variation in thickness and evaluate whether (and how) it could affect the performance of the final GWSs.

It must be noted that two levels of repeatability can be considered in our PLD procedure. The first level corresponds to the degree of repeatability of the deposition parameters, or how precisely the different deposition parameters can be set. This has been already quantified in section 3.1, where the errors on the ablation spot size, pulse energy, heating power, background pressure, etc, have been assessed. The second level of repeatability looks at the end result of the growth and uses metrics to quantify the difference between the results of two growths with an identical procedure.

Six Sc_2O_3 films were grown on (0001) sapphire substrates with the exact same process: we tried aiming for the same pulse energies (99.7 mJ), CO_2 laser powers (23.8 W), O_2 background pressures (0.020 mbar), etc. The spot size of 7.8 mm^2 was left untouched for all depositions. 10000 pulses were used for each deposition, and once again, the depositions were spread over the course of three days. Unfortunately, a mistake occurred when ramping down the CO_2 laser power after the last deposition: the laser was suddenly turned off halfway through the ramping down process, greatly accelerating the second half of the cooling process. Despite originally being a mistake, this slightly different sample helped us improving our understanding of the cooling down process and will be referred as “sample 6” in this section.

2θ XRD scans of the samples were recorded and analysed. The low-resolution scans from 20° to 80° did not reveal any visible difference between samples. High-resolution 2θ scans of the main (222) peak are plotted in Figure 4.5 (a) corrected to the substrate peak position, while the corresponding rocking curves (ω scans) are displayed in Figure 4.5 (b). The shape of the 2θ curves is consistent from one growth to another, and the height of the peaks remain in the range of 79000 ± 10%. In a similar way, little difference can be observed between the rocking curves heights and shapes. A quantitative comparison of the position and width of the peaks is presented in Table 4.2. Among the first five samples, the largest difference in 2θ-peak position is 0.011°, which is smaller than the 0.02° angular resolution of the source claimed by the manufacturer of the Rigaku SmartLab. This difference in 2θ translates in a change of 0.003 Å of the lattice constant, or 0.03%. Overall, looking at the variations in XRD characteristics, we come to the conclusion that our PLD setup has the capability of growing films of repeatable lattice constant within the limits of the measurement resolution.

Table 4.2: Characteristics of the (222) 2θ- and ω-peaks of 5 Sc_2O_3 films grown with an identical protocol (samples 1-5). Sample 6 had a faster cooling down post growth. The lattice constant was calculated from the peak position and the average and standard deviation only accounted for samples 1 to 5.

Sample number	2θ position (°)	2θ FWHM (°)	Lattice constant (Å)	Rocking curve FWHM (°)
sample 1	31.496	0.039	9.832	0.42
sample 2	31.490	0.039	9.834	0.48
sample 3	31.485	0.038	9.835	0.35
sample 4	31.486	0.042	9.835	0.45
sample 5	31.489	0.042	9.834	0.44
sample 6	31.504	0.042	9.829	0.40
Mean (1 to 5)	**31.489**	**0.040**	**9.834**	**0.43**
Standard deviation (1 to 5)	**0.0037**	**0.0017**	**0.0011**	**0.05**

a)

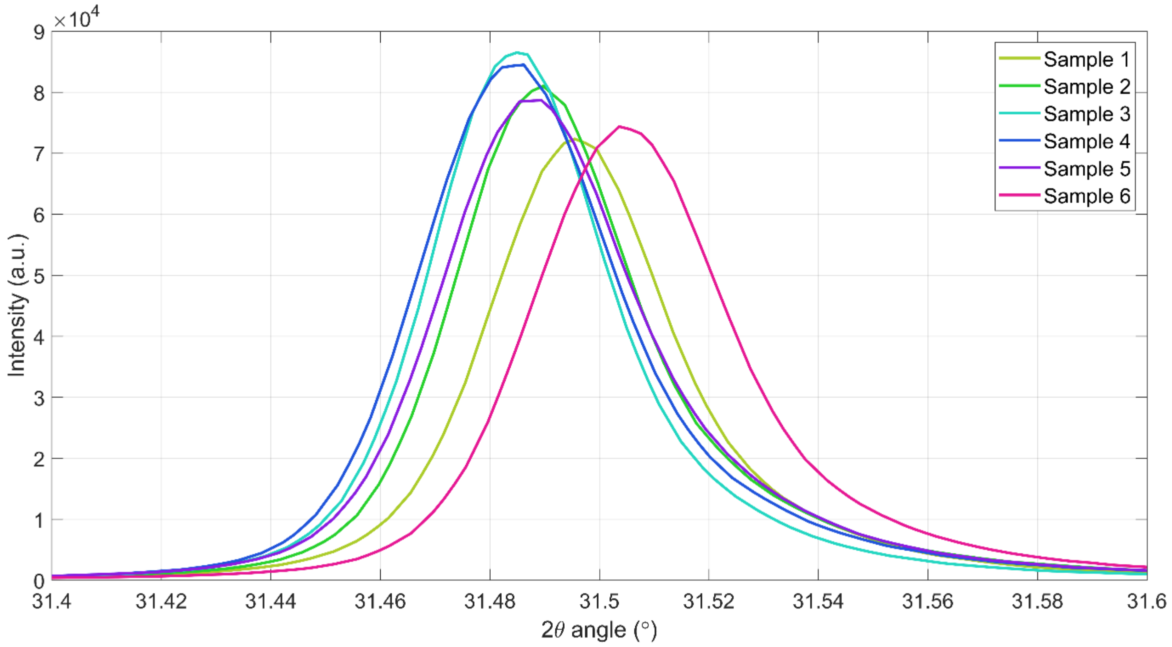

b)

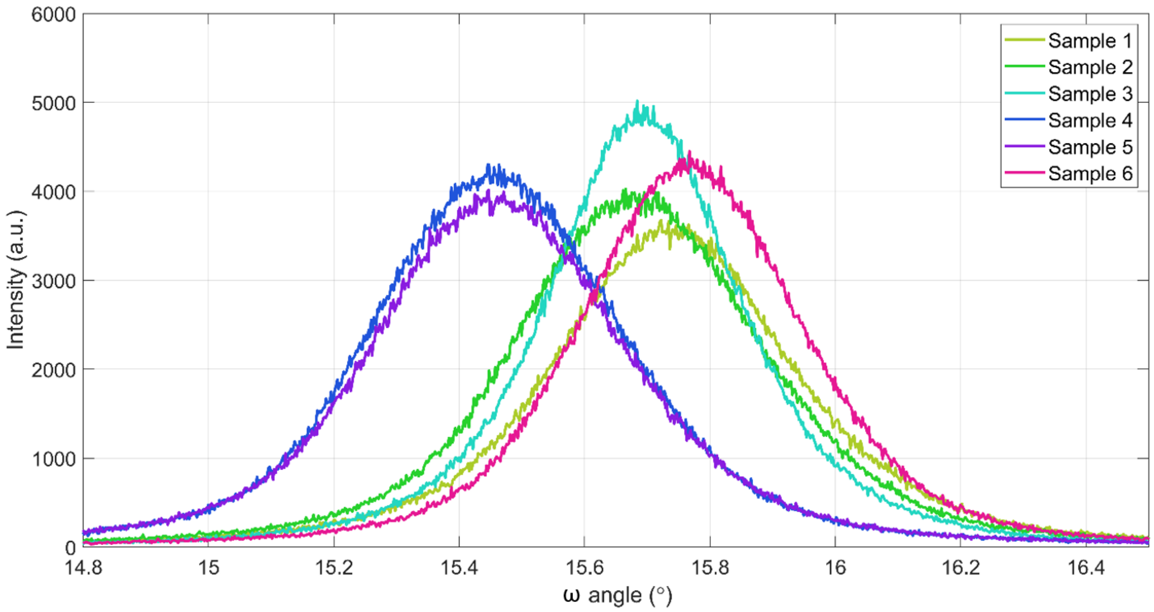

Figure 4.5: a) 2θ XRD scans and b) rocking curves of the (222) peak of 5 Sc_2O_3 films grown with an identical protocol (samples 1-5). Sample 6 had a faster cooling down post growth.

Another critical aspect to investigate is the repeatability of the film thickness. Indeed, in the absence of in-situ thickness monitoring, one must be able to predict the thickness of the film from the number of pulses alone. For this purpose, the growth rate of the film must not significantly vary between consecutive growths.

The thickness of the six films grown previously was calculated from their transmission spectra following the method in section 3.3.4. For each sample, five spectra were recorded with the white-light beam at random places on the film (as a reminder, the beam diameter is 2mm while the area of the sample is 10mm x 10mm). The resulting thicknesses are displayed in Figure 4.6. The mean value of the five thickness measurements was computed for each sample (in orange in Figure 4.6) and the standard deviation ranged from 5.3 nm (sample 2) to 14.3 nm (sample 5).

Interestingly, we observe that sample 6, which had a faster cooling down process than the other films, exhibits a significantly lower thickness. While this observation might suggest that the difference is caused by thermal expansion, a quick quantitative estimation dismisses this hypothesis. Indeed, looking back at the 2θ angles measured by XRD and the corresponding lattice constants summarised in Table 4.2, the difference in lattice constant between sample 6 and the others is lower than 0.1%. Therefore, for a given number of atomic layers in the film, the thickness should not deviate from more than 0.1% (~0.5nm in our case). The difference that we observe is several tens of nm, from which we can conclude that thermal expansion cannot be the main cause for this disparity.

An estimation of the average growth rate from the first five films can be calculated in case we would like to start a new growth by following the exact same protocol. A weighted average taking into account the uncertainty of each film thickness is more meaningful than a simple arithmetic average. The standard error σ_i of each set of five measurements is used to define the weight w_i of each sample thickness as follow:

$$w_i = \frac{1}{\sigma_i^2}$$

The weighted average thickness <t> is therefore:

$$< t > = \frac{\sum_i w_i t_i}{\sum_i w_i}$$

Where t_i is the thickness of a sample i computed as the mean of the five measurements. The equivalent standard error σ can then be calculated as:

$$\frac{1}{\sigma^2} = \sum_i \frac{1}{\sigma_i^2}$$

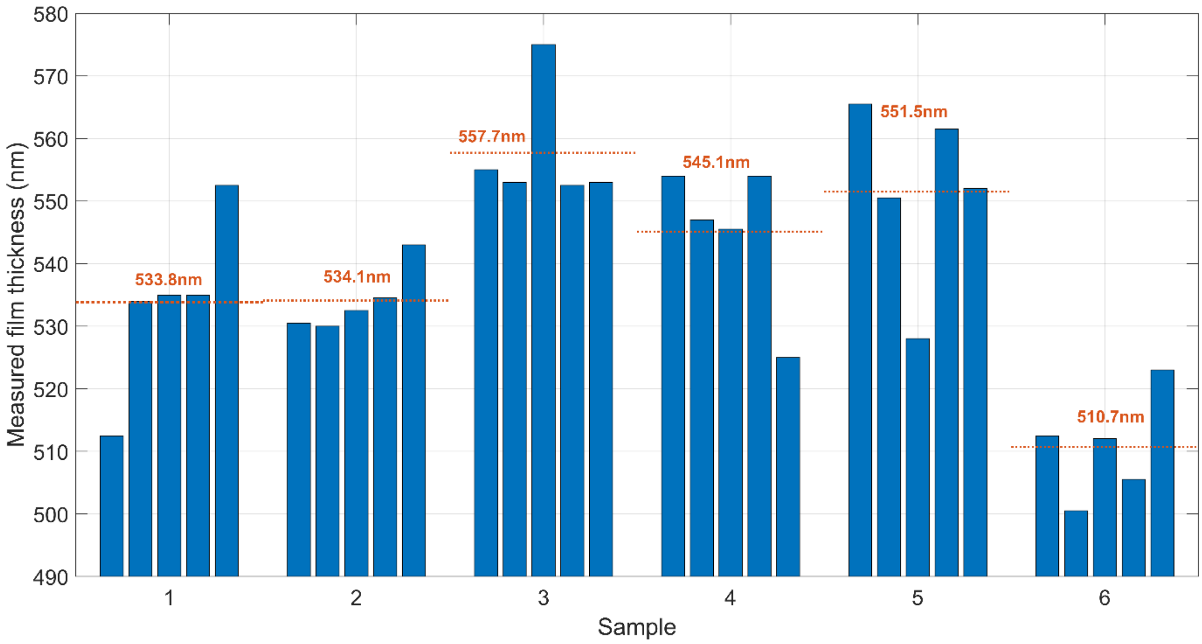

Figure 4.6: Film thicknesses calculated from the transmission spectra of the six samples of the repeatability study. Five measurements were recorded for each sample; the dotted line in orange corresponds to the mean of the five measurements for each sample.

This calculation results in a weighted average and standard error of (540.6 ± 4) nm. 10000 pulses were used for the growth of the films, which translates to a growth rate of 0.054 nm/pulse. Considering an uncertainty of ±σ, the next growth with identical conditions should therefore produce a film thickness of 540.6 nm ± 12.0 nm. In practice, we know that the dispersion of the measurements is even lower when we measure the thickness at the same spot on the film (e.g. centre of the film) since it removes the uncertainty related to the film flatness and curvature.

4.4 Variation of film properties with thickness

The last section determined the growth rate and film thickness of a 10000-pulse growth of Sc_2O_3 on a c-cut sapphire substrate, and how repeatable it is. In PLD, the common assumption is that the growth rate of the film remains constant, and therefore the thickness of the film scales linearly with the number of ablation pulses. There are two situations when this hypothesis might not hold true. At the early stages of the growth, the crystal structure of the film is not well-defined yet, and therefore one can suppose that the formation of the first few layers might be longer than the subsequent ones. Furthermore, beyond a certain critical thickness, the accumulated stress and defects in the film might slow down the growth process. In this section, we will verify how well the linear scaling of the film thickness with the number of pulses fits within our range of interest. As a reminder, the fabrication of the GWSs requires the growth of a 500nm waveguide for 1030nm application, and a 1000nm waveguide for 2µm application. However, we also need a precise control of the thickness of thin layers under 100 nm for the growth of quarter-wave Bragg stacks in chapter 9.

A first Sc_2O_3 film was grown on a c-cut sapphire substrate with a similar process as before: pulse energy of 102.6 mJ, CO_2 laser power of 23.7W, and O_2 background pressures of 0.020 mbar, ablation spot size of 7.8 mm^2. 10000 pulses were used for this first deposition, and the growth rate was estimated to be ~0.057 nm/pulse (average of five measurements using the transmission spectrum fitting). An additional five films were grown with identical conditions, but with a number of ablation pulses of 1760, 3520, 7040, 14080 and 28160. The targeted thicknesses were 100 nm, 200 nm, 400 nm, 800 nm, and 1600 nm, respectively.

Excluding the 100 nm film, five transmission measurements were recorded for each film to estimate the thickness. The arithmetical average of the five measurements of each sample is summarised in Table 4.3 and plotted in Figure 4.7 with error bars representing the standard deviation. This calculation could not be done with the 100nm sample because the transmission spectrum exhibited less than one oscillation, which reduced the accuracy of the fit. The weighed growth rate over the other four samples (400nm-1600nm) and the associated standard deviation were (0.055 ± 0.001) nm/pulse. The linear plot in Figure 4.7 has a slope corresponding to this weighted growth rate and shows that the linear approximation between film thickness and number of pulses is justified.

Table 4.3: Expected and measured thickness of Sc_2O_3 films grown with different numbers of ablation pulses. FWHM of the (222) 2θ- and ω-peaks measured via XRD. Note: the thickness of the 100nm film could not be measured with the usual method.

Expected thickness (nm)	Measured thickness (nm)	2θ peak FWHM (°)	Rocking curve FWHM (°)
100	-	0.102	0.60
200	206.4	0.060	0.46
400	399.7	0.048	0.42
800	717.8	0.042	0.38
1600	1588	0.051	0.39

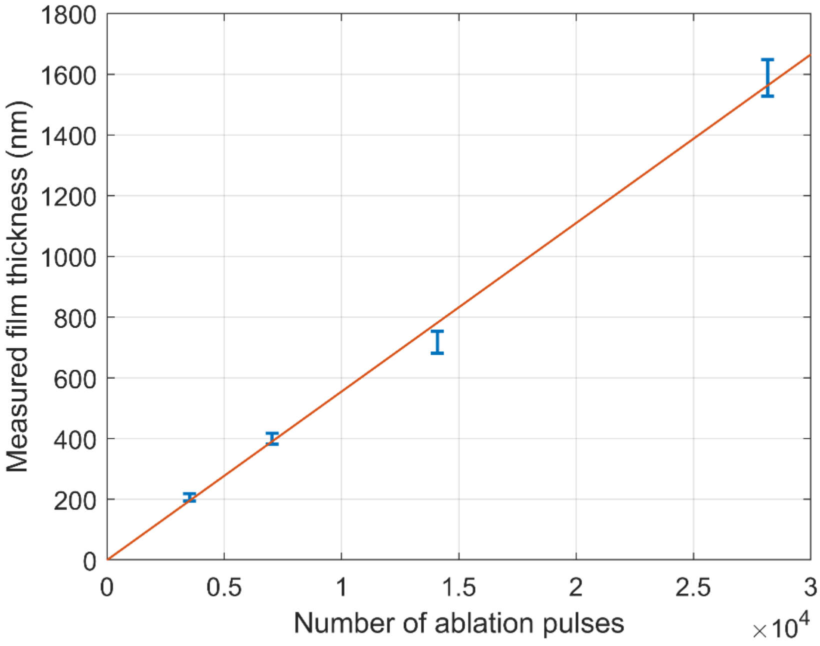

Figure 4.7: Measured thickness of Sc_2O_3 films versus number of ablation pulses. The error bars correspond to the standard deviation over five thickness measurements and the slope of the orange line is the weighted average of the growth rates.

The crystal structure of the films of different thicknesses was studied to reveal any difference. Low-resolution 2θ XRD scans were recorded from 20° to 80° with a 0.02° step and a 20°/min speed. High-resolution scans were also recorded from 31° to 32° with a 0.002° step and a 1°/min speed. The low-resolution scans did not highlight any difference between samples of different thicknesses. A reasonable interpretation is that if the film grows predominantly in the <111> direction in the early stage, there is a low probability of a different orientation spontaneously growing until reaching a thickness of 1600 nm. On the other hand, the high-resolution scans focussing on the (222) peak exhibit an increase in height and decrease in FWHM from 100 nm to 800 nm, as displayed in Figure 4.8 (a). Beyond 800 nm, the peak becomes larger. The same evolution can be observed from ω-scans (rocking curves) in Figure 4.8 (b).

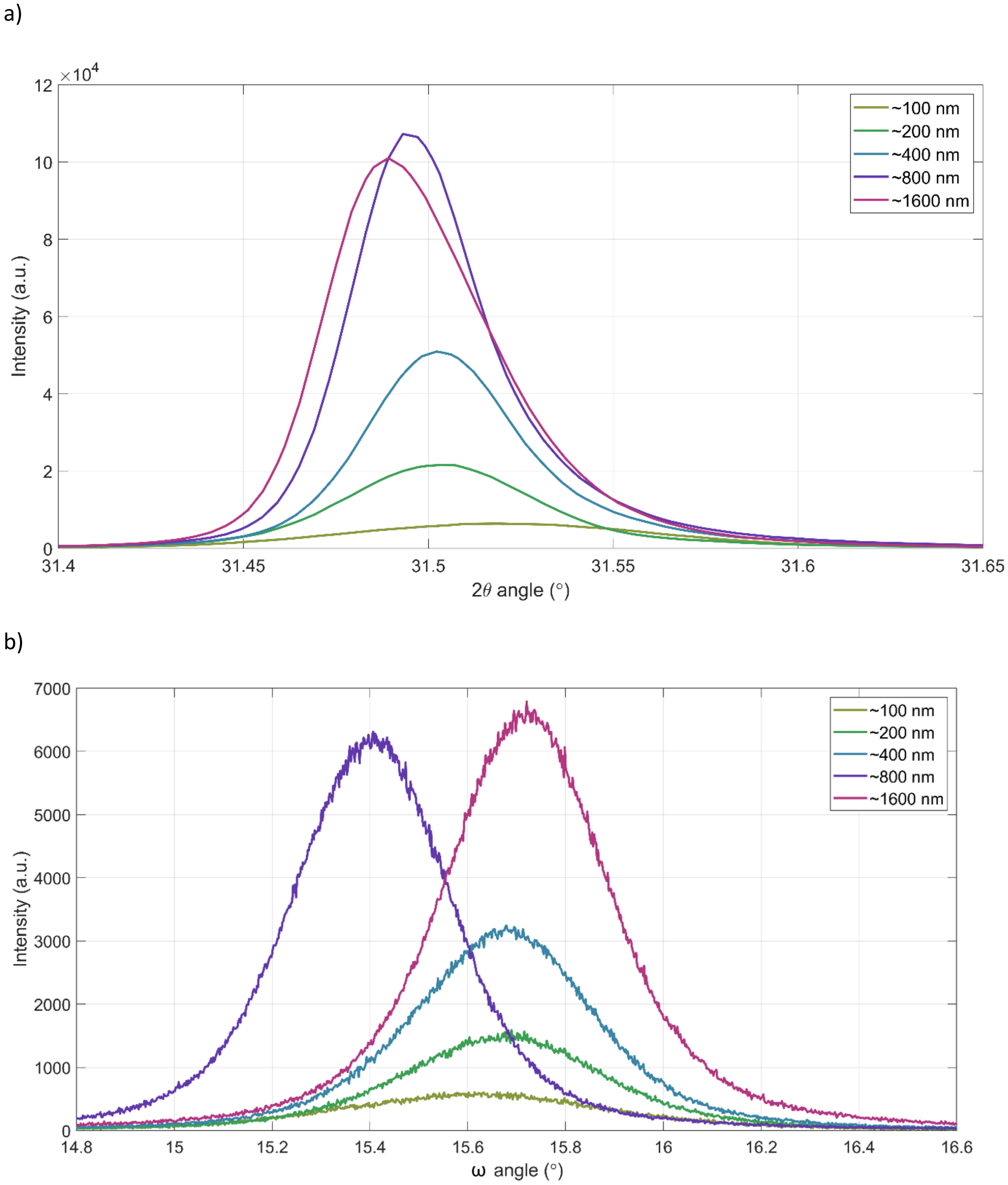

Figure 4.8: a) 2θ XRD scans and b) rocking curves of the (222) peak of 5 Sc_2O_3 films grown the same deposition parameters but different thicknesses.

In this section, we confirmed that the linear scaling of the thickness of the film with the number of ablation pulses was justified as a first approximation. The crystalline properties of the film do not vary significantly within the range of thicknesses that we are interested in.

4.5 Optical properties

4.5.1 Variation of the dispersion

In the chapter detailing our experimental methods, we showed that the thickness of the film can be calculated from its transmission spectrum if we assume the dispersion curve of the material. Most deposition techniques do not systematically produce the same dispersion curve even if a deposition is repeated with identical parameters, mainly due to slight variations of density. Consequently, it is legitimate to question our methodology, which assumes that the dispersion does not change significantly from one film to another. This is the purpose of this section, where we present the optimisation of the growth of Y_2O_3 thin films on sapphire substrates and demonstrate that, despite significant changes in crystallinity between samples, the change in refractive index stays well within our tolerances. Additional arguments are also given to further justify our assumption.

4.5.1.1 Y_2O_3 growth optimisation

The objective of this section is to determine the optimal CO_2 laser power for the growth Y_2O_3 on sapphire.

The excimer pulse energy was set to 82.3 mJ (± 0.3 mJ), and the spot size on the target's surface was 7.1 mm^2 (± 0.2 mm^2), resulting in a fluence of ~1.16 J/cm^2. A pulse repetition rate of 100 Hz was selected. The substrate consisted in a 10 x 10 x 1 mm sapphire c-cut substrate, which has the lowest lattice mismatch with the <111> orientation of Y_2O_3. The target-substrate distance for the depositions was 55 mm (± 2 mm).

The procedure for each deposition was the same:

- Vacuum pumps were activated to evacuate the air from the chamber.
- When the pressure reached ~1 µbar, the O_2 gas inlet was opened and the gas flow was adjusted via a needle valve to obtain a pressure of 20 µbar in the chamber.
- The power of the CO_2 laser was ramped up from 0 W to its final value. This gradual increase lasted between 10 and 15 minutes depending on the deposition power.
- Pre-ablation: before the actual deposition, a pre-ablation of 36000 pulses was performed to remove any contaminant from the target's surface. The substrate is shielded during this step. The pre-ablation was done only for the first deposition of a given day.
- Deposition: 36000 pulses were used for the deposition.
- At the end of the deposition, the CO_2 laser power was ramped down to zero. This gradual decrease lasted between 30 and 45 minutes depending on the deposition power.

- Vacuum pumps were deactivated and air was reintroduced in the chamber.

The heating power investigated in this study ranged from 16 W to 26.5 W.

Two XRD scans were recorded for each sample. A first scan for 2θ values from 20° to 80°, with a step size of 0.02° and scanning speed of 20°/min aimed at revealing the presence of additional orientations besides the expected Y_2O_3 <111>. A second scan with a smaller step size of 0.002 and a scanning speed of 1/min was centred around our main peak of interest, the (222) peak lying around 29.2°.

Figure 4.9 compares the wide XRD patterns of the Y_2O_3 films grown with a CO_2 laser power of 18 W and 25 W. We observe that the height of the (222) XRD peak has been reduced by a factor of ~50 for the 25 W (note the logarithmic scale). Moreover, the height of other peaks has also increased, which indicates the growth of new orientations that were not present in the film deposited at 18 W. Nevertheless, Y_2O_3 <111> remains predominant, since the height of the (222) peak is still ~100 times higher than the second highest.

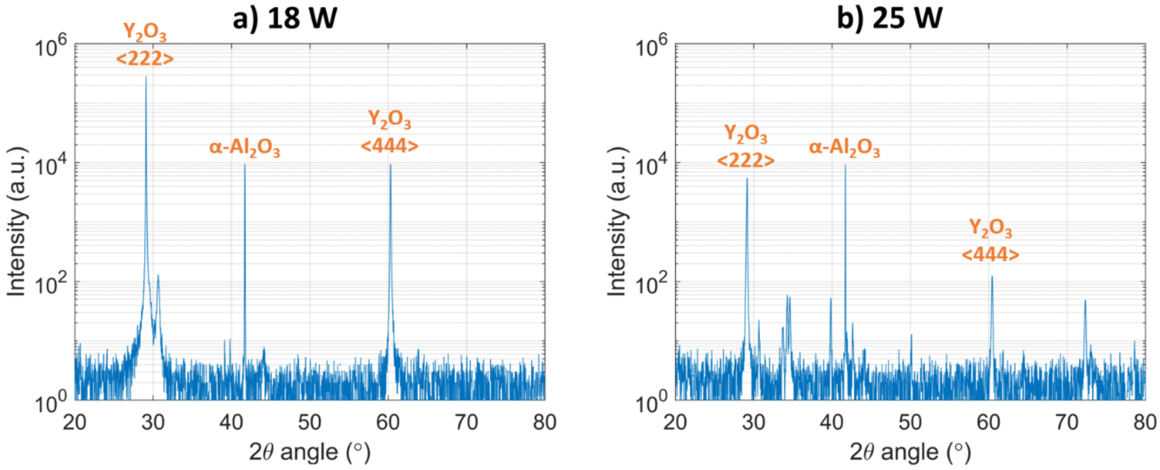

Figure 4.9: XRD patterns of the Y_2O_3 films deposited with a CO_2 laser power of a) 18 W and b) 25 W.

To confirm our observations, the (222) peak of all the Y_2O_3 films were plotted in Figure 4.10. The diffraction patterns were shifted horizontally to make their substrate peak coincide. Figure 4.10 (a) demonstrates how the crystallinity of the film is affected by the sample's temperature. A clear optimum of 18 W is found: beyond this heating power, a significant and progressive reduction of the peak height is observed; in the same way, the sample grown at 16.5 W not only decreased in height but also increased in width. Furthermore, a normalised plot of the (222) peaks (Figure 4.10

(b)) reveals that the resonance moves to higher angles when the temperature of deposition is increased. This shift in 2θ angle from 29.094° to 29.160° (± 0.01°) corresponds to a change of lattice constant from 10.632Å for 18 W to 10.609Å for 26.5 W, i.e. a reduction of ~0.2%.c

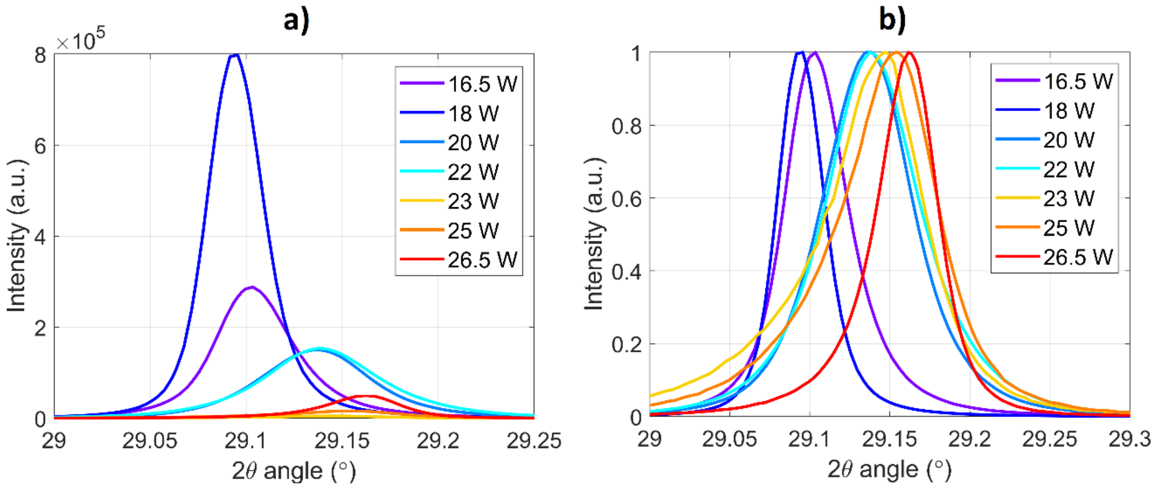

Figure 4.10: (222) XRD peaks of the Y_2O_3 films. a) raw data shifted in 2θ to make the substrate peaks coincide and b) same plot but normalised to peak maximum.

4.5.1.2 Prism coupling measurements on Y_2O_3 films

The TE and TM refractive indices of Y_2O_3 films were recorded with a prism coupling device equipped with a HeNe laser operating at 633 nm. Figure 4.11 illustrates the working principle of such a device. Depending on the refractive index of the prism, film and substrate at the laser wavelength, only a specific set of incident angles will allow the excitation of propagation modes in the waveguide. This causes a dip in the power of the reflected beam, which is monitored by a photodetector. The measurements consist in varying the angle of incidence to determine those excitation angles, and using the theoretical equations to deduce the refractive index of the film and its thickness. Note that the indices of the prism and the substrate must be already known.

The results are displayed in Table 2.1. The Y_2O_3 films were grown with CO_2 laser powers ranging from 16.5 W to 23 W. Beyond that range, the quality of the films decreases significantly; we can thus safely assume that no film will be deposited with a heating power outside that range. We observe that both TE and TM refractive indices decrease when the deposition temperature is increased. However, the variation is only in the 3rd and 4th decimal, which is close to the resolution of the device. This observation is in good agreement with previous reports on the deposition of Er(1%)-doped YGG on YAG, where a variation of 14 W in the CO_2 laser power only led to a difference of 0.003 in refractive index (Grant-Jacob et al., 2017). In a similar way, I investigated the effect of the ablation fluence on the refractive index of Sc_2O_3 films and, for a range from 1.09 to 1.36 J/cm^2, the variation was only 0.001.

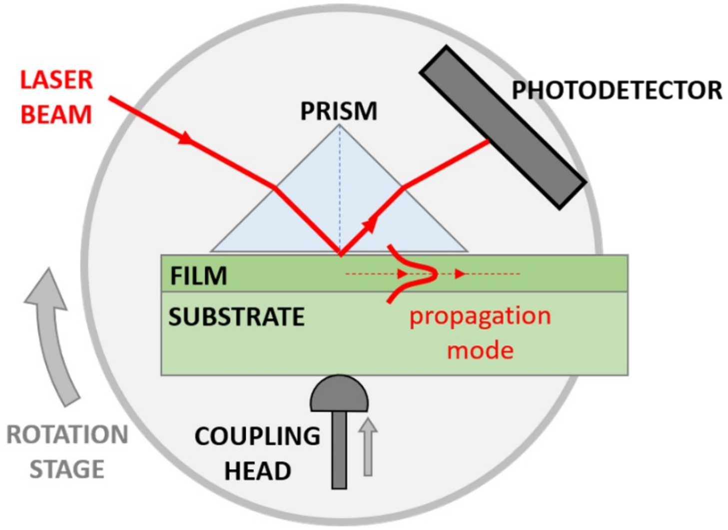

Figure 4.11: Working principle of a prism coupler.

For our intended application, we do not require a precision on the refractive index and thickness of more than 1%. The GWSs for spectral stabilisation are intended to be used in the Littrow configuration (incident and diffracted beams are coincident) with an angle of incidence of 10° from the normal of the surface. A small change in the GWSs parameters will only cause the resonance angle to move, without affecting the diffraction efficiency. During the fabrication process, it can be challenging to have an etching depth control better than 5% or a duty cycle variation less than 10%. The design ensures that the GWS will still be useable by simply tuning the angle of incidence, despite small variations between the initial design and the final GWS. Using the Metricon prism coupler, I proved that the refractive index of our films varies by less than 0.1% with large changes in the deposition parameter. A refractive index change beyond 1% is impossible without compromising epitaxial growth, which is easily noticeable in the XRD scans. It is therefore unnecessary to perform systematic ellipsometry measurements and we can assume that the dispersion curve of our crystalline films does not change sufficiently to affect the use of our final GWSs.

Table 4.4: Refractive indices of Y_2O_3 films deposited with different heating powers.

Substrate	**Film**	**Heating power during growth (W)**	**TE index at 633 nm**	**TM index at 633 nm**
sapphire	Y_2O_3	16.5	1.9111	1.9106
sapphire	Y_2O_3	18	1.9109	1.9105
sapphire	Y_2O_3	20	1.9101	1.9094
sapphire	Y_2O_3	23	1.9096	1.9093

4.5.1.3 Additional arguments

Variations of refractive index in thin films deposited via CVD, PVD or Magnetron sputtering are sometimes related and/or caused by variations in density. In our case, we are epitaxially growing crystalline films and the lattice constant is directly determined via 2θ XRD measurements. During our repeatability study in section 4.3, we demonstrated that the position of the (222) peak did not shift by more than 0.011°, corresponding to a change in lattice constant smaller than 0.03%. The value of the lattice constant directly reflects the separation between crystal planes, which is directly related to the density. We can therefore claim that the density of two Sc_2O_3 films grown with the same conditions in our PLD system will not vary by more than 0.03%. From this observation, we can deduce that the refractive index (and dispersion curve) will not vary significantly from one sample to another.

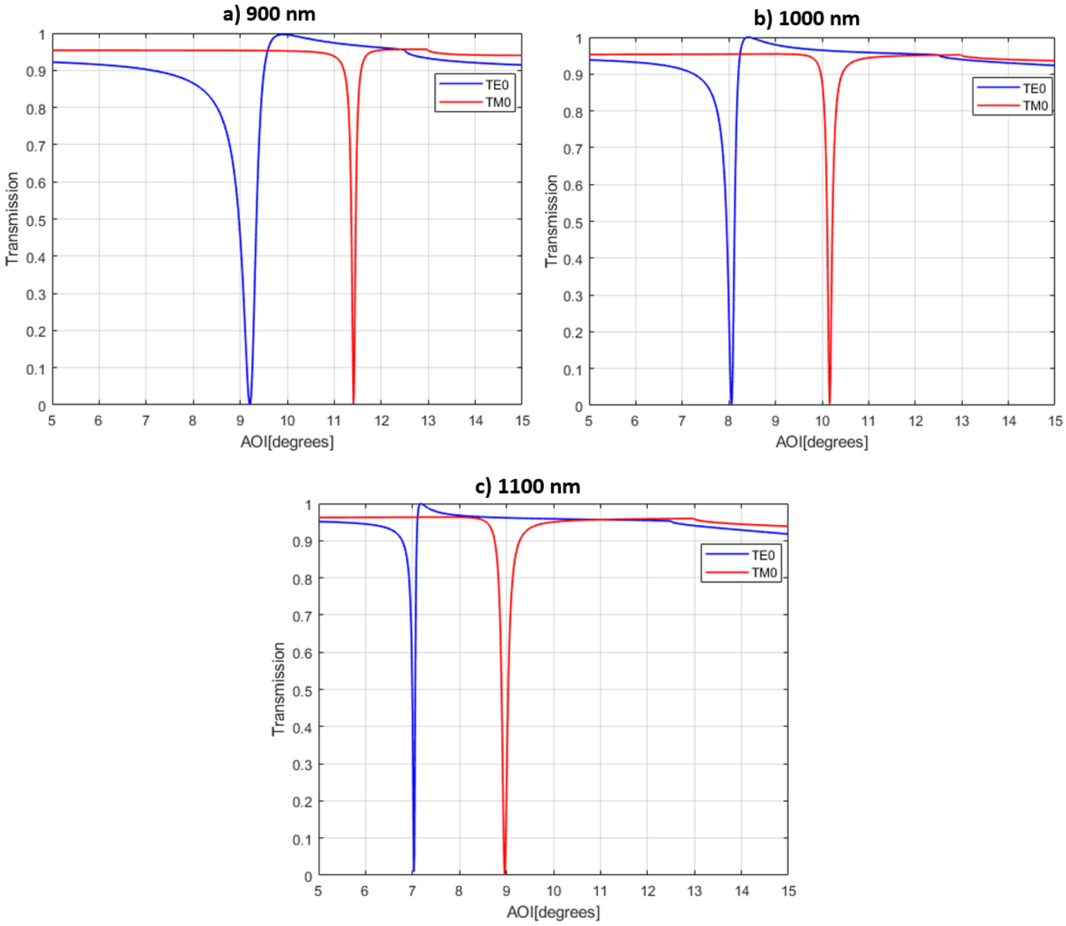

Figure 4.12: Theoretical GWS diffraction efficiency as a function of the angle incidence for a TE- and TM-polarised beam at 1970 nm. Waveguide thickness of a) 900 nm, b) 1000 nm (original design) and c) 1100 nm.

Finally, the last argument is that the tolerance on the thickness of the waveguide in our GWS design is relatively large. Our partner Danish Bashir from Institut fur Strahlwerkzeuge (Germany) calculated the theoretical diffraction efficiency of the GWS with an error of ± 10% on the thickness of the waveguide. While the angle of resonance and the width of the TE resonance were impacted, the diffraction efficiency remained unchanged (Figure 4.12). This last observation confirms that a precise control of the thickness is not required for GWS growth.

4.5.2 LIDT tests

The LIDT evaluation of optical components started promptly after the invention of the laser in the 1960s. Laser damage resistance rapidly became the main limiting factor for the upscaling of laser power, especially in pulsed laser systems (Soileau, 2015). New design techniques were developed to optimise the LIDT of coatings (Chen et al., 2012, Willemsen et al., 2017) and since thereafter, a wide range of materials were investigated as potential coating materials. Despite being mainly driven by the goal of increasing the damage resistance of optical components, the LIDT field also provides a better understanding of the mechanics behind damage initiation, which is paramount for laser material processing (Gattass and Mazur, 2008).

It has been demonstrated in the current chapter that our PLD setup enables the epitaxial growth of highly crystalline sesquioxide films on sapphire. Bulk sesquioxides and sapphire generally have better mechanical and thermal properties than traditional coating materials. Evaluating the LIDT of our PLD-grown films and comparing them to the state-of-the-art is therefore the most effective way of validating the potential of PLD for the fabrication of high-LIDT optical coatings. The samples used for comparison were deposited via Magnetron Sputtering by Janis Zideluns in Institut Fresnel. The materials selected were the usual candidates for multilayer optical coatings: SiO_2 as a low-refractive-index material, and NbO_5, Ta_2O_5 and HfO_2 as high-refractive-index materials. They have been widely used in novel cutting-edge optical coatings and have been investigated with various deposition techniques.

This chapter summarises the LIDT tests conducted on sesquioxide films deposited via PLD. The deposition of the films and their preliminary characterisation (XRD, thickness, refractive index, scattering and bandgap) were performed by me at the Optoelectronics Research Centre. The LIDT measurements and their analysis were almost entirely carried out by Marek Stehlik, PhD candidate at Institut Fresnel. I had the opportunity to visit their facilities for two weeks and participate on the LIDT campaign on YGG thin films that I grew on YAG (results not included in this thesis).

4.5.2.1 PLD growth and X-ray diffraction

Four sesquioxide films were grown via PLD for this LIDT study. Y_2O_3, Lu_2O_3 and Sc_2O_3 were grown on sapphire substrates with optimal deposition parameters previously identified during parametrical optimisations. Growing a single-crystal Lu_2O_3 film on sapphire was challenging, as the films were generally strongly polycrystalline even with our optimal set of deposition parameters. For this reason, a second Lu_2O_3 film was grown on a YAG substrate for comparison. The deposition parameters for the four films are summarised in Table 4.5. The films epitaxially grown on sapphire were expected to be <111>-orientated, since this orientation has the smallest lattice mismatch with sapphire <0001>: 2.5%, 2.9%, and 4.9% respectively for Sc_2O_3, Lu_2O_3 and Y_2O_3 <111>. Furthermore, Lu_2O3 <111> has a nearly perfect lattice match with YAG <001> and should therefore grow with minimal strain.

Table 4.5: Deposition parameters of the samples grown for the LIDT tests. The lattice constants were calculated from the position of the (222) peaks and the error was ± 0.004 Å.

Substrate	**Film**	**Target ablation fluence**	**Heating power**	**(222) XRD peak position**	**Film lattice constant**
YAG	Lu_2O_3	1.21 J/cm^2	26.7 W	29.788°	10.390 Å
sapphire	Lu_2O_3	1.27 J/cm^2	26.2 W	29.760°	10.399 Å
sapphire	Y_2O_3	1.19 J/cm^2	18.0 W	29.095°	10.632 Å
sapphire	Sc_2O_3	1.24 J/cm^2	24.0 W	31.495°	9.840 Å

A long XRD scan was performed on the samples with the 2θ angle varying from 20° to 80° and a step of 0.02°. The diffraction patterns are displayed in Figure 4.13 in logarithmic scale. Each diffraction peak was identified and labelled accordingly. The predominance of the <111> orientation is very clear in the Y_2O_3 and Sc_2O_3 films grown on sapphire: the (222) peak is 3 orders of magnitude higher than the peaks of the other orientations. On the other hand, multiple orientations are present inside the Lu_2O_3 film grown on sapphire, confirming the polycrystalline nature of the film. Finally, the Lu_2O_3 film grown on YAG <100> has a (222) peak almost coincident with the (400) peak of the substrate at 29.8°. The second highest peak is once again 3 orders of magnitude smaller and demonstrate that the film is highly textured in the <111> direction. It also confirms further that the growth of Lu_2O_3 on YAG is easier to control than on sapphire.

A high-resolution XRD scan with a step of 0.002° was recorded for each sample around the (222) peak. Figure 4.14 (a) compares the normalised (222) peaks of the films grown on sapphire, while Figure 4.14 (b) confronts the normalised (222) peaks of the two Lu_2O_3 films. The objective was two-folded: on the one hand, the scan on the Lu_2O_3/YAG sample aimed at resolving the Lu_2O_3 (222) and the YAG (400) peaks, as they could not be distinguished in the low-resolution scan; on the other hand, the exact position of the (222) peaks were used to compute the corresponding lattice constants (values in Table 4.5). It must be noted that this lattice constant value is not meaningful for the Lu_2O_3/sapphire sample, because of its polycrystalline nature. Nonetheless, the aim was to simply understand how this value differed from the Lu_2O_3/YAG sample.

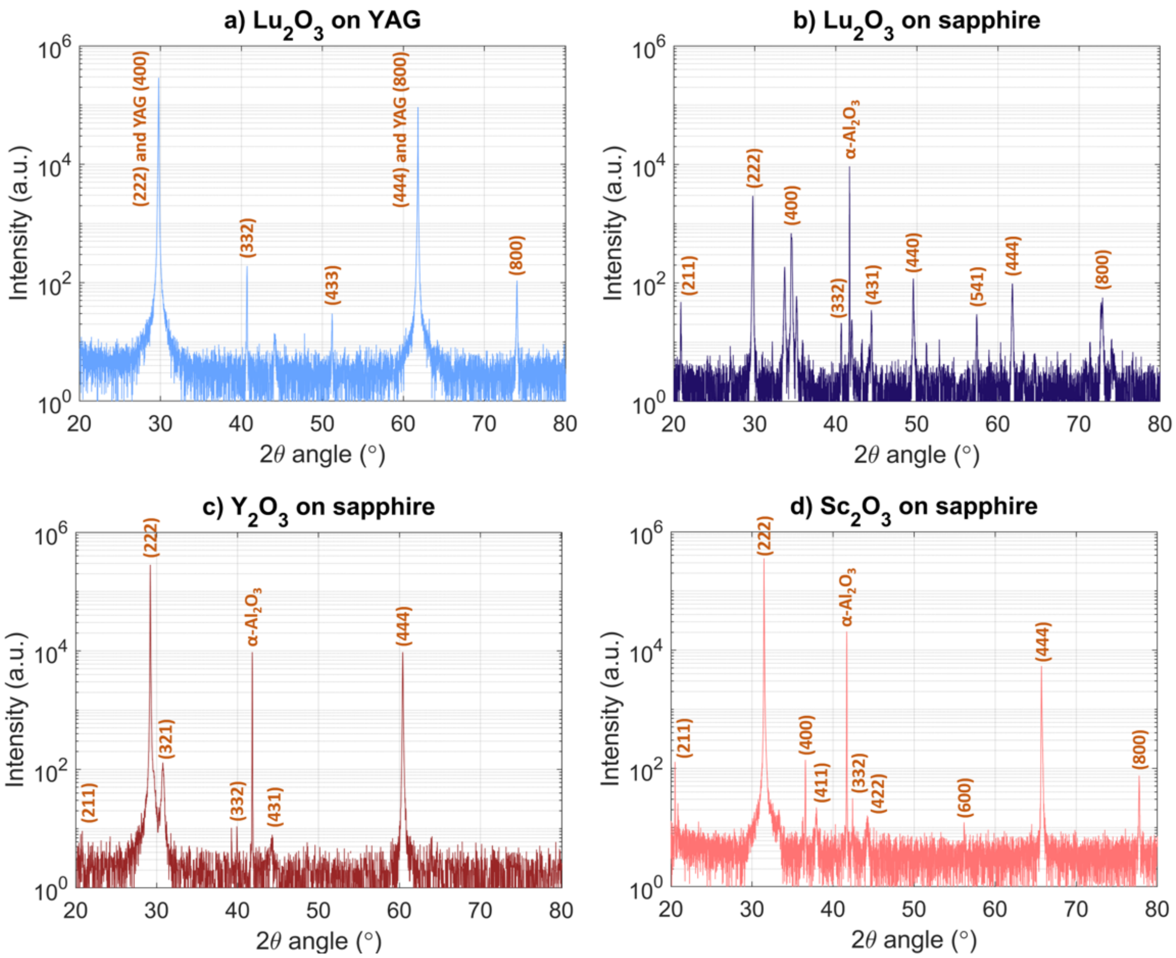

Figure 4.13: XRD patterns of the sesquioxides films grown for the LIDT tests: a) Lu_2O_3 on YAG, b) Lu_2O_3 on sapphire, c) Y_2O_3 on sapphire, and d) Sc_2O_3 on sapphire.

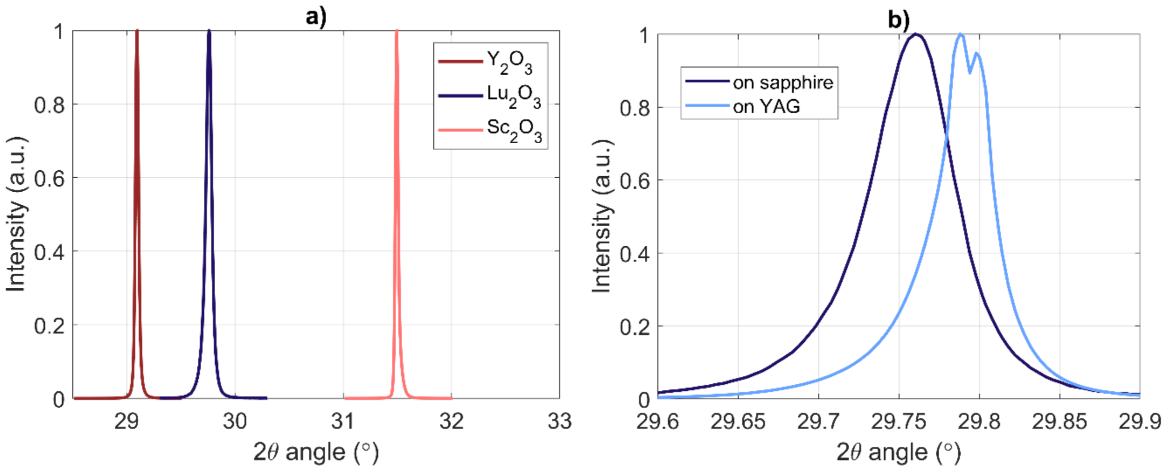

Figure 4.14: Normalised (222) XRD peaks of the sesquioxides films grown for the LIDT tests: a) all films grown on sapphire, b) Lu_2O_3 films on sapphire and YAG.

4.5.2.2 Bandgap measurements

Measuring the bandgap of the samples can helps us better understand the results of the LIDT campaign. In the femtosecond regime, the time scale of the light-matter interaction is so small that the single-shot LIDT of a material is strongly correlated to its bandgap. Therefore, performing both measurements and verifying the correlation between the results can helps us confirm the quality of the measurements and strengthen our arguments. It must be noted that, while the bandgap provides insight on the single-shot LIDT, it does not necessarily indicate anything about the multiple-shot LIDT. Thermal effects also play a significant role with multiple shots, which is actually where our crystalline samples will be at an advantage with their favourable thermal properties.

The bandgap measurements presented in this section were performed by me in the Optoelectronics Research Centre, on different samples from the ones used for the LIDT tests. In contrast, the bandgap values highlighted in Figure 4.19 were obtained with the original samples by Marek Stehlik.

Four new samples were produced by following the exact same PLD recipe as the original samples. The repeatability study from earlier strongly suggests that the properties of the new films must be very similar to the original ones.

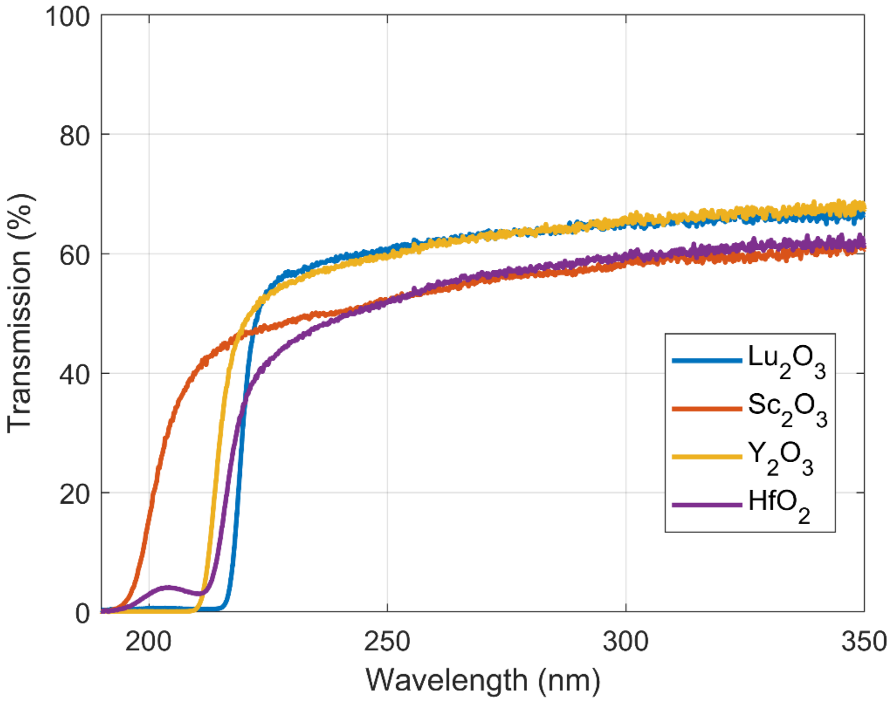

Figure 4.15: Transmission spectra of various films grown on sapphire via PLD: Lu_2O_3, Sc_2O_3, Y_2O_3 and HfO_2. The spectra were recorded with the Varian Cary 500 spectrophotometer for bandgap evaluation.

The Varian Cary spectrophotometer was used to record the transmission of the samples in the UV range. Figure 4.15 displays the spectra of the three films grown on sapphire, along with the spectrum of a HfO_2 film grown via PLD for reference. The drop of the transmission, which corresponds to a rise of the absorption, happens around 200 nm for all of them. The sapphire and YAG substrates respectively have bandgaps close to 9.2 eV and 8 eV, placing their band-edge at a much shorter wavelengths than these film materials (Hrabovsky et al., 2021, Moulton et al., 2019). This was confirmed by measuring the transmission of bare substrates of YAG and sapphire and observing no transition above 190 nm. We can therefore assume that in each spectrum, the transmission drop is mainly caused by the film and that the effects of the substrate are negligible. As a result, we calculate the Tauc plot of the sample by using the thickness of the film rather than the full thickness of the sample. As usual, the thickness of the film is obtained by measuring and fitting the transmission spectrum in the visible range (section 3.2.3).

The linear part of the Tauc plots was determined and fitted by the methodology described in section 3.2.4. The resulting bandgaps of the films grown on sapphire are 5.59 eV, 5.72 eV and 5.97 eV for Lu_2O_3, Y_2O_3 and Sc_2O_3, respectively. Even though the error on such bandgap evaluation is difficult to estimate, it is interesting to observe that, by rigorously applying the method from section 3.2.4, we obtained the same bandgap value for Lu_2O_3 on YAG and Lu_2O_3 on sapphire within ± 0.1%. The strong polycrystalline nature of the Lu_2O_3 film grown on sapphire does not seem to make a significant difference in terms of bandgap.

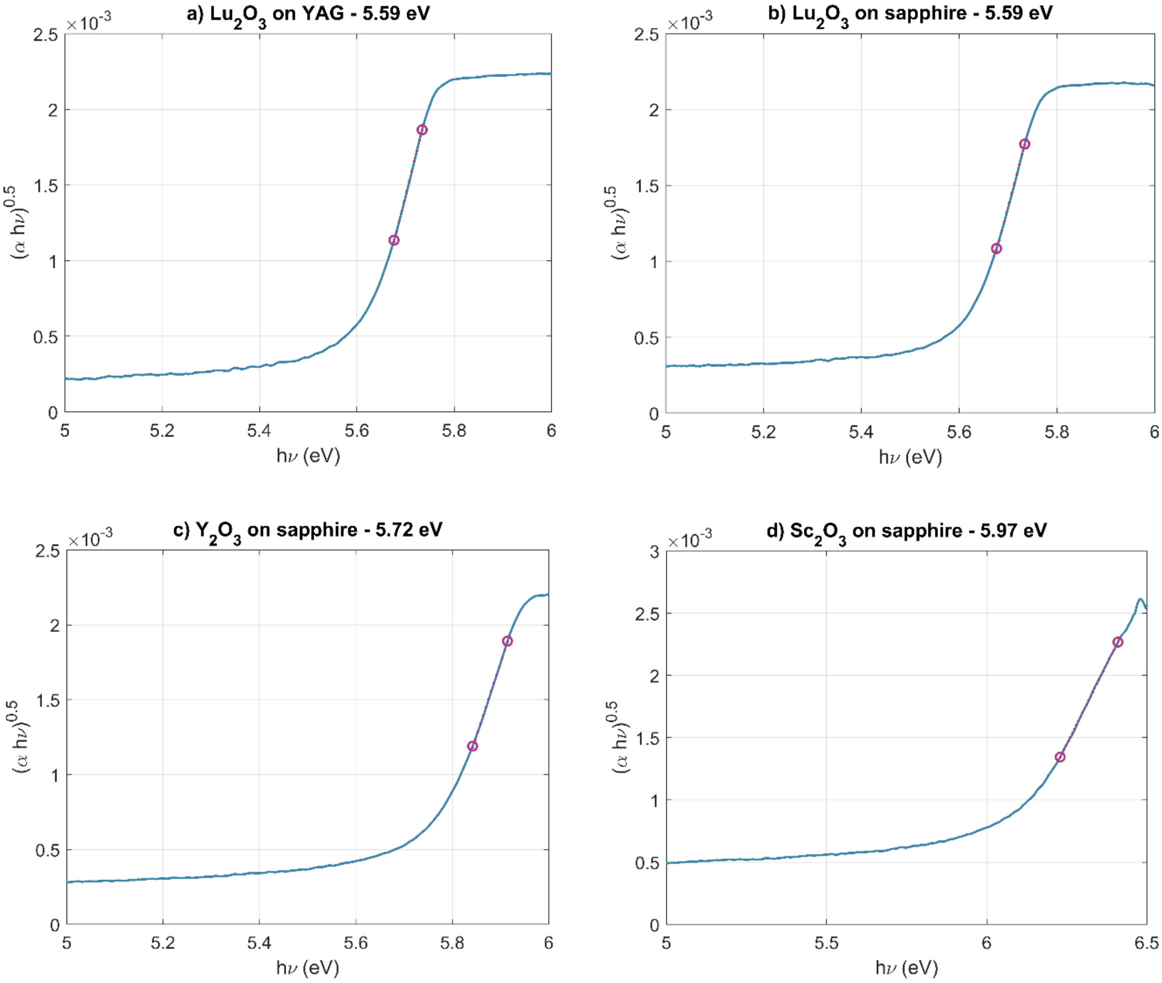

a) Lu_2O_3 on YAG - 5.59 eV

b) Lu_2O_3 on sapphire - 5.59 eV

c) Y_2O_3 on sapphire - 5.72 eV

d) Sc_2O_3 on sapphire - 5.97 eV

Figure 4.16: Tauc plots of a) Lu_2O_3 on YAG, b) Lu_2O_3 on sapphire, c) Y_2O_3 on sapphire, and d) Sc_2O_3 on sapphire. The two purple circles highlight the portion of curve used for the linear fit, while the dotted purple line between them represent the best fit.

The bandgap results from Marek Stehlik were obtained with a similar spectrophotometer in Institut Fresnel. Although Marek's bandgap values were ~0.3 eV lower than mine (Figure 4.19), the overall trend was comparable: the Sc_2O_3 film exhibited the highest bandgap, while the three others had similar bandgaps. The difference in values can be explained by the fact that the thickness measurement method was not the same. The original samples for LIDT tests were measured by Metricon, which only provides the thickness at the point of contact of the film with the prism. A punctual measurement on a film exhibiting a non-uninform thickness is therefore not precise enough. On the other hand, the newer samples were measured with the white light transmission method, where the diameter of the beam is 2.5 mm, and five measurements are performed across the sample. The measurements on the newer samples must thus be more accurate. Another explanation for the bandgap discrepancy is the difficulty of identifying the region on the Tauc plot where the linear fit must be performed. Depending on the selected region, the bandgap values might vary. In the literature, reports of the bandgap of Sc_2O_3 film can range from 5.6 eV on ion-beam sputtered films (Mende et al., 2013) to 6.5 eV on electron-beam deposited samples (Hervy et al., 2017).

4.5.2.3 LIDT evaluation

Definitions

The **LIDT fluence** is defined as the highest laser fluence that does not cause damage to the surface. To be more specific, it is the highest fluence that was shown to have a zero probability of causing damage during the tests. In this context, **"damage"** corresponds to any modification experienced by the material, including a change in topology, in colour, or even in refractive index. The detection of the damage is partially subjective, as minor alterations can sometimes be hardly visible on a microscope by the operator. However, by increasing the number of tests around the suspected LIDT value, it is generally possible to reduce this uncertainty.

From the experimental tests, it is possible to determine the **external LIDT fluence** F_{exp}, which corresponds to the laser fluence incident on the sample at the threshold. However, inside the film, the interference effect creates oscillations of the electric field amplitude between the air-film interface and the film-substrate interface (example in Figure 4.17). The strength of the electric field is therefore not uniform inside the film and its distribution depends on the film thickness and substrate material. That is why the external LIDT fluence is specific to a particular film. As a matter of fact, the final objective is to obtain the **intrinsic LIDT fluence** F_{int} of the film material, which only depends on the material itself. The distribution of the electric field can be computed in the different media if their refractive index at the laser wavelength and the thickness of the film are known (Figure 4.17). The intrinsic LIDT fluence is related to the external LIDT fluence by the simple scaling formula :

$$F_{int} = \left|\frac{E_{max}}{E_{inc}}\right|^2 \times F_{exp}$$

where E_{inc} is the amplitude of the incident electric field and E_{max} is the maximum amplitude of the electric field inside the film.

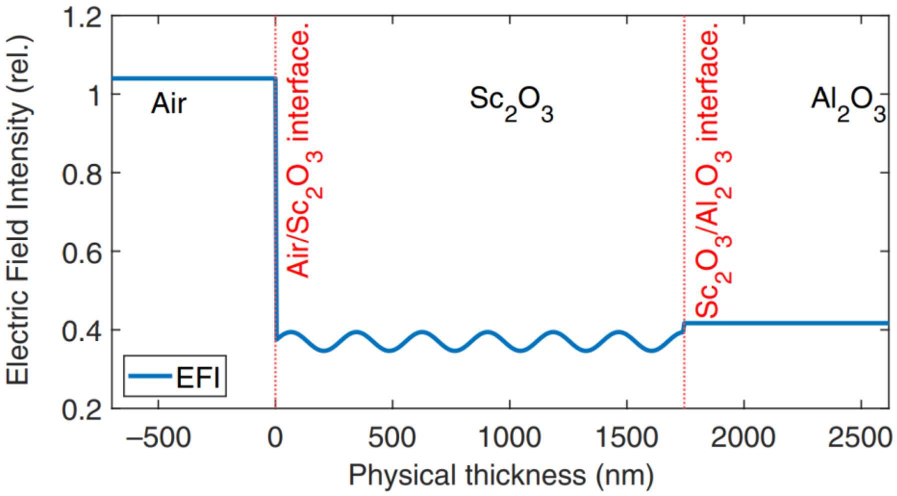

Figure 4.17: Distribution of the electric field intensity normalised to the incident one in air. This distribution was computed for a Sc_2O_3 film thickness of 1745 nm and a P-polarised 1030-nm beam incident at 45°.

Procedure

The full description of the LIDT setup can be found in (Stehlík et al., 2021). The 1030-nm laser beam was P-polarised and incident on the samples at an angle of 45°. A beam profiler confirmed that the beam was nearly Gaussian and had a diameter of 84 µm after being focussed by a lens of 300 mm focal length. The pulse repetition rate was 10 Hz and the pulse duration, measured with an autocorrelator, was 525 fs.

The single-shot LIDT test consisted in irradiating several spots on the sample with single pulses of different energies. The energy was increased by ~1% between each spot. Damage could be observed in-situ with a bright-field microscope camera, which allowed the operator to estimate approximatively the external LIDT fluence during the test. The operator would then collect more data points around the estimated LIDT in order to improve the precision of the measurement. Multiple-shot LIDT tests followed the same procedure, but the single pulses were replaced by series of 10, 100, and 1000 pulses.

While the in-situ monitoring of the damage helped roughly identifying the external LIDT fluence, a second ex-situ examination was conducted through a Zeiss Axiotech differential interference contrast microscope with a 20x objective magnification. This additional examination helped detecting some damage that was not properly identified in-situ.

The thickness of the films had been determined by Metricon measurements. A simulation akin to the one in Figure 4.17 was performed for each sample to determine the distribution of the electric field inside of them. From these results, the intrinsic LIDT fluence could be computed for each material and each number of shots (1, 10, 100, 1000 pulses).

Results and discussion

HfO_2 is a good comparison for our sesquioxides, as it is a widely used material with high refractive index. HfO_2 exhibits a higher damage threshold than other high index materials like Nb_2O_5, which is why it is generally preferred in multilayer optical coatings. The LIDT results are presented in Figure 4.18 and include LIDT tests on HfO_2, Nb_2O_5 and SiO_2 films grown on fused silica via magnetron sputtering, for comparison. The single-shot intrinsic LIDT of HfO_2 was around 2.3 J/cm^2, while the literature reports values closer to 2.0 J/cm^2 (Gallais et al., 2011, Hervy et al., 2014). This discrepancy was attributed to the fact that the coated HfO_2 layer included 1-2% SiO_2, which might have effectively increased the LIDT.

On the other hand, Sc_2O_3 reached a single-shot LIDT above 2.7 J/cm^2, while Y_2O_3 was around 2.3 J/cm^2. An interesting observation is that the Lu_2O_3 film grown on sapphire exhibited a ~20% lower intrinsic LIDT than the one grown on YAG. This result highlights the fact that the polycrystalline nature of the former has an actual effect on the damage threshold. The discontinuity of the crystal between domains of different orientation might be responsible for this difference, and the boundaries between them is likely the place where the damage is initiated.

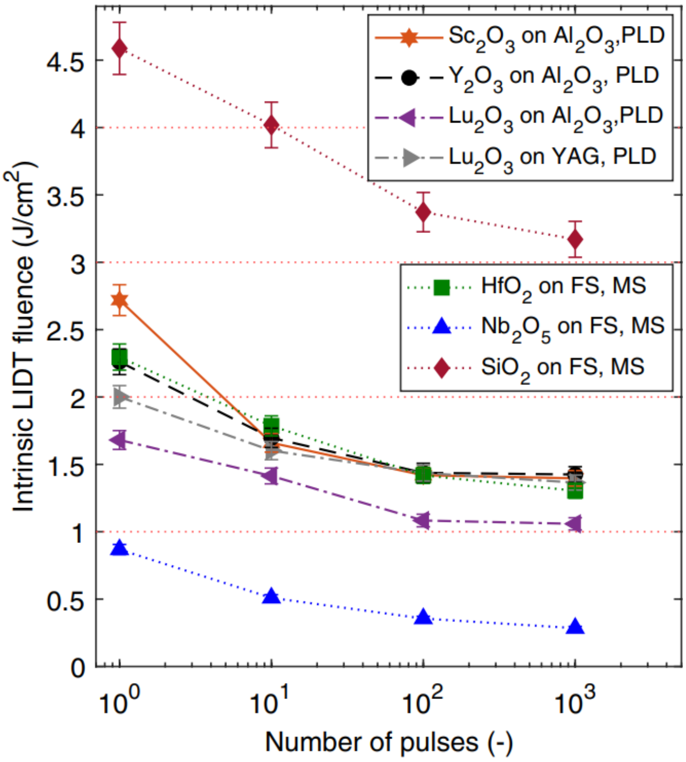

Figure 4.18: Evolution of the intrinsic LIDT fluence for a number of shots ranging from 1 to 1000 pulses. The Sc_2O_3, Y_2O_3 and Lu_2O_3 films were grown via PLD, while the HfO_2, Nb_2O_5 and SiO_2 were deposited on fused silica (FS) substrates via magnetron sputtering (MS).

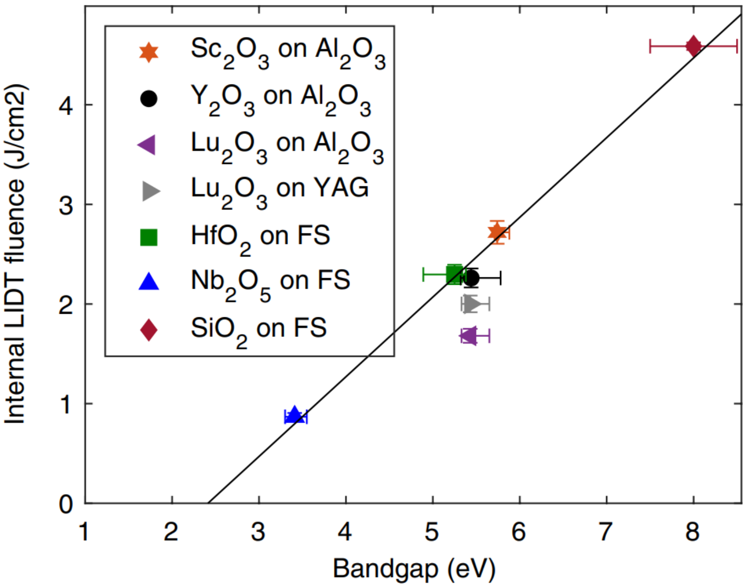

Figure 4.19: Correlation of the single-shot internal LIDT fluence with the material bandgap. The line of best fit satisfies the equation: $LIDT = 0.8 \times E_g - 1.93$.

In terms of multiple-shot LIDT, excluding the Lu_2O_3/sapphire sample, all the PLD films as well as the HfO_2 film converge to the same value of (1.4 ± 1) J/cm^2. This indicates that all these materials are equivalent in terms of LIDT for a use in high power sub-picosecond laser systems.

Finally, in the sub-picosecond regime, the light-matter interaction is so short that ionisation is the major mechanism initiating damage in the film. A direct correlation between the bandgap and the single-shot intrinsic LIDT should normally be observed. Figure 4.19 displays a plot of the LIDT as a function of the bandgap Eg, which as expected, exhibits a clear linear trend. The curve was linearly fitted with the function $LIDT = 0.8 \times E_g - 1.93$. Both errors on the LIDT and the bandgap are sufficiently high to make this fit very approximative.

4.5.2.4 Conclusion on the LIDT

We presented the results of the LIDT tests on the PLD-grown sesquioxides conducted in Institut Fresnel. Single-shot LIDT tests revealed that Sc_2O_3 has a ~20% higher intrinsic LIDT than HfO_2, which is generally the high-index material of choice for multilayer coatings, owing to its larger bandgap than Nb_2O_5. The multiple-shot tests demonstrated that all PLD-grown sesquioxides were comparable to HfO_2 and therefore suitable for high power laser applications. A linear relationship was found between the single-shot intrinsic LIDT and bandgap, confirming the fact that ionisation is the primary effect initiating damage.

The applications targeted by our samples are involving CW lasers, unlike the LIDT tests that we performed in this section. The interactions involved in the CW regime are not the same as the femtosecond regime: thermal effects have a more important role than the bandgap, which further confirms that our crystalline samples have a high potential for becoming new materials of interest in the coating industry.

4.6 Island growth vs layer-by-layer growth

The surface morphology of a film epitaxially grown via PLD depends on two energetic processes: a thermally driven low-energetic process allowing the adatoms to diffuse on the growth surface until they reach their nucleation site, and a high kinetic energy process where the ions and atoms from the plasma plume have enough momentum to break islands (Eres et al., 2016, Ulbrandt et al., 2020b, Willmott et al., 2006a). In a similar way to other thin film deposition methods such as MBE or CVD, the thermal energy of adatoms on the surface, generally lying around a few tens of eV, determines their average diffusion length. More specifically, transient mobility of the adatoms is governed by the Arrhenius equation, which relates the hopping rate of adatoms to their diffusion activation energy and their second-neighbours interaction energy (Guan et al., 2008). With sufficient knowledge about these energy levels, Montecarlo simulations of the film growth may illustrate the formation of 2D and 3D islands and predict their average size and density. However, PLD presents two other specificities: the adatoms are introduced periodically within a brief time window, making the instantaneous adatoms flux several orders of magnitude higher than MBE or CVD; moreover, the landing ions and atoms may have energy levels above 100 eV, which can effectively break islands upon collision and therefore frustrate Ostwald island ripening. Considering these additional parameters, a more accurate representation of PLD epitaxial growth could be simulated (Gabriel et al., 2020a, Jacobsen et al., 1998, Willmott et al., 2006a).

A critical observation from these studies is the importance of interlayer transport to minimise 3D island growth and favour layer-by-layer growth. The high-energy plasma plume has been identified as a paramount element for the periodic redistribution of the adatoms on the surface, causing the interlayer transport to spike for a short µs-scale duration, before the slow thermal diffusion process becomes the dominant mechanism during the inter-pulse time (Eres et al., 2011). Eres et al. demonstrated that, in the case of $SrTiO_3$ growth, interlayer migration was four orders of magnitude slower during the inter-pulse time compared to when the plasma is occurring; the high-energy plasma is mostly responsible for filling holes in incomplete layers due to increased transient mobility. A novel technique called “Pulsed Laser Interval Deposition” was tested by Blank et al. to favour the layer-by-layer growth of $SrTiO_3$ (Blank et al., 2000b). The idea was to use a fast burst of pulses to deposit the exact amount of material required to grow a monolayer, and wait for a duration longer than the characteristic relaxation time of the adatoms (a few 100ms) before launching the following burst of pulses. As a result, enough time is given to the atoms to rearrange their structure and complete the layer while the average island size is kept to a minimum.

Although the crystal unit cell of Sc_2O_3 is more complex than $SrTiO_3$, the mechanisms driving the epitaxial growth of the films are the same, and it gives ground for the investigation of the adatoms dynamics during the growth of Sc_2O_3. The final goal is to identify the optimal growth regime that produces the smoothest film and hence minimises interface scattering. Through ion probe measurements, the first section of this chapter aims at estimating the energy distribution of the ions from the plasma plume and understanding how it depends on deposition parameters such as the background pressure and the ablation fluence. A thorough investigation of the effect of pulse repetition rate on the properties of the film was conducted to determine the optimal value producing the best results, in terms of both surface morphology and crystallinity. The last part of this chapter explores how the background pressure can significantly alter the roughness of the film.

4.6.1 Plume kinetic energy

Understanding the dynamics of the plasma plume is crucial to control the film growth mechanisms and successfully favour layer-by-layer growth over 3D-island growth. Ion probing was used to study this aspect of PLD and bring to light the effects of PLD parameters on the plasma kinetics.

4.6.1.1 Methodology

The planar Langmuir probe (Lobbia and Beal, 2017, Mott-Smith, 1961) used for our measurements is a simple copper layer on a circuit board, placed on the usual position of the sample (Figure 4.20). The copper plate is connected to a Koopman circuit via an insulated wire. A bias voltage is applied to the probe and when the charged particles from the plume arrive at the copper plate, a current is generated. The intensity of the output signal depends on the ion density, the plume velocity, and the total area of the copper plate. Furthermore, the sign of the bias voltage determines whether the probe collects positive ions, or negative ions and electrons.

From the ion probe measurements, it is possible to deduce the time-of-flight of the plume from target to probe. Indeed, Figure 4.21 shows an example of probe record that exhibits a pre-pulse corresponding to the arrival of the UV pulse in the chamber. This pre-pulse can be used as a reference for time 0. As explained in section 2.1, the plasma plume expands and accelerates within the duration of the laser pulse (~20 ns), so the time between the pre-pulse and the arrival of the plume front is mainly due to the time-of-flight (typically 1-3 μs for a target-probe distance of 55 mm).

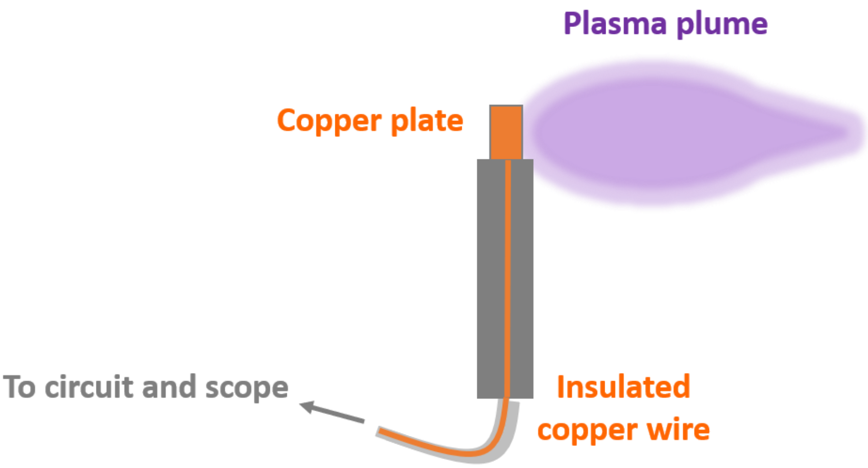

Figure 4.20: Schematic of the planar Langmuir probe.

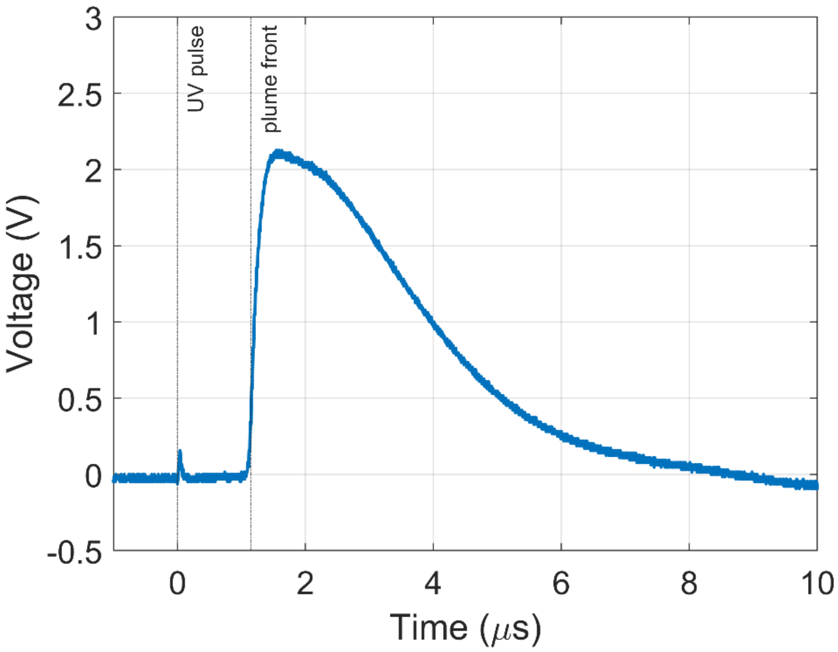

Figure 4.21: Example of an ion probe trace from a plasma plume produced by a Sc_2O_3 target. The time delay between the two vertical dashed lines is the time-of-flight.

Consider a negatively biased probe of area A positioned at distance *x* from the ablation spot. It is assumed that the ions in the plasma have mass *m* and mainly carry a charge of +e. The current at time *t* recorded by the probe is $I = eA\frac{dN}{dt}$, where $\frac{dN}{dt}$ is the number of ions per unit area arriving at the probe per unit time. Thus $dN = \frac{I}{eA}dt$.

It is assumed that the plasma is created at t = 0 and is accelerated over short time near the target and is in free flight to the probe. If *E* is the ion energy in eV, $eE = {}^{1}/{}_{2}\,mv^2 = {}^{1}/{}_{2}\,m\frac{x^2}{t^2}$.

Differentiating and rearranging gives $dt = \frac{et^3}{mx^2}dE$.

Substituting for *dt* in the previous equation gives $\frac{dN}{dE} = \frac{It^3}{Amx^2}$, where $\frac{dN}{dE}$ is the number of ions per unit area per eV.

Thus $\frac{dN}{dE}$ can be calculated for the probe current signal.

For all ion probe measurements described in this section, the Langmuir probe was placed at 55mm from the target, at the exact same location as the substrate during growth. The bias voltage was set to -25V to collect the positive ions of the plasma. During preliminary measurements, it had been observed that when launching a burst of 10 UV pulses at 100 Hz on a stationary Sc_2O_3 target, all ion probe traces were identical except the first one which might present a higher peak. This is due to the fact that the target surface might present some contaminants or a thin oxidated layer, which can be removed from the first pulse alone according to our observations. As a result, our standard measurement consisted in launching a burst of 3 pulses at 100 Hz on a stationary Sc_2O_3 target; the purpose of the first two pulses was to “clean” the target, while the last pulse was the only one recorded for analysis. Each measurement was recorded at a different random spot on the target to avoid overablating the same spot. It had also been verified that the signal from the probe started dropping after ~1000 pulses due to the layer deposited on the copper becoming thick enough to damp the signal. In each of our studies, less than ~200 pulses were used to ensure that the probe was in optimal condition for the entirety of the experiment and that all the traces recorded were comparable. Between studies, we either removed the coated layer with sandpaper or changed the ion probe.

4.6.1.2 Effect of pressure on the plasma plume

The deposition chamber was filled with O_2 and the pressure was varied from 1.4 µbar to 96 µbar. Note that the pressure of 1.4 µbar was the lowest chamber pressure reachable with both turbomolecular and dry pump, with the O_2 gas inlet completely shut, meaning that the background gas was air. Ion probe traces were recorded for different values of pressures with an ablation fluence of 1.2 J/cm^2, and the data processing and the transform introduced earlier was applied to each trace to obtain the corresponding ion energy distribution in the plasma. As a reminder, the main assumption to apply this transform is that the cations of the plasma are mostly single charged (Sc^+).

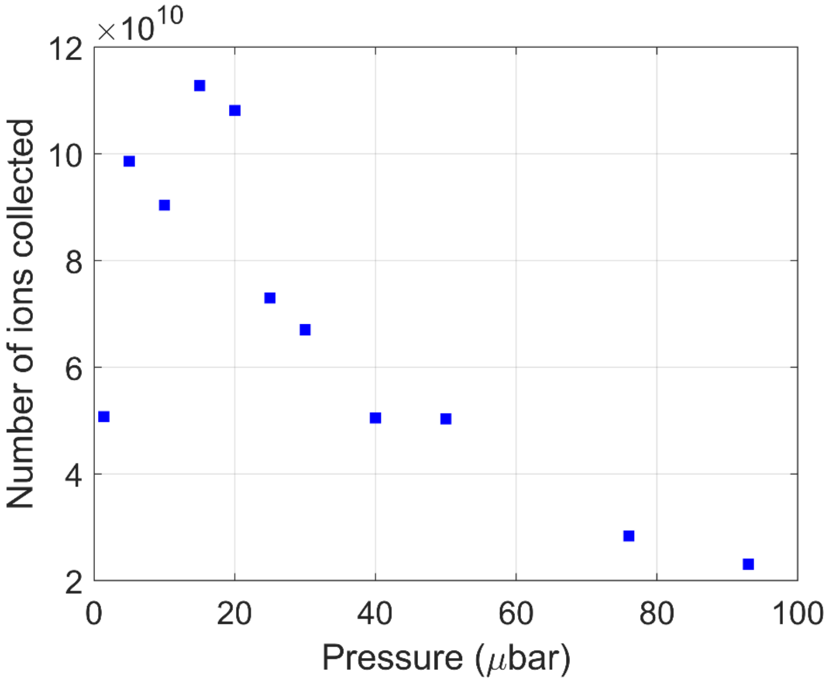

Figure 4.22: Number of ions collected by the ion probe for different chamber pressure with an ablation fluence of 1.2 J/cm².

By integrating an ion energy distribution curve, it is possible to calculate the total number of ions collected by the probe. Since all traces were recorded with the same probe size and target-probe distances, the number of ions collected directly reflects the potential deposition rate for a given pressure (assuming that most ions contribute to the growth of the film, which is definitely not guaranteed for all pressures, but realistic around our nominal growth pressure of 20 µbar). The evolution of the number of ions with the pressure presented in Figure 4.22 do not exhibit a categorical trend, not only due to the lack of points, but probably because the target is not perfectly uniform and the plasma kinetics might slightly change from one spot to another. Ideally, it would have been preferable to average the ion probe trace for each pressure from several measurements across the target. However, recording and analysing the measurements would have been much more laborious, which led to the decision of recording a single measurement per pressure on a random spot of the Sc_2O_3 target. Nevertheless, it is still possible to extract a general trend from Figure 4.22: the number of ions collected by the probe rises quickly from 1.4 µbar to 15-20 µbar, and then progressively decreases as the pressure rises.

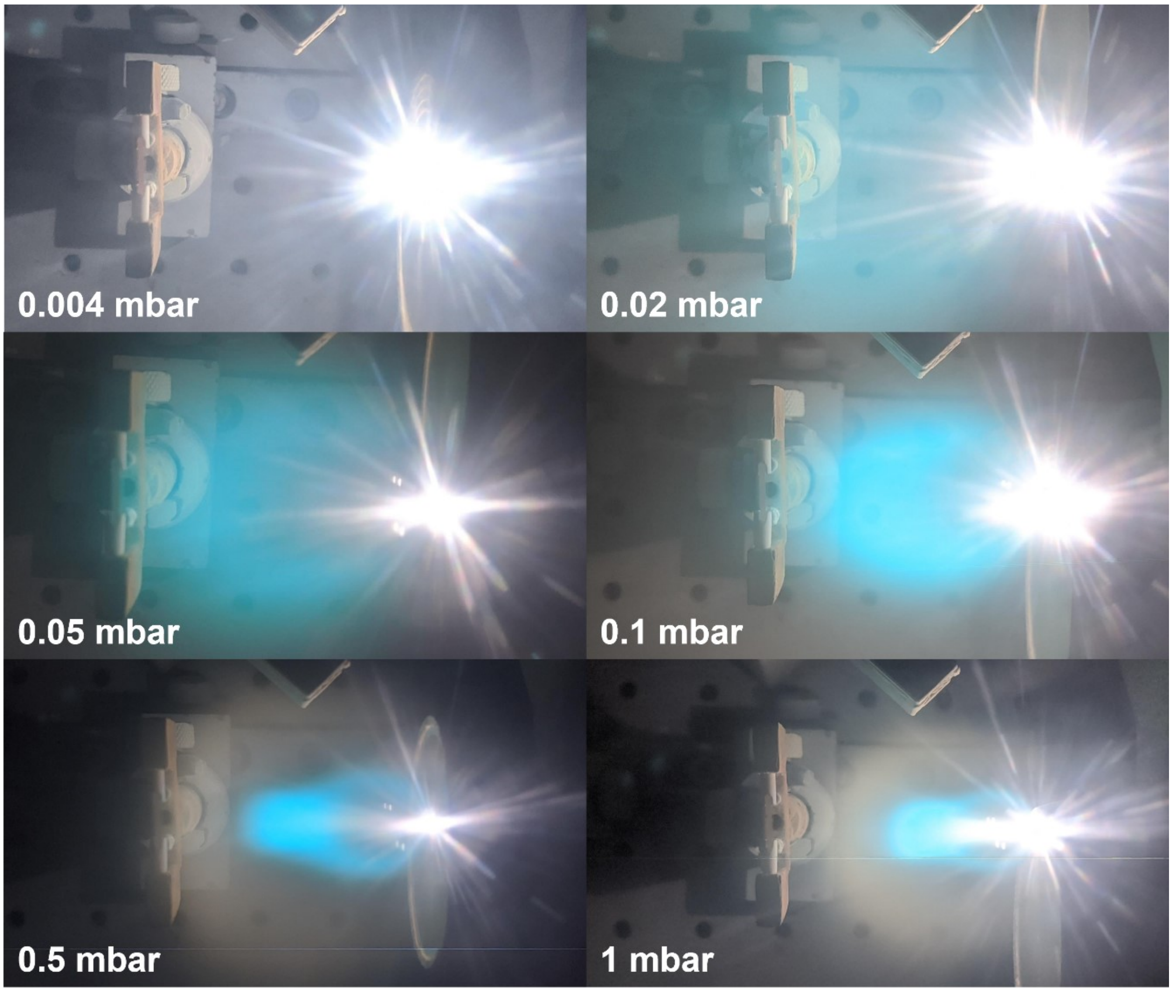

Figure 4.23: Photos of the Sc_2O_3 plasma plume for various O_2 background pressures and an ablation fluence of 1.20 J/cm^2

The progressive decrease of the number of ions collected from 15 µbar to 96 µbar is caused by the increased probability of collision of the plasma ions with O_2 molecules, effectively reducing their speed and altering their trajectory. On the other hand, the increase from 1.4 µbar to 15 µbar might be attributed to the change in plasma shape, which tends to become less directional at low pressures (Leboeuf et al., 1996, Sambri et al., 2008). Photos of the plasma plume in Figure 4.23 illustrate in a qualitative way how the shape and density of the plasma changes. At the lowest pressure of 4 µbar, the plasma is scattered in all directions and barely visible, while at a pressure of 1 mbar, the density of O_2 prevents the plasma from reaching the sample.

The ion energy distributions were normalised to the total number of ions and plotted in Figure 4.24. As expected, the graph reveals that the low-pressure curves have a significant portion stretching beyond the 100-eV level. On the opposite side, high-pressure curves manifest a large percentage of ions below 20 eV. In order to have a more quantitative comparison, the median ion energy was determined for each pressure and plotted in Figure 4.25. Apart from the 5 µbar data point, the rest of the medians follow an almost linear trend with respect to pressure. The data was fitted with the equation y = -0.81x + 77.8.

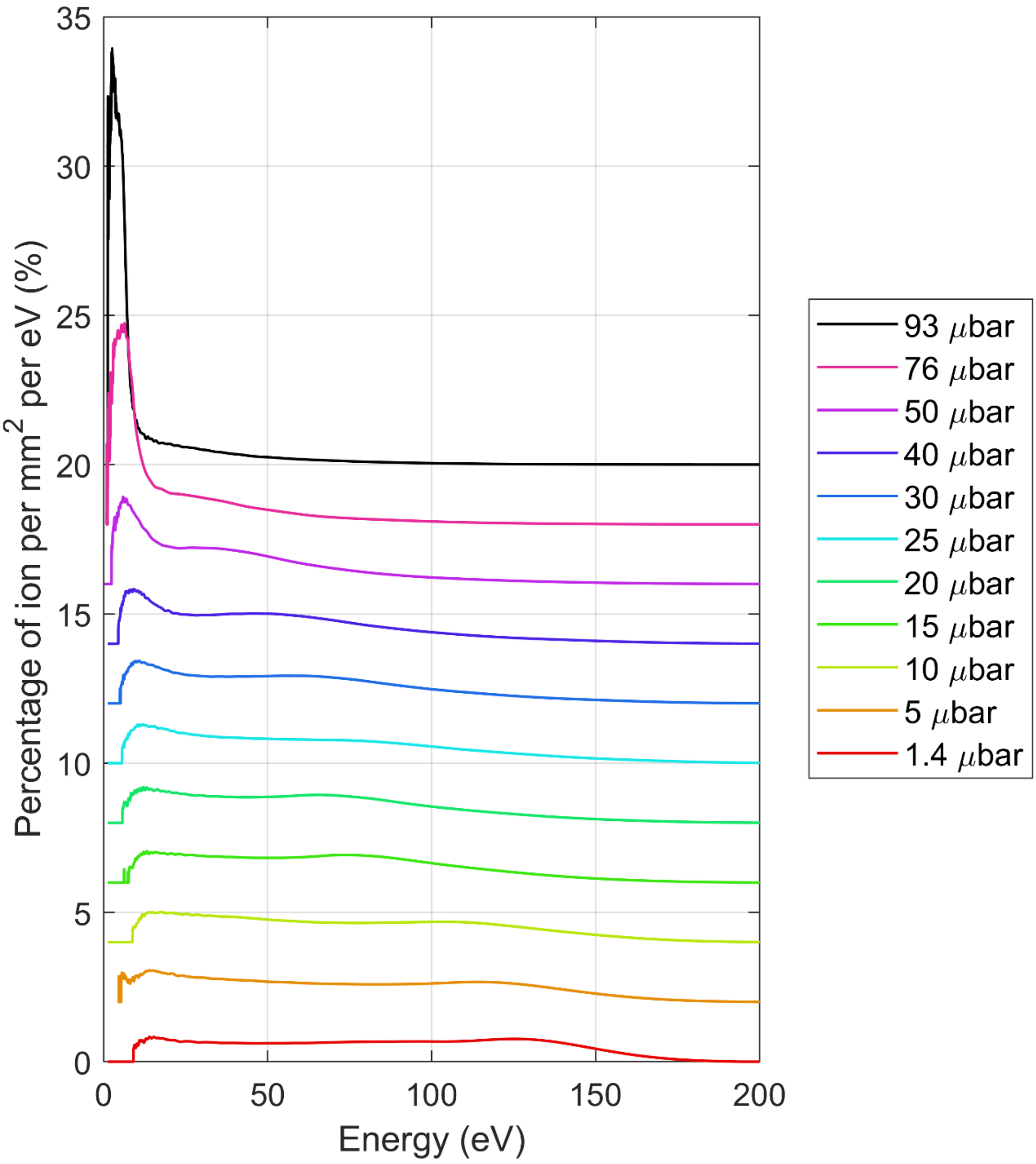

Figure 4.24: Ion energy distributions for various pressures normalised to the number of ions collected by the probe. An offset of 2% was added between curves for a clearer view.

Defining an exact ion energy threshold for efficient island breaking is challenging. While several publications mention the 100-eV level, it seems more like a general rule of thumb rather than a precisely estimated value. It would seem natural to use as a reference an energy level specific to the crystal to be grown. The Arrhenius equation for hopping rate would suggest referring to the diffusion activation energy, which is generally in the order of a few hundred meV. On the other hand, the bond energy between crystal atoms may also be a reasonable choice, since the ultimate goal is to frustrate the ripening of 3D islands. In our case, the energy of the Sc-O bond is around 6.97 eV. However, this energy level remains quite low compared to the typical median energy measured and therefore do not seem to be a meaningful threshold. As stated above, it is complicated to define a legitimate threshold to pinpoint a pressure value above which 3D island growth would be favoured over layer-by-layer growth.

Another major conclusion from this study is that the highest number of ions was collected in the 15-20 µbar regime, which happens to be our nominal pressure empirically determined over the years. Furthermore, this pressure regime also exhibits a high median ion energy of ~60 eV, which is critical to ensure layer-by-layer growth.

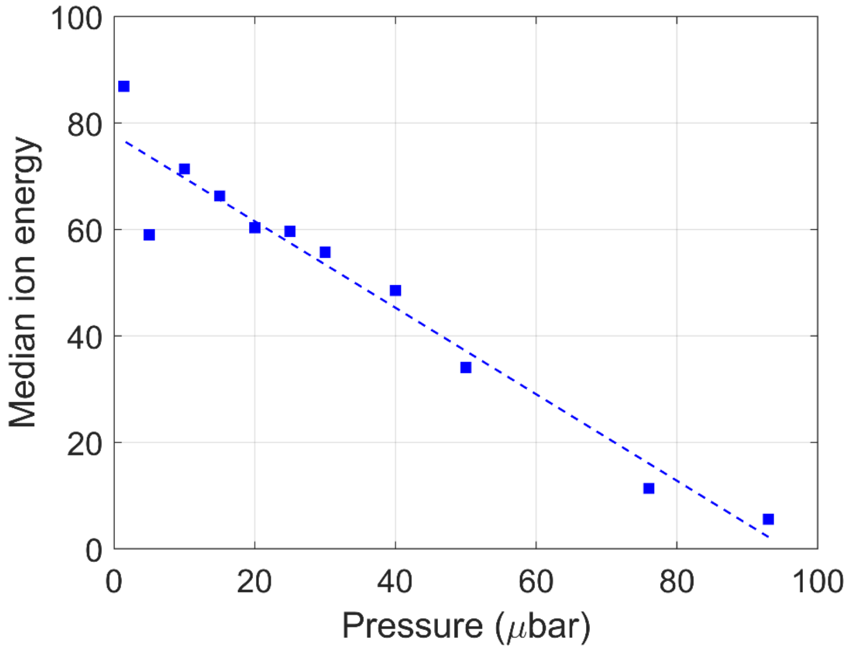

Figure 4.25: Evolution of the median ion energy in eV with chamber pressure, and linear fit of the data with the equation: y = -0.81x + 77.8

Note that in this experiment, not only was the pressure varied, but the quantity of O_2 inside the chamber was also changing at the same time because of our methodology. Indeed, since the pressure was regulated by adjusting the flux of O_2 inlet, we could not decorrelate the two effects. An alternative way would be to increase the pressure with an inert gas like neon, which also has a similar atomic mass as oxygen. This way, we would be able to purely observe the effect of the pressure variations without changing the amount of oxygen in the chamber.

4.6.1.3 Effect of fluence on the plasma plume

The optimisation of the fluence for the growth of Sc_2O_3 was done in the previous chapter with the aim of minimising the number of scattering points in the film. The crystallinity was observed to be minimally impacted within the range of fluences studied (1.00 to 1.37 J/cm^2). Since the UV pulse is responsible for forming and accelerating the plasma, it is reasonable to wonder how the ablation affects the kinetics of the plasma plume. We will now that in a similar manner to crystallinity, the ion energy distribution does not vary significantly with the fluence.

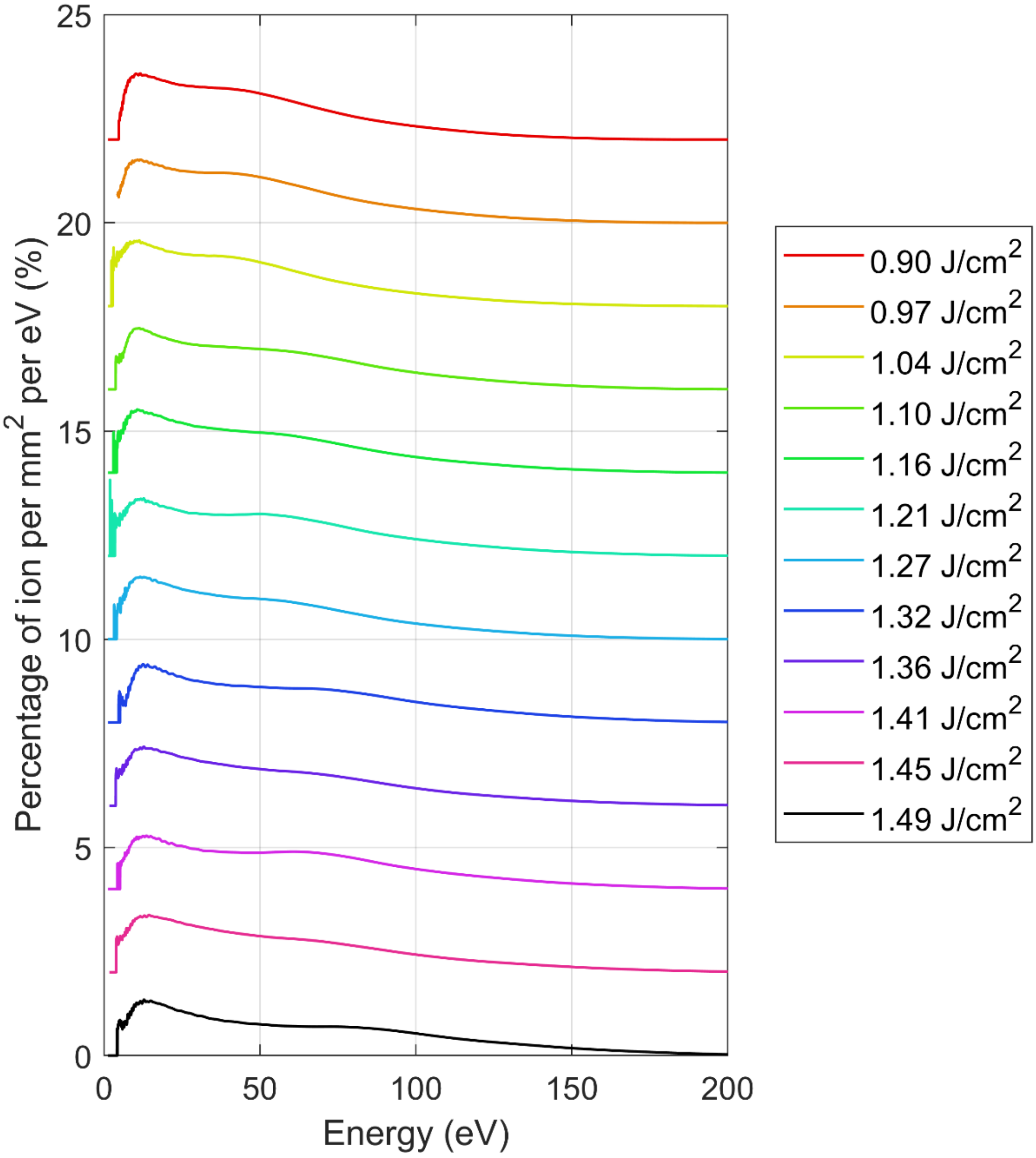

Figure 4.26: Ion energy distributions for various ablation fluences normalised to the number of ions collected by the probe. An offset of 2% was added between curves for a clearer view.

The ion probe measurements were recorded with the same methodology described earlier. The pressure was fixed to 20 µbar and the fluence varied from 0.90 to 1.49 J/cm^2. The ion probe trace was recorded for each value of fluence and the normalised ion energy distribution was computed and plotted in Figure 4.26. While the right side of the curve extends more towards higher energies, it is quite evident that the magnitude of the change is minimal compared to the pressure study. As a result, we can once again validate our choice of fluence range (1.10 to 1.30 J/cm^2) determined based on the amount of scattering.

4.6.2 Effect of the ablation repetition rate

The pulse repetition rate is a parameter that is seldom investigated in PLD. In our setup, the excimer is regularly used at 100 Hz since it provides the highest deposition rate. However, since the plasma plume has a critical role in defining the growth mechanism of the film, the repetition rate and hence the inter-pulse timing may have an effect on the properties of the film, and in particular on the surface morphology. The objective of this study is to identify this effect.

4.6.2.1 Description of experiment

Several Sc_2O_3 films were deposited on sapphire with values of repetition rate ranging from 1 Hz to 100 Hz and an ablation fluence of 1.15 J/cm^2. The same number of pulses was used for all depositions, namely 18000 pulses. As the influence of repetition rate may not be the same for all substrate temperatures, three sets of samples were grown with three different CO_2 laser powers. During a deposition, not only is the sample heated by the CO_2 laser, but the plasma plume itself adds some energy to the deposition surface. Since a lower repetition rate results in a smaller contribution to the surface heating, I chose to investigate CO_2 laser powers that are higher than the optimal range of 21-25 W determined previously: 23 W, 27 W and 29.5 W.

XRD measurements were performed on all the samples and the three main observations presented in the next sections concern the appearance of islands in the film, the predominance of the <111> orientation, and the effect on the lattice constant of the film.

4.6.2.2 Island growth

Scanning electron microscopy images (SEM) of the films were recorded to analyse their morphology. Figure 4.27 exhibits the top surface of the films and shows a clear effect of the repetition rate on their structure. The film deposited at 100 Hz with a heating power of 23 W (Figure 4.27 (a)) looks compact and uniform, indicating that the film has grown as a single crystal. However, we notice a progressive deterioration of the surface uniformity when the repetition rate is decreased. In particular, the set of films deposited with a CO_2 laser power of 29.5 W reveal the presence of islands (Figure 4.27 (d), (e) and (f)). While the 100 Hz sample is only partially covered with islands, the 20 Hz sample is fully covered and the average size of the islands becomes much larger in the 2 Hz sample.

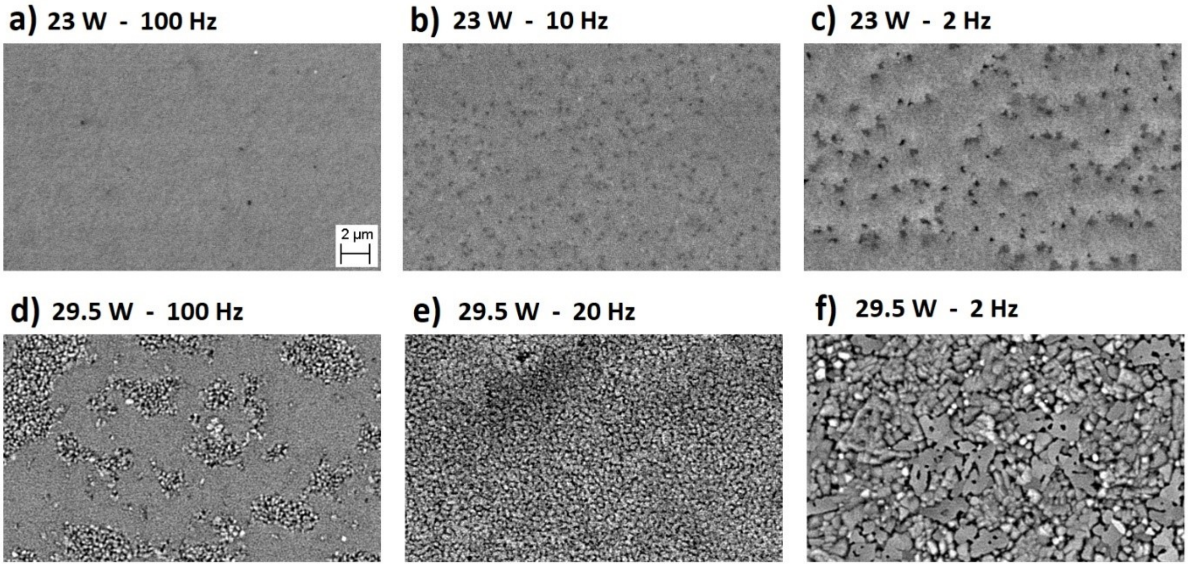

Figure 4.27: SEM images of the surface of films deposited with different pulse repetition rates and CO_2 laser powers. The magnification is the same for all images and thus the scale on the upper left image is valid for all images.

This behaviour can be explained by the theory of island growth described earlier in section 2.5. As a matter of fact, the plasma plume plays an important role in the shattering of growing islands. The highly energetic particles of the plume periodically break islands and therefore, the average size of the islands is directly related to the inter-pulse time. In the case of the sample deposited at 100 Hz with a CO_2 laser power of 23 W, the adatoms only have 10 ms to diffuse on the surface and aggregate into islands, before the next pulse arrives and breaks the islands. This time scale is too short to form any island and explains why the film is growing uniformly. Nevertheless, a simple increase of the heating power to 29.5 W gives the adatoms enough additional thermal energy to travel on the surface and start forming islands large enough, so that they will only be partially shattered by the following plasma plume. Moreover, as expected from the theory, the sample deposited at 2 Hz and 29.5 W clearly demonstrates that an increasing inter-pulse time significantly reduces the ability of the plasma plume to slow down the build-up of islands.

In order to check whether the particles in the plume have indeed a sufficient energy to produce that smoothing effect, an ion probe was used to estimate their velocity. The ion probe was placed at different distances from the target; the time-of-flight of the plume from the target to the probe was recorded for each distance. The results, plotted in Figure 4.28, indicate that the plume does not slow down during propagation. It is interesting to notice that this observation is different from the behaviour predicted by (Sambri et al., 2008). A possible explanation is that our background pressure is too low to observe a significant decrease of the plume's speed. Using a linear fit, we deduce that the front velocity of the plume is ~27.7 km/s. For an Sc^+ ion, this velocity corresponds to a kinetic energy of ~ 179 eV, which is the typical order of magnitude at which the smoothing effect should occur.

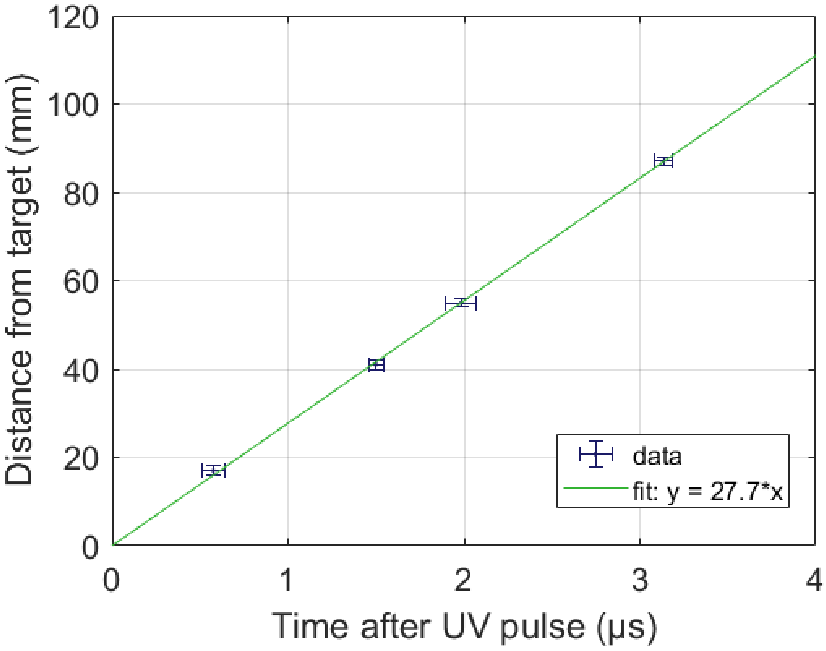

Figure 4.28: Distance between the target and the plume front as a function of time.

4.6.2.3 Predominance of the <111> orientation

As expected from preliminary experiments, the film grown at 100 Hz with a CO_2 power of 23 W is mainly textured in the <111> direction (Figure 4.29 (a)). On the other hand, the XRD pattern of the thin film deposited at 2 Hz reveals the presence of other orientations of Sc_2O_3, in the form of the (400) peak that has a height only ~ 50 times smaller than the (222) peak. A similar behaviour is observed for all heating powers: the number of side peaks and their height increase progressively when the repetition rate is reduced.

It is not precise enough to evaluate the predominance of the (222) peak only with height ratios. As a means to compare objectively the different samples, I decided to create a new metric based on the area under a peak. The advantage of this method is that it also considers the width of a peak (and not only its height) and compares the main orientation to all the other orientations together.

The XRD pattern is split in three parts, highlighted in Figure 5.9:

- the (222) peak is defined from 30° to 33°, wide enough to include the large wings.
- the substrate peak is defined from 41.4° to 42°.
- the rest of the curve represents all the other orientations.

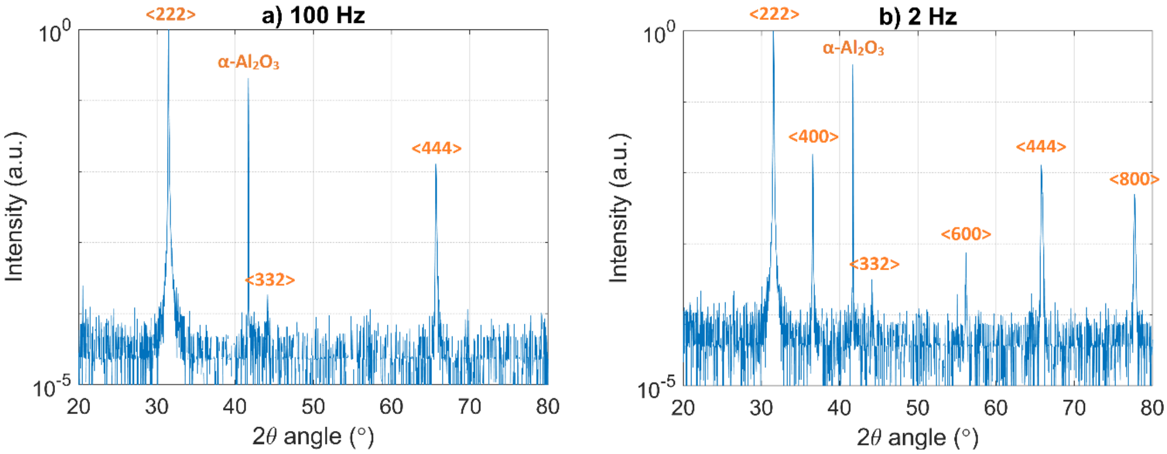

Figure 4.29: XRD patterns of Sc_2O_3 films deposited with a heating power of 23 W and a repetition rate of a) 100 Hz and b) 2 Hz.

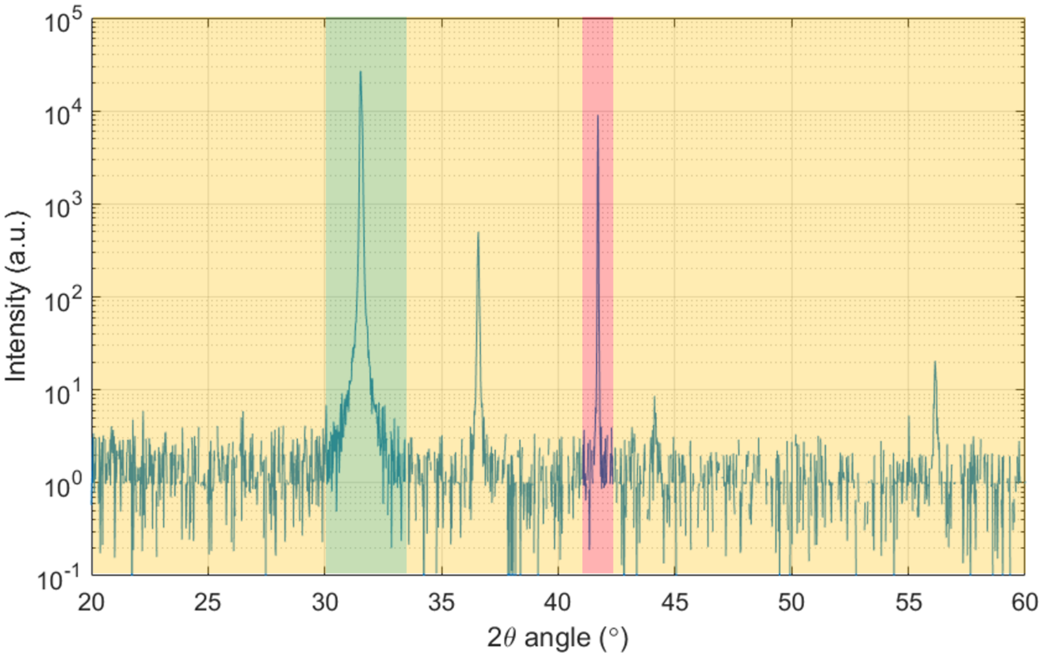

Figure 4.30: Visual representation of the three zones defined for the calculation of the are ratio. Green: (222) peak. Red: substrate peak. Orange: other orientations.

The “area ratio” is thus defined by the ratio of the area below the (222) peak and the area below the rest of the curve, excluding the substrate peak. Using the colour code of Figure 4.30: the “area ratio” is the area under the curve in the green zone and the area under the curve in the orange zone. Note that the area ratio is only computed from 20° to 60°, in order to exclude the (444) peak at 65.7°, which corresponds to the same orientation as the (222) peak.

The area ratio was computed for all the samples of this study and is plotted in Figure 4.31. This graph confirms our initial observation, showing a clear trend in the evolution of the area ratio with the repetition rate. A higher pulse repetition rate tends to minimise the apparition of unexpected orientations, i.e. orientations that do not have a good lattice match with the substrate. This result might be related to the formation of islands; the gaps between islands may allow the growth of orientations that would not normally grow on a uniform surface. Nonetheless, there is no definite proof that these two phenomena are directly related.

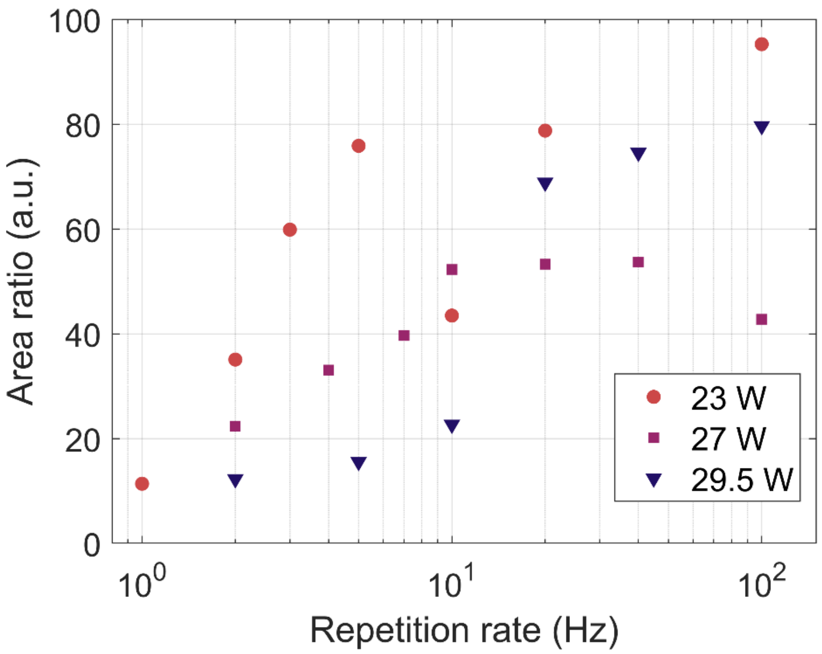

Figure 4.31: Area ratios computed from the XRD patterns of all the samples deposited. CO_2 laser power of 23 W (red disk), 27 W (purple square) and 29.5 W (blue triangle).

4.6.2.4 Effect on the lattice constant of the film

Figure 4.32 compares the (222) peak for all the films grown in this study. A first interesting feature is that lower repetition rates present multiple sub-peaks within the main peak. The appearance of sub-peaks can be associated to the presence of islands in the film. In the SEM images from Figure 4.27, we observe that two neighbouring islands do not necessarily have bounds, and hence may grow with slightly different lattice constants. On the other hand, the film deposited at 100 Hz and 23 W shows no sign of sub-peaks, since it is has grown as a single crystal.

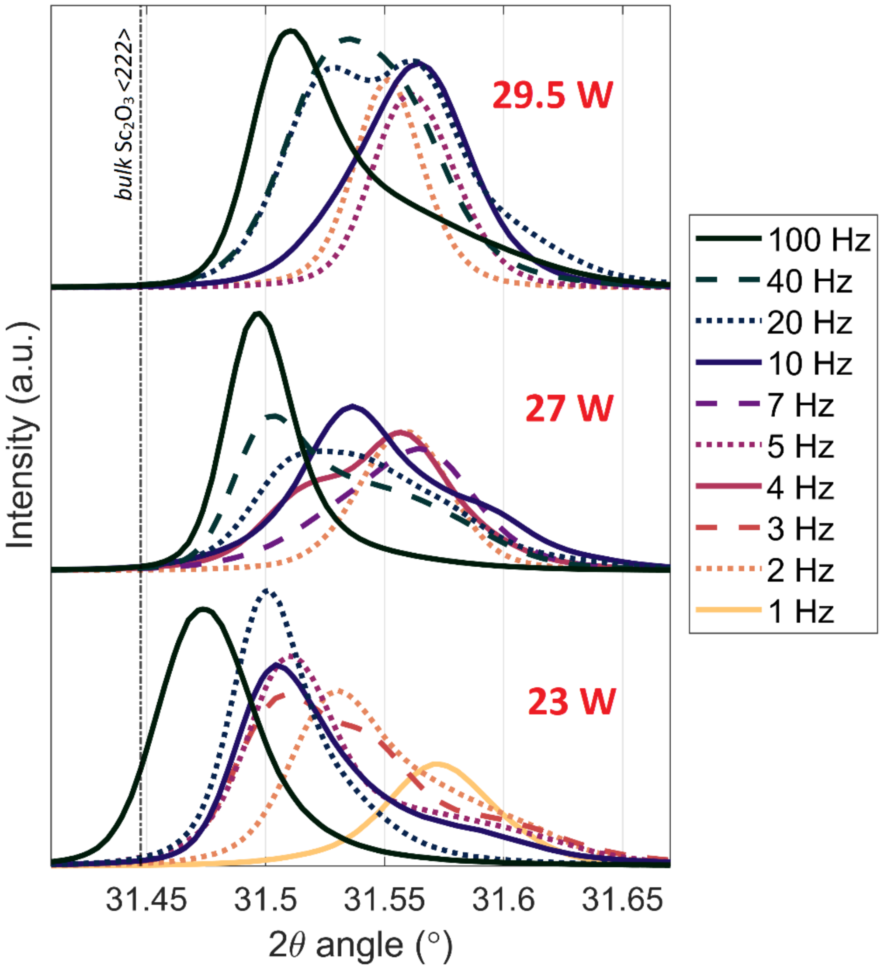

Figure 4.32:XRD of the (222) peak for the three set of samples. From bottom to top: CO_2 laser power of 23 W, 27 W and 29.5 W. The XRD patterns were translated horizontally so that their sapphire peaks were all coincident.

Figure 4.32 also illustrates the fact that the peak moves to higher angles for low repetition rates, which indicates a smaller crystal plane spacing and thus an increasing compressive strain in the film. This behaviour is observed for the three CO_2 laser powers investigated. Due to the strong asymmetry of some of the peaks, using the maximum of a peak to define its position is not precise enough. Therefore, the centre of gravity of the peak was selected as the best option to evaluate how the peak is shifted. Figure 4.33 shows the centre of gravity of the (222) peak of all the samples. When the repetition rate is decreased, the peak initially moves towards higher angle values, but then remains within the 31.545º-31.565º zone. The peak deposited at 1 Hz with a heating power of 23 W is outside that area, but this deposition was much longer than the others (5 hours for 1 Hz versus 2.5 hours for 2 Hz), and thus some parameters like the laser power and the pressure in the chamber are difficult to maintain during the entire deposition.

This increase in the peak position, and thus decrease in the lattice constant, is related to the duration of the deposition. As a matter of fact, a deposition at 2 Hz lasts for 2h30, while a deposition at 100 Hz only lasts 3 minutes. During a longer deposition, the film is virtually annealed due to the prolonged exposure to a high temperature. This is further supported by the fact that samples deposited with a higher temperature reach the final zone faster.

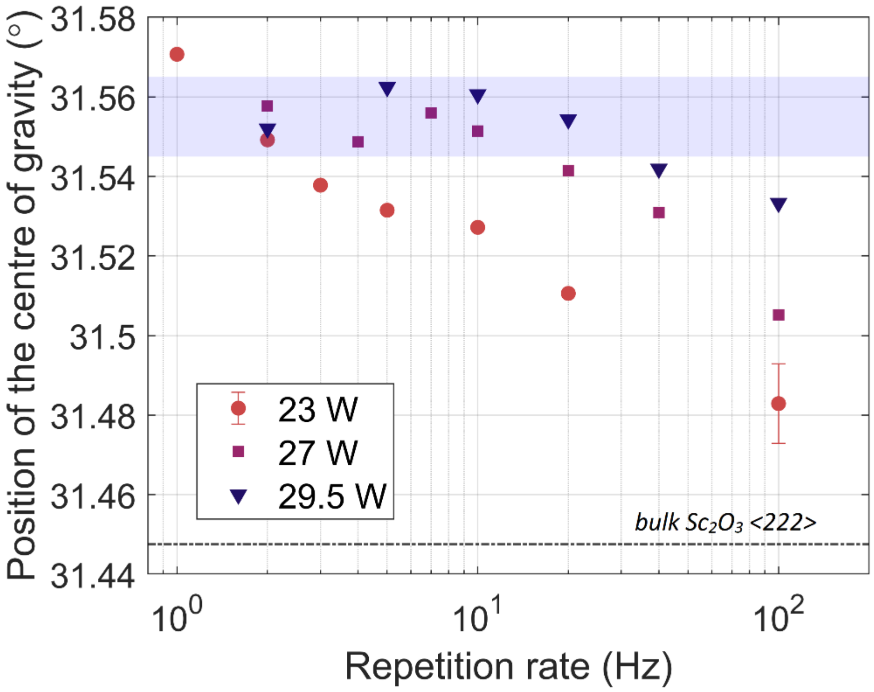

Figure 4.33: Position of the (222) peak for all the samples deposited. CO_2 laser power of 23 W (red disk), 27 W (purple square) and 29.5 W (blue triangle). The error bars in the bottom right correspond to the XRD equipment resolution (+/- 0.01°) and is valid for all points in this graph.

To confirm the effect of annealing on the film, two Sc_2O_3 films were deposited with the same conditions, but the second one was post-annealed in-situ for 60 minutes. The (222) XRD peaks of the films are plotted in Figure 4.34 and demonstrate that annealing a film reduces its lattice constant. The first film was later annealed for 40 minutes and proved again that an exposure to high temperatures can shift the (222) peak. This confirms our theory that low repetition rates induce a smaller lattice constant mainly because of the duration their deposition.

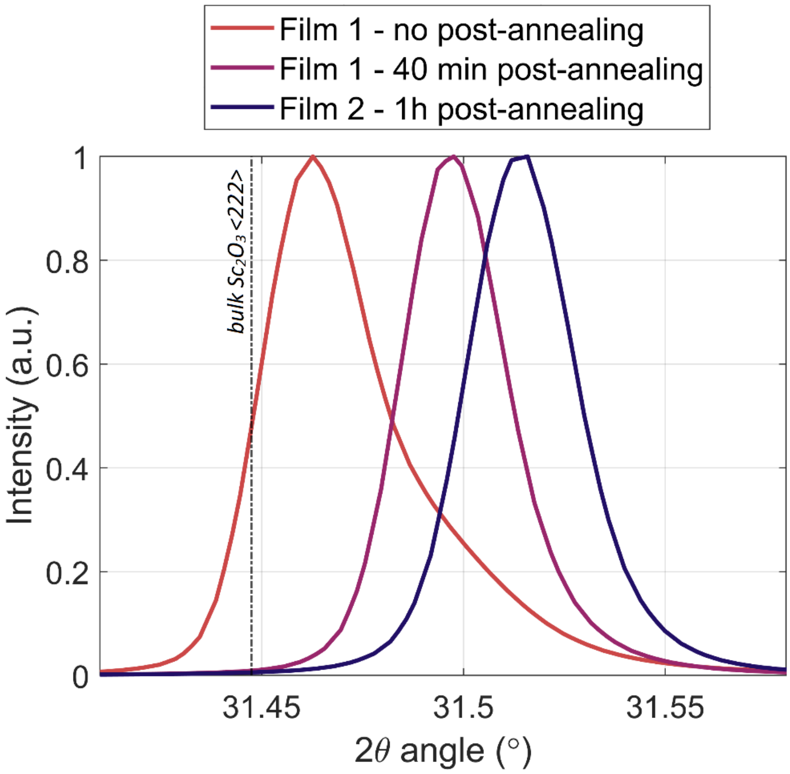

Figure 4.34: (222) XRD peaks of two samples grown with the same deposition conditions, but different post-annealing times.

The remaining question is: why does the lattice constant decrease because of annealing? Two hypotheses stand out. The first possibility is related to the lattice mismatch between the substrate and the film. The lattice constant of bulk Sc_2O_3 is 2.5% too small compared to the ideal match with sapphire. During annealing, the lattice is more flexible and will expand in the direction parallel to the interface to have a better match with the substrate. This expansion will result in a compression of the lattice in the direction perpendicular to the interface. The second possibility is that the film is losing oxygen during the annealing process, which will also translate into a compression of the film. At this stage, it is still unclear which hypothesis is correct.

4.6.3 Influence of pressure on Sc_2O_3 topology

To further confirm the effect of the plasma kinetic energy on the growth mode of the film, two Sc_2O_3 films were grown with higher O_2 background pressures than our nominal 0.02 mbar pressure.

Figure 4.35 shows SEM images of the surface of films grown with 0.1 mbar and 0.05 mbar pressures, keeping the other deposition parameters nominal. 3D-island growth is becoming dominant with rising pressure, which correlates well with the ion energy distributions in Figure 4.24. The AFM scans in Figure 4.36 confirm the clear increase in roughness with the high-pressure sample. These additional proofs once again strengthen our argument that the chamber pressure plays a key role in the morphology of the growing film.

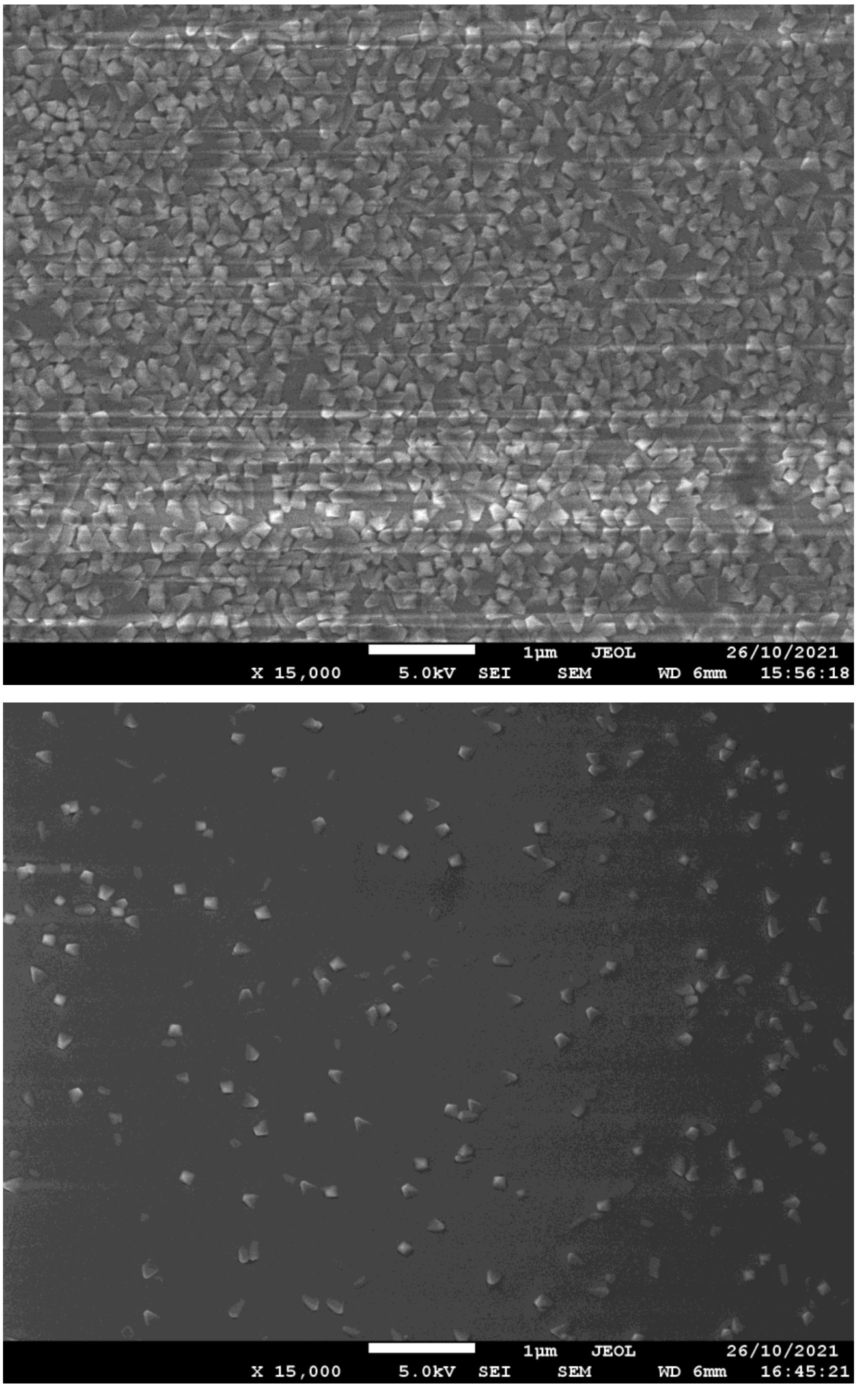

Figure 4.35: SEM images of a Sc_2O_3 film grown with a 0.1 mbar (top) and 0.05 mbar (bottom) O_2 background pressure.

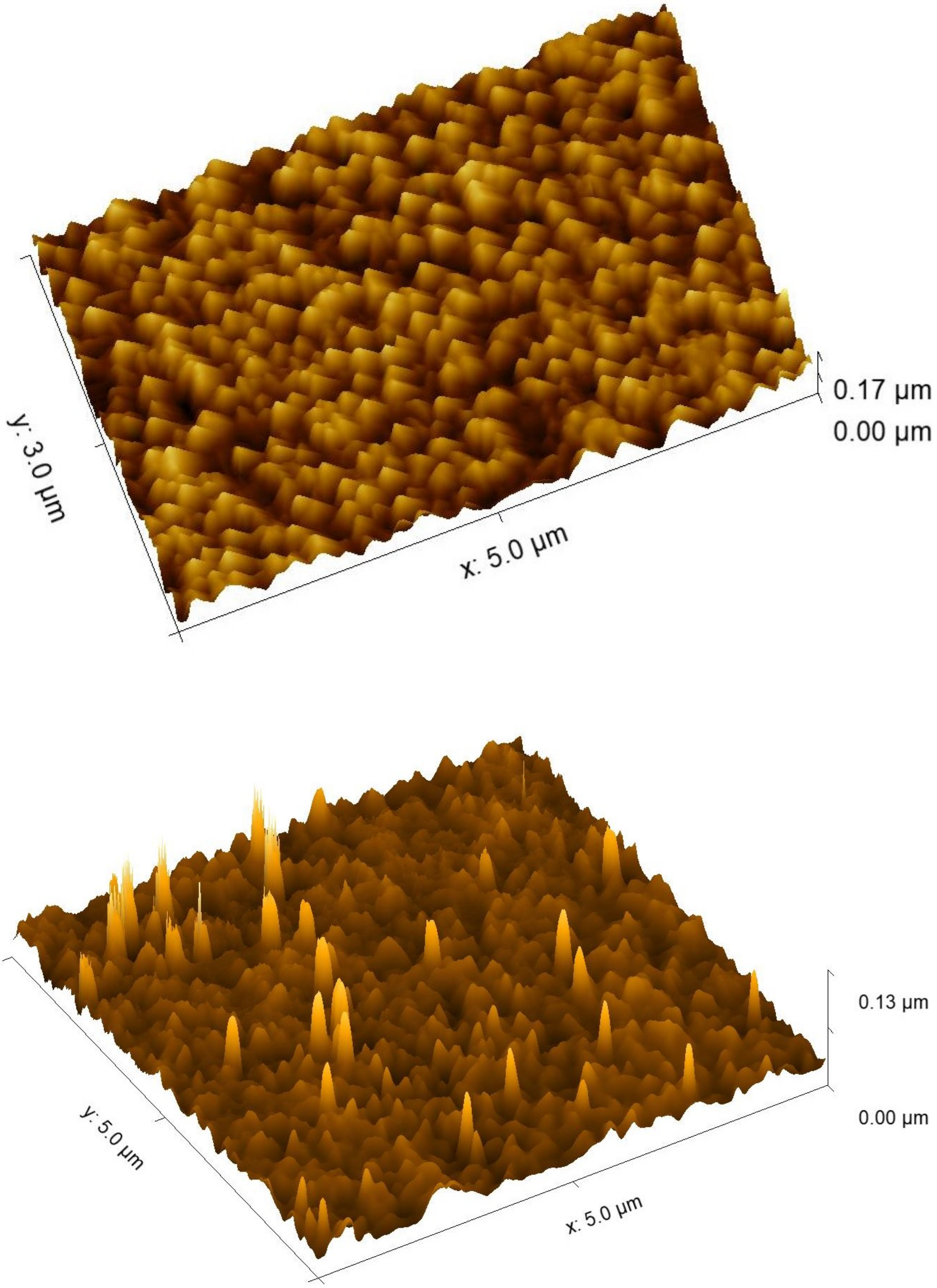

Figure 4.36: AFM measurement of a Sc_2O_3 film grown with a 0.1 mbar (top) and 0.05 mbar (bottom) O_2 background pressure.

4.7 Conclusion

The optimisation of the sesquioxide growth was presented in this chapter. Sc_2O_3 was our main material of interest for GWS because of its higher refractive index, and was used as an example to illustrate the principle of the optimisation process. The characterisation methods most frequently used were dark-field microscopy, which helped identifying the optimal ablation fluence, and XRD, which provided insights on the crystal structure. The heating laser power was identifyed to be an important parameter, which led us to define the range of temperature for the optimal growth of each material. This temperature range of 1250-1490 K was much higher than the one for garnets (1000-1100 K), which could be anticipated by the fact that the melting point of sesquioxides is higher than garnets.

An important step was to guaranty the repeatability of the deposition method. Indeed, since the film growth rate is evaluated ex-situ, we had to ensure that this growth rate and the film quality did not vary between depositions. Six identical deposition attempts have confirmed the repeatability of the method, with a standard error of ± 2% on the film thickness. The linearity of the film thickness with the number of ablation pulses was also verified.

Y_2O_3 was used as an example to demonstrate that, despite largely tuning the deposition temperature, the refractive index of the film did not change significantly enough to affect the performance of a potential GWS. A LIDT campaign proved that our sesquioxide films are on par with state-of-the-art coatings deposited with Magnetron Sputtering, further confirming their potential use in optical coatings for high-power lasers.

Finally, the last part of the chapter aimed at better understanding the plume dynamics and how they affect the growth of the film. Ion probing was used to evaluate the ion energy distribution in the plasma plume as a function of the pressure and the ablation fluence. We observed that the ion energy was related to an important mechanism slowing down the formation of 3D-islands and hence favouring layer-by-layer growth. This mechanism was also detected in the repetition rate study, where films grown at a high ablation rate had a smoother surface because of the shorter inter-pulse time limiting the buildup of islands.

Chapter 5 Fabrication of Crystalline Resonant Reflectors

5.1 Fabrication of Grating Waveguide Structures

5.1.1 Design and theoretical efficiencies

The simulation work presented in this section was conducted by Danish Bashir (Institut für Strahlwerkzeuge, University of Stuttgart).

The expression "Grating Waveguide Structure" can refer to a wide range of structures. A simple planar waveguide with a grating on the top surface can be considered a GWS, but also a complex multi-layered structure deposited on an etched substrate. Therefore, the designer of a GWS has a lot of freedom on the type of structure that can be proposed for a given application.

The goal of our study was to fabricate the GWSs and evaluate their potential use in real laser systems. The first step was to determine our fabrication limits to produce a design that can be realistically fabricated. From a PLD perspective, the only possible limitation was the thickness of the waveguide, as the crystallinity of the film might degrade beyond a critical thickness. However, for the targeted wavelengths of use, the thickness of the required waveguides was within the range of thicknesses successfully grown during previous studies. Another important aspect was that the multi-target deposition system did not exist yet at the start of the project, causing us to focus on single-layered GWS designs. Concerning the etching of the diffraction grating, the main limitation was the list of materials that could be etched in our facilities. Sesquioxides like Sc_2O_3 could not be etched, which left us with the only option of etching the sapphire substrate. All these limitations already defined a base for a fabricable GWS: the sapphire substrate must be etched first and the Sc_2O_3 layer is grown on top of it.

Starting from this base, GWS designs were produced for each application. Figure 5.1 illustrates how the key parameters of the GWS are defined: W_g is the thickness of the waveguide, Λ the period of the grating, and σ the etching depth. Several assumptions were made in the model:

- The duty cycle of the grating is 50%.
- The walls of the grating are perfectly perpendicular to the surface.
- The top surface of the waveguide follows exactly the same shape as the substrate.
- Roughness of the interfaces and scattering inside the waveguide were not included in the model.

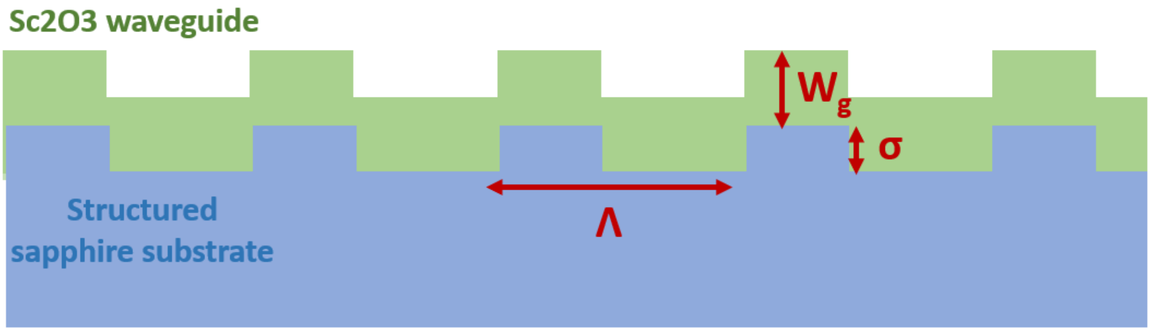

Figure 5.1: Definition of the GWS parameters: Wg waveguide thickness, σ grating modulation and Λ grating period.

Table 5.1: Parameters of the nominal GWS designs for 1030-nm and 1970-nm applications.

Wavelength	**1030 nm**	**1970 nm**
Λ	515 nm	984 nm
σ	100 nm	200 nm
W_g	500 nm	1000 nm

The simulations employed rigorous coupled-wave analysis to compute the efficiency of the theoretical structures (Gaylord and Moharam, 1985, Botten et al., 1981). The methodology applied to converge towards our final design was the same as the one established in (Sharon et al., 1997, Wang and Magnusson, 1993, Wang et al., 1990). The waveguide thickness was selected to obtain destructive interferences on the transmission side of the structure at the wavelength of design. The period of the grating and the duty-cycle were chosen to create the coupling resonance at the same wavelength for the intended angle of incidence. Designing our GWS for normal incidence might be problematic if the fabricated sample deviates from the ideal parameters. By designing the GWS for a small angle of incidence of 10°, an error in waveguide thickness would simply shift the angle of resonance without impacting the efficiency. The nominal GWS parameters calculated for both 1030-nm and 1970-nm wavelength stabilisation are summarised in Table 5.1.

With the assumptions stated above, the GWS can theoretically achieve an efficiency greater than 99.9% for a given wavelength and angle of incidence. The two polarisations have distinct resonances, which ensures that one of them prevails during intra-cavity operation. The spectral reflectivity of the 1030-nm GWS design for a 10.2° angle of incidence is plotted in Figure 5.2.

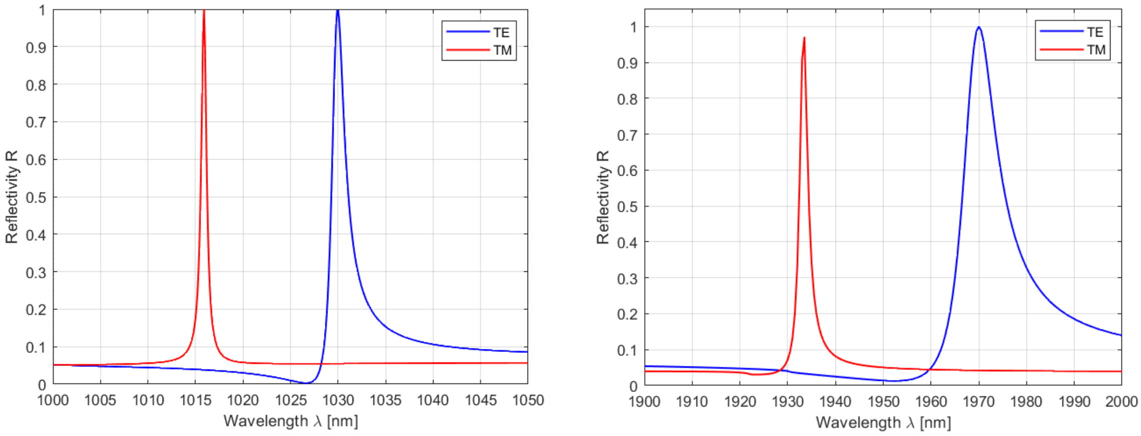

Figure 5.2: Efficiency of the nominal GWS design for 1030-nm application with an angle of incidence of 10.2°.

5.1.2 Fabrication process

The fabrication process was divided into two parts: the etching of the substrate and the deposition of the waveguide. My involvement in this process was limited to the second part. The structuring of the sapphire substrate was conducted by Fangfang Li (University of Eastern Finland) and Georgia Mourkioti (Optoelectronics Research Centre, University of Southampton).

The sapphire etching process was entirely developed for this study. The main steps are as follow:

- Depositing a SiO_2 layer on the sapphire substrate via RF-magnetron sputtering.
- Depositing a Cr layer on top of the SiO_2 via DC-magnetron sputtering.
- Coating the Cr layer with E-beam resist.
- Patterning the resist with E-beam lithography to create the grating lines.
- Dry etching of the Cr layer via Inductively Coupled-Plasma (ICP) etching with a gas mixture of Cl_2/O_2, which results in patterned Cr layer that will be used as a hard mask for the etching of SiO_2.
- Dry etching of the SiO_2 layer via ICP etching with a gas mixture of CHF_3/Ar, which results in patterned SiO_2 layer that will be used as a hard mask for the etching of sapphire.
- Dry etching of the sapphire substrate via ICP etching with a gas mixture of $SiCl_4/Cl_2/Ar$. The residual SiO_2 was removed with hydrofluoric acid.

More details about the etching process can be found in (Mourkioti et al., 2023). At the end of the process, the wafers were diced into square substrates of approximatively 10 x 10 mm^2 in order to fit in the PLD sample holder.

The PLD procedure for the epitaxial growth of the Sc_2O_3 waveguide was similar to the one used for the growth on flat substrates in the previous chapters: O_2 pressure of 0.02 mbar, ablation fluence of 1.2 J/cm^2. The only difference is the thickness of the substrate, which used to be 1.0 mm for our previous growth, but only 0.65 mm for our GWS. To account for this reduced thickness, the CO_2 heating power was reduced from the optimal value of 23-24 W to a lower value of 21-22 W. To minimise the risk of cracking during the cooling down process after deposition, the speed of laser power ramping down was reduced from the nominal value of 0.5 W/min to a lower value of 0.25 W/min.

A 30-min pre-annealing step was also added before starting the ablation, to remove any contaminant on the substrate's surface. This pre-annealing was conducted with a CO_2 laser heating power of 28 W, which is higher than the deposition power.

5.1.3 Characterisation of the Sc_2O_3 waveguide

The Sc_2O_3 waveguide was grown on a structured substrate and may therefore have properties different from the previous waveguides grown on flat substrates. In this section, we employ different characterisation methods to highlight any difference between the two types of waveguides. The XRD and bandgap measurements were performed by me, whereas the AFM profiles were obtained by Georgia Mourkioti.

5.1.3.1 X-ray diffraction

The crystallinity of the structured waveguide for 1970-nm application was assessed with XRD. A low-resolution scan with a step size of 0.02° was performed to obtain the full diffraction pattern of the GWS from 20° to 80° (Figure 5.3). The grating lines were placed parallel to the direction of propagation of the X-ray beam.

In a similar way to the previous growths on flat substrates, the <111> direction of Sc_2O_3 prevails, with the diffraction peaks of the (222) and (444) crystal planes being the largest ones apart from the sapphire peak. The (332) peak around 44° is barely standing out from the noise, with an amplitude more than 4000 smaller than the (222) peak. This result proves that the crystal quality of the as-grown film is not impacted by the structure of the waveguide.

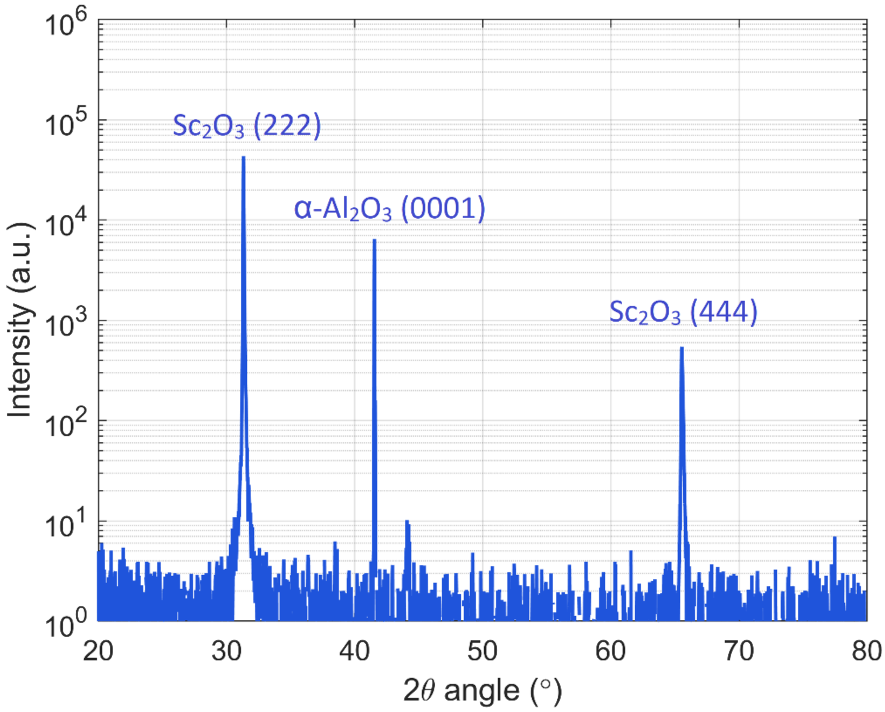

Figure 5.3: XRD pattern of the GWS recorded with the X-ray beam parallel to the grating lines. The peak at 31.5° shows that the <111> orientation of Sc_2O_3 is predominant.

5.1.3.2 Bandgap measurements

One key motivation for the investigation of all-crystalline GWSs is their potential as high-LIDT reflectors. The single-shot LIDT can be directly related to the bandgap in the femtosecond regime. It is therefore critical to verify whether the bandgap of Sc_2O_3 decreases when it is grown on a structured substrate.

The transmission of a GWS for 1970-nm application was measured with the Varian Cary 500 spectrophotometer (Figure 5.4 (a)). The drop of the transmission around 200 nm is sharper for the GWS because of its thickness, which is twice the thickness of the flat film used here as a reference. The Tauc plot was calculated and a linear fit performed to evaluate bandgap. The linear fit in Figure 5.4 b was obtained by rigorously applying the method from section 3.2.4 based on the maximum of the derivative, and results in a bandgap of 6.01 eV. However, it appears that the rise of the curve is progressive and therefore the portion to fit is difficult to define. If we try to do the linear fit on the portion of the curve where the rise is starting, we can obtain a bandgap value as low as 5.7 eV. For this reason, we decide to take the average of the two values: the bandgap of the Sc_2O_3 waveguide deposited on the structured sapphire substrate is (5.85 ± 0.15) eV.

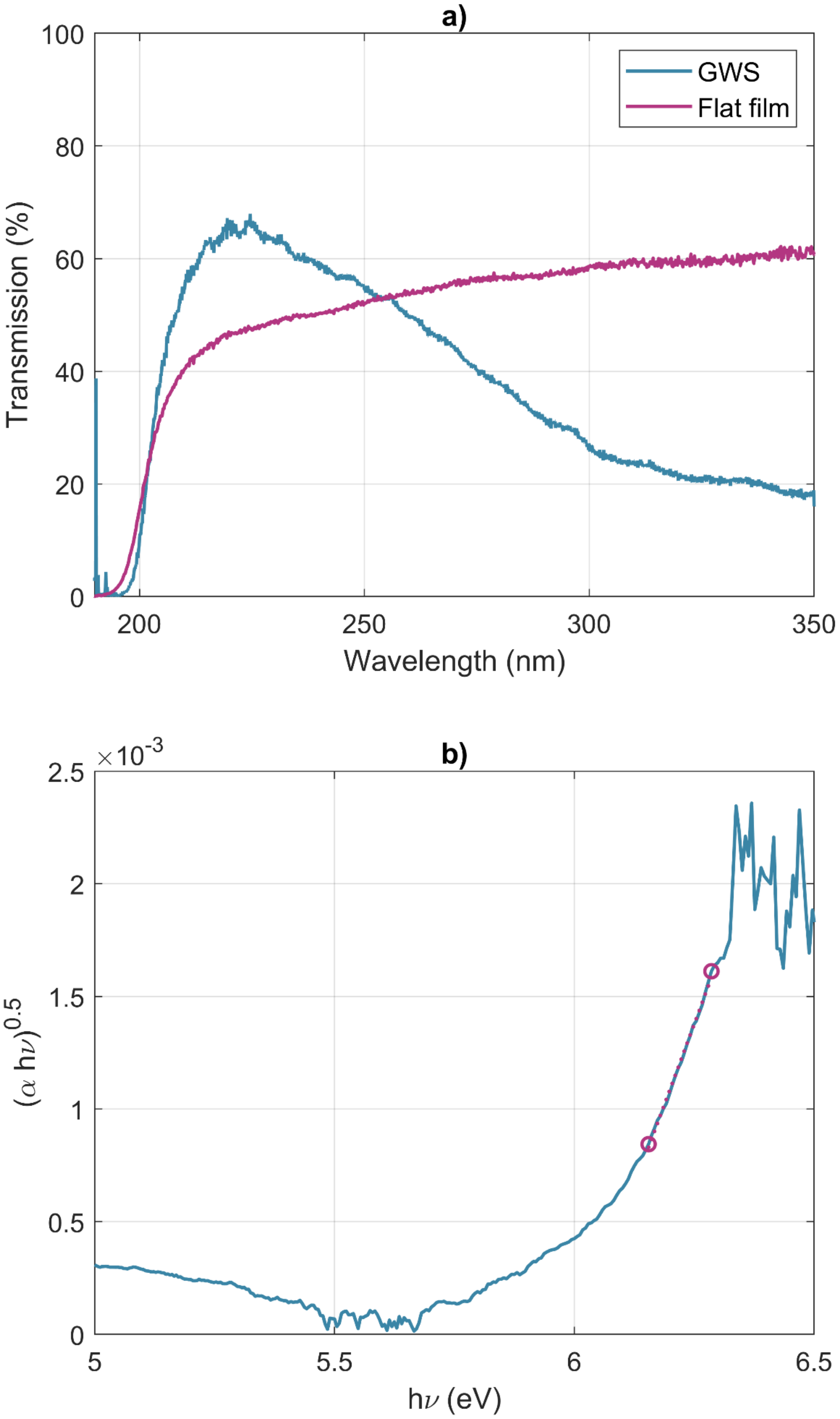

Figure 5.4: a) Transmission of a Sc_2O_3 film grown on a flat substrate (purple) and on a structured substrate (blue). b) Tauc plot of the GWS (blue) and linear fit determining the bandgap of the sample (purple). This linear fit results in a bandgap of 6.01 eV.

5.1.3.3 Groove shape

The efficiency of a grating is mainly defined by its groove shape. In the GWS model, one important assumption was that the groove shape of the air-Sc_2O_3 interface would be identical to the groove shape of the Sc_2O_3-sapphire interface. A deviation from the expected shape might cause a decrease of the efficiency at the resonance. Therefore, it is relevant to measure and compare the groove shape of the two interfaces.

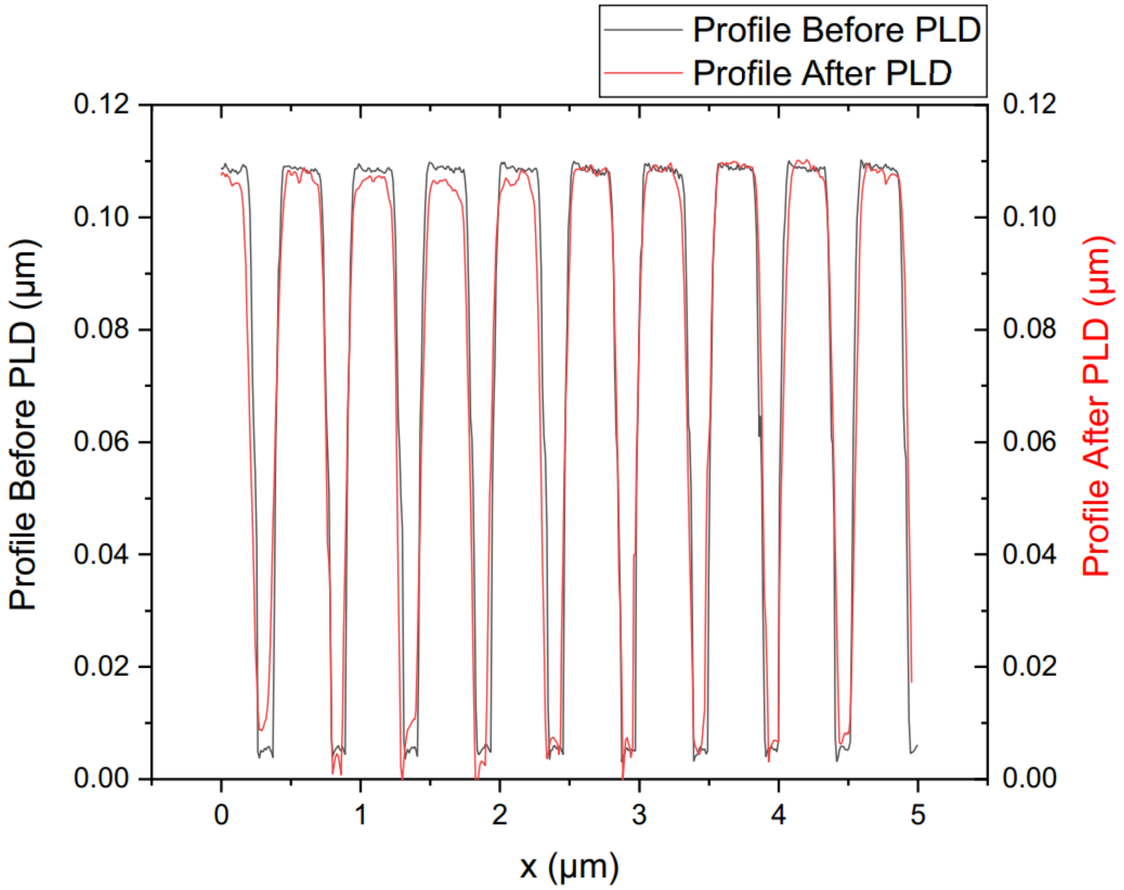

Figure 5.5: Groove shape of the a) air-Sc_2O_3 interface and the b) Sc_2O_3-sapphire interface, measured with Atomic Force Microscopy. The groove shape is consistent before and after PLD.

In order to compare both groove shapes, AFM was regularly employed during the development of the fabrication process. Figure 5.5 exhibits an example of groove shape before and after the deposition of the Sc_2O_3 layer. The AFM profiles plotted in this figure were measured on a sample for 1030-nm application, whose efficiency results will be presented in section 7.5.1. We observe that the shape of the top interface follows the shape of the bottom interface, proving that the PLD process is conformal. This property can be attributed to the high directionality of the plasma plume in PLD. Classical sputtering methods generally exhibit a larger divergence, which may result in a deformation of the top grating (Poole et al., 2013). The extreme case is that of Atomic Layer Deposition, where the precursors are introduced at a slow pace with no sense of direction. The thickness of the layer coated on the sidewalls of the grating is similar to thickness coated on the land and ridge, dramatically reducing the duty-cycle (Saleem et al., 2015).

Although PLD was able to maintain the shape of the groove, it should be noted that the substrate groove shape before PLD already deviated from the original design. The SEM measurement in Figure 5.6 shows that the sapphire substrate after etching had a clear trapezoidal groove with a sidewall angle of 73°. The modulation of the grating was also extracted from the AFM profiles. A modulation of (105 ± 2) nm was obtained, which is 5% higher than the design modulation. This difference in sidewall angle and modulation might potentially affect the performance of the GWS.

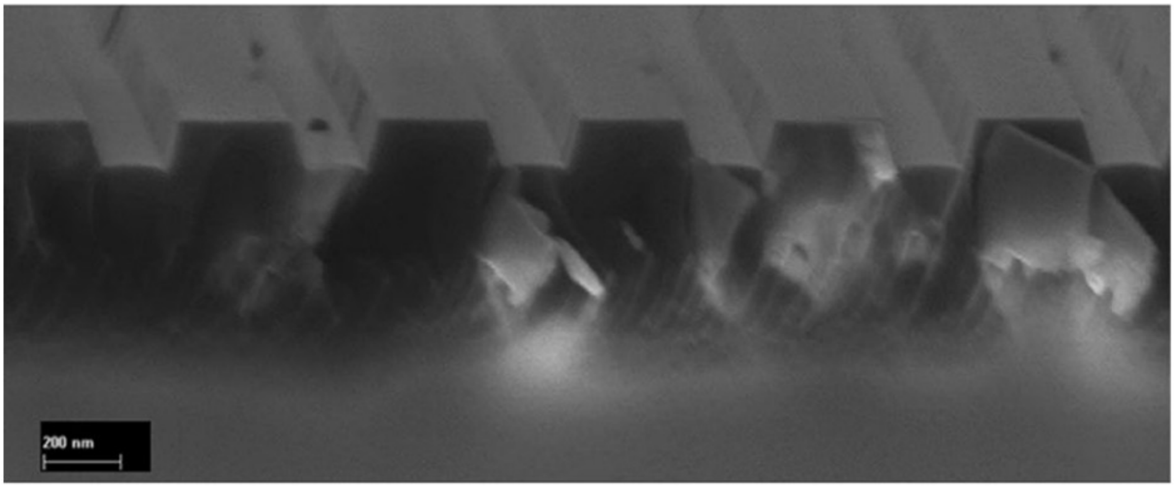

Figure 5.6: Cross-sectional view of the bare substrate after ICP etching, recorded with SEM.

5.1.4 Efficiency of the GWS

The efficiency of the GWSs was measured with several setups. For both wavelengths of application, the measurements on the preliminary samples were conducted in the Optoelectronics Research Centre. Results on the final samples were obtained with better experimental setups in Institut für Strahlwerkzeuge for 1030-nm measurements and in ALPhANOV (University of Bordeaux) for the 1970-nm measurements.

5.1.4.1 GWS for 1030-nm application

In this section, we report how the limitations of the preliminary samples were identified and what strategies were followed to further improve their efficiency.

Preliminary results

During the early stage of the development of the fabrication process, it was necessary to have an experimental setup within our facilities to regularly measure the efficiency of new samples. The simple optical bench presented in Figure 5.7 was set up to perform such measurements. The diameter of the 1031-nm laser beam was around 2 mm. The polarisation of the beam could be controlled with a half-wave plate. The GWS was mounted on a manual rotation stage and the Fresnel reflection was used for the auto-collimation, defining our 0° reference angle. Two powermeters were used to record both transmitted and reflected powers. The position of the powermeter used in reflection had to be re-adjusted when the angle of incidence of the beam was varied.

The transmittance and reflectance of one of the preliminary GWSs are plotted as a function of the incident angle in Figure 5.8. As expected from the theoretical design, the TE and TM resonances are distinct, which validates the polarising effect of the GWS. However, we observe that the TM reflectance do not exceed 47% and the TE reflectance only reaches 30%.

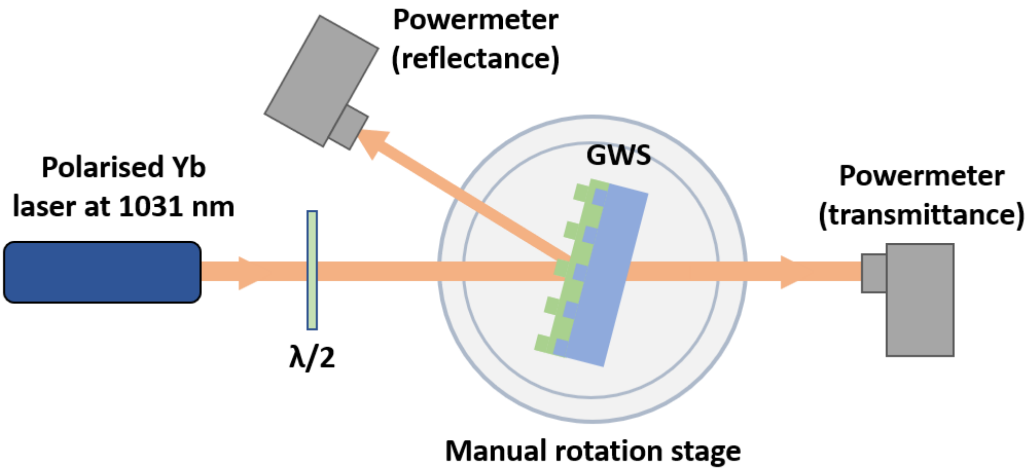

Figure 5.7: Experimental setup for the transmittance / reflectance measurements of the preliminary samples at the Optoelectronics Research Centre.

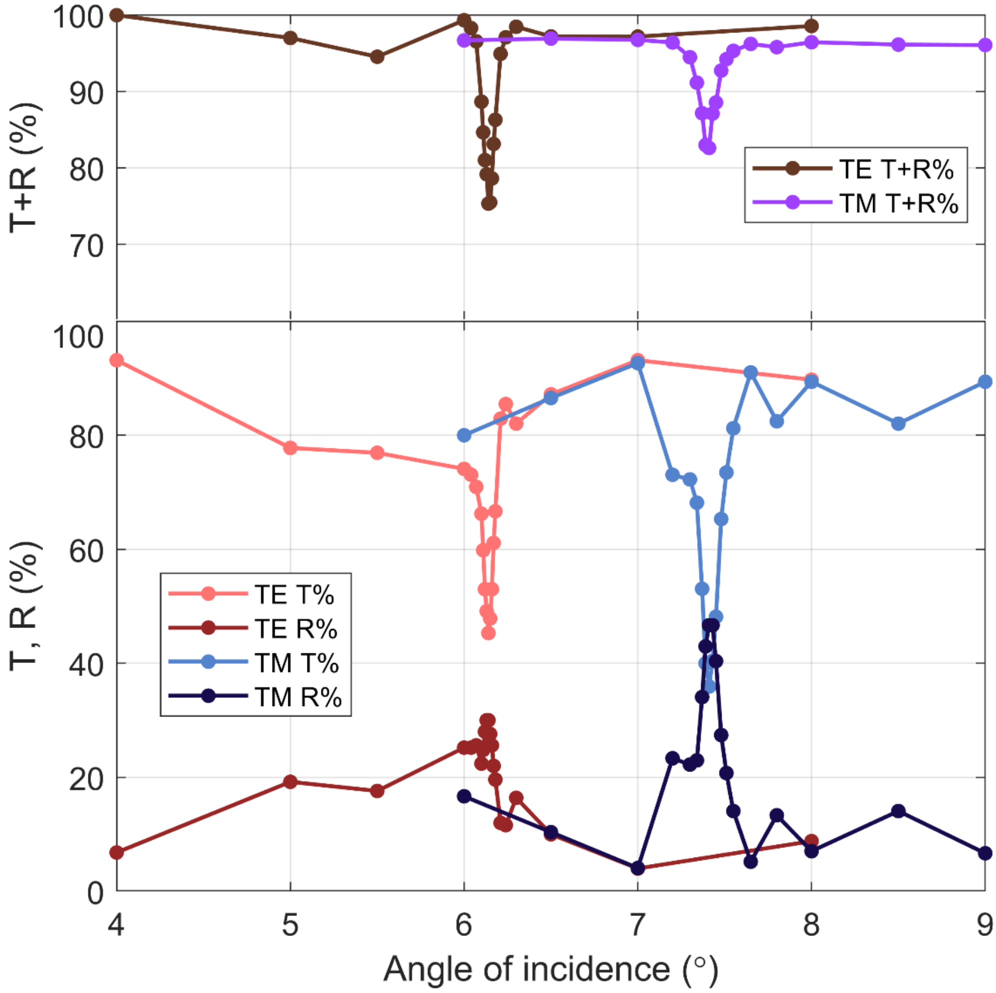

Figure 5.8: Efficiency measurements with a preliminary GWS sample. The transmission and reflection of the GWS were measured as a function of the angle of incidence for both polarisations (bottom graph). The sum of the transmission and reflection is plotted in top graph to highlight losses.

Additionally, the sum of the transmittance and reflectance was computed and plotted in Figure 5.8 to verify how much energy is lost. We observe that the sum is nearly constant off-resonance and close to 100% for both TE and TM. However, significant loss is happening at the resonance and the loss curve follows the same shape as the resonance. This observation proves that the losses occur after the beam gets effectively coupled in the waveguide. Several possible causes were identified to explain the significant energy losses:

- Scattering points inside the waveguide causing propagation losses.
- Roughness of the air-Sc_2O_3 interface causing propagation losses.

- The beam is trapped inside the waveguide and leaks from the edge of the samples. This phenomenon had been observed by our partners from Institut für Strahlwerkzeuge during previous studies.
- The thickness of the waveguide is not uniform enough which causes the resonance conditions to rapidly change across the samples.

The last reason mentioned in this list can also explain why the resonance is weaker than expected and a large portion of the beam is transmitted: if within the 2-mm diameter laser beam, the thickness of the waveguide changes significantly, only a portion of the beam would meet the resonance conditions and the rest of the beam would be off-resonance. As a consequence, the portion off-resonance would be transmitted. This hypothesis was explored and confirmed in the next section to improve the performance of the GWS.

Improved samples

The deposition profile of the PLD setup can be determined by growing a Sc_2O_3 film on sapphire and measuring the transmission spectrum in different parts of the film. This methodology was followed and revealed that the centre of the plasma plume was several millimetres off-axis compared to the substrate. The position of the substrate was readjusted (along with the CO_2 laser beam) to coincide its centre with the centre of the plasma plume.

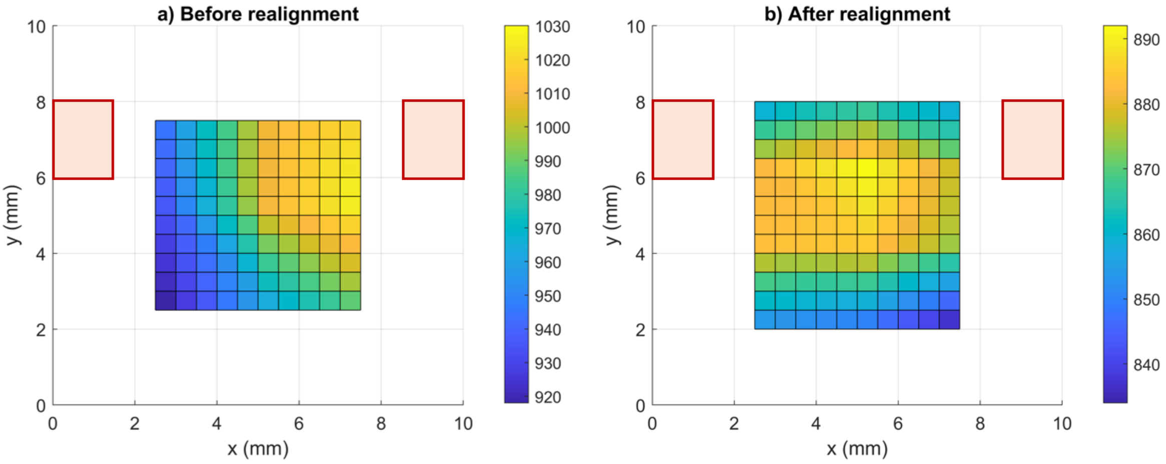

Figure 5.9: Thickness profile across the 10 x 10 mm^2 sample a) before and b) after realignment of the sample with plasma plume. The left profile was interpolated from 9 measurements across the sample, while the right profile was interpolated from 12 measurements.

The comparison of the thickness profiles before and after realignment is displayed in Figure 5.9. The profile before realignment consists in 9 thickness measurements that were interpolated to obtain the 121-point profile for visualisation purpose. The profile after realignment consists in 12 thickness measurements that were interpolated to obtain the 143-point profile. It should be noted that the diameter of the white-light beam is around 2.5 mm, and therefore each measurement corresponds to the average thickness over that beam area. Nevertheless, these profiles reveal a clear improvement in thickness uniformity at the centre of the sample, with the variation of thickness being halved in that area (from ~11% to ~6%).

With this improved thickness uniformity, new samples were fabricated. The efficiency measurements were conducted with a different setup in Institut für Strahlwerkzeuge, with the guidance of Danish Bashir. I had the opportunity to visit their facilities in three different occasions to participate in the measurements.

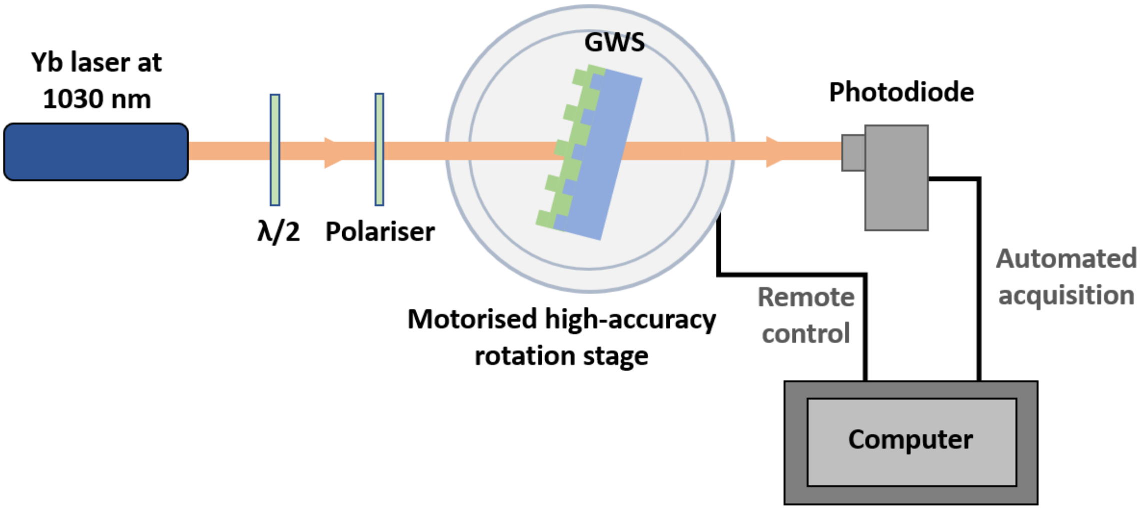

Figure 5.10: M-lines setup for the determination of the TE and TM angles of resonance at the Institut für Strahlwerkzeuge.

Two experimental setups were used for the efficiency measurements. The M-lines setup illustrated in Figure 5.10 is similar to the setup used for the preliminary measurements in the Optoelectronics Research Centre, but presents the advantage of being partially automated. The rotation stage was motorised with an encoder enabling precise control of the angle of incidence It was remotely controlled via the computer, which could also perform the acquisition of the data through the photodiode. Once again, the 0° reference angle was set by auto-collimation with the Fresnel reflection. The main purpose of this setup was to determine the angle of resonance of the GWS for our wavelength of interest. This measurement was performed on our GWS and revealed a TE resonance at 7.34° and a TM resonance at 8.95° (Figure 5.11). This angle of incidence can then be used for the reflectivity measurements, where the incidence is fixed and the wavelength is tuned.

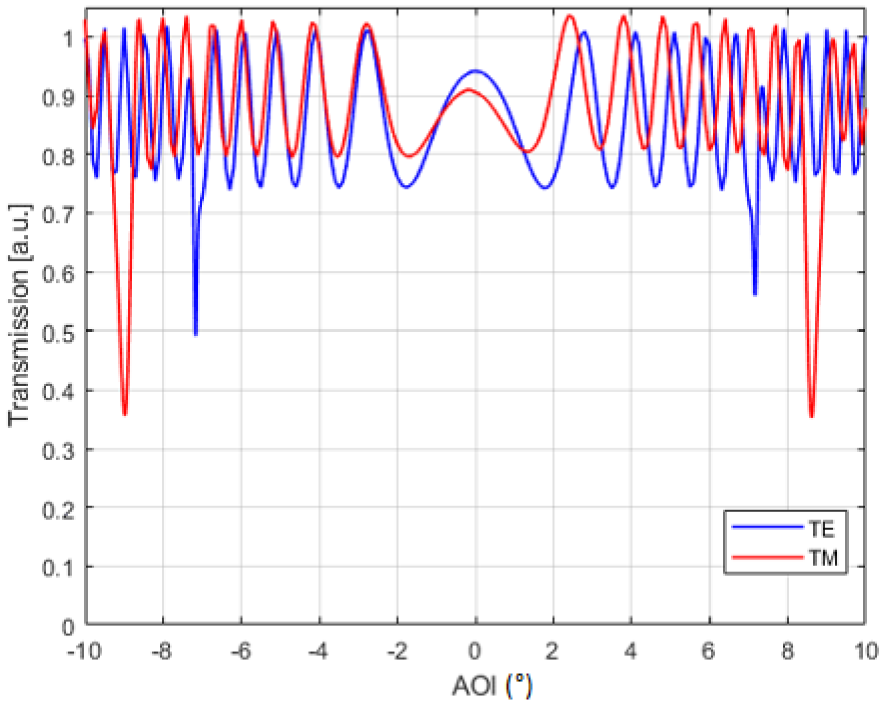

Figure 5.11: M-lines measurements with our GWS, leading to an angle of resonance of 7.34° for TE and 8.95° for TM.

The second setup illustrated in Figure 5.12 is the reflectivity setup, which was used for the precise evaluation of the sample reflectivity. The source was a tuneable diode laser, enabling the measurement of the spectral reflectivity from 1000 nm to 1070 nm. The laser beam had a diameter close to 1.5 mm. The power and polarisation of the beam could be controlled via a half-wave plate and a polariser. The signal was modulated by a first chopper to allow synchronous detection with a lock-in amplifier. A mirror chopper was also used as reference to monitor the potential fluctuations of the laser power: this type of chopper reflects the beam during half of the rotation and transmits it during the second half. The GWS was placed in a double-pass configuration at the angle of resonance previously determined with the M-lines setup. A high-reflectivity mirror was sending the beam back through the same path. The detection was done via a photodiode mounted on an integrating sphere. Despite dramatically reducing the signal, the integrating sphere presents the advantage of not being sensitive to the beam size or divergence.

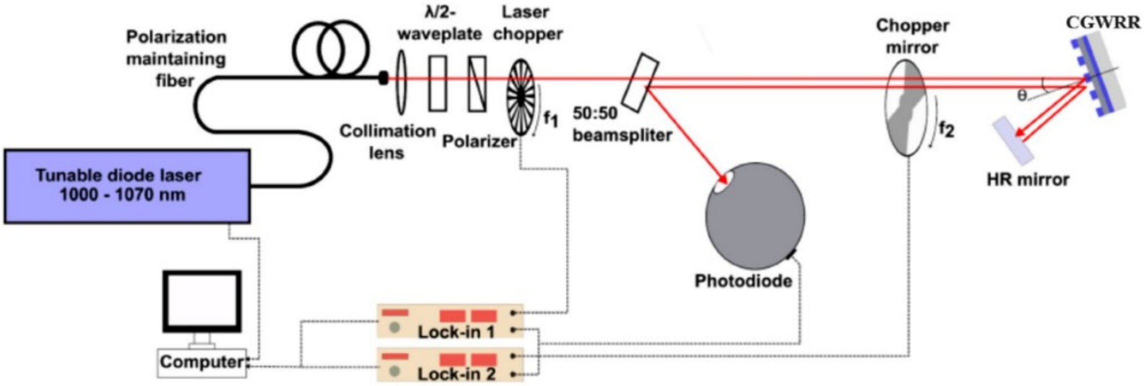

Figure 5.12: Reflectivity setup from Institut für Strahlwerkzeuge, allowing a spectral measurement of the crystalline grating waveguide resonant reflector (CGWRR).

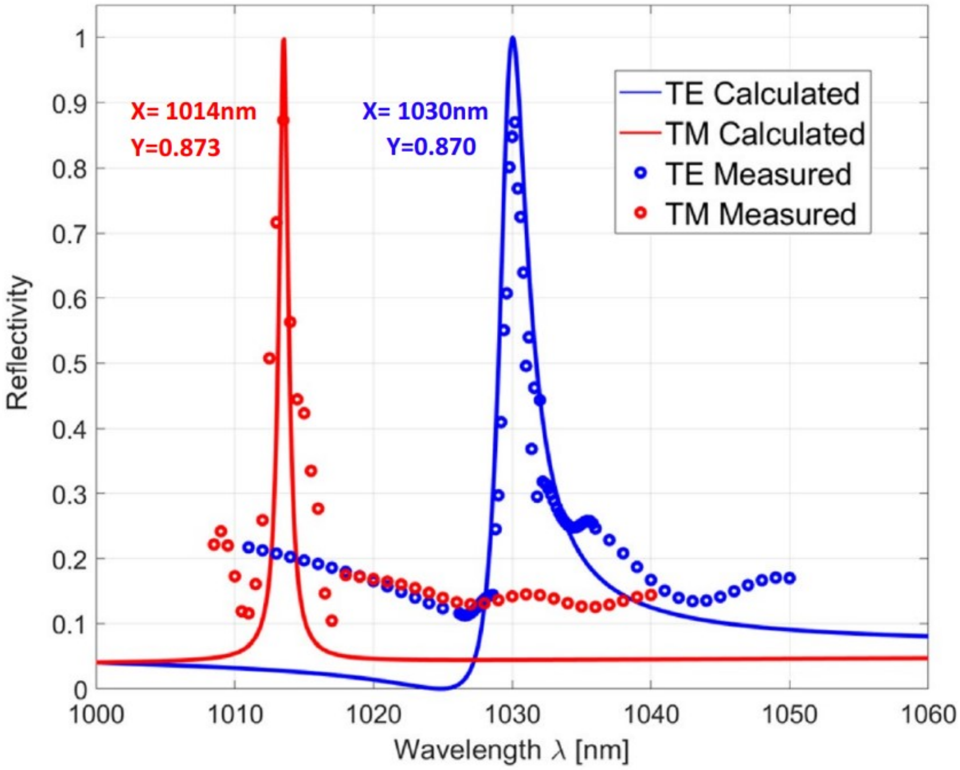

Figure 5.13: Spectral reflectivity of GWS for TE and TM polarisation, at the angles of incidence determined with M-lines measurements.

The reflectivity measurements on the samples with improved thickness uniformity are plotted in Figure 5.13. They revealed a higher resonance than the preliminary samples, with both TM and TE reflectivity reaching 87% reflectivity. This result confirmed our hypothesis that the uniformity of the film thickness plays a critical role.

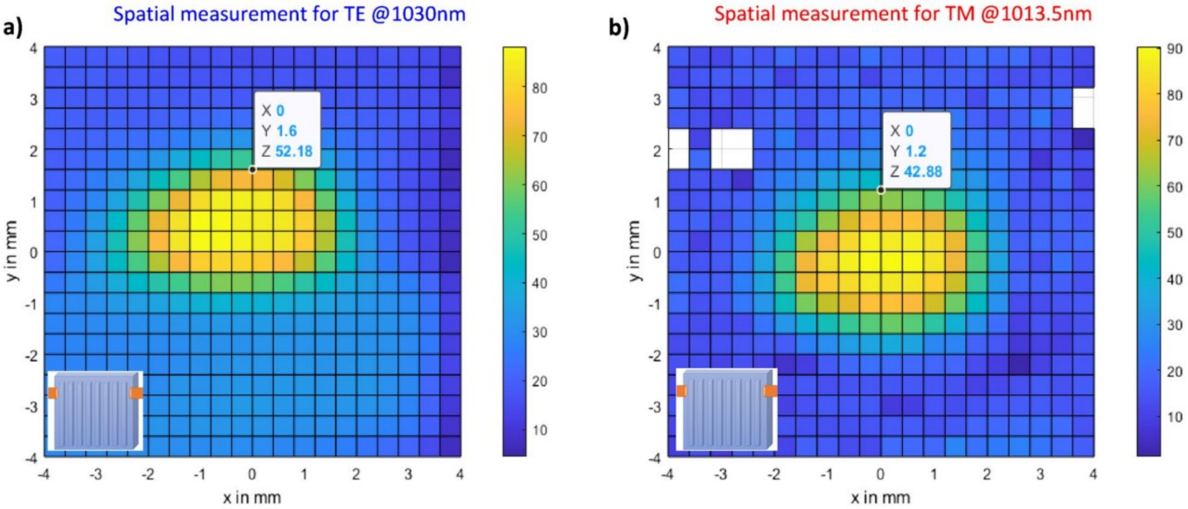

Figure 5.14: Mapping of the reflectivity of the GWS for a) TE polarisation with a wavelength of 1030 nm and b) TM polarisation with a wavelength of 1013.5 nm.

To further confirm this conclusion, a mapping of the sample reflectivity was performed. The GWS was placed on a 2D motorised stage and, for a given angle of incidence and wavelength, the reflectivity could be measured across the sample. Setting the angles and wavelengths to the values obtained in Figure 5.11, the TE and TM efficiency maps were recorded over an area of 4 x 4 mm^2 (Figure 5.14). The measurements reveal a rapid decrease of the GWS reflectivity when moving away from the resonance: a translation of ~1.2 mm away from the point with the highest reflectivity is sufficient to drop the TE reflectivity to 52% and the TM reflectivity to 43%. This distance is smaller than the beam diameter of 1.5 mm, suggesting that the thickness uniformity is still the main limitation for reaching higher efficiencies.

5.1.4.2 GWS for 1970-nm application

An optical bench similar to the 1030-nm setup was installed for the measurement of the 1970-nm reflectivity, but with a Tm laser source. For the preliminary tests, a 1940-nm Tm fibre laser source was built at the Optoelectronics Research Centre with the help of Martin Buckthorpe, which facilitated the evaluation of the first samples. However, the more complete characterisation of the final samples was done in ALPhANOV, where a tuneable 2-micron source was available to perform spectral measurements. In ALPhANOV, Adrian Grande helped me familiarising myself with the equipment, which I was able to use in full autonomy later on.

The setup, illustrated in Figure 5.15, was similar to the one presented in the 1030-nm GWS section. The source was a Tm fibre laser with a grating in Littrow configuration acting as an end-cavity mirror. The grating was placed on a rotation stage and allowed precise tuning of the wavelength from 1900 nm to 2020 nm by adjusting the angle of operation.

The TE and TM resonances were measured as a function of the angle of incidence on the grating, for several wavelengths ranging from 1920 nm to 2000 nm. The transmittance curves are plotted in Figure 5.16.

As expected from the design, the TE and TM resonances are distinct. The angle difference between the TE and TM resonances remains at (1.6 ± 0.02)° for the full range of wavelengths. However, the transmission does not drop below 27% and suggest that the problem of uniformity of the waveguide thickness highlighted in the previous section might be responsible.

To estimate any potential loss during waveguide propagation, both transmittance and reflectance of the GWS were measured at the 1970-nm TE and TM resonances. At the TE resonance, the reflectance reached (70.2 ± 1)% and the transmittance (28.4 ± 1)%, indicating a potential ~1.6% loss. The TM resonance had a (71.9 ± 1)% reflectance and a (22.2 ± 1)% transmittance, resulting in a ~5.9% loss.

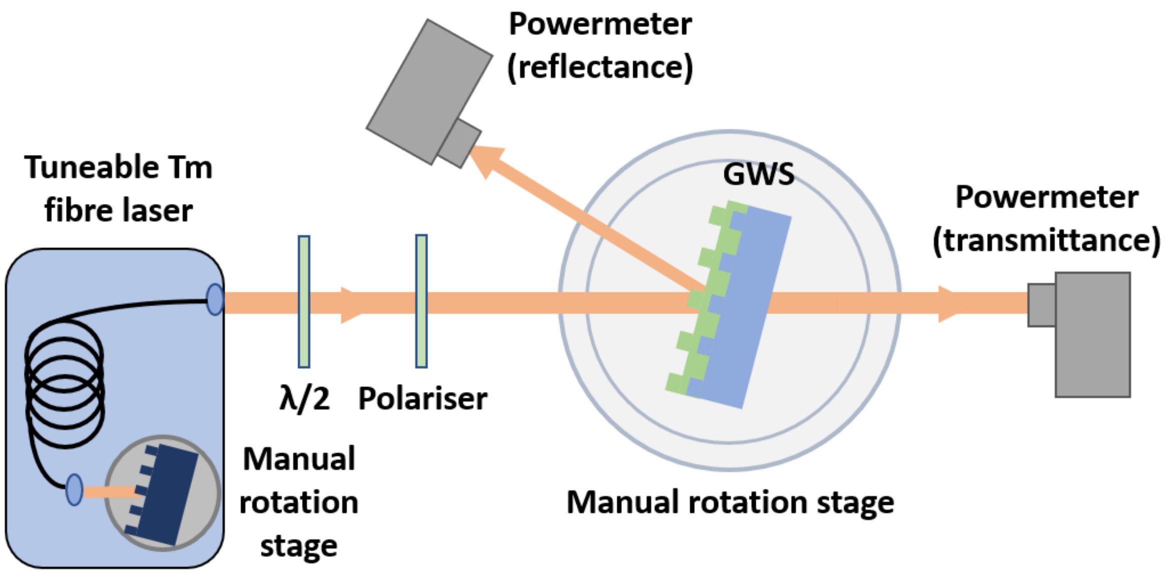

Figure 5.15: Experimental setup for the measurement of the transmittance / reflectance of the GWS with a tuneable Tm fibre laser.

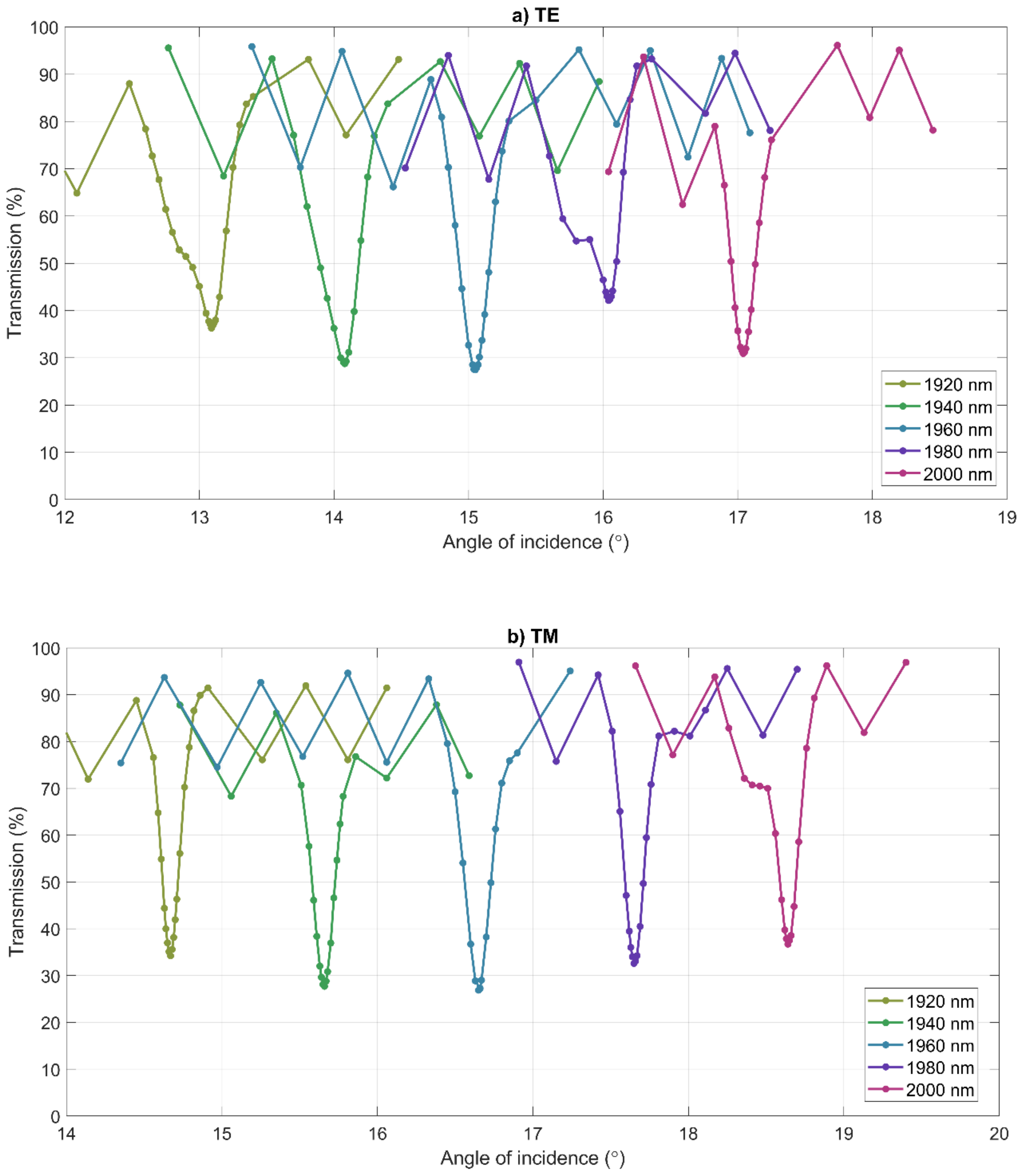

Figure 5.16: a) TE and b) TM resonances of the GWS for wavelengths ranging from 1920 nm to 2000 nm.

The angle of the TE resonance of the GWS was determined for the full wavelength range using steps of 2 nm. A linear dependency was observed within this range of wavelengths (Figure 5.17). A linear fit was therefore attempted and resulted in the equation θ = λ/1172-1.432 with λ in nm and θ in rad. The effective index n_{eff}^{TE} of the TE mode is related to the angle of resonance θ_r and the grating period Λ by:

$$n_{eff}^{TE} = \sin(\theta_r) + \frac{\lambda}{\Lambda}$$

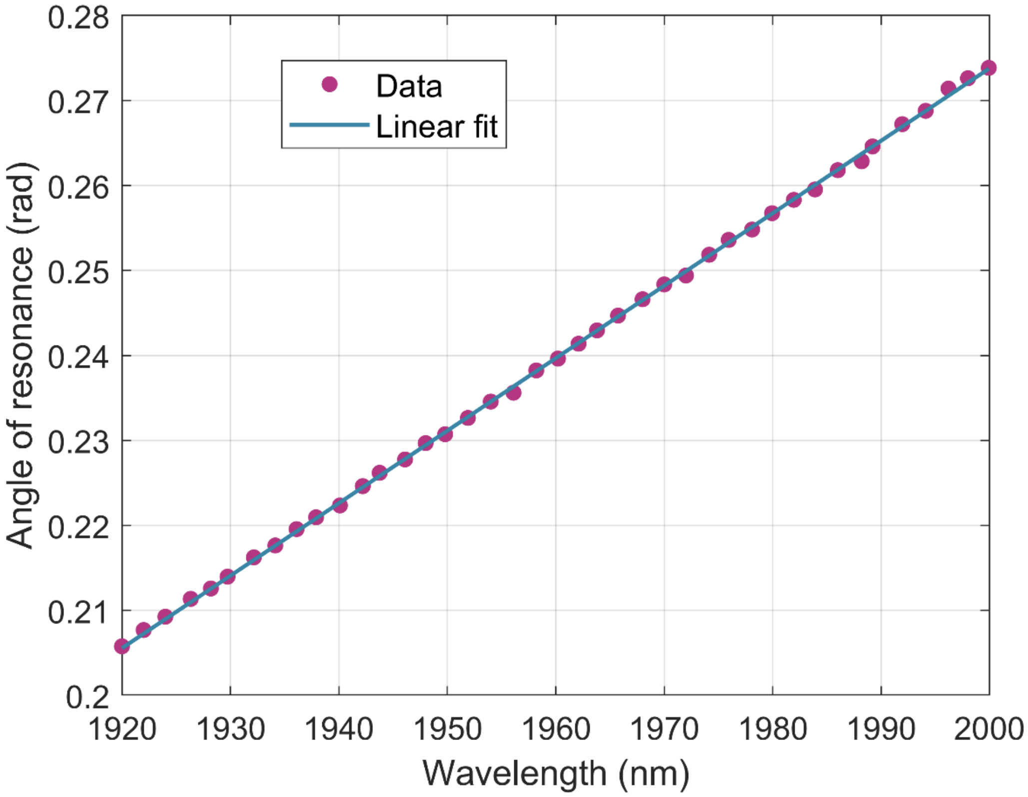

Figure 5.17: Angle of the TE resonance measured with a laser wavelength ranging from 1920 nm to 2000 nm. The linear fit corresponds to the equation : $\theta = \lambda/1172-1.432$ with λ in nm and θ in rad.

5.1.5 Conclusion

In the first half of this chapter, we demonstrated the first instance of an all-crystalline dielectric GWS reflector. The GWSs were designed for two wavelengths of application: 1030 nm and 1970 nm. The Sc_2O_3 waveguides were grown on etched sapphire substrates. AFM scans confirmed that the shape of the waveguide followed well the shape of the grating, owing to the high directionality of PLD. XRD patterns showed that the waveguide grew predominantly in the <111> orientation, which was similar to the growth on flat substrates. The Tauc plots revealed that the bandgap of the waveguide was around 5.85 eV, which remained relatively close to the value obtained on flat films (6.1 eV). The reflectivity of the 1030-nm GWSs reached around 87% for both polarisations, while the reflectivity of the 1970-nm GWSs was around 70% for TE and 72% for TM. The main limitation that was identified was the lack of uniformity of the waveguide thickness, which caused the resonance condition to vary across the beam area. Finally, with the help of a tuneable Tm source, we demonstrated that the angle of resonance around 1970 nm had a linear relationship with the wavelength.

5.2 Deposition of multilayer coatings

5.2.1 Simulation and growth of multilayers

5.2.1.1 Design

The multi-target system that I developed for this study enabled the growth of multilayer coatings constituted of up to three different materials. Our objective was to produce an all-crystalline multilayer coating acting as a resonant reflector. A simple quarter-wave Bragg stack was considered to achieve this objective. The work principle of this multilayer structure is explained in section 2.6.

Among the sesquioxides investigated during the previous studies, Sc_2O_3 and Y_2O_3 exhibit the largest refractive index contrast, and would therefore minimise the number of layers to deposit to achieve a specific reflectivity. Another advantage is that the ranges of temperatures enabling a good quality epitaxial growth of Sc_2O_3 and Y_2O_3 are relatively large and have a significant overlap: their optimal heating laser power ranges are 20-27 W and 16-23 W, respectively. On the other hand, Lu_2O_3 was more complicated to grow on sapphire, with multiple orientations competing and a narrower window of heating power (24-28 W).

Figure 5.18 illustrates the generic design of the crystalline Bragg mirrors presented in this chapter. The choice of Sc_2O_3 as the first layer grown on the substrate fulfilled two purposes. The high refractive index material is commonly used first if the substrate has a low refractive index, in order to enhance the reflectivity of that interface. In reality, this would not make a significant difference in our case, as Sc_2O_3 and Y_2O_3 have very close refractive indices and the number of layers (and hence interfaces) is very large. This choice would be more critical if the index contrast was > 1 and the coating had less than 10 layers. The second motive is that we gained considerable experience on the growth Sc_2O_3 on sapphire owing to all the previous studies. The quality of the first layer deposited is critical to the rest of the deposition, which naturally lead to selecting Sc_2O_3 as the first layer.

The transmission measurement setup with the collimated white light source (Figure 3.13) was intended to be the main validation of the reflectivity of the samples. Since the setup allows measurements from 370 nm to 1000 nm, it seemed reasonable to choose a wavelength of design around the centre of this spectrum, i.e. ~650 nm. In this wavelength range, the refractive indices of Sc_2O_3 and Y_2O_3 are close to 1.994 and 1.917, respectively. To achieve the desired quarter-wave optical thickness, Sc_2O_3 and Y_2O_3 layers required a physical thickness of 81 nm and 84 nm, respectively.

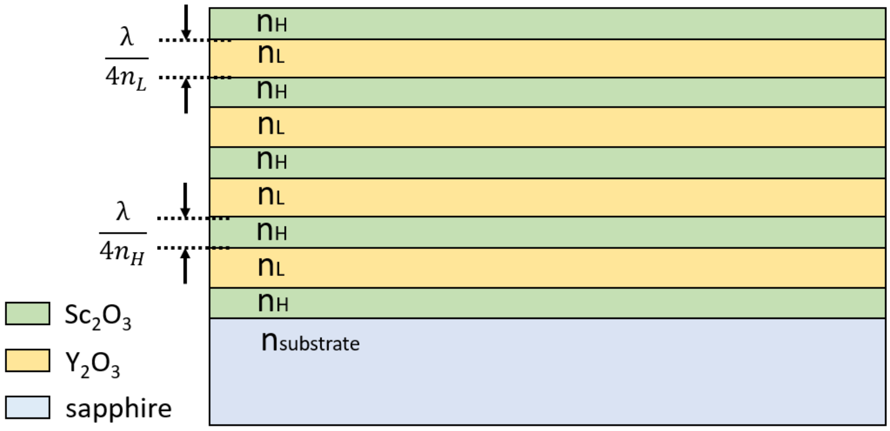

Figure 5.18: Generic design of the multilayers grown in this study. The first and last layers were always a Sc_2O_3 layer. The optical thickness of each layer was a quarter of the wavelength of design.

The theoretical spectral reflectivity of the Bragg mirrors was computed using the widely used transfer matrix method (Knittl, 1983, Macleod, 2010). In this method, the effect of a thin film on a propagating electromagnetic wave is described by a characteristic matrix. By writing the boundary conditions of the electric and magnetic fields at both interfaces and by adding the phase term related to the propagation between the two interfaces, it is possible to express the output electric and magnetic fields as functions of the input fields. These equations can be written in matrixial form, with the transfer matrix depending on the refractive indices of the three media, the thickness of the film and the angle of incidence. The effect of a multilayer coating can therefore be simply expressed as the product of the matrices of all individual layers. The matrices are different for TE and TM polarisations, as the boundary conditions at an interface differ for the tangential and normal components of the electromagnetic field.

I implemented this transfer matrix formalism in MATLAB to compute the theoretical spectral transmission of the coatings to be deposited (see Appendix B). Figure 5.19 shows the spectra for Bragg mirrors of 41, 101 and 151 layers. They prove that a theoretical reflectivity > 95% can be achieved with a perfect 101-layer coating at the resonance. Figure 5.20 reveals how the resonance of a 101-layer coating shifts to lower wavelengths with an increasing angle of incidence. This observation is in good accordance with the fact that the optical path difference between reflections at two parallel interfaces is proportional to the cosine of the angle of incidence: the optical path difference decreases with an increasing angle of incidence, and therefore the quarter-wave condition for resonance is met at a lower wavelength.

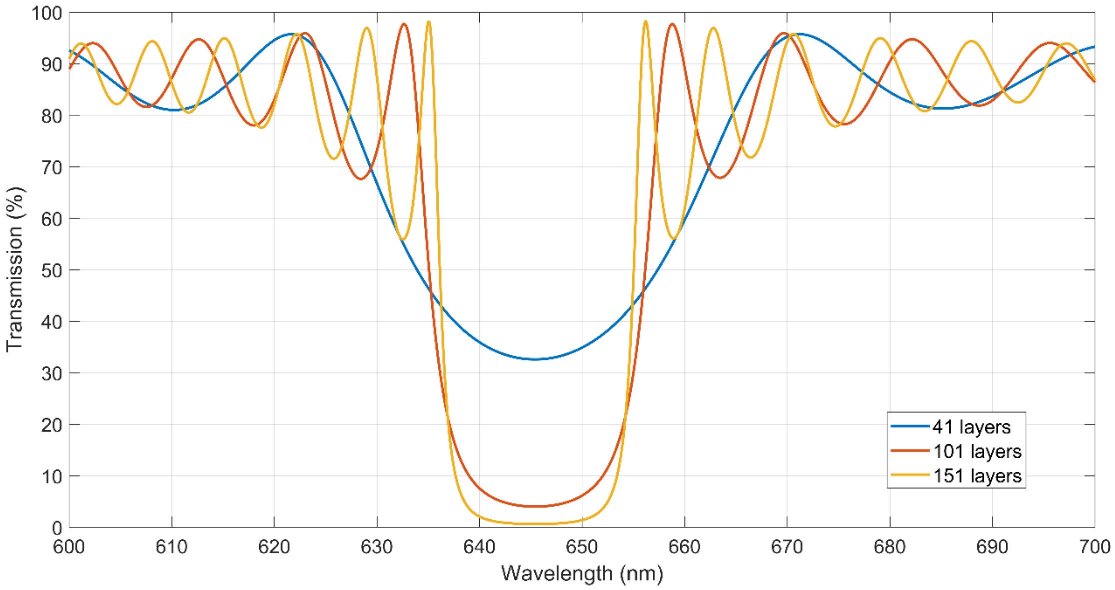

Figure 5.19: Transmission spectra of quarter-wave Bragg stacks constituted of 41, 101 and 151 layers of Sc_2O_3 / Y_2O_3 at normal incidence. The reflection of the sapphire substrate's back surface was not included in the calculations.

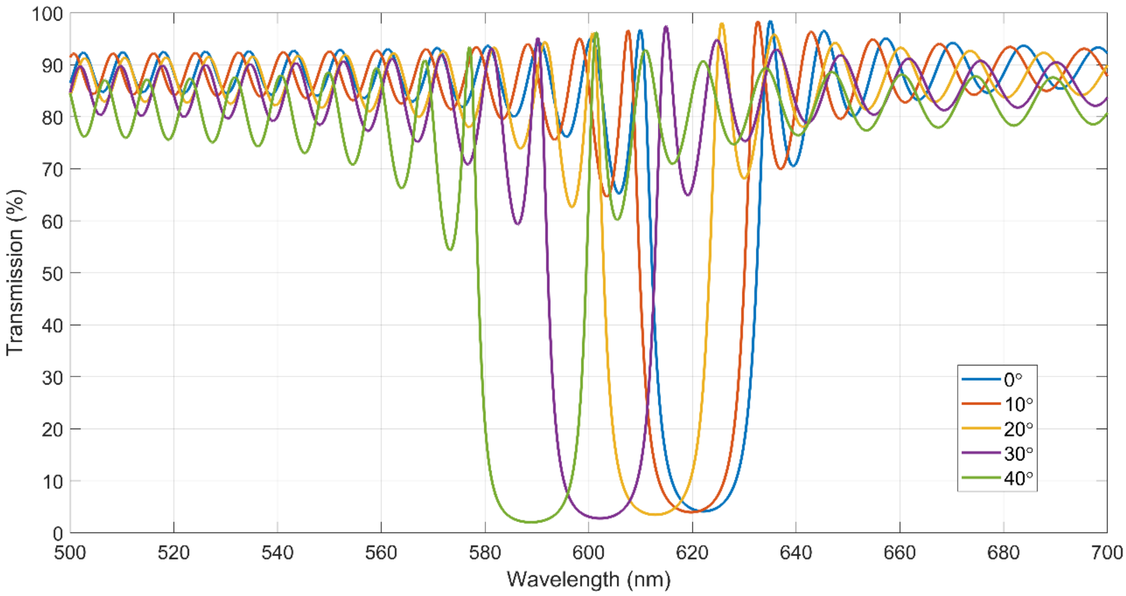

Figure 5.20: Transmission spectra of quarter-wave Bragg stacks constituted of 101 layers of Sc_2O_3 / Y_2O_3 at various incident angles. The reflection of the sapphire substrate's back surface was not included in the calculations. These calculations were done with a TE-polarised beam, and thicknesses of 78 nm and 80.7 nm for the Sc2O3 and Y2O3 layers, respectively.

5.2.1.2 Evaluation of the growth rate

A CO_2 laser power of 21 W was selected as a compromise to meet the conditions of epitaxial growth for both Sc_2O_3 and Y_2O_3. A possible alternative was to modulate the power of the laser between 18 W and 24 W, respectively for each Y_2O_3 and Sc_2O_3 layer. Nevertheless, the duration of growth per layer was only around 45 seconds and therefore a change of power of 8 W within this timescale was considered too risky in terms of thermal stress, all the more that this variation would be repeated 100 times during the growth of a 101-layer coating. As a result, a constant CO_2 laser power of 21 W was applied to heat the samples during the entire duration of the growths. This is valid for all the growths discussed in this chapter.

A precise evaluation of the growth rate of both materials was paramount to ensure that they had the exact same wavelength of resonance. The growth rate of Sc_2O_3 was determined in the same way as before, i.e. by growing a test sample and fitting its transmission spectrum. However, the spectrum of films thinner than 200 nm are difficult to fit because they do not exhibit enough oscillations. For that reason, we aimed for a thickness in the range of 500-1000 nm to have a more precise evaluation of the growth rate. A growth rate of (0.0383 ± 0.0002) nm was measured, suggesting a number of 2115 pulses to reach a thickness of 81 nm.

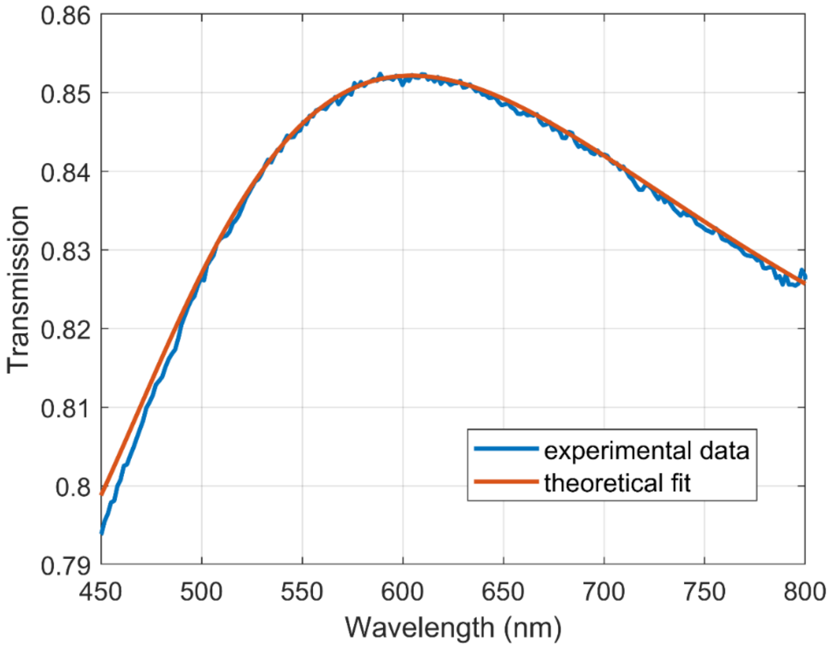

Figure 5.21: Measured transmission of the Y_2O_3/Sc_2O_3/sapphire structure (blue) and theoretical fit for thicknesses of 84 nm and 81 nm, for Sc_2O_3 nm and Y_2O_3 respectively (orange).

For the evaluation of the growth rate of Y_2O_3, an 81-nm-thick Sc_2O_3 layer was first deposited on the sapphire substrate with 2115 ablation pulses, followed by an Y_2O_3 layer with 2900 pulses. This number of pulses was calculated with the objective of depositing 84 nm of Y_2O_3, assuming that the growth rate is close to that of a previous Y_2O_3 film grown on sapphire. By fitting the transmission spectrum with a Y_2O_3 / Sc_2O_3 bi-layer model (Figure 5.21), we find that the actual thickness of the Y_2O_3 film is 81 nm. From this result, we deduce that a number of 3000 ablation pulses must be used to obtain the expected thickness of 84 nm.

5.2.1.3 Growth of Bragg reflectors

Two Y_2O_3/Sc_2O_3 multilayers were grown on 10 x 10 mm^2 sapphire (0001) substrates, with 41 and 101 alternating layers. The fluence of the ablation laser was 1.14 J/cm^2. 2115 pulses were used for the Sc_2O_3 layers and 3000 pulses for the Y_2O_3 layers. As described in the previous section, the power of the CO_2 laser was 21 W. The RMS stability of that power was 0.9% for the 41-layer sample and 2.9% for the 101-layer sample. A third coating with 151 layers was grown with identical conditions, except that the number of pulses for Y_2O_3 samples was increased to 3050. Another major difference was that a 60-min post- annealing with a 25 W heating power was performed at the end of the growth. Despite the longer deposition, the RMS stability of the CO_2 laser power was 2.4%.

With an ablation repetition rate of 100 Hz, the growth of a Sc_2O_3 layer lasted ~21 seconds, while an Y_2O_3 layer required ~30 seconds. After finishing the growth of a layer, the system took around 10 seconds to switch targets by rotating the carousel, and another 10 seconds before starting to fire the new series of pulses. There was thus a delay of ~20 seconds between the end of a layer and the start of the next one, potentially allowing adatom diffusion mechanisms on the surface and island ripening. In total, the 41-, 101- and 151-layer growths lasted respectively 30 min, 1 hour 15 min and 1 hour 53 min.

The visual inspection of the samples after growth highlighted the graded deposition rate across the sample: coloured rings were visible on the samples, mapping the shape of the plasma plume. The graded deposition rate for both Sc_2O_3 and Y_2O_3 would inevitably shift the wavelength of maximum reflection of the Bragg stack, hence the variation of colour depending on the layer thickness. We also noticed that the coatings exhibited some significant scattering, increasing with the number of layers. This aspect differed significantly from single layers presented in other chapters, which were generally clear and transparent. This cloudiness was mainly attributed to the particulates in the coating and the cumulated scattering from the roughness of each interface.

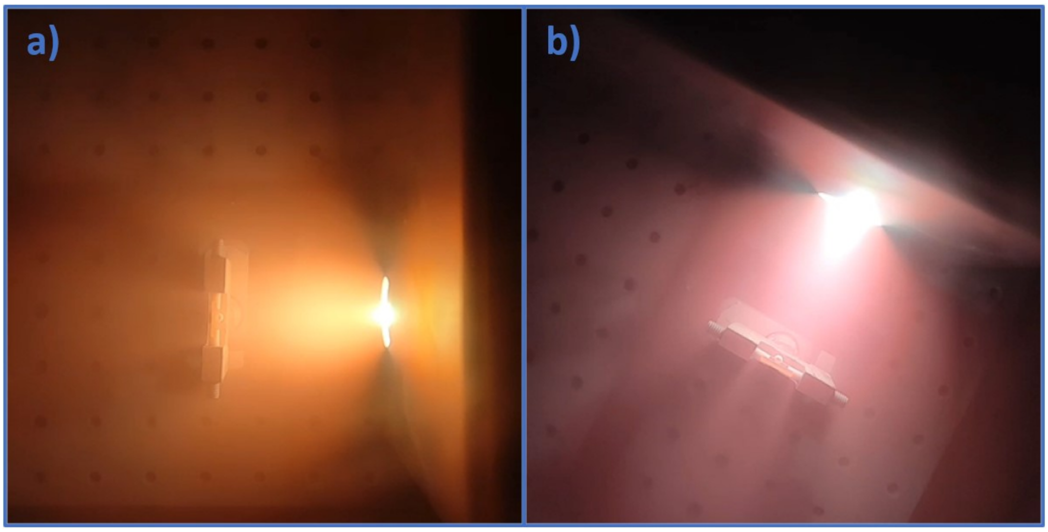

Figure 5.22: Photos of the plasma plume produced by the ablation of a) a Sc_2O_3 target and b) a Y_2O_3 target. Their colour depends on the energy level transitions of the plume species.

5.2.2 Transmission and reflection measurements

The transmission spectra of the three multilayers were recorded with the setup from Figure 3.13. The beam diameter was around 2.5 mm, suggesting that the resulting spectra represent the average resonance across the beam area. To highlight the graded thickness deposition across the samples, the transmission spectra were measured at different distances from the position where the centre of the plasma plume was hitting. The measurements are plotted in Figure 5.23. For simplification, in the rest of this section, we will use the word “centre” to designate the location on the sample where the centre of the plasma was incident.

From the wavelength of resonance, the growth rates of the Sc_2O_3 and Y_2O_3 layers could be roughly estimated. The 41-layer sample had the lowest number of layers and the fastest deposition, implying that it had the best uniformity between all the layers. It was therefore the ideal choice for this estimation. The wavelength of minimum transmission at the centre was ~638 nm (note that the wavelength step was 1.4 nm). At this wavelength, the refractive index of Sc_2O_3 and Y_2O_3 are 1.995 and 1.918, respectively. Assuming that the optical thickness of one layer is exactly a quarter of the wavelength, we compute a physical thickness of 80.0 nm for Sc_2O_3 and 83.2 nm for Y_2O_3, slightly lower than we expected. This discrepancy can be explained by the fact that: 1) the alignment of the white light beam with the centre of the coloured rings (point of highest growth rate, where the centre of the plasma is incident) had only a ± 1.5 mm precision, and deviating from that position lowers the wavelength of resonance; 2) the estimation of the Sc_2O_3 and Y_2O_3 growth rates in section 5.2.1.2 had respective errors of ± 0.5% and ± 1.2%; 3) because of the large diameter of the beam (2.5 mm), the thickness of the layers vary across the beam and hence the wavelength of resonance. This last possibility is explored in more details later with the 101-layer sample.

a) 41 layers

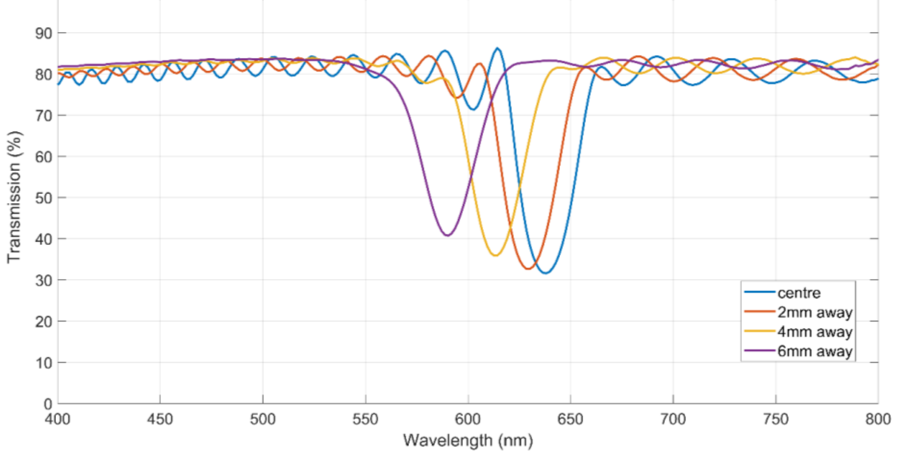

b) 101 layers

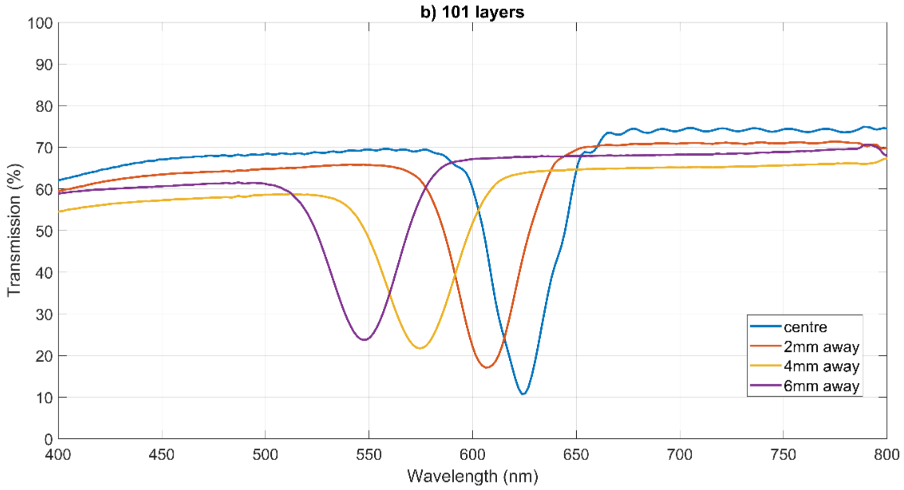

c) 151 layers

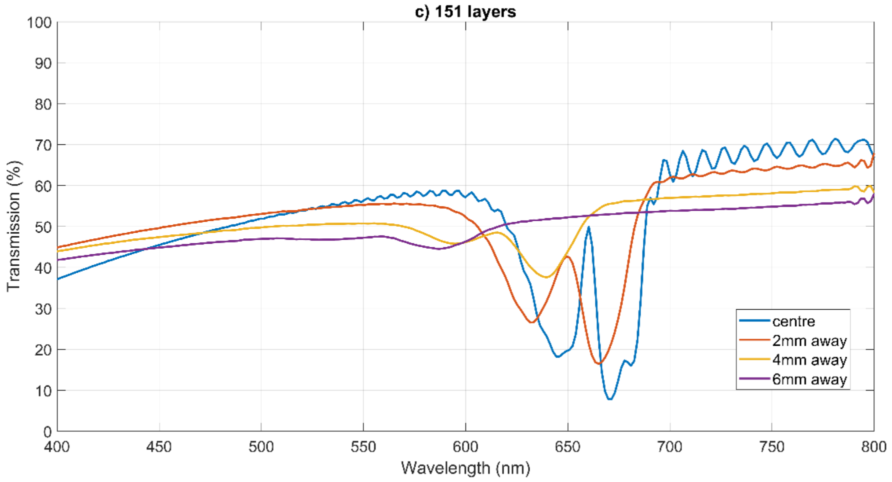

Figure 5.23: Transmission spectra of the a) 41-, b) 101- and c) 151-layer quarter-wave Bragg stacks of Sc_2O_3/Y_2O_3. The blue spectra were recorded at the point of highest growth rate, i.e. where the centre of the plasma was incident. The other spectra were measured at various distances form that point.

The decrease of the wavelength of resonance away from the centre is caused by the decrease of layer thickness. In a similar way to how it was calculated in the previous paragraph, the thickness of the individual layers at different distances from the centre can be extrapolated from each spectrum in Figure 5.23 (a). During the PLD process, the flux of material deposited on the sample is dependent on the angle from the normal of the target at the ablation point. It is potentially possible to verify whether the graded layer thickness across the sample matches well the theory of the angular deposition rate in PLD. However, it is unlikely that the Sc_2O_3 and Y_2O_3 plasmas have the same angular deposition rate, adding a degree of complexity to this problem. Such a verification was therefore not attempted.

The transmission spectrum of the 41-layer sample at the centre is in good accordance with the simulations from Figure 5.19. The base transmission of the coating outside resonance is predicted to be around 88% by the simulations. The sapphire-air interface at the substrate's back has a reflectivity ranging from 7.6% to 8.0% in the 400-800 nm spectral range; the beam reflected at this surface would then only be ~88% transmitted through the coating. The base transmission of the full sample should therefore oscillate around 82%, which is close to what is observed in our measurements, therefore validating that the scattering is negligible for this 41-layer sample.

The transmission spectrum of the 101-layer sample at the centre (Figure 5.23 (b)) exhibits a resonance at 625 nm, which is a lower wavelength than the 41-layer sample. However, the shape of the spectrum is non-symmetrical, and we notice a visible deformation around 643 nm, which indicates the presence of a dip. The triangular shape of the resonance can be interpreted as a graded resonance with the centre of the sample having its resonance around 643 nm and the surrounding rings shifting to lower wavelengths: the resulting resonance across the full area of the white-light beam is the blue spectrum displayed in Figure 5.23 (b). The difference in shape of the spectra recorded at the centre and away from the centre can also be explained by picturing how the thickness of the layers varies across the beam. When the beam is incident on the centre, it experiences an area of flat thickness at the central region and rings of equal film thickness surrounding it. When the beam is moved away from the centre, it sees portions of rings, and hence an increasing thickness from one side of the beam to the opposite. If the distance from the centre is large enough, these portions of rings can be approximated by lines of equal film thickness. In summary, at the centre of the sample, the wavelength of resonance decreases from the centre of the beam to the edges, while away from the centre, it decreases from one edge of the beam to the opposite. It therefore explains the difference in shape between the spectra.

Unlike the two previous samples, the 151-layer coating presents a double-resonance (Figure 5.23 (c)). Two possible causes may explain the origin of this feature. Firstly, the number of pulses for the growth of the Y_2O_3 layers was increased from 3000 to 3050, while the number of pulses for Sc_2O_3 remained unchanged. As a result, the thickness of the Y_2O_3 layers would increase by 1.67%, and the wavelength of resonance by ~10 nm. The second explanation is that a new Y_2O_3 target was used for this growth, potentially causing a change in growth rate. In a previous multilayer growth study from (Sloyan, 2012), it has been estimated that the growth rate decreased by up to 1% during the extended growth (6 hours) of a GGG/YAG multilayer coating. The degradation of the targets was identified as the main reason for the slowdown of the growth by the researcher. In our case, the Y_2O_3 target of the first two coatings had been heavily used before the study, which suggest that the growth rate with that target was slower than with the new target used for the 151-layer coating. These two differences explain how the 151-layer can exhibit two dips in the transmission: the dip around 640-645 nm corresponds to the Sc_2O_3 layers and this wavelength of resonance is unchanged compared to the other two coatings; the second dip around 670 nm is caused by the Y_2O_3 layer and has shifted by ~25-30 nm due to the increased layer thickness.

One of the motivations for the use of Sc_2O_3/Y_2O_3 coatings over GGG/YAG was the smaller bandwidth of the resonance caused by the smaller refractive index contrast. For the determination of the bandwidth, we decided to take the FWHM of the resonance. However, the oscillations of the transmission curves made the estimation of the full amplitude difficult. For simplification, the full amplitude of the resonance was defined from the top of the oscillations outside resonance, to the minimum of the transmission at the resonance. Using this definition, we find that the simulated transmissions of the 41-, 101- and 151-layer coatings had bandwidths of 30 nm, 21 nm, and 19 nm, respectively (Figure 5.19). From the spectra in Figure 5.23, we find bandwidths of (30 ± 1) nm and (32 ± 1) nm for the deposited 41- and 101- layer coatings, respectively. While the 41-layer coating matches the theory, the bandwidth does not seem to decrease further for a higher number of layers. Nevertheless, the graded thickness across the measurement beam might be responsible for this stagnant bandwidth, as the resonance wavelength is thus not rigorously the same across the beam area. Another possible explanation, explored in the next paragraph, is that the base transmission of the curve outside resonance is lower than it should theoretically be, resulting in an inaccurate evaluation of the resonance amplitude.

As the main objective of this thesis is to produce high-reflectance resonators, the amplitude of the resonance is a critical parameter to determine. This parameter cannot be established accurately from the transmission spectra obtained with a broadband white light source. Looking at the theoretical transmission curves in Figure 5.19, we deduce that the base transmission of the three coatings outside resonance must be similar. We already demonstrated earlier that the base transmission of the deposited 41-layer sample matches well the theory, if we include the reflection from the back surface of the sapphire substrate. Nonetheless, the spectra of the deposited 101-

and 151-layer samples have a lower base transmission than the 41-layer sample. Two elements can potentially explain this difference: the increased scattering for thicker samples and the coherence length of the source. The first one comes naturally from the visual inspection of the samples, which looked cloudier with increased thickness. Yet, scattering from the coating is not enough to explain a decrease of the transmission larger than 10%. We will indeed demonstrate later in this section that the scattering from the 101-layer sample only amounts for ~3%. The real cause is the coherence length of the white light source, which generally do not exceed a few microns in this type of setup. In contrast, the thicknesses of our three coatings are 3.4 µm, 8.3 µm and 12.5 µm. The lack of coherence between beams reflected at sufficiently distant interfaces (e.g., the first few and last few interfaces of the coating) results in an increased base reflection. Another evidence confirming this hypothesis is that the base transmission did not decrease uniformly in the spectrum: the decrease is larger for shorter wavelengths. This is a consequence of the fact that the refractive index contrast between Y_2O_3 and Sc_2O_3 is larger for shorter wavelengths: 0.088 at 400 nm, 0.079 at 600 nm, and 0.072 at 800 nm. The strength of the Fresnel reflection at an interface is proportional to the square of the index contrast, which confirms that we should get a higher base reflectivity at shorter wavelengths.

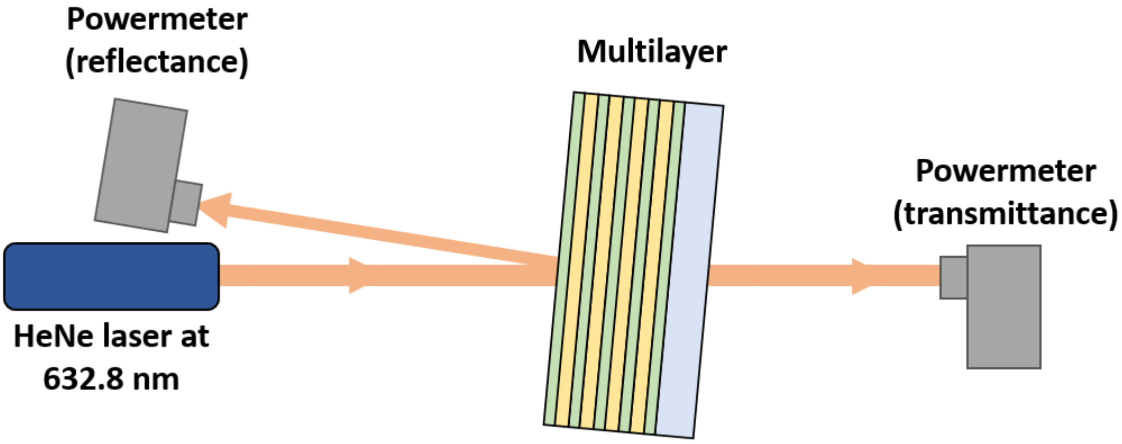

Figure 5.24: Experimental setup for the measurement of the multilayer transmittance and reflectance.

We demonstrated that the reflectance could not be determined with a broadband source because of the short coherence length. As an alternative, a simple experimental setup illustrated in aimed at measuring the reflectivity and transmittance of the sample with a HeNe laser, hence solving the coherence issue. The 632.8-nm beam was close to normal incidence, with a small angle of incidence of 1°04’ ± 2’ allowing the reflected beam to be collected by a powermeter. To estimate the scattering losses, a second powermeter collected the transmitted beam. The beam size was around 3 mm. The power incident on the sample was (4.37 ± 0.03) mW. After adjusting the position of the beam on the sample to maximise the reflected power, we measured a reflected power of (3.37 ± 0.03) mW and a transmitted power of (0.87 ± 0.01) mW. We deduce a reflectance of (77.1 ± 1.1)%, a transmittance of (19.9 ± 1.3)% and a total loss of (3.0 ± 1.7)%. The fact that the reflectance does not reach the expected value > 95% can be attributed to the wavelength of the laser. Indeed, the spectra in Figure 5.23 (b) showed that the resonance of the 101-layer coating at the centre was at 625 nm, and that this wavelength decreased when moving away from the centre. In our measurement, we maximised the reflected power of the 632.8 nm beam, which corresponds to the laser being incident on the centre of the coating. In the blue spectra in Figure 5.23 (b), while the transmission goes down to 10.8% at 625 nm, it is only around 26% at 632.8 nm. This difference clarifies why the reflectance cannot be > 95% for a 632.8 nm beam. Ideally, the reflectance should have been tested with a coherent source at a wavelength of 625 nm, or slightly lower. In any case, these reflectance measurements provide the proof that, with further improvements, a high-reflectance sesquioxide Bragg mirror can be epitaxially grown.

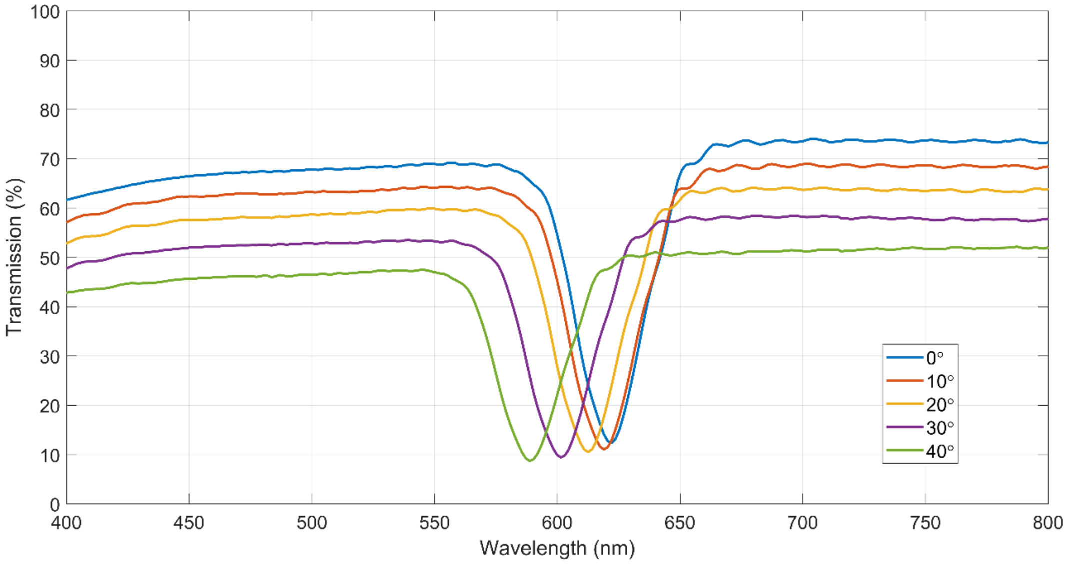

Figure 5.25: Transmission spectra of a 101-layer Sc_2O_3/Y_2O_3 coating at different incident angles.

Finally, the evolution of the wavelength of resonance with the angle of incidence was compared to the theory. While Figure 5.23 demonstrates the tunability of the wavelength of maximum reflection by scanning the surface of the samples, the simulations from Figure 5.20 show that this tunability should also be possible by varying the angle of incidence. The transmission spectrum of the 101-layer sample was measured with the collimated white light at different angles of incidence (Figure 5.25). With an increasing angle of incidence, the beam was shifting laterally because of the refraction when entering the sample. This shift was enough to significantly clip the beam at the detector and overall reduce the measured transmission. Nonetheless, while the transmission values in Figure 5.25 might not be accurate for high incident angles, the position of the wavelength of resonance should not be affected. Therefore, we will only extract the wavelength of resonance at different incident angles from these spectra.

To simulate the transmission spectrum of our 101-layer sample, we computed the thicknesses of the Sc_2O_3 and Y_2O_3 layers that would produce a resonance at 625 nm: 78 nm and 80.7 nm, respectively. The transmission spectra at different incident angles were simulated in Figure 5.20. A comparison between the simulated and measured wavelengths of resonance at different incident angles is displayed in Figure 5.26. With a maximum mismatch of 0.5 nm, the experimental results are in accordance with the theory.

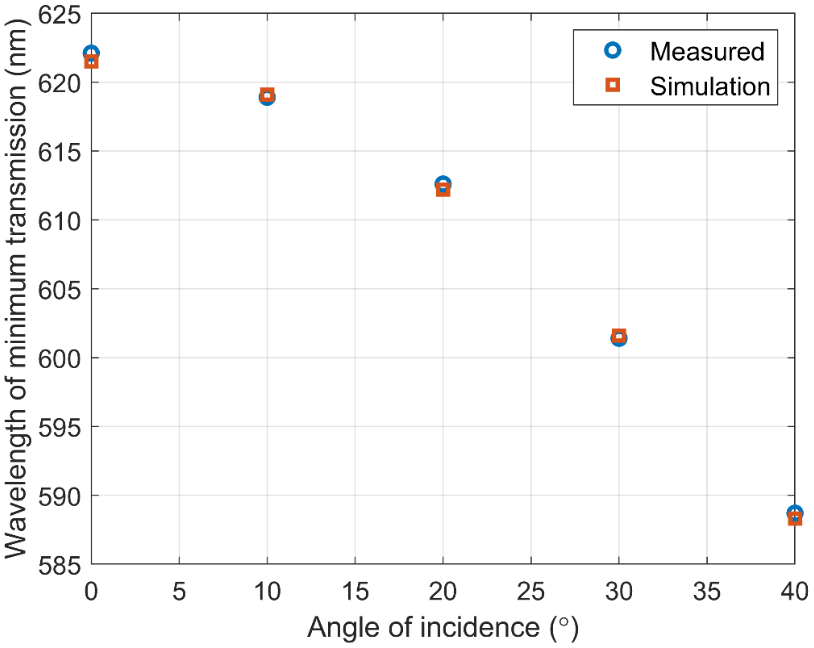

Figure 5.26: Theoretical and experimental comparison of the wavelength of resonance of a 101-layer Sc_2O_3/Y_2O_3 coating at different incident angles.

5.2.3 X-ray diffraction

X-ray patterns of the three coatings were recorded with a large angle step of 0.02°, from 10° to 100°, in order to confirm the presence of both sesquioxides in crystalline form. The curves are plotted in logarithmic scale in Figure 5.27. The material and orientation corresponding to each peak is identified and labelled in Figure 5.27 (a). To avoid redundancy and allow a more comfortable examination of the graphs, the peaks were not labelled in Figure 5.27 (b) and (c). We observe that all orientations appear in the form of doublets, highlighting the successful epitaxial growth of both Sc_2O_3 and Y_2O_3. However, the comparison of the three XRD patterns also reveals a progressive change in the dominating crystal orientation. It was already emphasised in the previous chapters that the <111> orientation of Sc_2O_3 and Y_2O_3 has the smallest lattice mismatch with sapphire <0001>. This orientation is thus prevailing at low thicknesses. Figure 5.27 (a) confirms it with the (222) peaks dominating by more than one order of magnitude over the (440) and (332) peaks. However, Figure 5.27 (b) shows that the <110> orientation progressively overtakes the <111> orientation with an increased number of layers. To further emphasise this change, it must be noted that in the powder diffraction pattern of both Sc_2O_3 and Y_2O_3, the (222) peak is around twice higher than the (440). In other words, when the <111> and <110> orientations are present in equal quantity, the (222) peak is twice stronger than the (440) peak.

A possible explanation for this behaviour is that our set of deposition parameters are more favourable for the growth of <110> if this orientation is given a proper platform to grow on. In our single-layer growths, the orientation of the substrate crystal was sufficient to essentially suppress the growth of <110> and initiate the growth of <111>. Since the growing <111> crystalline film was of high quality and exhibiting low amounts of defects, the <111> orientation would continue dominating as the film grew thicker. However, it seems like our multilayer coatings present an increasing number of defects as it grows thicker. Some defects might potentially be a platform for the growths of undesired orientations like <110>. These defects might be dislocations, or an excessive number of particulates, but it is also suspected that the prolonged delay between the end of a layer and the start of the next one (~20 seconds) might be responsible. Indeed, it has been demonstrated in Chapter 5 that allowing the diffusion of adatoms on the deposition surface for an extended duration would result in the formation of larger islands, which would affect the growth of subsequent atomic layers. The repetition rate study showed that a 500-ms inter-pulse time produced a highly textured Sc_2O_3 film with large islands and high scattering. During the growth of the 101-layer sample, we had 100 pauses of ~20 seconds, namely one pause per interface. It is therefore possible that these pauses are responsible for an increased film texture, which in turn favours the growth of the <110> orientation. To verify this hypothesis, we would need to modify the deposition system to allow a continuous deposition with a fast and seamless transition between targets.

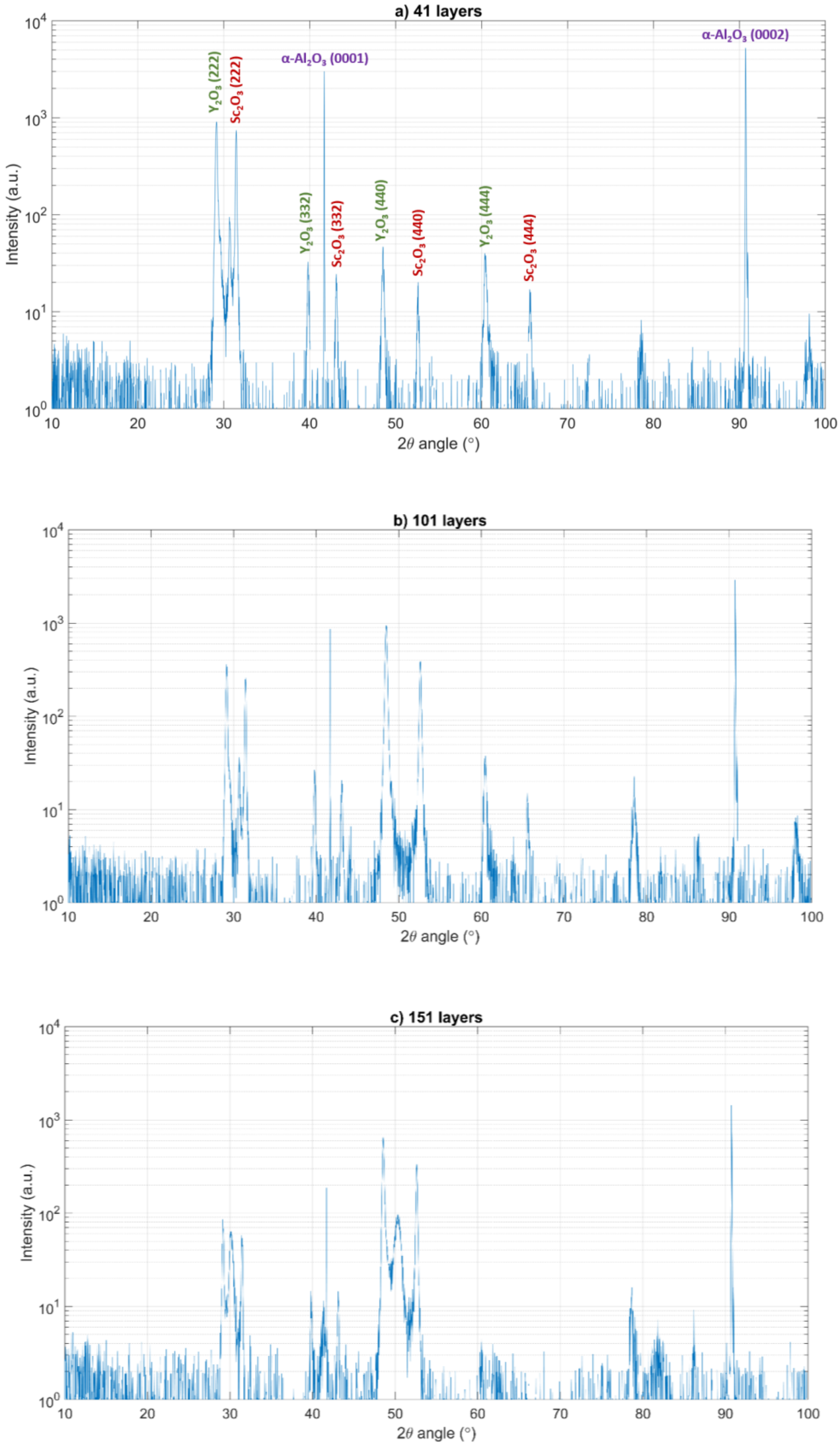

Figure 5.27: X-ray diffraction patterns of the a) 41-layer coating, b) 101-layer coating, and c) 151-layer coating in logarithmic scale.

The main conclusion is that the multilayer coatings are polycrystalline, potentially due to the high number of defects. Some further optimisation is required to grow single crystal Y_2O_3/Sc_2O_3 multilayers in the <111> orientation. One more conclusion can be drawn from the XRD pattern of the 151-layer sample (Figure 5.27 (c)). The effects of the 1-hour post-annealing are clearly visible in the XRD pattern: the double peaks of Sc_2O_3 and Y_2O_3 started merging, with the gap between them progressively being filled with a third larger peak. This phenomenon indicates that some interlayer diffusion is taking place, with the Y_2O_3 and Sc_2O_3 layers exchanging atoms and blurring the interfaces. It is therefore not recommended to post-anneal multilayer crystalline coatings, as their reflectance and atomic structure might be compromised.

5.2.4 Tauc plots

The UV transmittance of the three samples was measured with the Varian Cary 500 spectrophotometer and the Tauc curves were computed. The plots did not show a sharp increase of the absorption but rather a progressive one, probably owing to the large number of defects (Figure 5.28). Nonetheless, the methodology described in section 3.2.4 was strictly applied to identify the linear part and obtain a reasonable fit. Consequently, the bandgaps of the 41-, 101- and 151-layer coatings were 5.64 eV, 5.38 eV and 5.14 eV, respectively. In comparison, the bandgap of single layers of Sc_2O_3 and Y_2O_3 were 5.97 eV and 5.72 eV, respectively. As expected, the number of defects increased with coating thickness and caused the bandgap to progressively drop. Once again, reducing defects seems to be the key to better performance.

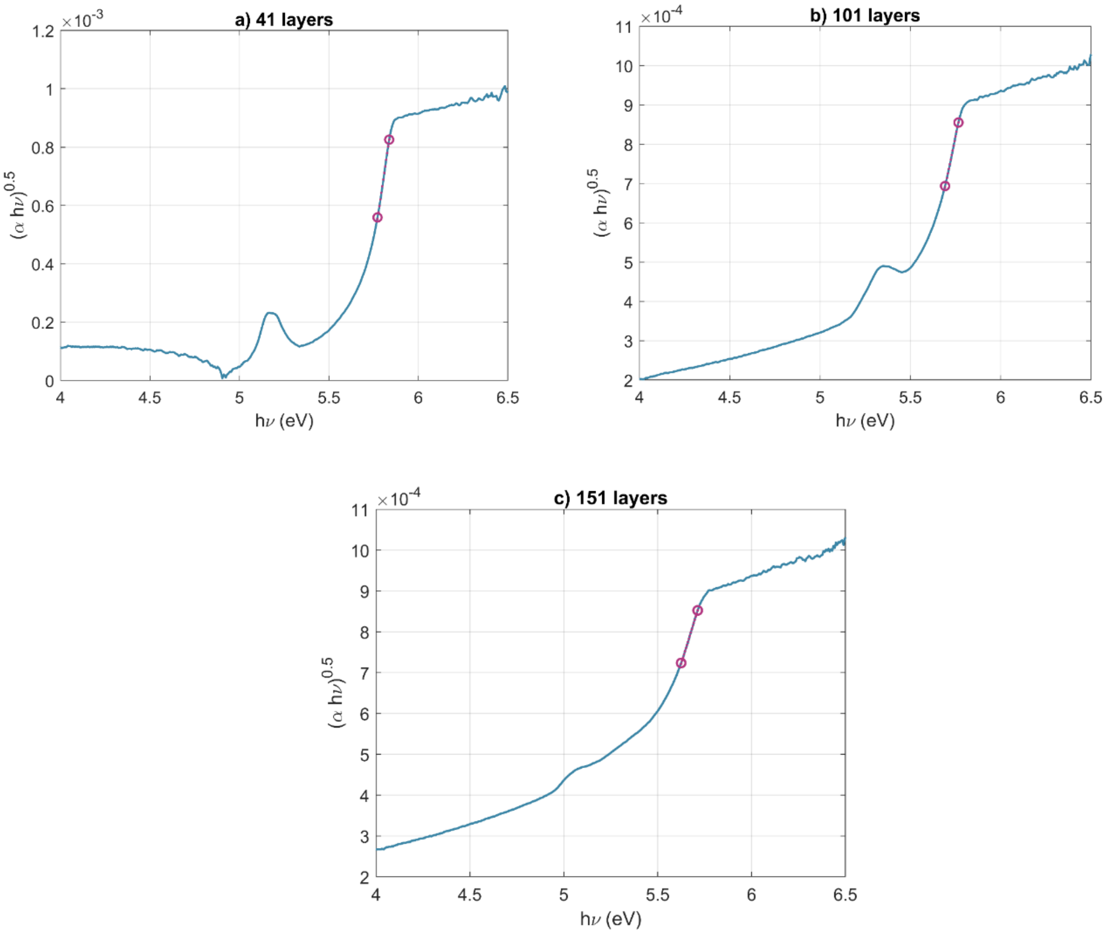

Figure 5.28: Tauc plots of the a) 41-layer coating, b) 101-layer coating, and c) 151-layer coating. The two purple circles highlight the portion of curve used for the linear fit, while the dotted purple line between them represent the best fit.

5.2.5 Conclusion

In this second half of the chapter, we presented the first instance of an epitaxially-grown sesquioxide quarter-wave Bragg stack. The reflectance of the multilayer coatings could be simulated by implementing the matrix transfer method in Matlab. Three samples were grown with 41, 101, and 151 alternating layers of Sc_2O_3 and Y_2O_3. The wavelength of resonance could be tuned by either scanning the surface of the sample (due to graded layer thickness) or by varying the angle of incidence. A reflectance of 77% was measured on the 101-layer sample, with a HeNe laser beam. The XRD measurements revealed that, while the growth of the <111> orientation of Y_2O_3 and Sc_2O_3 was initially favoured, the <110> orientation started to become dominant as the coating grew thicker. Finally, the Tauc plots showed that the bandgap dropped progressively with increasing thickness, which was again attributed to the excessive number of defects.

Chapter 6 Conclusion

6.1 Summary of work

In this thesis, we investigated the possibility of fabricating high-performance all-crystalline resonant reflectors for laser applications. The main motivation for this work was the current limitation of the state-of-the-art reflective/diffractive optics in terms of damage threshold. Crystalline materials exhibit better thermal and mechanical properties, which would make them candidates of choice as reflectors in high-power laser systems.

The GWSs investigated here consisted in a Sc_2O_3 waveguide deposited on a structured sapphire substrate. Therefore, the fabrication process involved two steps: the etching of the sapphire substrate and the epitaxial growth of the waveguide via PLD. The choice of Sc_2O_3 is justified by the fact that, among the sesquioxides presenting a relatively low lattice mismatch with sapphire, Sc_2O_3 has the highest refractive index, highest bandgap, and highest thermal conductivity.

PLD was proven to be a reliable method for the epitaxial growth of Sc_2O_3 on sapphire. An optimal set of deposition parameters were determined to favour the growth of the <111> orientation of Sc_2O_3 on the sapphire c-cut. Several characterisation methods were employed to fully assess the as-grown film, including XRD, bandgap measurement, evaluation of scattering, calculation of the film thickness from the transmission spectrum of the sample, etc. These characterisation methods also contributed to the evaluation of the repeatability of the growth process.

An extensive study aimed at revealing the key mechanism driving 3D-island growth and layer-by-layer growth in PLD. The energy of the plasma elements was identified as a critical parameter that can frustrate Ostwald Island ripening with sufficient energy or a high enough repetition rate. Ion probe measurements revealed that the background pressure and target ablation fluence had a clear impact on the ion energy distribution in the plasma plume. SEM images and AFM scans of the surface of the Sc_2O_3 films confirmed that island growth is the privileged mode when the O_2 background pressure is increased, which correlates well with the ion energy distributions.

PLD-grown films were tested for damage threshold with the LIDT station at Institut Fresnel. The tests were conducted on Y_2O_3, Lu_2O_3 and Sc_2O_3 films, with a P-polarised 1030-nm laser firing 500-fs pulses at a repetition rate of 10 Hz. The conclusion of the tests was that the multiple-shot LIDT of the sesquioxides were comparable to HfO_2, which is the high-index material of choice for high-LIDT coatings. The single-shot LIDT of Sc_2O_3 was also ~20% higher than HfO_2.

The GWSs produced during this project confirmed the possibility of using of a Sc_2O_3 / sapphire GWS in an actual laser device. Owing to the high directivity of the PLD plasma, the shape of the substrate grating was maintained as the waveguide grew thicker. Another key observation is that the waveguide grown on structured sapphire was highly textured in the <111> direction, which suggest that the quality of the epitaxial growth is not affected by the structuring of the substrate. While the samples fabricated for 1030-nm and 1970-nm wavelength-stabilisation did not exhibit reflectivity greater than 87% and 72%, respectively, we were able to identify our main limitation, which is the thickness uniformity of the waveguide. This is not a technological limitation, meaning that this parameter can be significantly improved with a careful design of the PLD setup, putting an emphasis on the uniformity of the coating process. In any case, the fabricated samples acted as a proof-of-concept and demonstrated that an all-crystalline dielectric GWS with high reflectivity is potentially within our reach.

The single-target PLD setup was upgraded to a multi-target system capable of holding three targets. Sc_2O_3 and Y_2O_3 were selected for the epitaxial growth of quarter-wave Bragg stacks on sapphire. The main reason was that they exhibited the largest refractive index contrast among sesquioxides, reducing the number of layers required and potentially producing a narrower resonance. Multilayers of 41, 101 and 151 layers showed that the wavelength of resonance could be tuned across the sample because of the non-uniformity of the thickness of the layers. The same effect could be achieved by tuning the angle of incidence. The reflectance of the 101-layer coating at 633 nm reached (77.1 ± 1.1)% with losses of only (3.0 ± 1.1)%. The limited reflectance was once again attributed to the non-uniformity of the layer thickness, with the wavelength of resonance supposedly varying too rapidly within the diameter of the test beam.

6.2 Future directions

It has been concluded in both GWS and multilayer studies that the uniformity of the thickness was the main limitation of the reflectance. This limitation is not technological, as the improvement of the thickness uniformity can be achieved by bringing modifications to the setup, essentially mechanical. With sufficient budget, a suitable solution can be realised to meet the requirements. One possibility would be to move the sample transversely in front of the plasma during deposition, in order to average the growth rate over the whole surface. Since our setup is using laser heating, the alignment of the CO_2 laser would need to be dynamically adjusted to match the motions of the substrate. Another solution would be to keep the sample fixed and rather move the plasma to scan the sample's surface. This could be achieved by moving the UV ablation spot on the target, either with raster-scan mirrors or with a rotating wedge slightly deviating the beam path. By solving this uniformity issue, the strength of the resonance would increase significantly.

The XRD scans on the multilayer coatings revealed that the dominant orientation was changing with an increasing number of layers, which proved that the multilayer coatings were strongly polycrystalline. With optimised growth conditions, it might be possible to force the multilayer to grow predominantly in the <111> orientation and as a single crystal. One potential cause for the polycrystalline nature of the coating is the 20-second gap between the end of a layer and the start of the next one. When investigating the different growth modes, we clearly demonstrated the importance of inter-pulse time in the aggregation of islands on the growth surface. Improving the system to have a fast and seamless transition between targets might limit the formation of islands and help the growth of the <111> orientation to sustain itself. Although we showed that Lu_2O_3 grown on sapphire vs YAG exhibited the same bandgap, the polycrystalline nature of the former lead to a ~20% lower intrinsic LIDT. It would therefore be beneficial to successfully grown single-crystal multilayer coatings.

The LIDT tests in Institut Fresnel were conducted with a sub-picosecond pulsed laser. In that regime, the interaction between light and matted is so brief that thermal effects do not play a significant role. The LIDT is therefore directly correlated to the bandgap. However, in the nanosecond regime or in continuous-wave operation, the high thermal conductivity of sesquioxides and sapphire might provide an upper edge to our samples. An LIDT study in these regimes would be interesting to potentially confirm that our samples present an advantage.

Finally, another important perspective for PLD would be the reduction of scattering points inside the film. The bi-directional ablation method was proven to dramatically reduce the number and size of particulates. However, for cutting-edge optical applications, the quantity of particulates must be further reduced. A potential direction to explore is multi-directional ablation: increasing the number of directions of ablation might slow down even further the alteration of the target surface and therefore reduce the number of particulates.

As a conclusion, PLD was proven to be a versatile method that successfully grew highly crystalline films for optical applications, in particular for all-crystalline resonant reflectors. Several directions of work have been proposed to further improve the results presented in this thesis. This long and exciting journey might be the start of a new one.

Appendix A Designing the multi-target system

Designing a multi-target deposition system with bi-directional ablation was particularly challenging, owing to the complexity of the movement required for each target and the limited space and number of ports in the vacuum chamber. Obviously, motors had to be kept outside of the chamber to avoid the evaporation of lubricant (and hence contamination) or overheating caused by the absence of air.

Figure 6.1 illustrates the configuration of the chamber and the available ports. Notice the absence of port with 90° angle with respect to the target port. A new port could have been added if necessary, but the welding work would have rendered the chamber unusable for several months, delaying our tight schedule.

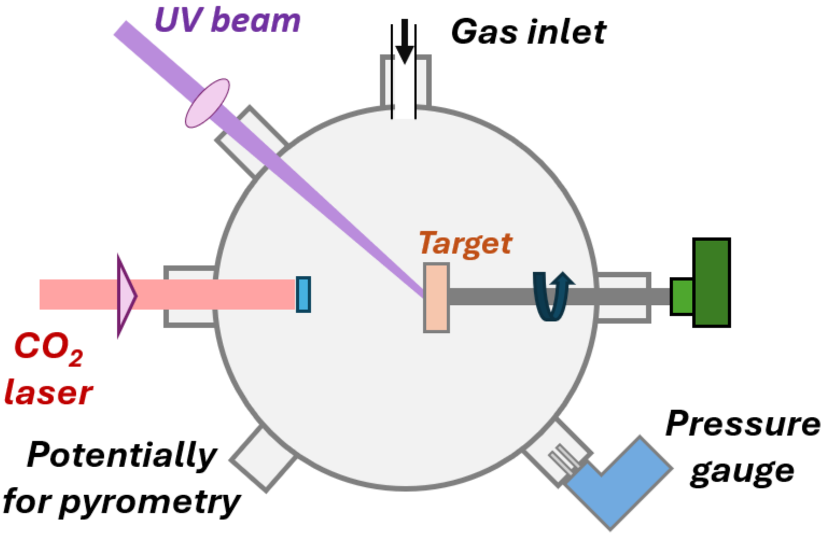

Figure 6.1: Layout of the PLD chamber.

<u>**Two targets with a translation**</u>

One basic idea was to adapt the single-target mechanical system to hold two targets next to each other. The motion of the targets would be driven by the same offset cam, allowing for bi-directional ablation. The issue was about translating the entire structure from left to right to switch targets. Not only would another port be needed to drive a translation stage, but the size of such a stage would be hard to fit inside the chamber. Lastly, even if this translation was possible, it would be difficult to keep spinning the targets via port E if the structure was moving with respect to the port axis.

One motor, two beams

The use of a multibeam chamber available in the lab was also considered. In the design illustrated in Figure 6.2, one motor drives a bevel gear, which in turn rotates two bi-directional systems based on the single-target system. Each target is ablated by its own excimer beam. The issue was the size of the system, which did not fit inside of the chamber.

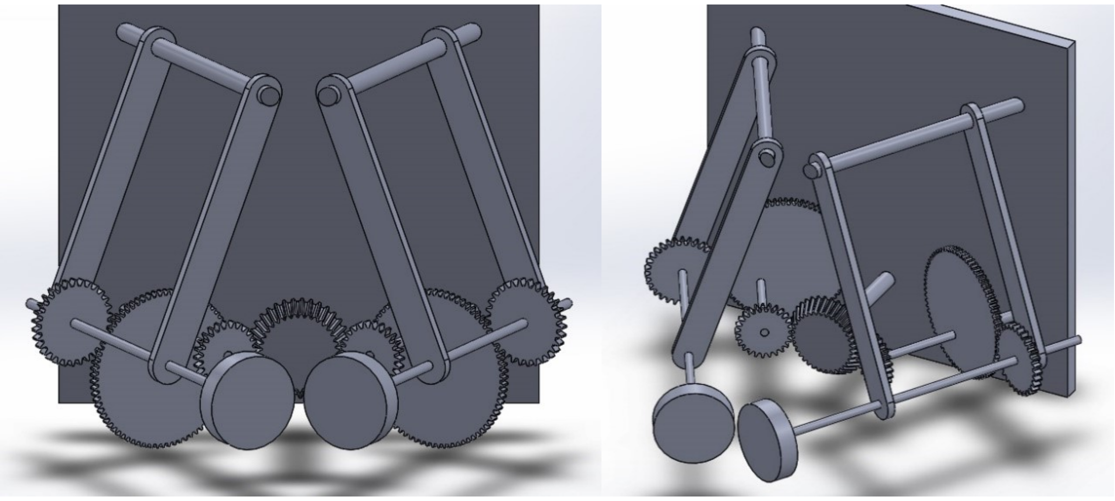

Figure 6.2: The bevel gear at the centre drives two bi-directional ablation systems.

One motor, two beams (compact)

I removed some useless components from the previous design to make it more compact: the main gears spinning the targets are directly in contact with the bevel gear (Figure 6.3). The two issues identified by the mechanical workshop are: 1) such a thick bevel gear needs to be custom-made and 2) the gear period (distance between the teeth) is not constant on the full thickness of the bevel gear because of its truncated conical shape, and this might compromise the contact with the teeth of other gears.

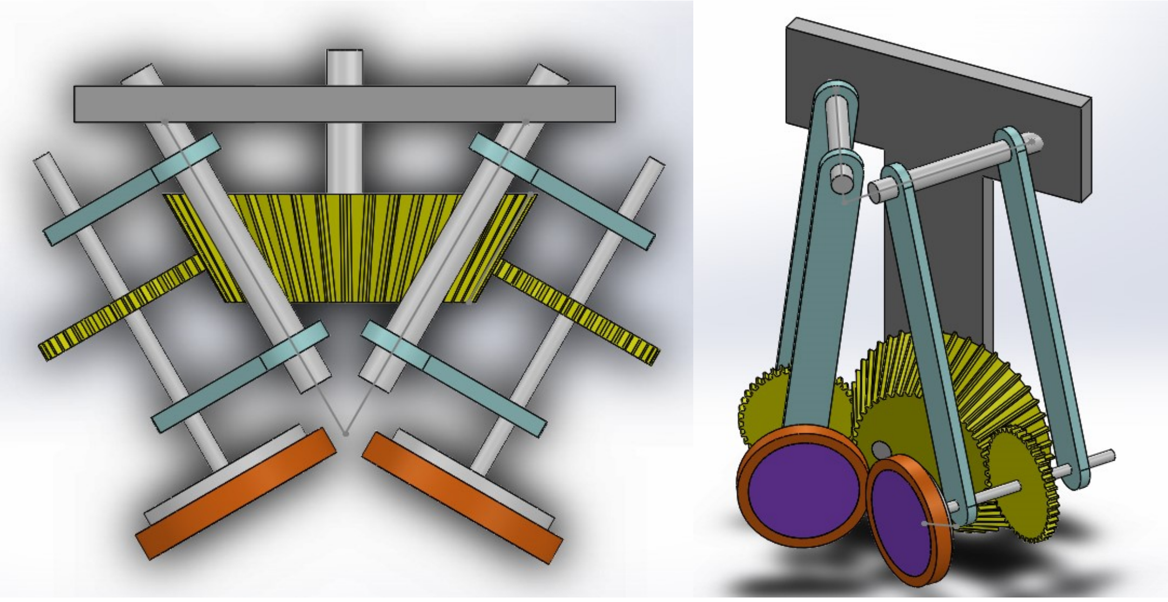

Figure 6.3: Compact version of the design in Figure B.1. The bevel gear is too thick, creating a difference in teeth spacing along the thickness.

Flipping with magnets

Back to the single-beam chamber, I considered keeping the existing single-target system and only replacing the target holder. The new one would be capable of holding two targets back-to-back and flip between them with the help of electromagnets and permanent magnets (Figure 6.4). In “locked” position, the polarity of the electromagnet would be set to the opposite of the permanent magnets to hold it in place with the attractive force when one of the two targets is in use. In order to switch targets, we would change the polarity to initiate the flip with the repulsive force and then change the polarity again to lock the new position.

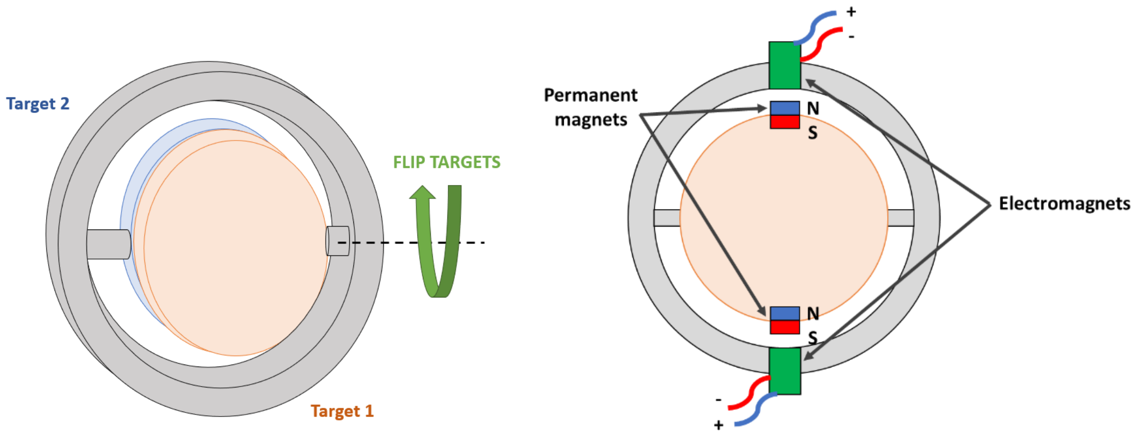

Figure 6.4: Targets 1 and 2 are back-to-back. The polarity of the electromagnets can be switched to flip the targets.

A 3D-printed version was created as a proof-of-concept, but the tests were unsuccessful because of the attractive/repulsive forces were too weak and the process was therefore unreliable. We were also apprehensive of the possible effects of the magnets on the plasma plume if they were too powerful.

Flipping with servomotor

In a similar way, I also considered flipping the two targets with a small servomotor (Figure B.4). A servomotor does not require lubrication because of the plastic gears, and the risk of overheating is limited since it would not be in continuous motion (the target flip would typically occur once or twice every minute).

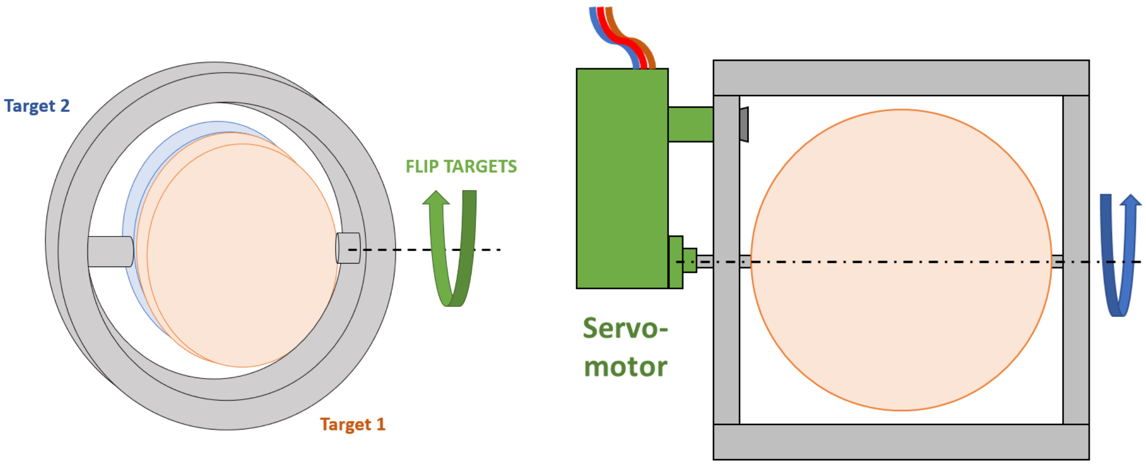

Figure 6.5: Targets 1 and 2 are back-to-back. A servomotor is used to flip the targets.

<u>Carousel</u>

The carousel holding three targets was the solution which was finally implemented in the PLD chamber. The description of its working principle can be found in Chapter 3, along with an explanation of the way it achieves bidirectional ablation.

Appendix B MATLAB simulation for multilayer coating

Different versions of the following MATLAB program have been developed depending on my needs, even though the core of the code remains the same. The key formulas to implement the transfer matrix method are taken from (Knittl, 1983, Macleod, 2010). In the following example, we compute the TE transmission of the coating for different angles of incidence, and compare the simulations to the actual measurements. The code is written with the purpose of simulating the behaviour of a quarter-wave Bragg stack starting with a high-index layer, but it can easily be adapted to study any type of multilayer coating.

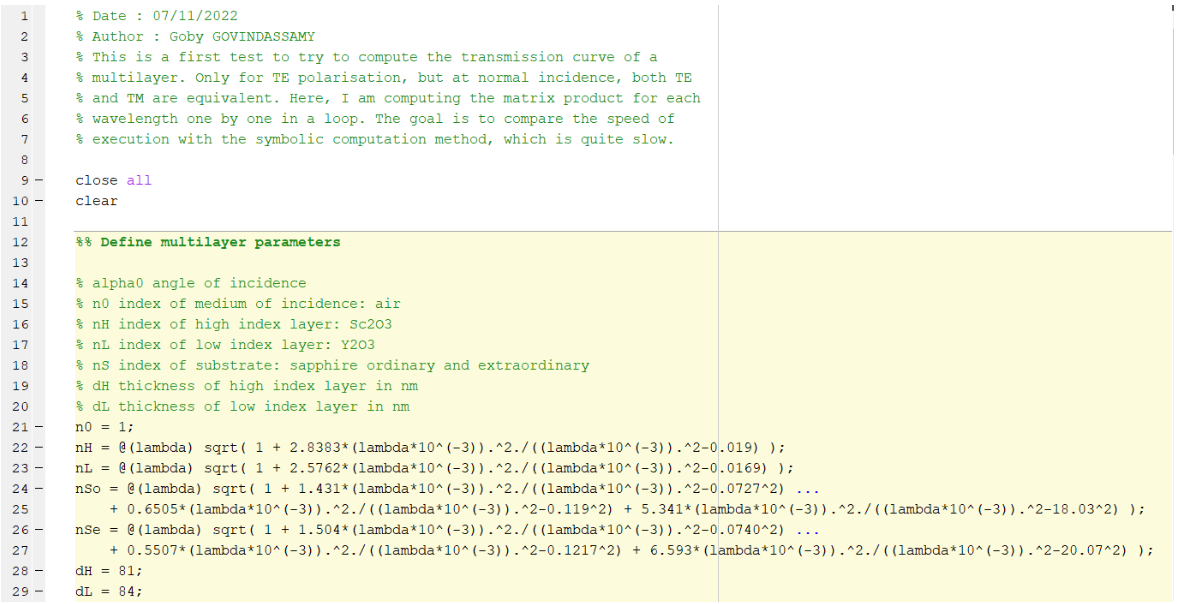

```
% Date : 07/11/2022
% Author : Goby GOVINDASSAMY
% This is a first test to try to compute the transmission curve of a
% multilayer. Only for TE polarisation, but at normal incidence, both TE
% and TM are equivalent. Here, I am computing the matrix product for each
% wavelength one by one in a loop. The goal is to compare the speed of
% execution with the symbolic computation method, which is quite slow.

close all
clear

%% Define multilayer parameters

% alpha0 angle of incidence
% n0 index of medium of incidence: air
% nH index of high index layer: Sc2O3
% nL index of low index layer: Y2O3
% nS index of substrate: sapphire ordinary and extraordinary
% dH thickness of high index layer in nm
% dL thickness of low index layer in nm
n0 = 1;
nH = @(lambda) sqrt( 1 + 2.8383*(lambda*10^(-3)).^2./((lambda*10^(-3)).^2-0.019) );
nL = @(lambda) sqrt( 1 + 2.5762*(lambda*10^(-3)).^2./((lambda*10^(-3)).^2-0.0169) );
nSo = @(lambda) sqrt( 1 + 1.431*(lambda*10^(-3)).^2./((lambda*10^(-3)).^2-0.0727^2) ...
    + 0.6505*(lambda*10^(-3)).^2./((lambda*10^(-3)).^2-0.119^2) + 5.341*(lambda*10^(-3)).^2./((lambda*10^(-3)).^2-18.03^2) );
nSe = @(lambda) sqrt( 1 + 1.504*(lambda*10^(-3)).^2./((lambda*10^(-3)).^2-0.0740^2) ...
    + 0.5507*(lambda*10^(-3)).^2./((lambda*10^(-3)).^2-0.1217^2) + 6.593*(lambda*10^(-3)).^2./((lambda*10^(-3)).^2-20.07^2) );
dH = 81;
dL = 84;
```

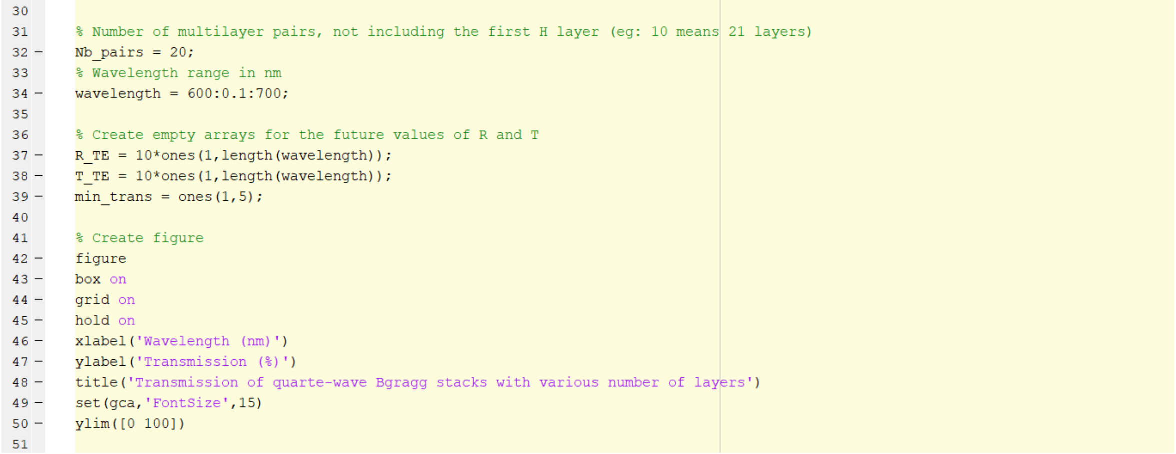

```

% Number of multilayer pairs, not including the first H layer (eg: 10 means 21 layers)
Nb_pairs = 20;
% Wavelength range in nm
wavelength = 600:0.1:700;

% Create empty arrays for the future values of R and T
R_TE = 10*ones(1,length(wavelength));
T_TE = 10*ones(1,length(wavelength));
min_trans = ones(1,5);

% Create figure
figure
box on
grid on
hold on
xlabel('Wavelength (nm)')
ylabel('Transmission (%)')
title('Transmission of quarte-wave Bgragg stacks with various number of layers')
set(gca,'FontSize',15)
ylim([0 100])

```

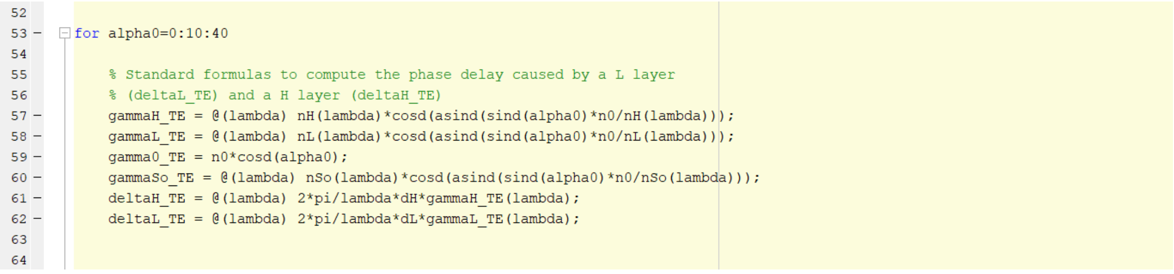

```
for alpha0=0:10:40

    % Standard formulas to compute the phase delay caused by a L layer
    % (deltaL_TE) and a H layer (deltaH_TE)
    gammaH_TE = @(lambda) nH(lambda)*cosd(asind(sind(alpha0)*n0/nH(lambda)));
    gammaL_TE = @(lambda) nL(lambda)*cosd(asind(sind(alpha0)*n0/nL(lambda)));
    gamma0_TE = n0*cosd(alpha0);
    gammaSo_TE = @(lambda) nSo(lambda)*cosd(asind(sind(alpha0)*n0/nSo(lambda)));
    deltaH_TE = @(lambda) 2*pi/lambda*dH*gammaH_TE(lambda);
    deltaL_TE = @(lambda) 2*pi/lambda*dL*gammaL_TE(lambda);

```

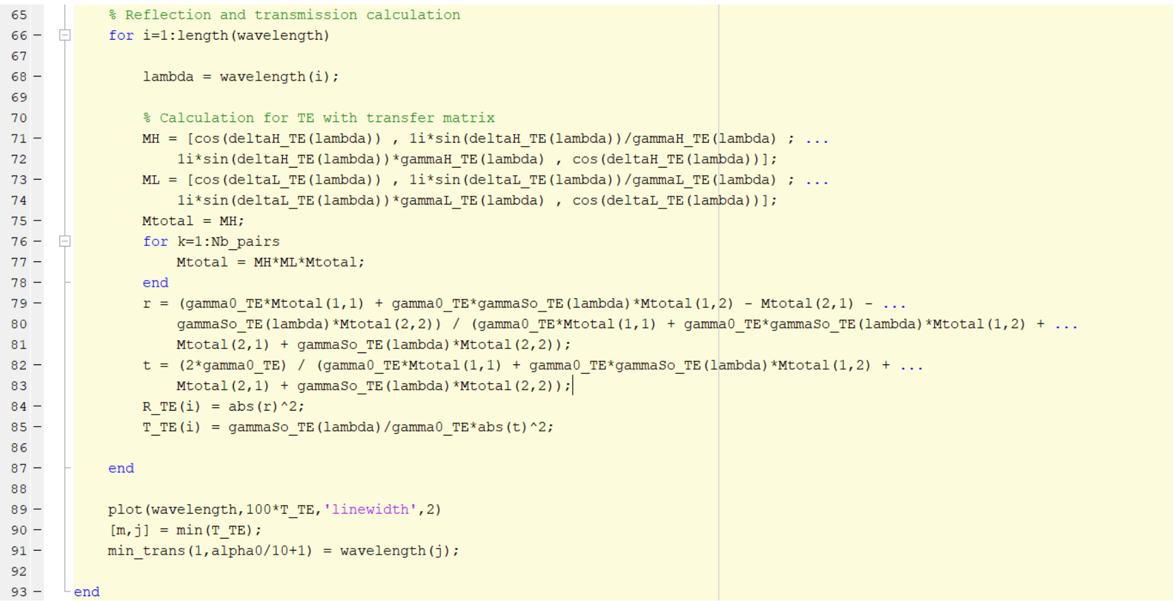

```
    % Reflection and transmission calculation
    for i=1:length(wavelength)

        lambda = wavelength(i);

        % Calculation for TE with transfer matrix
        MH = [cos(deltaH_TE(lambda)) , 1i*sin(deltaH_TE(lambda))/gammaH_TE(lambda) ; ...
            1i*sin(deltaH_TE(lambda))*gammaH_TE(lambda) , cos(deltaH_TE(lambda))];
        ML = [cos(deltaL_TE(lambda)) , 1i*sin(deltaL_TE(lambda))/gammaL_TE(lambda) ; ...
            1i*sin(deltaL_TE(lambda))*gammaL_TE(lambda) , cos(deltaL_TE(lambda))];
        Mtotal = MH;
        for k=1:Nb_pairs
            Mtotal = MH*ML*Mtotal;
        end
        r = (gamma0_TE*Mtotal(1,1) + gamma0_TE*gammaSo_TE(lambda)*Mtotal(1,2) - Mtotal(2,1) - ...
            gammaSo_TE(lambda)*Mtotal(2,2)) / (gamma0_TE*Mtotal(1,1) + gamma0_TE*gammaSo_TE(lambda)*Mtotal(1,2) + ...
            Mtotal(2,1) + gammaSo_TE(lambda)*Mtotal(2,2));
        t = (2*gamma0_TE) / (gamma0_TE*Mtotal(1,1) + gamma0_TE*gammaSo_TE(lambda)*Mtotal(1,2) + ...
            Mtotal(2,1) + gammaSo_TE(lambda)*Mtotal(2,2));
        R_TE(i) = abs(r)^2;
        T_TE(i) = gammaSo_TE(lambda)/gamma0_TE*abs(t)^2;

    end

    plot(wavelength,100*T_TE,'linewidth',2)
    [m,j] = min(T_TE);
    min_trans(1,alpha0/10+1) = wavelength(j);

end
```

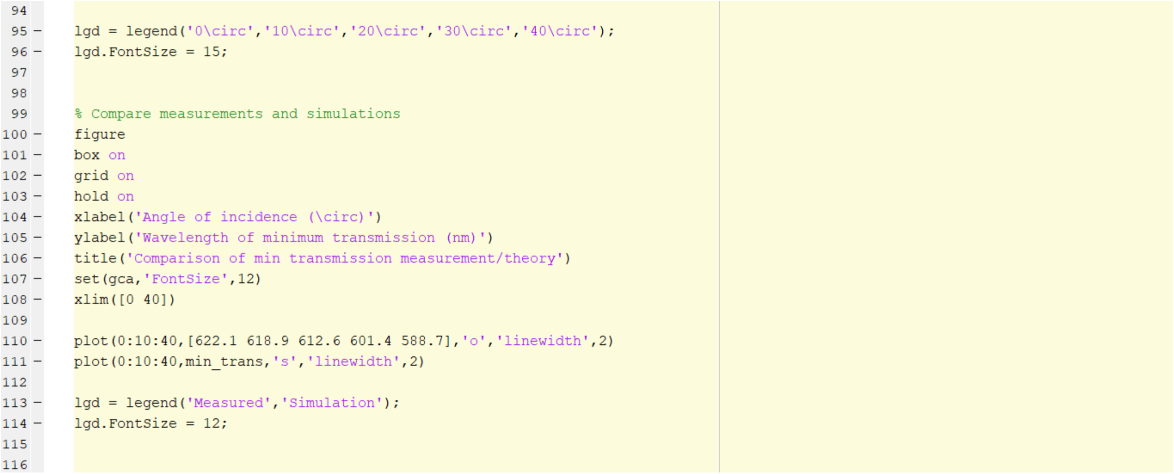

```

lgd = legend('0\circ','10\circ','20\circ','30\circ','40\circ');
lgd.FontSize = 15;


% Compare measurements and simulations
figure
box on
grid on
hold on
xlabel('Angle of incidence (\circ)')
ylabel('Wavelength of minimum transmission (nm)')
title('Comparison of min transmission measurement/theory')
set(gca,'FontSize',12)
xlim([0 40])

plot(0:10:40,[622.1 618.9 612.6 601.4 588.7],'o','linewidth',2)
plot(0:10:40,min_trans,'s','linewidth',2)

lgd = legend('Measured','Simulation');
lgd.FontSize = 12;


```

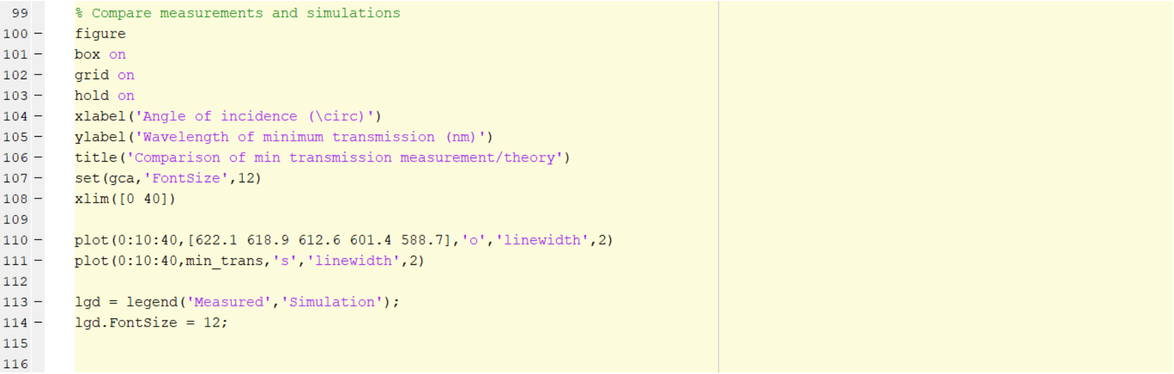

```
% Compare measurements and simulations
figure
box on
grid on
hold on
xlabel('Angle of incidence (\circ)')
ylabel('Wavelength of minimum transmission (nm)')
title('Comparison of min transmission measurement/theory')
set(gca,'FontSize',12)
xlim([0 40])

plot(0:10:40,[622.1 618.9 612.6 601.4 588.7],'o','linewidth',2)
plot(0:10:40,min_trans,'s','linewidth',2)

lgd = legend('Measured','Simulation');
lgd.FontSize = 12;


```

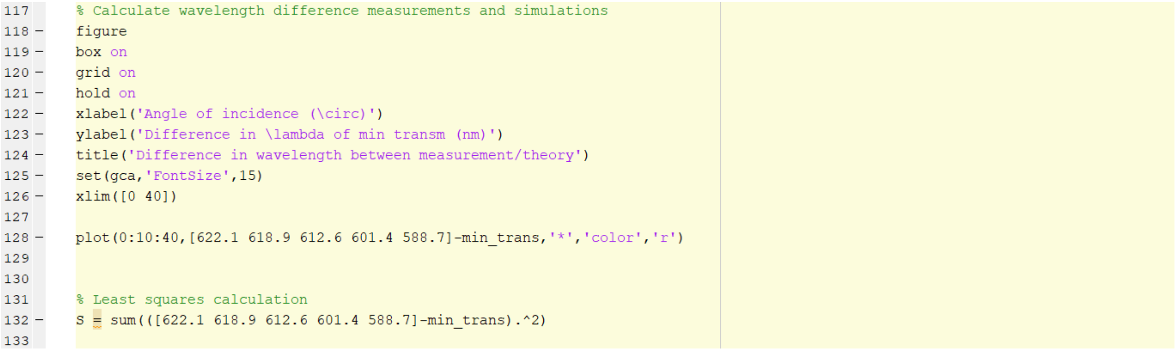

```
% Calculate wavelength difference measurements and simulations
figure
box on
grid on
hold on
xlabel('Angle of incidence (\circ)')
ylabel('Difference in \lambda of min transm (nm)')
title('Difference in wavelength between measurement/theory')
set(gca,'FontSize',15)
xlim([0 40])

plot(0:10:40,[622.1 618.9 612.6 601.4 588.7]-min_trans,'*','color','r')


% Least squares calculation
S = sum(([622.1 618.9 612.6 601.4 588.7]-min_trans).^2)

```

Appendix C Unprocessed ion probe traces

In this appendix, we display the raw ion probe traces that were used in the discussion on plume dynamics in Chapter 4. The data was minimally processed: it was extracted from the original file and the curves were only shifted along the x-axis to make their pre-pulse coincide.

Figure 6.6 corresponds to the study where the chamber pressure was varied to understand its effect on the plasma plume coming from the Sc_2O_3 target. Figure 6.7 exhibits the traces recorded on the same Sc_2O_3 with different ablation fluences, at a constant chamber pressure of 20 µbar. Figure 6.8 and Figure 6.9 are equivalent traces recorded with an Al_2O_3 target. The ablation fluence selected for the pressure test was 1.7 J/cm^2, as it had been previously identified as an optimal fluence for the growth of a sapphire film on a sapphire substrate.

Similar tests were conducted with a wide range of targets:

- Y_2O_3
- Lu_2O_3
- Mixture of 30% Sc_2O_3 + 70% Lu_2O_3 (the percentages represent the atomic ratio in the target)
- HfO_2
- Mixture of 97% Al_2O_3 + 3% Yb_2O_3

The raw data files of all these ion probe tests are available in a data repository. Please contact the Faculty of Engineering and Physical Sciences of the University of Southampton to access it.

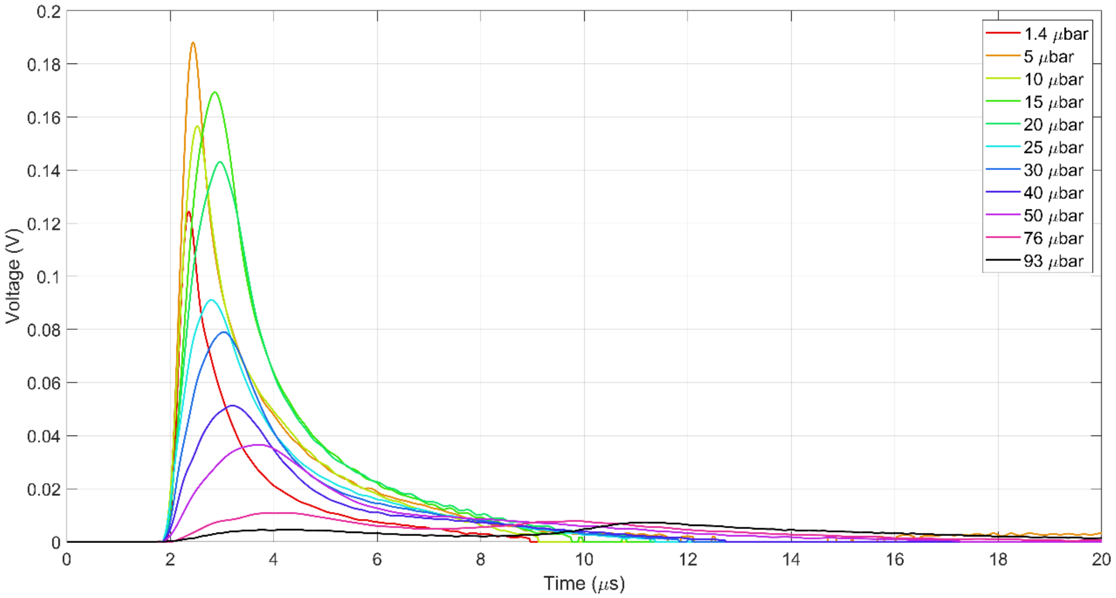

Figure 6.6: Ion probe traces recorded with a Sc_2O_3 target and an ablation fluence of 1.2 J/cm².

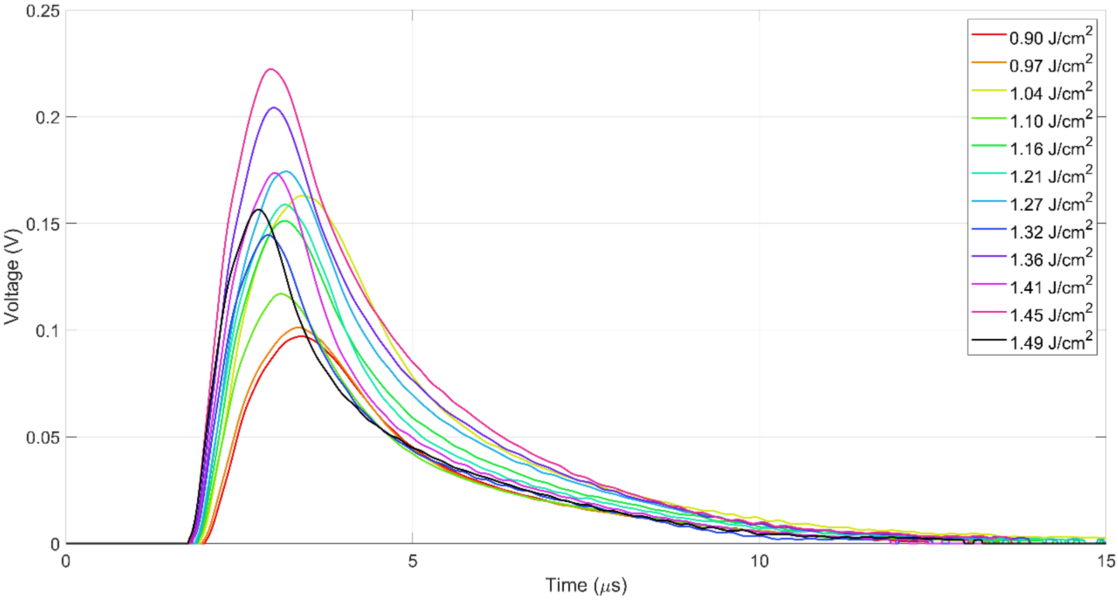

Figure 6.7: Ion probe traces recorded with a Sc_2O_3 target and a O_2 pressure of 20 µbar.

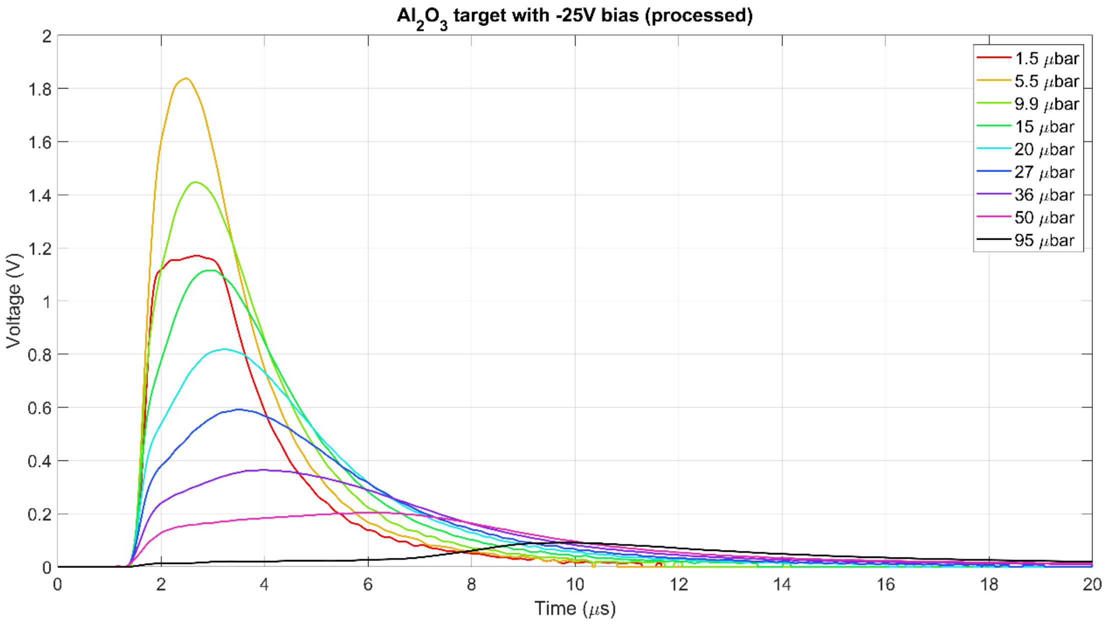

Figure 6.8: Ion probe traces recorded with a Al_2O_3 target and an ablation fluence of 1.7 J/cm².

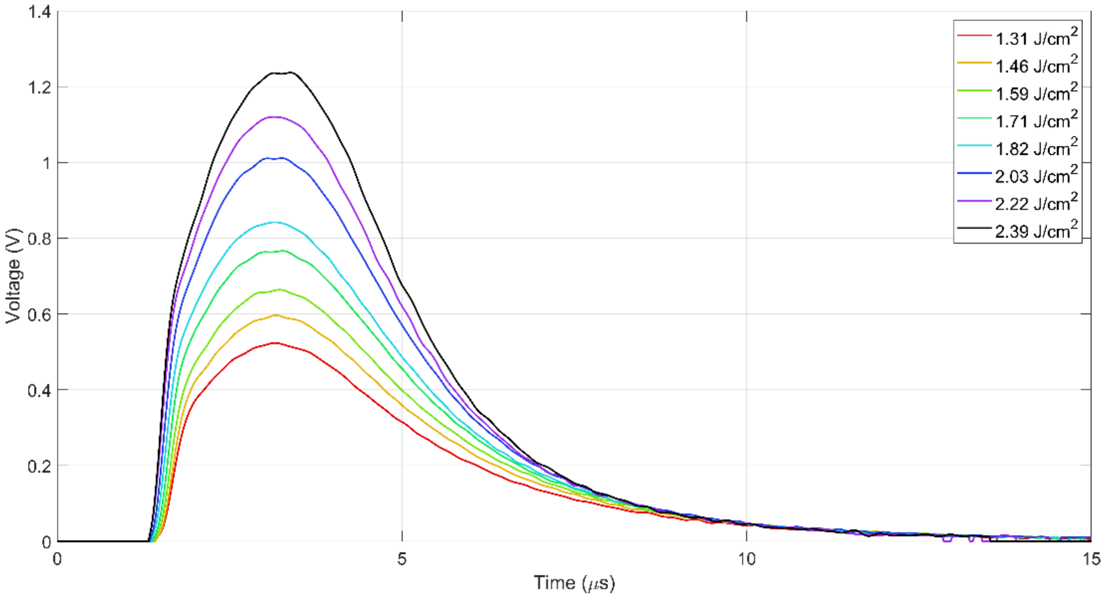

Figure 6.9: Ion probe traces recorded with a Al_2O_3 target and a O_2 pressure of 20 µbar.

Bibliography

AHMED, M. A., HAEFNER, M., VOGEL, M., PRUSS, C., VOSS, A., OSTEN, W. & GRAF, T. 2011. High-power radially polarized Yb:YAG thin-disk laser with high efficiency. *Optics Express,* 19**,** 5093-5104.

AMORUSO, S. 2018. Plume characterization in pulsed laser deposition of metal oxide thin films. *Metal Oxide-Based Thin Film Structures: Formation, Characterization, and Application of Interface-Based Phenomena***,** 133-160.

AMORUSO, S., SCHOU, J. & LUNNEY, J. G. 2008. Influence of the atomic mass of the background gas on laser ablation plume propagation. *Applied Physics a-Materials Science & Processing,* 92**,** 907-911.

ANTOINE, P., LHUILLIER, A. & LEWENSTEIN, M. 1996. Attosecond pulse trains using high-order harmonics. *Physical Review Letters,* 77**,** 1234-1237.

AZIZ, M. J. 2008. Film growth mechanisms in pulsed laser deposition. *Applied Physics a-Materials Science & Processing,* 93**,** 579-587.

BAR, S., HUBER, G., GONZALO, J., PEREA, A., CLIMENT, A. & PASZTI, F. 2003. Europium-doped sesquioxide thin films grown on sapphire by PLD. *Materials Science and Engineering B-Solid State Materials for Advanced Technology,* 105**,** 30-33.

BEECHER, S. J., PARSONAGE, T. L., MACKENZIE, J. I., SLOYAN, K. A., GRANT-JACOB, J. A. & EASON, R. W. 2014. Diode-end-pumped 1.2 W Yb:Y2O3 planar waveguide laser. *Optics Express,* 22**,** 22056-22061.

BIRKHOLZ, M., FEWSTER, P. & GENZEL, C. 2005. *Thin Film Analysis by X-ray Scattering*.

BLANK, D. H. A., KOSTER, G., RIJNDERS, G. A. J. H. M., EELCO VAN, S., SLYCKE, P. & ROGALLA, H. 2000a. Epitaxial growth of oxides with pulsed laser interval deposition. *Journal of Crystal Growth,* 211**,** 98-105.

BOTTEN, I. C., CRAIG, M. S., MCPHEDRAN, R. C., ADAMS, J. L. & ANDREWARTHA, J. R. 1981. The Dielectric Lamellar Diffraction Grating. *Optica Acta,* 28**,** 413-428.

BOYD, R. D., BRITTEN, J. A., DECKER, D. E., SHORE, B. W., STUART, B. C., PERRY, M. D. & LI, L. F. 1995. High-Efficiency Metallic Diffraction Gratings for Laser Applications. *Applied Optics,* 34**,** 1697-1706.

BUNKOWSKI, A., BURMEISTER, O., CLAUSNITZER, T., KLEY, E. B., TÜNNERMANN, A., DANZMANN, K. & SCHNABEL, R. 2006. Diffractive Optics for Gravitational Wave Detectors. *Sixth Edoardo Amaldi Conference on Gravitational Waves,* 32.

CHEN, S. L., ZHAO, Y. A., YU, Z. K., FANG, Z., LI, D. W., HE, H. B. & SHAO, J. D. 2012. Femtosecond laser-induced damage of HfO2/SiO2 mirror with different stack structure. *Applied Optics,* 51**,** 6188-6195.

CHIBA, H., MURAKAMI, K., ERYU, O., SHIHOYAMA, K., MOCHIZUKI, T. & MASUDA, K. 1991. Laser Excitation Effects on Laser Ablated Particles in Fabrication of High-Tc Superconducting Thin-Films. *Japanese Journal of Applied Physics Part 2-Letters,* 30**,** L732-L734.

CULLITY, B. D. 1956. *Elements of X-ray diffraction,* Reading, Mass., Addison-Wesley Pub. Co.

DIETRICH, T., PIEHLER, S., RUMPEL, M., VILLEVAL, P., LUPINSKI, D., ABDOU-AHMED, M. & GRAF, T. 2017. Highly-efficient continuous-wave intra-cavity frequency-doubled Yb:LuAG thin-disk laser with 1 kW of output power. *Optics Express,* 25**,** 4917-4925.

DINARA, T., BAYAN, N., SAMAT, Z., ADIL, M. & ASIYA, I. 2020. Using the Laser in Modern Medicine: World Trends. *Journal of Complementary Medicine Research,* 11**,** 322-332.

ERES, G., TISCHLER, J. Z., ROULEAU, C. M., LEE, H. N., CHRISTEN, H. M., ZSCHACK, P. & LARSON, B. C. 2016. Dynamic Scaling and Island Growth Kinetics in Pulsed Laser Deposition of SrTiO3. *Physical Review Letters,* 117.

ERES, G., TISCHLER, J. Z., ROULEAU, C. M., ZSCHACK, P., CHRISTEN, H. M. & LARSON, B. C. 2011. Quantitative determination of energy enhanced interlayer transport in pulsed laser deposition of SrTiO3. *Physical Review B,* 84.

GABRIEL, V., KOCAN, P. & HOLY, V. 2020a. Effective algorithm for simulations of layer-by-layer growth during pulsed-laser deposition. *Physical Review E,* 102.

GALES, S., BALABANSKI, D. L., NEGOITA, F., TESILEANU, O., UR, C. A., URSESCU, D. & ZAMFIR, N. V. 2016. New frontiers in nuclear physics with high-power lasers and brilliant monochromatic gamma beams. *Physica Scripta,* 91.

GALLAIS, L., MANGOTE, B., ZERRAD, M., COMMANDRÉ, M., MELNINKAITIS, A., MIRAUSKAS, J., JESKEVIC, M. & SIRUTKAITIS, V. 2011. Laser-induced damage of hafnia coatings as a function of pulse duration in the femtosecond to nanosecond range. *Applied Optics,* 50**,** C178-C187.

GALLAIS, L., RUMPEL, M., MOELLER, M., DIETRICH, T., GRAF, T. & AHMED, M. A. 2020. Investigation of laser damage of grating waveguide structures submitted to sub-picosecond pulses. *Applied Physics B-Lasers and Optics,* 126.

GATTASS, R. R. & MAZUR, E. 2008. Femtosecond laser micromachining in transparent materials. *Nature Photonics,* 2**,** 219-225.

GAYLORD, T. K. & MOHARAM, M. G. 1985. Analysis and Applications of Optical Diffraction by Gratings. *Proceedings of the IEEE,* 73**,** 894-937.

GIESTING, P. A. & HOFMEISTER, A. M. 2002. Thermal conductivity of disordered garnets from infrared spectroscopy. *Physical Review B,* 65.

GILA, B. P., JOHNSON, J. W., MEHANDRU, R., LUO, B., ONSTINE, A. H., ALLUMS, K. K., KRISHNAMOORTHY, V., BATES, S., ABERNATHY, C. R., REN, F. & PEARTON, S. J. 2001. Gadolinium oxide and scandium oxide: Gate dielectrics for GaN MOSFETs. *Physica Status Solidi a-Applications and Materials Science,* 188**,** 239-242.

GILL, D. S., ANDERSON, A. A., EASON, R. W., WARBURTON, T. J. & SHEPHERD, D. P. 1996. Laser operation of an Nd:Gd3Ga5O12 thin-film optical waveguide fabricated by pulsed laser deposition. *Applied Physics Letters,* 69**,** 10-12.

GRANT-JACOB, J. A., BEECHER, S. J., RIRIS, H., YU, A. W., SHEPHERD, D. P., EASON, R. W. & MACKENZIE, J. I. 2017. Dynamic control of refractive index during pulsed-laser-deposited waveguide growth. *Optical Materials Express,* 7**,** 4073-4081.

GRIEBNER, U., PETROV, V., PETERMANN, K. & PETERS, V. 2004. Passively mode-locked Yb : Lu2O3 laser. *Optics Express,* 12**,** 3125-3130.

GUAN, L., ZHANG, D. M., LI, X. & LI, Z. H. 2008. Role of pulse repetition rate in film growth of pulsed laser deposition. *Nuclear Instruments & Methods in Physics Research Section B-Beam Interactions with Materials and Atoms,* 266**,** 57-62.

HE, J. J., KOTELES, E. S., LAMONTAGNE, B., ERICKSON, L., DELAGE, A. & DAVIES, M. 1999. Integrated polarization compensator for WDM waveguide demultiplexers. *Ieee Photonics Technology Letters,* 11**,** 224-226.

HERVY, A., CHÉRIAUX, G., GALLAIS, L., MOURICAUD, D. & DJIDEL, S. 2014. Femtosecond laser-induced damage threshold of electron-beam deposited materials for broadband high-reflective coatings on large optics. *Pacific Rim Laser Damage 2014: Optical Materials for High Power Lasers,* 9238.

HERVY, A., GALLAIS, L., CHÉRIAUX, G. & MOURICAUD, D. 2017. Femtosecond laser-induced damage threshold of electron beam deposited dielectrics for 1-m class optics. *Optical Engineering,* 56.

HILLARD, T. C. 2020. Lasers in the era of evidence-based medicine. *Climacteric,* 23**,** S6-S10.

HRABOVSKY, J., KUCERA, M., PALOUSOVÁ, L., BI, L. & VEIS, M. 2021. Optical characterization of Y3Al5O12 and Lu3Al5O12 single crystals. *Optical Materials Express,* 11**,** 1218-1223.

JACOBSEN, J., COOPER, B. H. & SETHNA, J. P. 1998. Simulations of energetic beam deposition: From picoseconds to seconds. *Physical Review B,* 58**,** 15847-15865.

KANNATEY-ASIBU, E. 2009. *Principles of laser materials processing,* Hoboken, N.J., Wiley.

KAPPEL, C., SELLE, A., BADER, M. A. & MAROWSKY, G. 2004. Resonant double-grating waveguide structures as inverted Fabry-Perot interferometers. *Journal of the Optical Society of America B-Optical Physics,* 21**,** 1127-1136.

KNITTL, Z. 1983. Applications of Thin-Films in Optics and the Principles and Methods of Their Design. *Proceedings of the Society of Photo-Optical Instrumentation Engineers,* 401**,** 2-16.

KORTAN, A.R., KOPYLOV, N., KWO, J., HONG, M., CHEN, C.P., MANNAERTS, J.P. and LIOU, S.H., 2006. Structure of Sc_2O_3 films epitaxially grown on α-Al_2O_3 (0001). Applied Physics Letters, 88(2), p.021906.

KUZMINYKH, Y., KAHN, A. & HUBER, G. 2006. Nd3+ doped Sc2O3 waveguiding film produced by pulsed laser deposition. *Optical Materials,* 28**,** 883-887.

KUZMINYKH, Y., SCHEIFE, H., BAR, S., PETERMANN, K. & HUBER, G. 2007. PLD-grown Yb-doped sesquioxide films on sapphire and quartz substrates. *Cola'05: 8th International Conference on Laser Ablation,* 59**,** 462-+.

LEBOEUF, J. N., CHEN, K. R., DONATO, J. M., GEOHEGAN, D. B., LIU, C. L., PURETZKY, A. A. & WOOD, R. F. 1996. Modeling of plume dynamics in laser ablation processes for thin film deposition of materials. *Physics of Plasmas,* 3**,** 2203-2209.

LECOMTE, C. 2013. Understanding Single-Crystal X-ray Crystallography. By Dennis W. Bennett. Weinheim: Wiley-VCH, 2010. Pp. xx + 811. ISBN 978-3-527-32677-8. *Acta crystallographica. Section A, Foundations of crystallography,* 69**,** 208-9.

LEVY-YURISTA, G. & FRIESEM, A. A. 2000. Very narrow spectral filters with multilayered grating-waveguide structures. *Applied Physics Letters,* 77**,** 1596-1598.

LIU, C., CHOR, E. F., TAN, L. S. & DU, A. 2007. Epitaxial growth of Sc2O3 films on GaN (0001) by pulsed laser deposition. *Journal of Vacuum Science & Technology B,* 25**,** 754-759.

LOBBIA, R. B. & BEAL, B. E. 2017. Recommended Practice for Use of Langmuir Probes in Electric Propulsion Testing. *Journal of Propulsion and Power,* 33**,** 566-581.

LOEWEN, E.G. & POPOV, E. (1997). *Diffraction Gratings and Applications*. New York: Marcel Dekker.

MACLEOD, H. A. 2010. Thin-Film Optical Filters, Fourth Edition. *Thin-Film Optical Filters, Fourth Edition***,** 1-772.

MAY-SMITH, T. C., MUIR, A. C., DARBY, M. S. B. & EASON, R. W. 2008. Design and performance of a ZnSe tetra-prism for homogeneous substrate heating using a CO2 laser for pulsed laser deposition experiments. *Applied Optics,* 47**,** 1767-1780.

MEDENBACH, O., DETTMAR, D., SHANNON, R. D., FISCHER, R. X. & YEN, W. M. 2001. Refractive index and optical dispersion of rare earth oxides using a small-prism technique. *Journal of Optics a-Pure and Applied Optics,* 3**,** 174-177.

MENDE, M., SCHRAMEYER, S., EHLERS, H., RISTAU, D. & GALLAIS, L. 2013. Laser damage resistance of ion-beam sputtered Sc2O3/SiO2 mixture optical coatings. *Applied Optics,* 52**,** 1368-1376.

MOTT-SMITH, H. M. 1961. THE THEORY OF COLLECTORS IN GASEOUS DISCHARGES. *In:* SUITS, C. G. (ed.) *Electrical Discharge.* Pergamon.

MOULTON, P. F., CEDERBERG, J. G., STEVENS, K. T., FOUNDOS, G., KOSELJA, M. & PRECLIKOVA, J. 2019. Characterization of absorption bands in Ti:sapphire crystals. *Optical Materials Express,* 9**,** 2216-2251.

MOURKIOTI, G., BASHIR, D., GOVINDASSAMY, G. A., LI, F. F., EASON, R. W., GRAF, T., AHMED, M. A. & MACKENZIE, J. I. 2023. Sc2O3 on sapphire all-crystalline grating-waveguide resonant reflectors. *Applied Physics B-Lasers and Optics,* 129.

NEAUPORT, J., RIBEYRE, X., DAURIOS, J., VALLA, D., LAVERGNE, M., BEAU, V., & VIDEAU, L. (2005). Design, optical characterization, mounting, alignment, and operation of large transmission gratings. *Applied Optics*, 44(16), 3143–3153.

OJEDA-G-P, A., SCHNEIDER, C. W., DÖBELI, M., LIPPERT, T. & WOKAUN, A. 2015. The flip-over effect in pulsed laser deposition: Is it relevant at high background gas pressures? *Applied Surface Science,* 357**,** 2055-2062.

PARSONAGE, T. L., BEECHER, S. J., CHOUDHARY, A., GRANT-JACOB, J. A., HUA, P., MACKENZIE, J. I., SHEPHERD, D. P. & EASON, R. W. 2015. Pulsed laser deposited diode-pumped 7.4 W Yb:Lu2O3 planar waveguide laser. *Optics Express,* 23**,** 31691-31697.

PAULRAJ, J., WANG, R. P., SELLARS, M. & LUTHER-DAVIES, B. 2016. Epitaxial growth of Sc2O3 films on Gd2O3-buffered Si substrates by pulsed laser deposition. *Applied Physics a-Materials Science & Processing,* 122.

PERRY, M. D., PENNINGTON, D., STUART, B. C., TIETBOHL, G., BRITTEN, J. A., BROWN, C., HERMAN, S., GOLICK, B., KARTZ, M., MILLER, J., POWELL, H. T., VERGINO, M. & YANOVSKY, V. 1999. Petawatt laser pulses. *Optics Letters,* 24**,** 160-162.

PIETSCH, U., HOLY, V. & BAUMBACH, T. 2004. *High resolution X-ray scattering from thin films and lateral nanostructures*.

POOLE, P., TRENDAFILOV, S., SHVETS, G., SMITH, D. & CHOWDHURY, E. 2013. Femtosecond laser damage threshold of pulse compression gratings for petawatt scale laser systems. *Optics Express,* 21**,** 26341-26351.

PRENTICE, J. J., GRANT-JACOB, J. A., KURILCHIK, S. V., MACKENZIE, J. I. & EASON, R. W. 2019. Particulate reduction in PLD-grown crystalline films via bi-directional target irradiation. *Applied Physics a-Materials Science & Processing,* 125.

PRENTICE, J. J., GRANT-JACOB, J. A., SHEPHERD, D. P., EASON, R. W. & MACKENZIE, J. I. 2018. Yb-doped mixed-sesquioxide films grown by pulsed laser deposition. *Journal of Crystal Growth,* 491**,** 51-56.

RAKIC, A. D., DJURISIC, A. B., ELAZAR, J. M. & MAJEWSKI, M.L. 1998. Optical properties of metallic films for vertical-cavity optoelectronic devices, Appl. Opt. 37, 5271-5283.

ROSENBLATT, D., SHARON, A. & FRIESEM, A. A. 1997. Resonant grating waveguide structures. *Ieee Journal of Quantum Electronics,* 33**,** 2038-2059.

RUMPEL, M., MOELLER, M., MOORMANN, C., GRAF, T. & AHMED, M. A. 2014. Broadband pulse compression gratings with measured 99.7% diffraction efficiency. *Optics Letters,* 39**,** 323-326.

RUMPEL, M., AHMED, M. & WEINGARTEN, K.J. (2020). Resonant waveguide gratings – versatile devices for laser engineering. *Physik in unserer Zeit*, 51(6), pp. 282-289.

SALEEM, M. R., ALI, R., HONKANEN, S. & TURUNEN, J. 2015. Design and fabrication of sub-wavelength athermal resonant waveguide replicated gratings on different polymer substrates. *Advanced Fabrication Technologies for Micro/Nano Optics and Photonics Viii,* 9374.

SAMBRI, A., AMORUSO, S., WANG, X., GRANOZIO, F. M. & BRUZZESE, R. 2008. Plume propagation dynamics of complex oxides in oxygen. *Journal of Applied Physics,* 104.

SHANKS, K., SENTHILARASU, S. and MALLICK, T.K., 2016. Optics for concentrating photovoltaics: Trends, limits and opportunities for materials and design. Renewable and Sustainable Energy Reviews, 60, pp.394-407.

SHARON, A., ROSENBLATT, D. & FRIESEM, A. A. 1997. Resonant grating waveguide structures for visible and near-infrared radiation. *Journal of the Optical Society of America a-Optics Image Science and Vision,* 14**,** 2985-2993.

SLACK, G. A. & OLIVER, D. W. 1971. Thermal Conductivity of Garnets and Phonon Scattering by Rare-Earth Ions. *Physical Review B-Solid State,* 4**,** 592-&.

SLOYAN, K. A. 2012. *Multi-beam pulsed laser deposition for engineered crystal films.* University of Southampton.

SLOYAN, K. A., MAY-SMITH, T. C., ZERVAS, M. N. & EASON, R. W. 2012. Crystalline garnet Bragg reflectors for high power, high temperature, and integrated applications fabricated by multi-beam pulsed laser deposition. *Applied Physics Letters,* 101.

SMITH, H. M., TURNER, A.F. 1965. Vacuum deposited thin films using a ruby laser. *Applied Optics,* 4**,** 147-148.

SNYDER, A.W. & LOVE, J.D. (1983). *Optical Waveguide Theory*. London: Chapman and Hall.

SOILEAU, M. J. 2015. Laser-Induced Damage Phenomena in Optics: A Historical Overview. *Laser-Induced Damage in Optical Materials***,** 3-7.

STEHLÍK, M., WAGNER, F., ZIDELUNS, J., LEMARCHAND, F., LUMEAU, J. & GALLAIS, L. 2021. Beam-size effects on the measurement of sub-picosecond intrinsic laser induced damage threshold of dielectric oxide coatings. *Applied Optics,* 60**,** 8569-8578.

STRICKLAND, D. & MOUROU, G. (1985). Compression of amplified chirped optical pulses. *Optics Communications*, 56(3), pp. 219-221.

ULBRANDT, J. G., ZHANG, X., HEADRICK, R. L., LIU, R., DAWBER, M. & EVANS-LUTTERODT, K. 2020a. Fast nonthermal processes in pulsed laser deposition. *Physical Review B,* 101**,** 241406.

WANG, S. S. & MAGNUSSON, R. 1993. Theory and Applications of Guided-Mode Resonance Filters. *Applied Optics,* 32**,** 2606-2613.

WANG, S. S., MAGNUSSON, R., BAGBY, J. S. & MOHARAM, M. G. 1990. Guided-Mode Resonances in Planar Dielectric-Layer Diffraction Gratings. *Journal of the Optical Society of America a-Optics Image Science and Vision,* 7**,** 1470-1474.

WHITE, D. P. 1995. A Comparison of the Effect of Radiation on the Thermal-Conductivity of Sapphire at Low and High-Temperatures. *Journal of Nuclear Materials,* 219**,** 165-168.

WILLEMSEN, T., JUPÉ, M., GYAMFI, M., SCHLICHTING, S. & RISTAU, D. 2017. Enhancement of the damage resistance of ultra-fast optics by novel design approaches. *Optics Express,* 25**,** 31948-31959.

WILLMOTT, P. R., HERGER, R., SCHLEPÜTZ, C. M., MARTOCCIA, D. & PATTERSON, B. D. 2006b. Energetic Surface Smoothing of Complex Metal-Oxide Thin Films. *Physical Review Letters,* 96**,** 176102.

ZELINGER, Z., STRIZIK, M., KUBÁT, P., JANOUR, Z., BERGER, P., CERNY, A. & ENGST, P. 2004. Laser remote sensing and photoacoustic spectrometry applied in air pollution investigation. *Optics and Lasers in Engineering,* 42**,** 403-412.

ZYSKIND, J. L., GILES, C. R., SIMPSON, J. R. & DIGIOVANNI, D. J. 1992. Erbium-Doped Fiber Amplifiers and the Next Generation of Lightwave Systems. *At&T Technical Journal,* 71**,** 53-62.